

博士論文

Structural system evaluation under seismic excitation
using adaptive Kalman filter

(適応カルマンフィルターを用いた地震動下の構造システム評価)

楊 曜華

Abstract

Structure system estimation is of great importance for earthquake-prone countries. The lack of information about integrities of structure after an earthquake may conceal potential safety hazards and largely delay re-utilization of infrastructure, which may cause financial and life losses. The structure system estimation mainly includes two parts. One is structural parameter identification and the other is system response estimation. Once structural parameters, which reflect damage conditions, are estimated, corresponding measures can be taken to prevent structural failures or undesired structural responses in the subsequent earthquakes or operations. System responses, especially displacements, can also be used to evaluate structural conditions. For example, the inter-story drift ratio (IDR), defined as inter-story drift normalized by story height, is a key engineering parameter of building damage assessment. Additionally, displacement of a non-linear system under strong earthquake is important because hysteresis information can be assessed.

Structural Health Monitoring (SHM) based on vibration measurement progressed rapidly in the past decade. While most SHM methods based on modal analysis assume linear behaviors of structures, making the application to structure with hysteresis responses difficult, SHM based on data assimilation methods, e.g. Kalman filter (KF), Extended Kalman filter (EKF), Unscented Kalman filter (UKF) and particle filter (PF), capable of handling non-linear behaviors, have recently been developed. Generally, a reasonable system model is firstly assumed; unknown system parameters are then augmented in the state vector; the state vector can be estimated in a recursive manner in time domain using both the model and measured responses in a stochastic manner. In this way, the unknown physical parameters, as well as unmeasured system responses, can be estimated at the same time.

One of difficulties in this approach is that poor selection of noise characteristics in KF can lead to poor performance of the filter or even to divergence. There are two kinds of noise characteristics, i.e. process noise \mathbf{Q} and measurement noise \mathbf{R} , which represent the error of the assumed system model and error of measured signals, respectively. While measurement noise \mathbf{R} might be decided based on sensor characteristics, the process noise \mathbf{Q} requires a time-consuming and subjective trial-and-error tuning. Adaptive Kalman filters proposed to address these issues are so far applied only to a simple problem of parameter estimation of a single-degree-of-freedom (SDOF) system with known input excitation. In order to make the data assimilation method practical, automatic adaption of \mathbf{Q} should be investigated in more realistic problems.

First, parameter identification under known seismic excitation is studied with the extension to multi-degrees-of-freedom systems. An adaptive EKF with two computation modes are studied. The Robbins-Monro (RM) algorithm is combined with the EKF to adjust the process noise automatically. Two computation modes, corresponding to time-invariant (stable mode) and time-variant parameter identification (track mode), are employed in the extended Kalman filter-Robbins Monro (EKF-RM) method. The track mode is direct implementation of RM algorithm with EKF. The stable mode sets the \mathbf{Q} components corresponding to parameters zero while other components are set adaptively; the stable mode can thus handle systems which slowly change over time while the track mode can handle more general time-variant systems. The EKF-RM method is firstly numerically investigated with three simplified models, including a SDOF model, a 4-DOF lumped mass model and a 2D cable stayed bridge model. The ability of tracking parameter variation with the method is studied based on the 4-DOF lumped mass model as well. The EKF-RM method achieves accurate time-invariant parameter identification using stable mode and track stiffness variation instantaneously using track mode. The selection of the computation mode is decided by estimated velocity response. If large discrepancy exists between the estimated and real velocity, the track mode is used, otherwise stable mode is recommended. Additionally, the influence of the use of simplified models rather than accurate models in filter is studied based on a 3D four story frame model and a 3D cable stayed

bridge model numerically. The system models in KF play an important role. An inappropriate system model can result in inconsistent parameter estimates under different earthquake excitations. Furthermore, the EKF-RM method is validated by three shaking table experiments from E-defense database, including a full scale bridge pier experiment, a full scale four story building experiment and a substructure experiment. Time-invariant system parameters are identified using the bridge pier and four story building experiment. Modal frequencies computed by identified parameters show good agreement with those obtained from modal analysis. Also, the forward simulation using the identified parameters can reproduce the responses accurately. Time-variant parameter identification is then demonstrated by using the substructure experiment. The identified time-variant stiffness is consistent with measured hysteresis loops.

Subsequently, an EKF based displacement estimation method for nonlinear SDOF systems under seismic excitation is proposed. In this method, time interval with or without significant nonlinearity is firstly determined using the track mode of EKF-RM method. It is assumed that residual displacement is measured as static deformation after an earthquake. For the time interval of linear behavior, i.e. initial and ending parts of the time history, the observations are acceleration and displacement, which is the summation of double-integrated displacement with high-pass filtering and residual displacement. Regarding the time interval with strong nonlinearity, two EKF schemes are proposed, i.e. one using an augmented state vector with time-variant stiffness parameter estimation and the other assuming a bi-linear system model with optimized model parameters. For both schemes, the incremental Newmark-beta method is employed in the prediction step of EKF. The results are further smoothed by extended Kalman smoother (EKS). The proposed method is numerically verified with SDOF system of three hysteresis models, including bi-linear, tri-linear and Bouc-Wen model. The performance is studied under four different earthquakes of two amplitude levels. Furthermore, the proposed method is validated by shaking table experiments from E-defense database, i.e. a full scale bridge pier experiment and a full scale four story building experiment. The estimated displacements using the proposed method present good accuracies for both the numerical and experimental investigations.

Lastly, parameter identification under unknown seismic excitation is studied. Conventionally, KF based estimation methods require that measurements of seismic excitations be available. However, there are cases where input excitations are difficult or impossible to obtain. Therefore, a state vector including not only system response and parameter variables but also input is employed in the EKF method to solve the joint-state-parameter estimation problem. An offline noise estimation method is combined with the EKF method to adjust process noise covariance matrix \mathbf{Q} automatically. The adaptive EKF-UI (unknown input) method is firstly presented as well as some criteria about joint state-parameter-input estimation problem. Subsequently, the proposed method is numerically investigated with two simplified models of a bridge pier and a 2D four story frame structure. Additionally, the adaptive EKF-UI method is combined with a substructure method and studied on the bridge pier model and a 3D cable stayed bridge model numerically. Furthermore, the proposed method is validated by two shaking table experiments from E-defense database, i.e. a full scale bridge pier experiment and a full scale four story building experiment. System parameter identification results show agreement with those obtained considering known inputs condition. The estimated seismic excitation signals coincide with the measured ones well. Forward simulation using the identified parameters is shown to reproduce the structural responses.

The study in the thesis addresses problems in the application of filtering methods in structural system evaluation using seismic response data. The filtering methods had been limited to ideal numerical simulations and oversimplified experiments. This study improves the numerical stability and accuracy in the inverse problem and achieves parameter estimation and displacement estimation under realistic conditions. However, because of the complexity of some structures and their responses, the proposed methods are expected to be further improved for their wide-spread use in post-earthquake assessment of a variety of structures.

Contents

Abstract.....	I
Chapter 1 Introduction	1
1.1 Research background.....	1
1.2 Review of structure system estimation methods.....	2
1.2.1 Modal analysis method	2
1.2.2 Parameter identification with known input	2
1.2.3 Displacement estimation method	4
1.2.4 Parameter identification with unknown input	6
1.2.5 Adaptive Kalman filter method.....	7
1.3 Objectives of thesis.....	8
1.4 Outline of thesis.....	8
Chapter 2 Parameter identification under know seismic excitation	11
2.1 Chapter outline.....	11
2.2 Parameter identification based on EKF-RM method.....	11
2.2.1 Parameter identification using EKF method	11
2.2.2 RM algorithms for process noise adaption.....	13
2.2.3 Selection of stable mode and track mode.....	15
2.3 Numerical verifications of EKF-RM method	16
2.3.1 A SDOF model case	16
2.3.2 A 4-DOF lumped mass model case	18
2.3.3 A 2D cable stayed bridge model case.....	21
2.3.4 A 4-DOF lumped mass model considering time-variant parameters	24
2.3.5 Effect of input signal noise	27
2.4 Numerical examples considering inaccurate system models.....	28
2.4.1 A 3D four story frame building model	29
2.4.2 A 3D cable stayed bridge model case.....	32
2.4.3 Parameter identification consistency.....	35
2.5 Experiment validation of EKF-RM method	40
2.5.1 Full scale bridge pier experiment.....	40
2.5.2 Full scale four story frame building experiment	48
2.5.3 E-defense substructure experiment	58
2.5.4 Discussion about the application of EKF-RM method	66
Chapter 3 Displacement estimation of nonlinear SDOF system under seismic excitation.....	71
3.1 Chapter outline.....	71

3.2 Dynamic displacement estimation method	71
3.2.1 Equation of motion and acceleration-augmented state space model.....	71
3.2.2 Observation schemes.....	73
3.2.3 Estimation schemes during virtual displacement measurement part.....	74
3.2.4 Extended Kalman smoother	75
3.3 Numerical verification of the dynamic displacement estimation method.....	76
3.3.1 Application to a bi-linear SDOF model.....	76
3.3.2 Application to a Bouc-Wen SDOF model	83
3.3.3 Effect of input signal noise	87
3.3.4 Application to various hysteresis model and earthquake excitations	88
3.4 Experiment validation of the dynamic displacement estimation method	93
3.4.1 Full scale bridge pier experiment.....	93
3.4.2 Full scale four story building experiment	98
Chapter 4 Parameter identification under unknown seismic excitation	105
4.1 Chapter outline.....	105
4.2 Parameter identification under unknown seismic excitation based on adaptive EKF-UI method	105
4.2.1 Equation of motion and EKF system equation.....	105
4.2.2 Offline process noise adaption method	107
4.2.3 Acceleration augmented state vector.....	108
4.2.4 Discussion about observability of joint-input-state-parameter estimation problem.....	109
4.3 Numerical verification of adaptive EKF-UI method	110
4.3.1 A bridge pier model case	110
4.3.2 A 2D four story frame structure case.....	116
4.3.3 Bridge pier model of variant cross section stiffness with foundation	119
4.4 Numerical verification of adaptive EKF-UI method with substructure.....	122
4.4.1 Bridge pier model with substructure	123
4.4.2 A 3D cable stayed bridge case.....	126
4.5 Experimental validation of adaptive EKF-UI method	128
4.5.1 Full scale bridge pier experiment.....	128
4.5.2 Full scale four story frame building experiment	137
Chapter 5 Conclusions	141
Appendix A. SHAKE algorithm.....	145
A.1 Theory	145
A.2 Propagation of harmonic shear waves in a one-dimension system.....	145
A.3 Transition motion.....	148
A.4 Description of Program SHAKE	149

Appendix B. SR model computation for grouped pile foundation in layered soil	151
B.1 lateral vibration of single pile in Winkler medium	151
B.2 Interaction between two piles.....	151
B.3 Dynamic stiffness of SR model of a group of piles	154
References	155

Chapter 1 Introduction

1.1 Research background

Civil engineering structures serve as important roles in the daily life and production in society. The most common structures include: 1) multi-story buildings which provide people places of residence; 2) bridges which are vital links of transportation. These structures are expected to continue service after natural disasters such as earthquakes attack, and their health conditions are crucial for people's life properties and normal production activities. One specific challenge in Japan is that civil engineering structures, especially infrastructures, are facing aging problem in the recent future. According to the data from Ministry of Land, Infrastructure, Transport and Tourism [1], the total number of bridges longer than 15m in Japan now is about 157000 and there will be more than 84000 bridges aging 50 years or more in 10 years, because most of their construction time dates back to the 70s of last century. Furthermore, Japan is a highly earthquake prone country, both small and large earthquake occur very often. Considering these earthquake hazards as well as the situation of structure aging problem, post-earthquake structure evaluation is very necessary and imperative. Based on the evaluation results, corresponding maintenance measures can be taken for the structures.

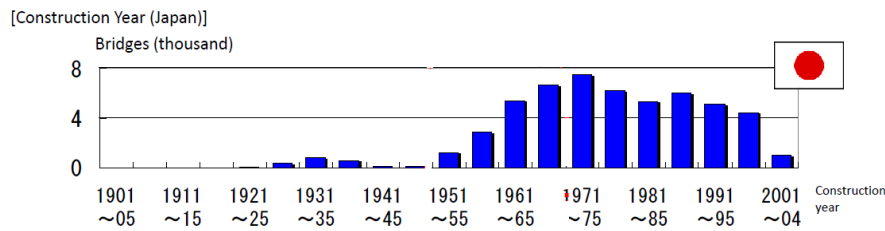


Figure 1.1 bridge construction year in Japan

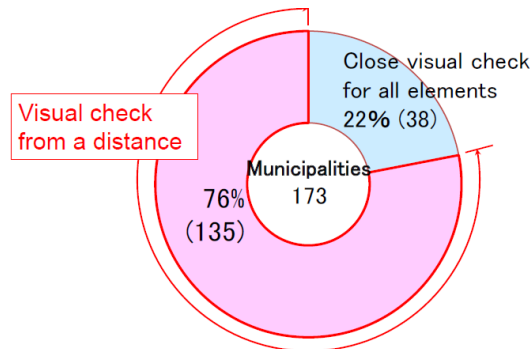


Figure 1.2 bridge inspection method stipulated by municipalities in Japan

So far, the most traditional and pragmatic way of structure evaluation is visual inspection. In Japan, 80% of the manuals on bridge inspection developed by municipalities stipulated visual checks from a distance as an appropriate method, but the quality of the inspection could be problematic [1]. The visual inspection method involves subjective judgement and significant variability of inspection results; it only detects local and visible flaws; and it is difficult in quantifying strength and deformation capacities of bridges [2]. Besides that, quick post-earthquake structure evaluation is hard to achieve using this manually inspection method when the number of structures is large, which is also the problem faced by Japan.

On the other hand, vibration measurement based SHM has progressed rapidly in the past decade taking advantage of advanced sensor system. By installing sensors at critical location of structures,

vibration data can be stored and transmitted wirelessly to structure managers. Then structure conditions can be evaluated based on the data in a remote and rapid manner. In this approach, the structural evaluation method, i.e. system estimation method which will be mainly used in following, is playing a crucial role. Different system estimation methods possess their own characteristics and application areas. A detailed summary review is given below.

1.2 Review of structure system estimation methods

In this section, several system estimation methods and aspects are discussed. At first, some modal analysis methods are presented as well as their limitations; study status of parameter identification based on KF method under known input and unknown input is subsequently discussed; Additionally, adaptive KF methods and their applications in the field of civil engineering are introduced; and finally some displacement estimation methods are reviewed.

1.2.1 Modal analysis method

Modal analysis method might be the most comprehensively studied system estimation method in the field of SHM. Methods such as FDD, ERA [3], SSI [4, 5] and etc. can be applied to structures under ambient excitation (white noise excitation). In the context of earthquake excitations, Chaudhary et al. [6-8] identified physical parameters of base-isolated bridges and soil using seismic records using a two-step system estimate method. The core of method is based on a modal analysis algorithm under in-stationary excitation. Smyth et al. [9] developed a modal analysis method based on Least-square method and successfully applied it to a real bridge under earthquake excitation. Similarly, Siringoringo et al. [10, 11] analyzed the modal properties of three long space cable stayed bridge under a series of earthquakes using System Realization using Information Matrix (SRIM) method. In the modal analysis method, modal frequency, modal damping and modal shape are the main and direct results.

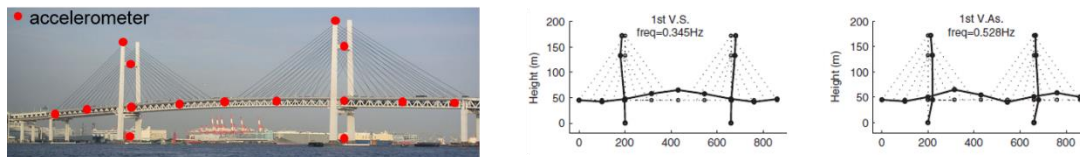


Figure 1.3 Yokohama bay bridge modal analysis [10]

Usually, in the modal analysis method, acceleration signals are measured in some limited positions of structure. Modal properties identified based on the acceleration signals only present information on these positions, e.g. modal shapes. Namely, unmeasured structure response, e.g. displacement, which may serve as important indicator of structure condition, cannot be obtained. This unmeasured response position might be where sensor is difficult to be deployed or the deployed sensor is failed.

When physical parameters are expected to be identified, conversion from modal properties to physical domain needs to be conducted using certain optimization method. This process could be time consuming when parameter space is large and also require empirical information in advance. Moreover, modal properties, especially in lower frequencies, are usually associated with global modes and not sensitive to changes in structural elements in a large system.

1.2.2 Parameter identification with known input

Time domain method has attracted more and more focus in the recent years. One appealing technique is the use of various filters, e.g. KF method, EKF method, unscented Kalman filter (UKF)

method and particle filter (PF) and etc. In this kind of method, generally, a reasonable system model is firstly assumed; system parameters and responses corresponding to the model are then augmented totally in an extended state vector; by taking advantage of noisy measured responses in a probabilistic sense, the state vector can be estimated in a recursive manner in time domain.

As mentioned, since parameters are sometime augmented into the state vector to be estimated, the problem becomes nonlinear even though the original system is linear. The nonlinearity here refers to system equation's characteristic in filter. When calculating error covariance of predicted state vector based on the system equation, the nonlinearity makes it theoretically unsolvable. In this case, EKF, UKF and PF are applicable for handling the nonlinear problem in some approximate manners. In EKF, the nonlinear system equation is approximated using Taylor series expansion, and only the first two terms of it is remained. In this way, the nonlinear system equation is transformed into a linear function, and calculating error covariance of state vector become same as normal KF method assuming Gaussian distribution. In the Taylor series expansion step, Jacobian matrix of state vector has to be calculated. However, sometimes, the Jacobian matrix calculation is not straightforward or even impossible. In UKF [12-14], on the other hand, no approximation is made for the nonlinear system equation, but the calculation of error covariance matrix is approximated. It is calculated based on $2n+1$ significant points, i.e. so called sigma points, using simple weighted sum equation, in which n stands for dimension of state vector. The sigma points are just state vectors with different values. In UKF, calculation of Jacobian matrix is eliminated and only system equation itself is needed, which brings significant convenience. The UKF is also more applicable in dealing with high nonlinearity. The estimation of state vector is exact for polynomials up to order three [15]. However, the cost is that computation time of UKF is much longer than EKF, because the system equation has to be calculated $2n+1$ times in UKF while only one system equation and one Jacobian matrix calculation are required in EKF. Some extension of UKF, e.g. SSUKF [16], can reduce the sigma points as least as $n+2$, the computation burden will still be high comparing to EKF. In PF method, similar to UKF, the error covariance matrix is calculated statistically based on a large number of points in order to remove the Gaussian distribution assumption made in previous two methods. Therefore, it is believed that the PF method is most versatile but time-consuming method among the three. Besides, the normal EKF, UKF and PF method, researchers also developed constrained EKF [17] /UKF [18-20], iterated EKF [21, 22] /UKF [23-26] to meet requirements in various problems.

Numerous works have been contributed to the topic of parameter identification using these filter methods. Yun et al. [27] applied EKF method to identify a nonlinear dynamic system. An offshore structure subjected to wave forces was studied numerically. Hoshiya et al. [28] also introduced EKF into the field of structure estimation soon after. A weighted global iteration procedure was involved into the method in order to obtain stable and convergent solution. Koh et al. [29] combined EKF method with a substructure approach so that computation efficiency can be enhanced when dealing systems with large number of DOF. Yang et al. [30] proposed an adaptive EKF method which can track sudden damage of structural stiffness. Numerical examples were used to prove its effectiveness. Similar work was also done by Lei et al. [31]. Corigliano et al. [32] studied the performance of EKF in parameter identification in explicit dynamics and the effects of process noise \mathbf{Q} and measurement noise \mathbf{R} were also discussed. Ebrahimian et al. [33] applied EKF to identify nonlinear material constitutive model parameters, in which direct differentiation method (DDM) was used to compute Jacobian matrix for EKF. UKF, because of its robustness for nonlinear system estimation, has also received wide investigation. Wu et al. [34] used UKF method for nonlinear system estimation. It was found that UKF can achieve more accurate estimation results than EKF. Mariani et al. [35] also applied UKF to nonlinear structural dynamics. Based on a softening SDOF system, it is shown the performance of UKF is superior to EKF. Omrani et al. [36] applied UKF to identify parameters of a non-degrading hysteresis model in a building model numerically. Xie et al. [24] further employed iterated UKF method to identify nonlinear systems indicating its excellent performance over common UKF. Chatzi et al. [37] compared the performance of UKF and PF method through several

nonlinear system numerical simulations. Similar to the adaptive EKF proposed by Yang et al. [30], Bisht et al. [38] proposed to use UKF to track sudden stiffness changes in structure.

Comparing to the widely available numerical studies about the filter methods, experimental studies are relatively rare. Zhou et al. [39] validated the adaptive EKF method mentioned above using an experimental three story building model under white noise excitations. The similar work was also done by Let et al. [31]. Structural damage of sudden stiffness reduction was validated experimentally in these studies. However, this type of work even possess valuable academic value, is not that much practical and meaningful when it comes to real engineering, since structure usually accumulate damages in a process, e.g. hysteresis loop. More complex one was done by Soyoz et al. [2] that damage conditions of a large scale bridge model under seismic excitations with different level were identified using EKF method. This study shows problems as well. Normal EKF method was applied and only acceleration signals were treated as observations. Results show that stiffness reduction of bridge pier was tracked. However, normal EKF does not possess such kind of tracking ability and acceleration is not very sensitive to stiffness change. Chatzi et al. [40] validated UKF method based on a four story building model under a series of seismic excitations. In this study, it is shown that displacement measurement is very necessary for consistent parameter results under various earthquake excitations. Besides, Chatzi et al. [41] also conduct parameter identification for nonlinear hysteretic systems based on UKF method.

1.2.3 Displacement estimation method

As mentioned earlier, displacement response can be an important indicator reflecting structural health condition after an earthquake excitation. For example, interstory drift ratio (IDR) [42], defined as inter-story drift normalized by story height; hysteresis loop of a SDOF system which could be drawn by displacement versus inertial force contain valuable energy dissipation information of the system [43]. Besides, in the context of system identification, dynamic displacement measurements are preferred because consistent stiffness identification results may not be easily obtained by observing accelerations only as reported by Chatzi et al. [40]. Generally, displacement measurements would be more beneficial in the field of earthquake engineering and structural health monitoring (SHM).

In practical engineering, measuring structural dynamic displacement is usually a challenging task. Since displacement is a relative physical quantity, a stationary platform is needed for contact displacement sensors, e.g. wire-type displacement transducer and LVDT. They might work well in indoor environment, but difficulties in finding reliable platform and deployment could become significant obstacles preventing it from applying them on site. Non-contact technologies, such as laser scanning instruments [44], global positioning systems (GPS) [45] and computer vision-based technique [46], possess as the alternatives. However, drawbacks of them include but not limited to high equipment cost, low sampling frequency and low resolution. A comprehensive review of various inter-story displacement measurement technique are found in [47]. Comparing to displacement transducer, accelerometer is more preferable in practical engineering considering its advantages such as high sampling frequency, robustness and ease of deployment. By double integrating acceleration signals then applying baseline correction and appropriate low pass filter reasonable dynamic displacement could be obtained [48, 49]. Besides, novel dynamic displacement estimation methods using acceleration measurement have been developed [50, 51] and applied to wireless displacement measurement system [52]. The acceleration integration based methods perform well in terms of linear system case, i.e. within 1%~4% error at peak displacement prediction as reported in [47]. However, due to the effect of high pass filter, they cannot be applied to system undergoing nonlinear deformations since low frequency displacement drift component including residual displacement are removed.

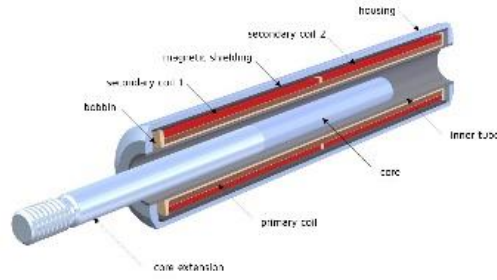


Figure 1.4 LVDT device

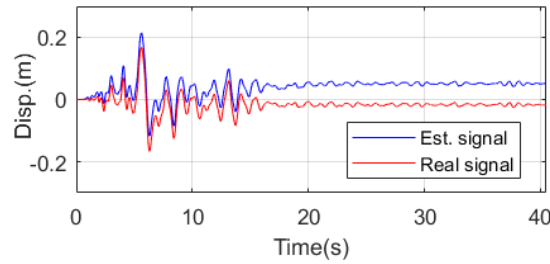


Figure 1.5 comparison of real and estimated displacement using method in [53]

One way to conduct dynamic displacement estimation based on filter method is to fuse acceleration signals with intermittent displacement measurements so that displacement results with high sampling frequency and accuracy could be obtained. Symth et al. [54] presented a multi-rate KF to achieve this purpose, the method was verified with several numerical examples. Chang et al. [55] applied it to an example based on acceleration and videogrammetric displacement measurement. Kim et al. [56, 57] improved the multi-rate KF method by further considering bias of acceleration which was augmented into state vector and estimated with other variables. Similar study was also done by Lei et al. [58], but in this case the bias was instead estimated as an unknown input to system. Additionally, displacement-like measurements, e.g. strain, are also allowed to involve into the estimation. Park et al. [59] applied acceleration and strain measurements to estimate dynamic displacement of a cable stayed bridge. Lourens et al. [60, 61] estimated system responses under unknown input with acceleration and strain data. In the aforementioned methods, displacement or strain measurements are essential and necessary, the problem may become unobservable if they are omitted [62]. Since The filter method could also be applied to estimate system parameters, if a nonlinear system is considered, e.g. Bouc-Wen model [63, 64], the nonlinear dynamic displacement could be estimated accurately along with nonlinear system parameters using acceleration measurements only. Studies have verified it by numerical examples [24, 34, 37]. However, as Li et al. [65] pointed out, in this case, the nonlinear system model should be assumed to be known and correct. Therefore, in fact, because of the existence of model error, most of the experiment validations of aforementioned method were conduct using direct displacement as measurements [41, 66-68]. Recently, a novel estimation method was proposed by Shan et al. [69, 70]. In the study, the hysteretic behavior of system was regarded as unknown input to a known equivalent linear system, and the nonlinear displacement can be estimated along with the unknown input based on KF method. The advantage of the method is that no special characteristic of hysteretic model is adopted in KF which indicate its potential for comprehensive application. However, the method is not stable because basically the problem of system estimation with unknown input is unobservable if only accelerations are observed [62]. Ishihara [53] proposed to estimate displacement of a nonlinear SDOF system based on bi-linear model and only acceleration signal is used. In the method the yielding displacement y_y and post-yielding stiffness ratio α of the bi-linear model are obtained at first using optimization method GA; based on them the displacement signal is estimated using a

phase-depended KF. The method is verified through numerical simulations; however it is found that the method is not robust for experiment data as shown in Figure 1.5.

1.2.4 Parameter identification with unknown input

For the study mentioned above, system inputs, e.g. white noise or earthquake input, are all assumed as measured signals. However, in practical engineering, situations where inputs are difficult or even impossible to measure are frequently encountered, e.g. wind load for a high level building, earthquake excitation for a bridge with deep water foundations as well as sensor failures. To overcome the challenge, researchers have developed approaches for joint input-state-parameter identification. To the best knowledge of the authors, Yang et al. [71] firstly extended the EKF method considering unknown input (EKF-UI). Lei et al. [72] proposed a more straightforward EKF-UI method. Lei et al. [73] further improve the method based on UKF for Bouc-Wen parameter identification with unknown input. In these two methods of Lei et al., the external inputs are actually estimated using linear or nonlinear optimization method, e.g. Least square estimation (LSE) method. Based on these schemes, external input can only be estimated when acceleration on the loading points are directly measured. A general EKF-UI method was proposed by Pan et al. [74] for more flexible measurement arrangement, i.e. acceleration measurement on the loading points are not necessary. Al-Hussein et al. [75] combined UKF method with the weighted global iteration scheme [28] for robust parameter identification. In the process, unknown external inputs are firstly estimated with an iterative LSE method similar to [76-78] based on certain substructures. Then using the estimated external inputs, parameter identification can be conduct for the whole structure. However, in the previous substructure estimation, measurements of all responses at the substructure interface DOFs are required which is not possible in practical engineering. Ding et al. [79] transformed the output-only problem into a joint state-parameter estimation problem by representing unknown inputs by a series of Chebyshev polynomials. The estimation of inputs is achieved by identification of those polynomial parameters. The limitation of the method is that the Chebyshev polynomial is an approximation of true external inputs which will induce implementation errors and difficulties, such as the selection of order of polynomial. Naets et al. [80] proposed a modal coordinate based EKF method for joint input-state-parameter estimation. In this method, an augmented state vector, which includes not only parameter and state but also input variables, is employed. Specifically, random walk model is employed for input estimation. By applying the same random walk model of input, Dertimanis et al. [81] proposed a dual UKF method for the problem. In this method, one UKF is applied to input estimation and the other is devoted to joint state-parameter estimation. By decoupling input from state and parameter, it was claimed that the identifiability of the problem can be improved. Song [82] extended the Gillijins-De Moor filter (GDF) [83, 84], which is already employed for dynamic load estimation of linear system [60, 62, 85, 86], with the unscented transform scheme for nonlinear system estimation with unknown input. More complex numerical investigations of the problem were contributed by Astroza et al [87] in which a 3D frame model with nonlinear material constitutive model was considered. Recently, Erazo et al. [88] proposed an offline approach for nonlinear system estimation with unknown input, in which the Markov chain Monte Carlo (MCMC) method was employed. The offline method was proven to be more robust and accurate than its corresponding online counterpart. In some of the methods mentioned above [71] [72] [81], only acceleration signals are treated as observations. However, from the understanding of the author, by measuring acceleration only, the problem is basically unsolvable, because even inputs cannot be estimated stably [62] not to mention parameter.

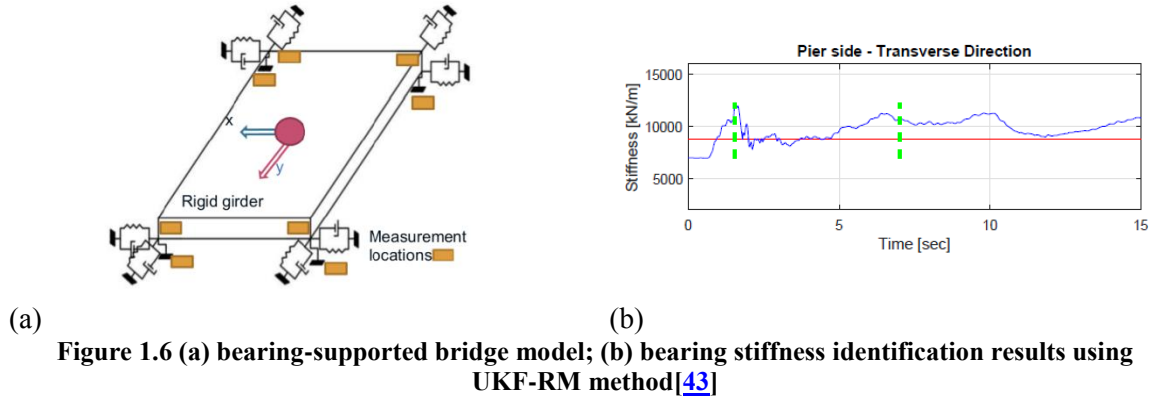
In terms of experiment validations of the joint-state-parameter-input estimation problem, Huang et al. [89] validated their proposed method with a scaled three story model in which external loads of white noise were estimated. Lei et al. [90] estimated unknown earthquake input based on method proposed in [72] for a multi-story shear building model. However, due to observability problem, the

stiffness of bottom floor was identified from modal information. Naets et al. [80] employed a cantilever beam model to demonstrate the effectiveness of their method. Beam length rather than stiffness was identified in that study. More complex experiment was done in [73, 88] in which a full scale 7 story building consisting of a nonlinear chain was considered. Generally, experiment validations are relatively rare comparing with those numerical studies.

1.2.5 Adaptive Kalman filter method

One common problem of the experiments as well as the numerical studies in the last sections, i.e. parameter identification with known input, displacement estimation and parameter identification with unknown input, is that the process noise, which heavily influences the performance of KF and estimation results, is assumed to be known. However, it is not the case in practice. Problem of process noise selection should be addressed appropriately in order to fully take advantage of the KF based method to practical engineering.

It is well known that poor selection of noise characteristics in KF can lead to deterioration of performance of the filter or even divergence. In fact, two kinds of noise characteristics are involved in KF, i.e. process noise and measurement noise, which reflect the error of assumed system model in KF and error of measured signals respectively. Measurement noise might be decided beforehand, since it is usually related to sensor system. As for the process noise, a trial and error manner is usually used to tune the value which might be time-consuming and subjective. Researchers have studied so-called adaptive Kalman filter (AKF) methods to deal with this problem for a long time. (Note that the adaptive EKF method [30] [31] mentioned above is different from the one here because parameter change rather than process noise was addressed in those studies.) An early review of this field back in the 1970s can be found in the work of Mehra [91]. With respect to offline noise adaption method, Bavdekar et al. [92] proposed an expectation-maximization (EM) based noise adaption framework in which extended Kalman smoothing was involved. Similar work was done by Kukkala et al. [93] while results from unscented Kalman smoothing and particle smoothing were discussed. One natural drawback of these methods is that iteration computation has to be conducted which is not favorable for online identification. In terms of online noise adaption method, Soken et al. [94-96] employed a covariance matching based method to adjust process and measurement noise, in which, however, only sudden change of noise characteristics was considered. Van Der Merwe [12, 97] dealt with the problem by augmenting both process and measurement noise into state vector. This method might not be practical for real application when a large multi-degree of freedom (MDOF) system is considered because dimension of state vector may become too large to handle. Calabrese et al. [98] employed a Sage-Husa noise estimator for measurement noise adaption only. Similar method was also introduced in the work of Wang et al. [66] for process noise adaption only. A novel online noise adaption method combined with UKF was investigated in the work of Kontoroupi et al. [68], in which both measurement and process noise were considered. A moving window EKF method was used by Lai et al. [99] to adapt unknown process and measurement noise as well. These two aforementioned methods, however, are quite complicated and a more concise method is expected. Recently, Kuleli [43, 100] proposed the so called UKF-RM method. In this method, the adaption of process noise and measurement noise is achieved by Robbins-Monro algorithm [101]. The method has been applied to a full scale bridge pier experiment and in-situ recorded data from real bridge bearings. The method is numerically verified extensively and presents its robustness with respect to inappropriate initial values in UKF. However, when it comes to responses of physical models, the method cannot always guarantee stable parameter identification results as shown in the Figure 1.6 below.



1.3 Objectives of thesis

Based on the background and literature review introduced in previous sections, research of this thesis is mainly to overcome the inherit problem of Kalman filter method, i.e. automatic adaption of noise parameter, and based on that make the method more practical in real engineering application. The objectives of the thesis mainly include three parts:

- 1) Propose a stable adaptive EKF method for parameter identification under seismic excitation, verify and validate the proposed method through numerical simulations and experiment data;
- 2) Propose a displacement estimation method for nonlinear SDOF system under seismic excitation; verify and validate the proposed method through numerical simulations and experiment data.
- 3) Propose an adaptive EKF-UI (unknown input) method for parameter identification under unknown seismic excitation; verify and validate the proposed method through numerical simulations and experiment data;

1.4 Outline of thesis

Chapter 1 presents background of this research, reviews of system estimation method comprehensively as well as their limitations.

In chapter 2, EKF-RM method is proposed for parameter identification under known seismic excitation. The RM algorithm is combined with the EKF to adjust the process noise automatically. Two computation modes, i.e. stable mode and track mode, are employed for the EKF-RM method for time-invariant and variant parameter identification. Their performance is verified through several numerical simulation cases. Besides, the effect of inaccuracy of system model in KF is studied based on numerical models. The significant role of system model in KF is emphasized. The EKF-RM method is further validated by three shaking table experiments from E-defense database, including a full scale bridge pier experiment, a full scale four story building experiment and a substructure experiment. The stable mode of EKF-RM method is validated using the first two experiments and the track mode is validated using the substructure experiments. Issues about proper selection of computation mode are discussed based on the experiment data.

In chapter 3, displacement estimation methods for nonlinear SDOF system under seismic excitation are proposed. The methods are presented in detail using a bi-linear and a Bouc-Wen SDOF model. Then in order to verify its robustness and practicability, various cases considering 3 hysteresis models, 4 earthquake excitations and 2 amplitude levels, i.e. total 24 cases, are employed for verification. Situations where the performances of the proposed methods are limited are pointed out and explained. The methods are also validated through the bridge pier and four story building experiments. In total 8 cases in which structure experienced strong nonlinearities are selected for the

validation. The estimation displacement signals, especially maximum displacement values, are compared with directly measured ones.

In chapter 4, an adaptive EKF-UI method is proposed for parameter identification under unknown seismic excitation. Similarly, the method is firstly verified by numerical simulation cases considering accurate and inaccurate modes in KF. Subsequently, the combination of the method with substructure method is investigated numerically. Issues about substructure selection and effect of measurement noise are also discussed. Moreover, the adaptive EKF-UI method is validated through the bridge pier and four story building experiments. Parameter results based on the method are compared with those identified considering known input using EKF-RM method.

Finally, conclusions are given in chapter 5.

Chapter 2 Parameter identification under know seismic excitation

2.1 Chapter outline

In this chapter, a simple yet effective RM algorithm [43] is introduced into EKF method for online process noise adaptation. The process noise is estimated based on innovation of estimated state vector in a moving average manner by using a forgetting factor. For the following parts of the chapter, the EKF method and RM algorithm are reviewed in detail in the section 2. Then in the section 3, the EKF-RM method is numerically investigated through three models simplified from real civil structures, including a SDOF model, a 4-DOF lumped mass model and a 2D cable stayed bridge model. The ability of tracking parameter variation, especially stiffness, is also shown in this section based on the 4-DOF lumped mass model. In the section 4, cases where using simplified models rather than accurate models in filter, which may represent the most usual situations in real civil engineering, are also numerically studied based on a 3D four story frame model and a 3D cable stayed bridge model. In the section 5, three shaking table experiments from E-defense database [102-104], i.e. a full scale bridge pier experiment, a full scale four story building experiment and a substructure experiment, are used to validate the method. For the bridge pier and four story building experiment, modal frequencies computed using identified parameters and those obtained from SRIM method are compared. For the substructure experiment which shows strong nonlinearity, reasonable time-variant stiffness results are obtained with the method and compared with measured hysteresis loop.

2.2 Parameter identification based on EKF-RM method

Equation of motion (EOM) of structure system in linear range under seismic excitation can be written as

$$M\ddot{\mathbf{x}}(t) + C\dot{\mathbf{x}}(t) + K\mathbf{x}(t) = -M\mathbf{L}\ddot{\mathbf{u}}_g \quad (2.1)$$

in which $\mathbf{x}(t)$, $\dot{\mathbf{x}}(t)$, $\ddot{\mathbf{x}}(t)$ are vectors of displacement, velocity and acceleration respectively; M , C and K are mass, damping and stiffness matrix, respectively which are all constant if linear elastic assumption is considered; $\ddot{\mathbf{u}}_g$ is input ground acceleration while L is an associated influence vector. Usually, the mass matrix M can be determined with accuracy using geometry and material information from design drawings; the mass matrix is thus regarded as known in this study. The objective of system estimation here is to estimate system parameters, i.e. stiffness and damping coefficients corresponding to K and C , as well as unmeasured system responses based on known input acceleration and partially measured system responses.

2.2.1 Parameter identification using EKF method

EKF method, compared to UKF method, possesses much higher computation efficiency and similar accuracy for linear system parameter identification [34]. Because this thesis mainly focuses linear system parameter identification, in the following EKF will be applied if there is no special notation. In order to estimate system parameters and responses simultaneously, the parameters are augmented into the state vector as

$$\mathbf{X}_a = \begin{bmatrix} \mathbf{x}(t)^T & \dot{\mathbf{x}}(t)^T & \boldsymbol{\theta}^T \end{bmatrix}^T \quad (2.2)$$

in which $\boldsymbol{\theta}$ is an vector containing unknown system parameters to be identified. The system equation is written with the augmented state vector as follow

$$\frac{d\mathbf{X}_a(t)}{dt} = \frac{d}{dt} \begin{bmatrix} \mathbf{x}(t) \\ \dot{\mathbf{x}}(t) \\ \boldsymbol{\theta} \end{bmatrix} = \begin{bmatrix} \dot{\mathbf{x}}(t) \\ \mathbf{M}^{-1}[-\mathbf{M}\mathbf{I}\ddot{\mathbf{u}}_g - \mathbf{K}(\boldsymbol{\theta})\mathbf{x}(t) - \mathbf{C}(\boldsymbol{\theta})\dot{\mathbf{x}}(t)] \\ \mathbf{0} \end{bmatrix} \quad (2.3)$$

where \mathbf{K} and \mathbf{C} are written as functions of unknown parameter vector $\boldsymbol{\theta}$. For example, the stiffness matrix \mathbf{K} in most cases is written as

$$\mathbf{K} = k_1\mathbf{S}_1 + k_2\mathbf{S}_2 + \dots + k_n\mathbf{S}_n \quad (2.4)$$

when N unknown stiffness parameters are considered. $\mathbf{S}_i (i=1 \sim n)$ is an unit stiffness matrix corresponding to stiffness parameter k_i ; matrix \mathbf{C} can also be assembled in the same way.

If the continuous form equation is transformed into a discrete form and model error of system is further considered, the nonlinear system equation, Eq.(2.3), can be written as

$$\mathbf{X}_a(k+1) = \mathbf{f}(\mathbf{X}_a(k), \ddot{\mathbf{u}}_g(k)) + \mathbf{w}(k) \quad (2.5)$$

in which $\mathbf{w}(k)$ stands for the process noise vector consisting of uncorrelated zero mean noises; k stands for time instant; function $\mathbf{f}(\bullet)$ can be achieved by any numerical integration algorithms, e.g. Newmark-beta method, Runge-Kutta method.

Usually, only a limited number of system responses are measured for a multi-degree of freedom (MDOF) system. The equation corresponding to measurement information, known as observation equation, is written as

$$\mathbf{y}(k+1) = \mathbf{h}(\mathbf{X}_a(k+1), \ddot{\mathbf{u}}_g(k+1)) + \mathbf{v}(k+1) \quad (2.6)$$

in which $\mathbf{v}(k+1)$ stands for measurement noise vector consisting of uncorrelated zero mean noises as well; \mathbf{y} is observation vector containing various system responses, e.g. displacement, velocity, acceleration, strain and etc. $\mathbf{h}(\bullet)$ could be a linear function when observations only include displacements, velocities or ones calculated from them directly, or be a nonlinear function when observations need to be extracted from state vector indirectly, e.g. accelerations.

In EKF, optimal estimation of state vector is achieved by prediction step using system equation (2.5) and correction step using observation equation (2.6) for each time instant in a recursive manner. Suppose $\hat{\mathbf{X}}_a(k/k)$ and $\mathbf{P}(k/k)$ are estimated value and error covariance matrix of state vector at k instant based on $\mathbf{y}_{1:k}$, i.e. measurements from 1 to k instant, a prior estimation and covariance matrix of state vector at $k+1$ instant can be obtained using system equation

$$\hat{\mathbf{X}}_a(k+1/k) = \mathbf{f}(\hat{\mathbf{X}}_a(k/k), \ddot{\mathbf{u}}_g(k)) \quad (2.7)$$

$$\mathbf{P}(k+1/k) = \mathbf{F}(k)\mathbf{P}(k/k)\mathbf{F}^T(k) + \mathbf{Q}(k) \quad (2.8)$$

in which $F(k)$ is sensitivity matrix or Jacobian matrix of function $f(\bullet)$, namely

$$F(k) = \left. \frac{\partial f(X_a, \ddot{u}_g)}{\partial X_a} \right|_{X_a = \hat{X}_a(k/k)} \quad (2.9)$$

$Q(k)$ is the process noise variance- covariance matrix, i.e. $Q(k) = E[w(k)w(k)^T] = Q_k \delta_{ij}$.

Based on this prior estimation of state vector, a posterior estimation and covariance matrix of state vector at $k+1$ instant can be obtained by using observation equation

$$\hat{X}_a(k+1/k+1) = \hat{X}_a(k+1/k) + G[y(k+1) - h(\hat{X}_a(k+1/k), \ddot{u}_g(k+1))] \quad (2.10)$$

$$P(k+1/k+1) = P(k+1/k) - G(k)P_y(k+1/k)G(k)^T \quad (2.11)$$

in which $G(k)$ is the so called Kalman filter gain matrix and $P_y(k+1/k)$ is prior estimation of observation covariance matrix

$$G(k) = P(k+1/k)H^T(k+1)/P_y(k+1/k) \quad (2.12)$$

$$P_y(k+1/k) = H(k+1)P(k+1/k)H^T(k+1) + R(k+1) \quad (2.13)$$

in which $H(k+1)$ is Jacobian matrix of function $h(\bullet)$, namely

$$H(k+1) = \left. \frac{\partial h(X_a, \ddot{u}_g)}{\partial X_a} \right|_{X_a = \hat{X}_a(k+1/k)} \quad (2.14)$$

This procedure is supposed to be conducted recursively, regarding posterior estimation of previous instant as initial value for current instant.

2.2.2 RM algorithms for process noise adaption

In fact, the application of adaptive Kalman filter mainly focuses on the field of aerospace engineering and navigation [21, 94-96, 105-115] as well as neural network training [116, 117], imaging processing [118] and etc. One simple yet effective noise adaption method is Robbins-Monro stochastic approximation method which is introduced by Kuleli [43] in the field of civil engineering. The method is originally an algorithm to find root of function which may not be computed directly but estimated from noisy observations [101, 119]. Estimation of Q matrix using RM method can be formulated as below

$$Q(k+1) = (1 - \alpha_Q)Q(k) + \alpha_Q d(k+1)d(k+1)^T \quad (2.15)$$

$$d(k+1) = \hat{X}_a(k+1/k+1) - \hat{X}_a(k+1/k) \quad (2.16)$$

in which $Q(k+1)$ and $Q(k)$ are the process noise variance-covariance matrix of next step and current step respectively; $d(k+1)$ is the so called state innovation vector based on prior and posterior

estimation of state vector. The $\mathbf{Q}(k+1)$ matrix is further constrained to have a diagonal form assuming the process noise is uncorrelated, as mentioned above. α_Q is a small positive value, $0 < \alpha_Q < 1$, served as a forgetting factor to average estimation of \mathbf{Q} over a period of time. The flowchart of the proposed EKF-RM method is shown in Figure 2.1.

This method is similar to the ones used in [66] and the formula of it is presented as below:

$$\mathbf{Q}(k+1) = (1 - \alpha_Q)\mathbf{Q}(k) + \alpha_Q \left[\mathbf{d}(k+1)\mathbf{d}(k+1)^T + \mathbf{P}(k+1) - \mathbf{F}(k)\mathbf{P}(k/k)\mathbf{F}^T(k) \right] \quad (2.17)$$

In this formula, besides the innovation vector $\mathbf{d}(k+1)$, the state vector error covariance matrix terms $\mathbf{P}(k+1)$ and $\mathbf{F}(k)\mathbf{P}(k/k)\mathbf{F}^T(k)$ are also involved which might result in instability problems of the filter. To avoid filter divergence, the authors also introduce divergence judgment criteria and related counter-measures which make the method complex.

Specially, the parameter variables in state vector should be concerned. When system parameters are treated as constant value to be identified, elements corresponding to parameters in \mathbf{Q} matrix should be constrained as zero, so that stable parameter estimation time history can be achieved. This computational mode will be referred as stable mode in the following. On the other hand, when the process noise of parameters is non-zero, the filter is able to track parameter variation in time domain based on formulations in section 2.2.1. This is because the process noise can actually be understood as change of parameters.

$$\boldsymbol{\theta}(k+1) = \boldsymbol{\theta}(k) + \mathbf{w}_\theta(k) \quad (2.18)$$

Beside the adaption of \mathbf{Q} matrix, the RM algorithms can also be applied to adapt \mathbf{R} matrix in a same manner as (2.15)

$$\mathbf{R}(k+1) = (1 - \alpha_R)\mathbf{R}(k) + \alpha_R \boldsymbol{\varepsilon}(k+1)\boldsymbol{\varepsilon}(k+1)^T \quad (2.19)$$

$$\boldsymbol{\varepsilon}(k+1) = \mathbf{y}(k+1) - \mathbf{h}(\hat{\mathbf{X}}_a(k+1/k), \ddot{\mathbf{u}}_g) \quad (2.20)$$

In which $\mathbf{R}(k+1)$ and $\mathbf{R}(k)$ are the variance-covariance matrix of measurement noise of next step and current step respectively; $\boldsymbol{\varepsilon}(k+1)$ is the measurement innovation vector.

In case of KF based state estimation (system response only), the adaption of \mathbf{Q} and \mathbf{R} matrix can be conduct at the same time [120]. Even for joint state-parameter estimation, the simultaneous adaption has been shown to work in some cases [68, 99]. However, considering parameters are unknown values and system model assumed in filter may not be close to physical model in reality, the adaption of \mathbf{R} matrix is not included for stability concern in this study. As mentioned previously, the measurement noise can be readily available from properties of sensor devices.

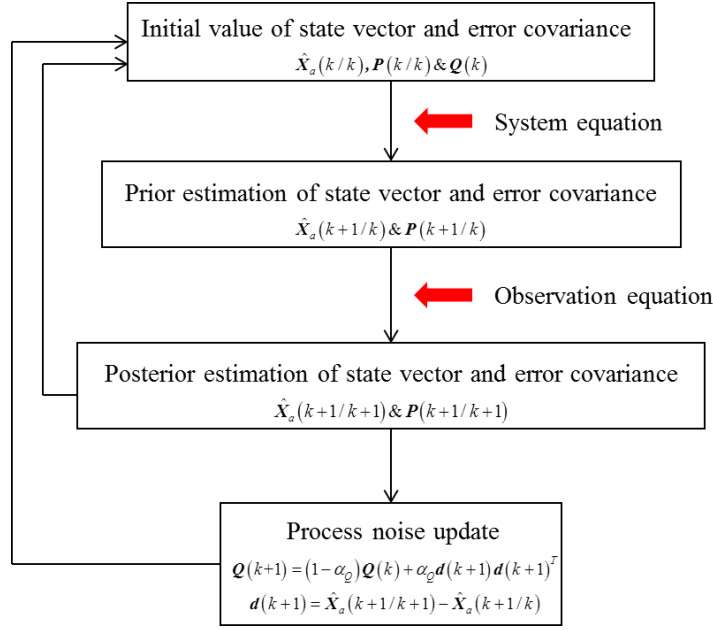


Figure 2.1 flow chart of EKF-RM method

2.2.3 Selection of stable mode and track mode

In terms of selection of the two computation modes, a criterion has to be set so that the two modes can be applied appropriately depending on situations. In fact, if system model in filter is same as physical model exactly, track mode can always be applied even parameters to be identified are actually time-invariant. However, in practical engineering, because of existence of model error especially in MDOF system, applying track model to a no-damage or slight-damage system can sometimes induce significant parameter fluctuations which may contain trivial information and even divergence for a large system. In this case, stable mode is preferred. Conversely, applying stable mode to a system with strong nonlinearity may induce to loss of important parameter variation information. Track model has to be applied in this situation.

In practice, accelerometers are mostly commonly used sensors. However, using only acceleration measurements in filter may result in inconsistent and inaccurate parameter estimation especially stiffness. Displacement are recommended to be included in observation as reported by Chatzi et al. [40]. In reality, dynamic displacement and velocity, if not measured directly, can be obtained by integrating measured acceleration and conducting proper high-pass filter in sequence. Therefore, acceleration measurement and corresponding integrated displacement at same point can be applied to filter simultaneously. Nonlinear residual displacement estimation is out of scope of this study. If system performs mainly in linear phase, estimated velocity based on stable mode using acceleration and the integrated displacement can usually fit with the integrated velocity well. While for system with strong nonlinearity, estimated velocity based on stable mode cannot fit with the integrated one well and present strong discrepancy. Track mode is preferable in this situation. During the process of system estimation using EKF-RM method, the stable mode is suggested to be firstly employed with accelerations and integrated displacements as observations. By checking the fitness of estimated velocities and corresponding integrated velocities, whether the system perform linearly or nonlinearly can be roughly confirmed. If the fitness is low, the track mode is employed. The appropriate computation mode is thus selected.

The use of integrated displacements as observations only with the fitness check of velocities and accelerations simultaneously is also applicable. In this case, however, the system model in filter should be accurate enough. From a conservative point of view, a system model may not match with

physical model well and accelerations may be too difficult to fit precisely. Therefore, acceleration and the integrated displacement are employed as observations in this study.

2.3 Numerical verifications of EKF-RM method

In this section, the effectiveness of the proposed EKF-RM method is demonstrated with several numerical examples. A SDOF model, a 4-DOF lumped mass model and a 2D cable stayed bridge model is used to verify the stable mode of the proposed method. The number of DOFs of these models is becoming larger. While, in the end, the 4-DOF lumped mass model considering time-variant stiffness on its bottom floor is used to demonstrate the track mode of this EKF-RM method. In this part of numerical simulations, acceleration responses will be firstly superimposed by white noise to consider sensor noise in reality; then velocity and displacement are obtained by integrating and double integrating the noisy acceleration, which is the same way employed in practical engineering. Specifically, the 4th order Butterworth filter is applied and the cut-off frequency of it is decided based on the procedures presented in [43].

2.3.1 A SDOF model case

This SDOF system model is simplified from a full scale bridge pier experiment, called C1-1 experiments, in E-defense shaking table laboratory [103], as showing in the figure below. The reinforced concrete (RC) bridge pier was designed based on 1964 Japanese bridge design code as a typical flexural failure dominant column. The column was mounted on the shake table, with its deck and weights supported by steel frames, to represent inertial force transferred from superstructure. Details about the setup and monitoring system of this experiment will be given in section 2.5.1 .

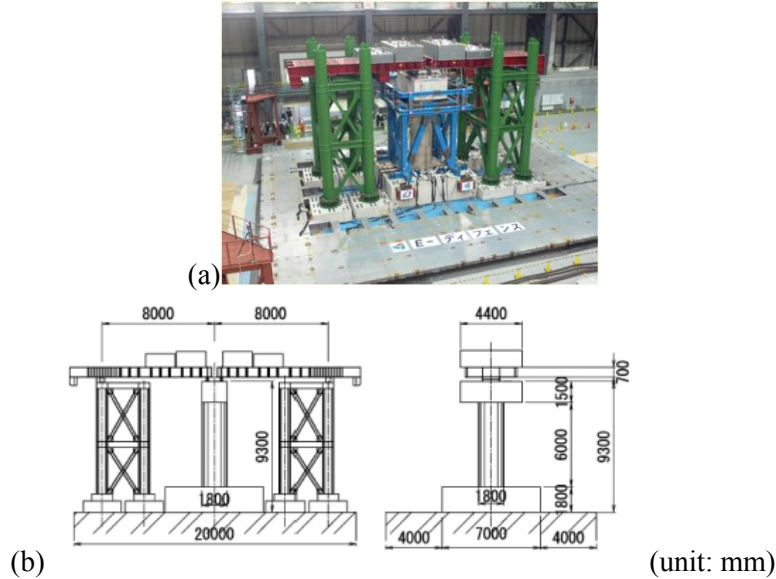


Figure 2.2 E-defense C1-1 experiment model ;

(a) C1-1 experiment setup on E-defense shaking table; (b) supporting system for C1-1 experiment model

The total weight of the superstructure above the pier cap is 2080kN; additionally, the weight of pier itself is 794.5kN according to the experiment report. Therefore, the equivalent SDOF mass is calculated as the sum of whole superstructure weight and half of pier weight which is 252.5ton. The design value for stiffness is also given from the report as $k=32506\text{kN/m}$. 5% damping ratio is considered in this model which corresponds to $c=286.5\text{kNs/m}$.

The forward analysis is conducted using Newmark-beta method with time sample equals to 0.005s. Takatori earthquake shown in Figure 2.3 is treated as excitation. White noise whose RMS are 5% of acceleration signal's RMS (around 2.0 m/s²) are added. The double integrated displacement and the original acceleration are treated as observations. Two situations are compared here, i.e. one applying the stable mode of the EKF-RM method and the other using a wrongly assumed \mathbf{Q} matrix in which the process noise for displacement and velocity equal to 10^{-4} , namely $\mathbf{Q} = \text{diag}([10^{-4}, 10^{-4}, 0, 0])$ (for displacement, velocity and parameters, respectively). The \mathbf{Q} matrix is also the initial one for EKF-RM method. The process noise used here is intentionally set as a large value and also applied as the initial one for EKF-RM method so that the capability of noise adaption of the proposed method could be presented. For both situations, \mathbf{R} matrix is same, i.e. $\mathbf{R} = \text{diag}([10^{-6}, 10^{-2}])$ which means 10^{-6} and 10^{-2} are measurement noise variances for displacement and acceleration respectively. The filter starts working with initial parameter vector set as $1.5\theta_{real}$, initial error covariance matrix for parameter vector as $\text{diag}([0.1\theta_{real}]^2)$. Besides, the α_Q coefficient of RM algorithm is set as 1/30. The time interval for identification is shown in Figure 2.3(a) specifically.

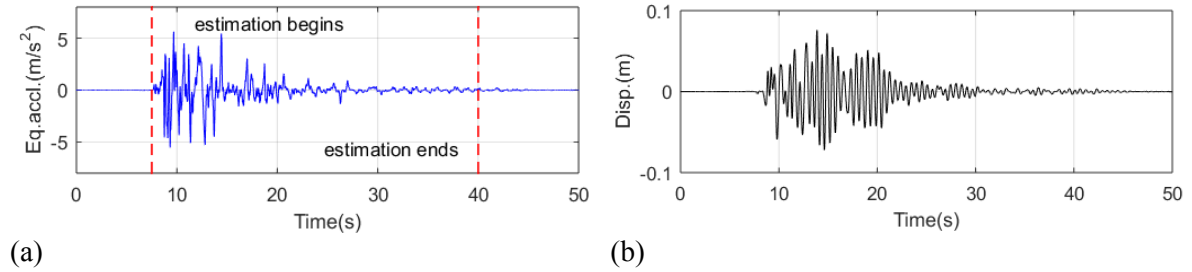


Figure 2.3 (a) Takatori earthquake; (b) displacement of SDOF model

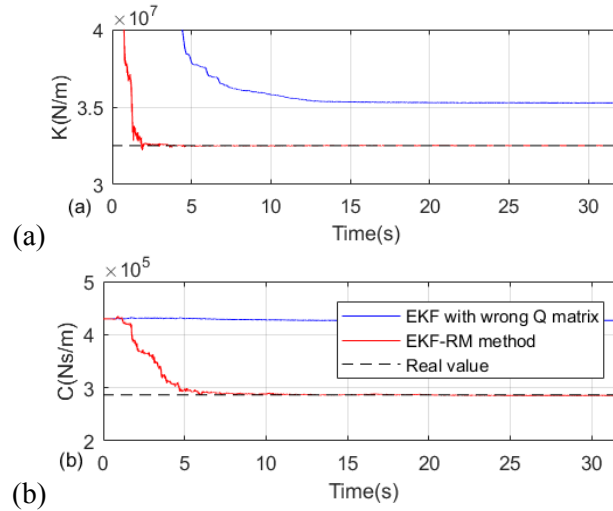


Figure 2.4 parameter convergence of SDOF model; (a) comparison of stiffness; (b) comparison of damping

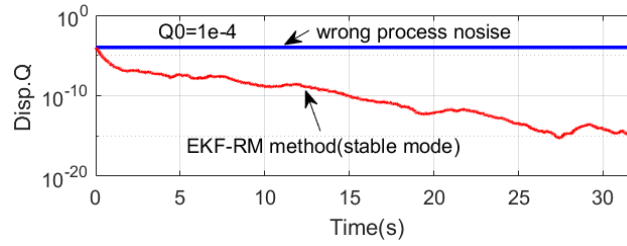


Figure 2.5 comparison of displacement process noise

The parameter estimation results are shown in Figure 2.4. It can be found that, by using EKF-RM method, stiffness parameter converges to the real value with only 2 seconds while it takes a bit longer time for damping factor to converge which is a common phenomenon. The converged parameter results almost coincide with the real values. The error of stiffness is less than 0.01% while the error of damping factor is about 0.2%. On the other hand, by using the wrong process noise, even though the parameters seem to converge to stable values, they are far away from the real ones especially for damping factor. Figure 2.5 shows the comparison of process noise during estimation. Theoretically speaking, the process noise here should be zero because the model assumed in filter is exactly the model used for generating signals. Both of the two situations start from the same initial values. The EKF-RM method continues to find appropriate process noise towards a small value especially after parameter convergences. Comparing to that, the wrongly set process noise is far beyond reasonable value by which a complete convergence of parameter cannot be achieved.

2.3.2 A 4-DOF lumped mass model case

A 4-DOF lumped mass model is simplified from a full scale four story frame building in E-defense shaking table laboratory [102]. This prototype experiment model is used to test the seismic-resistant performance and damage level of existent steel frame structure under the seismic load designated by current Japanese seismic design code. Structural redundancy from large earthquake excitation till complete collapse is also supposed to be confirmed. This building, with three dimensions of 10m, 6m and 14.375m, is a typical representation of multi-story steel frame building in Japan. The height of each floor is 3.875m, 3.5m, 3.5m, 3.5m from the bottom to top as shown in Figure 2.6(a). The column of it is of 300×300×9 (unit: mm) box section, deployed two and three in a row in the north-south (X) and west-east (Y) direction respectively. Each floor of this building was constructed by various H steel beam and concrete decks which were connected by stud bolts. Besides those structural members, accessory members such as steel stairs, exterior walls windows were also included.

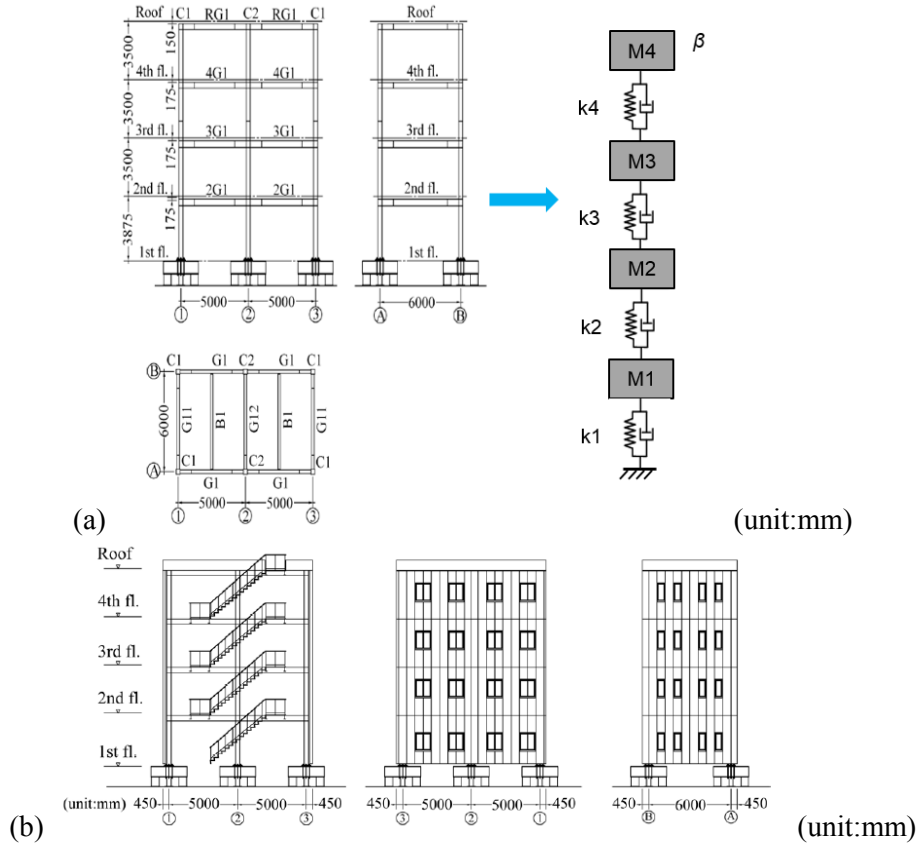


Figure 2.6 (a) frame structure of the building mode; (b) outlook of the building model

In terms of the simplified 4-DOF lumped mass model, the equivalent concentration mass for each floor are 49.1, 48.8, 48.4 and 59.9 ton from the bottom to top according to the experiment report. The stiffness for each floor is 23800 kN/m. The damping matrix for the numerical model is assumed to be Rayleigh damping form with stiffness damping coefficient $\beta=0.01$. The natural frequencies of this model are 1.16Hz, 3.39Hz, 5.30Hz, and 6.58Hz.

Firstly, signals are generated using Newmark-beta method with time interval of 0.005 s considering Takatori-earthquake shown in Figure 2.7 as excitation. White noise whose RMS are 5% of signals' RMS (around 0.5 m/s²) are added. Double integrated displacement signals on the first three floors are employed in order to identify the four stiffness parameters $k1$, $k2$, $k3$, $k4$ from bottom to top floor and one damping factor β . By using the partial measurement arrangement, the accuracy of estimated responses of top floor could also be checked. Similarly, two situations are compared here, i.e. one applying the stable mode of the EKF-RM method and the other using a wrongly assumed \mathbf{Q} matrix in which the process noise for displacement and velocity equal to 10^{-4} , namely $\mathbf{Q}=\text{diag}([10^{-4}\mathbf{I}_{4\times1}, 10^{-4}\mathbf{I}_{4\times1}, \mathbf{0}_{5\times1}])$. The \mathbf{R} matrix is set as $\text{diag}([10^{-7}\mathbf{I}_{3\times1}, 10^{-3}\mathbf{I}_{3\times1}])$. The filter starts working with initial parameter values as $1.5\theta_{\text{real}}$ and error covariance matrix as $\text{diag}([0.1\theta_{\text{real}}]^2)$. Besides, the α_Q coefficient of RM algorithm is set as 1/30. The period of time of estimation is shown in Figure 2.7 specifically.

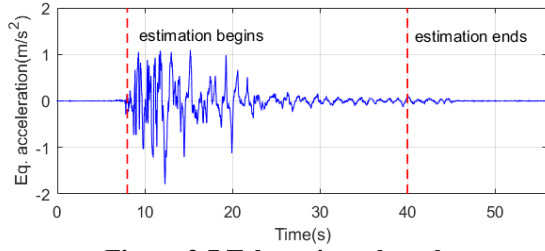


Figure 2.7 Takatori earthquake

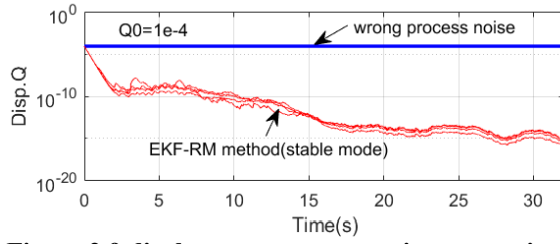


Figure 2.9 displacement process noise comparison

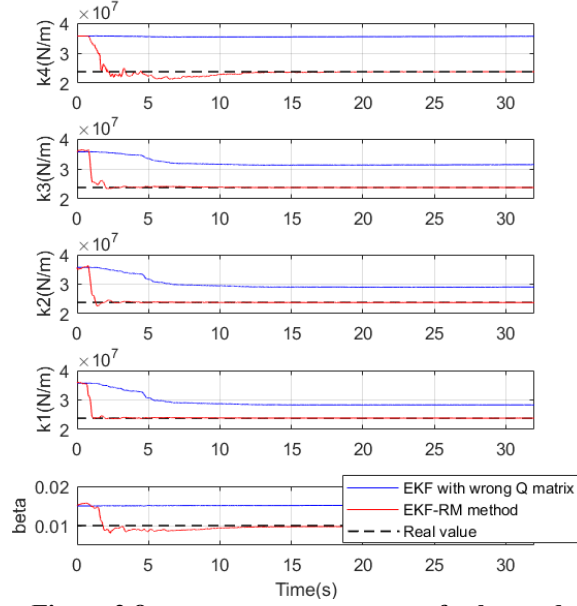


Figure 2.8 parameter convergences for lumped mass model

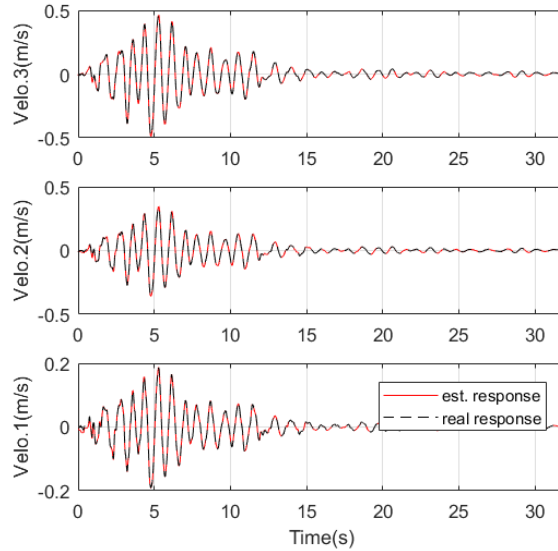


Figure 2.10 the 1st~3rd floor velocity comparison

The parameter identification results are shown in Figure 2.8. In this case, by applying EKF-RM method, parameters can converge to accurate values after a short period of time. For parameter k_1 , k_2 and k_3 , for which corresponding floors are directly measured, convergence is achieved within about 2 seconds while it takes approximately 10 seconds for parameter k_4 to completely converge to the real value since the top floor is unmeasured. The errors of all converged parameters are about 0.1%. The results using incorrect \mathbf{Q} matrix cannot converge to the true values even though convergence to some values are observed. Figure 2.9 shows the comparison of process noise adapted using EKF-RM method and the initially assumed one. Obviously, the EKF-RM method possesses robust ability to find appropriate process noise value automatically. Figure 2.10 compares the estimated velocity and real velocity signals from the 1st to 3rd floor. The high coincidence shows that the system is in linear phase and it is reasonable to apply the stable mode here.

In terms of the unmeasured system response, Figure 2.11 shows the comparison of estimated and real displacement, velocity and acceleration on the top floor. Good estimation accuracy is obtained. The errors of the responses, calculated using the equation(2.21), are 2.9%, 4.3% and 6.6% for displacement, velocity and acceleration respectively.

$$error = RMS(x_{real} - x_{est.}) / RMS(x_{real}) \quad (2.21)$$

in which x_{real} and $x_{est.}$ stand for real and estimated system response in any kinds.

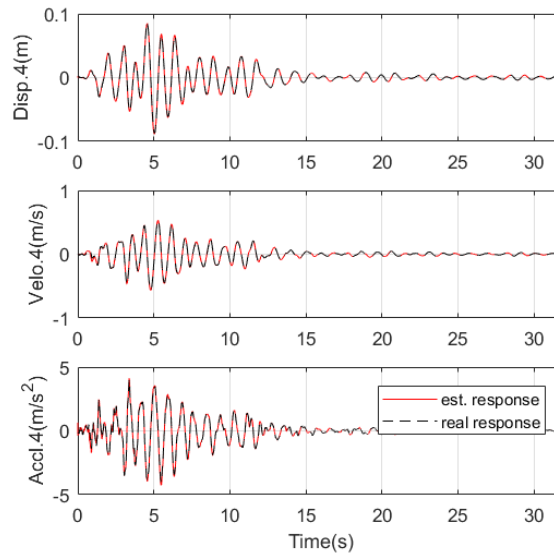


Figure 2.11 comparison of top floor response

2.3.3 A 2D cable stayed bridge model case

In this section, a 2D cable stayed bridge model simplified from a scaled cable stayed bridge experiment done in the shaking table laboratory, Tongji University [121], is regarded as the study target here. The model was originally used to validate seismic-resistant performance of a pre-designed long span cable stayed bridge considering soil-structure interaction and multi-excitation effects. Span length of the bridge is 38.2m with height of tower equals to 5m. Six side piers are deployed beside main towers. Figure 2.12 shows the real outlook of the experiment model. Design details of the model can be found in the paper [121].

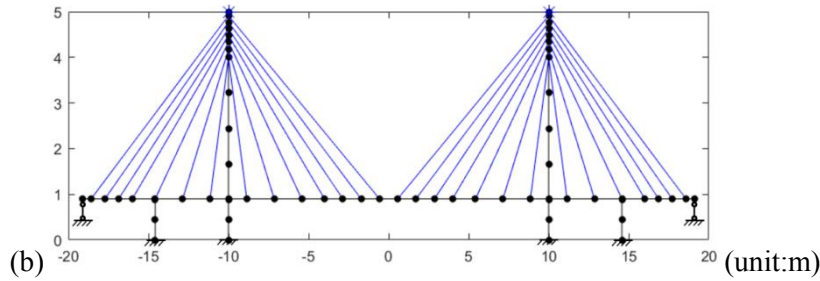
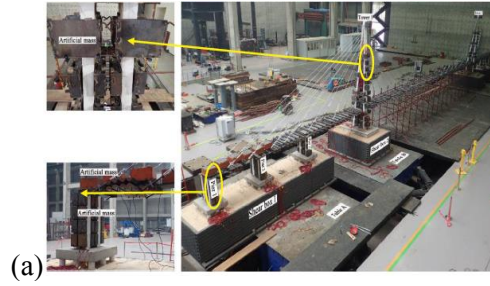
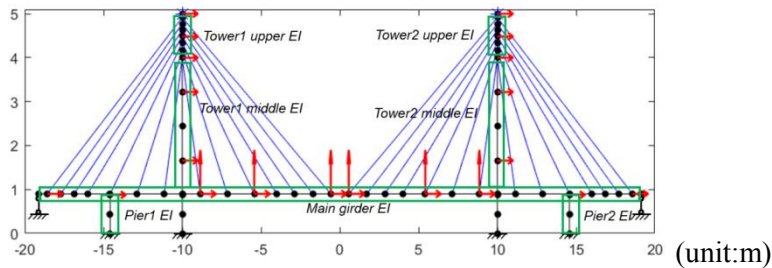
The original model is simplified into a 2D FEM model here, as shown in Figure 2.12. In this simplified 2D FEM model, two vertical pins at two ends of the main girder replace two piers in same locations in the original model, considering their designed bearing conditions. Besides, the two piers in 2D model coupled with the main girder in two translation DOFs on corresponding nodes while rotational DOFs are set free. The connection between main towers and the main girder is achieved by vertical DOF couple only on relevant nodes. Bridge piers and towers are of concrete materials, while steel material is for main girder and cables. The whole structure is symmetric with respect to the middle point of the main girder. Material and cross section properties of each type of members are list in the Table 2.1.

In this table, middle and upper part of main towers are divided as 0~1m, 1~4m and 4~5m along their longitudinal direction. Densities here also involve contributions from extra weights; therefore, they are much larger than pure concrete or steel material.

Table 2.1 summary of cross section and material properties

	E (N/m ²)	ρ (kg/m ³)	I (m ⁴)	A (m ²)
Pier	2.00×10^{10}	22000	5.40×10^{-5}	2.01×10^{-2}
Bottom tower	2.00×10^{10}	35000	2.80×10^{-4}	3.14×10^{-2}
Middle tower	2.00×10^{10}	26000	1.52×10^{-4}	2.55×10^{-2}
Upper tower	2.00×10^{10}	2400	6.20×10^{-5}	2.44×10^{-2}
Main girder	2.06×10^{11}	470000	4.10×10^{-7}	4.15×10^{-3}
cable	2.10×10^{11}	7800	N.A.	1.00×10^{-4}

In this 2D FEM model, Euler-Bernoulli beam elements are used for pier, main tower and main girder members, truss elements are used for cable members ignoring their geometry nonlinearity effect. Additionally, consistent mass matrix is used in the model. For damping effect, Rayleigh damping with stiffness damping coefficient $\beta=0.01$ is also applied here. The 2D FEM model contains totally 66 nodes, 89 elements and 146 DOFs after constraining all axial deformations of pier and tower elements and necessary boundary conditions. The first five natural frequencies of this 2D model are: 1.43Hz (1st vertical symmetric mode), 1.67Hz (1st vertical anti-symmetric mode), 1.79Hz (1st longitudinal mode), 2.30Hz (2nd vertical symmetric mode), 2.61Hz (2nd vertical anti-symmetric mode).

**Figure 2.12 (a) outlook of experiment model [121]; (b) simplified 2D FEM model****Figure 2.13 observation configuration for 2D cable stayed bridge FEM model**

The observation configuration in this case is shown in Figure 2.13. These observation points are selected so that the overall dynamic motion can be well-captured and the points do not correspond to

sensor arrangement commonly found in structural monitoring system. The red arrows stand for the DOFs of which displacement and accelerations are measured simultaneously. The parameters to be identified include cross section stiffness EI of pier 1, pier 2, middle part of tower1, upper part of tower1, middle part of tower2, upper part of tower2, and main girder as show in Figure 2.13, as well as damping coefficient β . The stiffness of bottom part of tower is regarded as known value here, because the responses here are too tiny to be practically measured in reality.

Firstly, forward analysis is conduct using Newmark-beta method with time sample equals to 0.005s considering Takatori earthquake in Figure 2.3(a) as excitation. Then white noise processes with magnitude equals to 5% RMS of corresponding accelerations are added to simulate measurement noise. In terms of the filter method, \mathbf{Q} matrix is initially wrongly assumed as $\text{diag}([10^{-6}\mathbf{I}_{146 \times 1}, 10^{-4}\mathbf{I}_{146 \times 1}, \mathbf{0}_{8 \times 1}])$ (for displacement, velocity and parameter, respectively); initial parameter vector and its corresponding error variance-covariance matrix are defined as $1.5\theta_{\text{real}}$ and $\text{diag}([0.1\theta_{\text{real}}]^2)$; the α_Q coefficient of RM algorithm is set as 1/30; stable mode is applied here. The parameter convergences are shown in Figure 2.14.

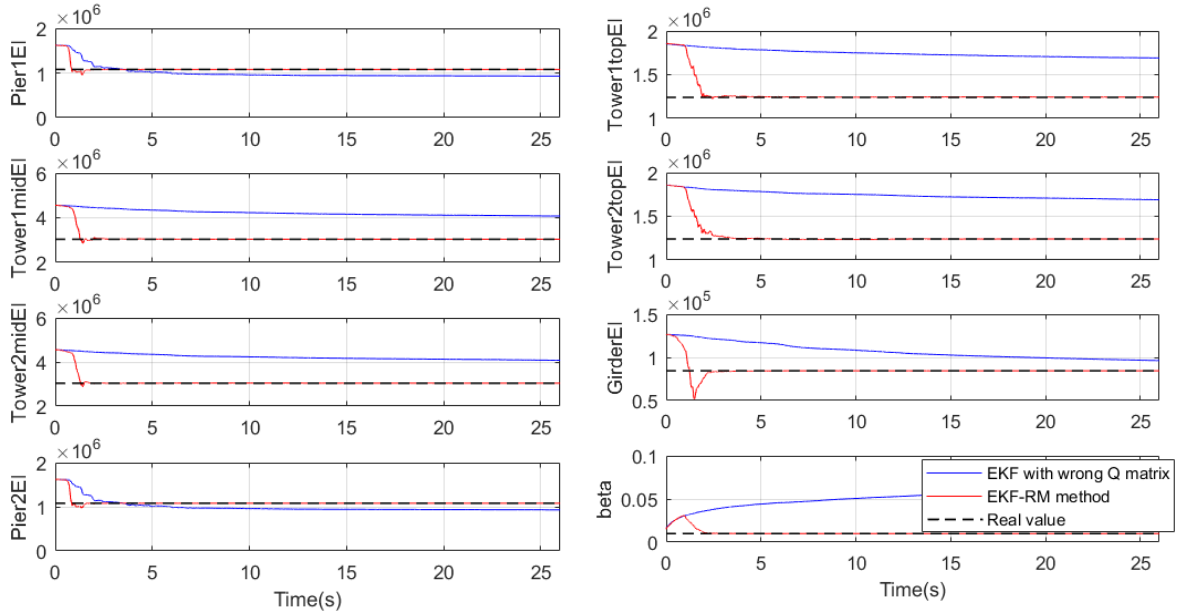


Figure 2.14 parameter convergences for 2D cable stayed bridge FEM model

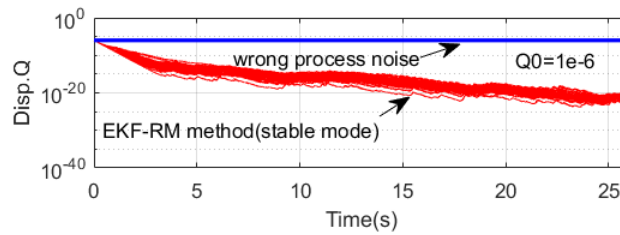


Figure 2.15 comparison of displacement process noise

The parameters, as shown in the figures, converge with approximately 2 seconds. The estimation errors of pier, main girder EI and damping coefficient β is less than 0.1%, while the errors are bit larger for tower EI , i.e. around 0.3% for middle tower EI and 0.5% for top tower EI . This is normal because the vibrations of upper part of towers tend to present characteristics of rigid body motion to certain extent which will deteriorate estimation accuracy. The results here using wrong \mathbf{Q} matrix cannot converge to real value and β seems to diverge. In fact, it can be found that, for pier EI , the

assumed process noise is relatively reasonable so that the final converged values are close to the real ones. While for other parameters, the process noise still needs to be carefully tuned. This tuning process might be acceptable for simple structure model presented in previous sections, but could be time-consuming for complex structures with large number of DOFs since the filter computation itself takes certain amount of time.

Additionally, a more complex cable stayed bridge numerical case is considered here in which the Rayleigh mass damping factor $\alpha=0.5$ is involved. The damping ratios of the first two modes of the structure are $\zeta_1=0.073$ and $\zeta_2=0.076$ respectively. An observation configuration which is more realistic for practical SHM system is also employed here as shown in Figure 2.16. Based on that, parameter identification is conducted using the same computation information as previous case. The results are shown in Figure 2.17 which still possesses good accuracies compared to the real values.

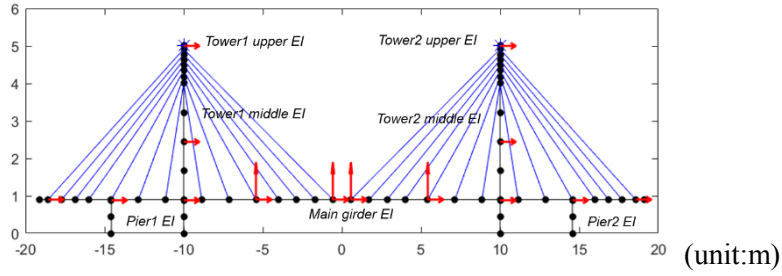


Figure 2.16 observation configuration2 for 2D cable stayed bridge FEM model

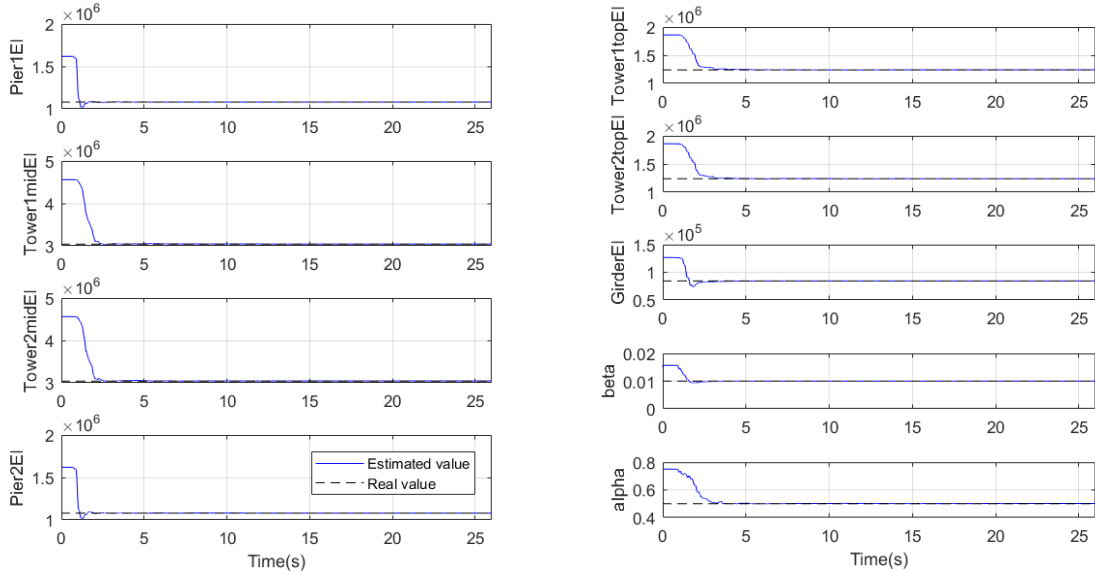


Figure 2.17 parameter convergences for 2D cable stayed based on observation configuration2

While in numerical case, the damping factors β and α can be identified accurately at the same time, damping factors are more difficult to obtain in practical engineering. In the following numerical simulation studies, β factor is still employed to represent structure damping effect. In fact, in the experiment validation studies of the proposed method in section 2.5, it is found that the identified β values are more reasonable than α values.

2.3.4 A 4-DOF lumped mass model considering time-variant parameters

In the last part of this section, the tracking ability of the proposed EKF-RM method for

time-variant parameter identification is verified through numerical case taking advantage of the 4-DOF lumped mass model in section 2.3.2 , except that the stiffness on the bottom floor is time-variant for simulating earthquake induced damage. Two cases are considered here, i.e. 1) stiffness suffers from an abrupt reduction at an instant, which is already studied by some researchers [30, 31, 38]; 2) stiffness gradually reduces and recovers to a residual value, which is a more realistic situation.

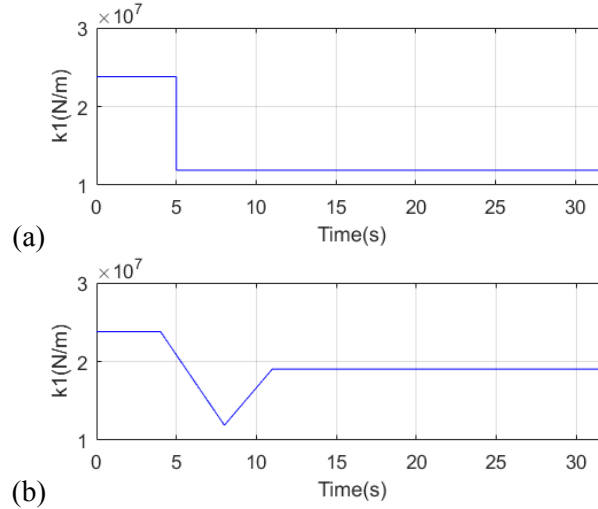


Figure 2.18 (a) stiffness sudden reduction case; (b) stiffness continuous variation case

As shown in Figure 2.18, in the first case, k_1 stiffness suddenly reduces to 50% of the initial value at 5.0 s, while in the second case, k_1 stiffness gradually reduces to 50% of the initial value from 4.0 s to 8.0 s, then it regains its value to 80% of initial one from 8.0 s to 11.0 s, and remains unchanged. White noise processes corresponding to 5% of signals' RMS (around 0.6 m/s^2) are added to the simulated response. In terms of observation configuration, displacement and acceleration on each floor are measured. Track mode of EKF-RM method is used here. Except information aforementioned, other computation and system information applied are exactly same as section 2.3.2 . The results of the two cases are shown in Figure 2.19 .

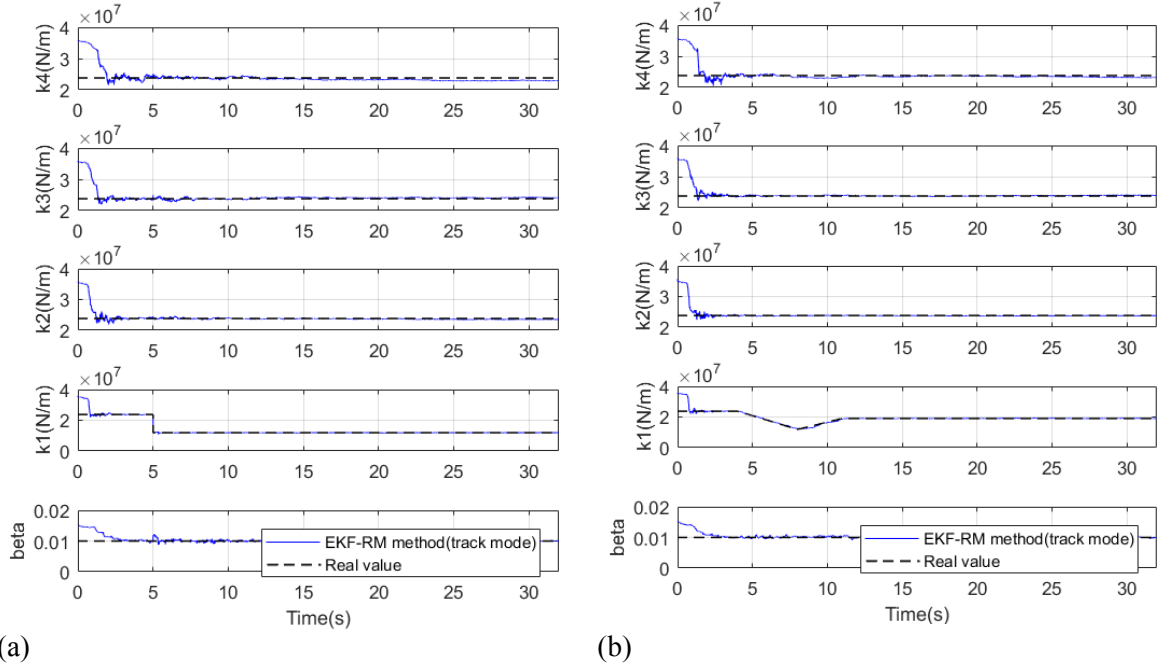


Figure 2.19 parameter convergences;
(a) stiffness sudden reduction case;(b) stiffness continuous variation case

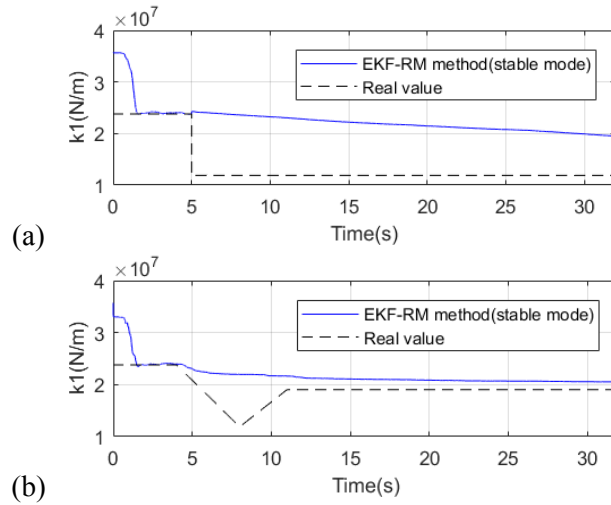
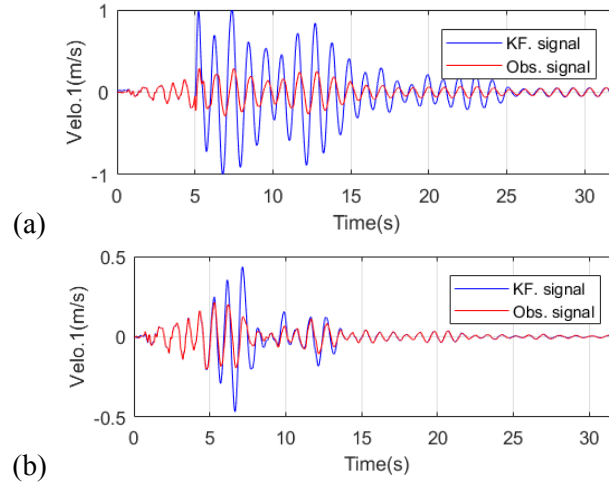


Figure 2.20 parameter convergences using EKF-RM stable mode;
(a) stiffness sudden reduction case;(b) stiffness continuous variation case

By using the track mode of the proposed EKF-RM method, stiffness variations of k_1 are tracked successfully. There is almost no time shift discrepancy between real values and estimated ones which proves its excellent instantaneous tracking ability of the method.

However, if stable mode of the EKF-RM method is applied to these two situations, there is a danger that parameter variation process, especially sudden change, will be completely omitted, as Figure 2.20 shown. In this case, as aforementioned, the estimated and integrated velocities of the 1st floor are compared as shown in Figure 2.21. Significant amplitude discrepancy starts from 5.0 s in the first case, while discrepancy exists from 5.0~13.0 s in the second case. Both of the phenomena approximately match with the real stiffness variation interval. In section 2.5.4 of this article, the two computational modes will continue to discuss taking advantage of experiment data.



**Figure 2.21 comparison between estimated and measured velocity of the 1st floor;
(a) stiffness sudden reduction case;(b) stiffness continuous variation case**

2.3.5 Effect of input signal noise

In practical engineering, since earthquake ground acceleration is also measured using seismometer, the input excitation actually also contains certain level of measurement noise. To consider that, the 4-DOF lumped mass model in the previous sections is also investigated here except that white noise process is added to the input signal as Figure 2.22. The RMS of the measurement noise in the input signal is 0.02m/s^2 . The value is similar to the response measurement noise used in the previous section.

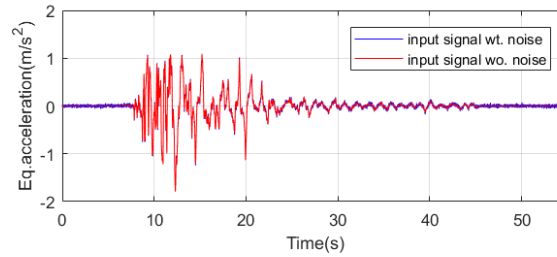


Figure 2.22 comparison between input signal with or without noise

Based on the noisy input signal, time-invariant and time-variant parameters, which are presented in section 2.3.2 and 2.3.4, are identified here. The parameter results are shown in Figure 2.23 and Figure 2.24. Compared to the previous results, no significant deterioration of accuracy is found. By increasing the noise in the input signal constantly, the filter diverges when noise of 0.05m/s^2 is used. However, by tuning the \mathbf{R} matrix slightly larger, the filter could work stably again and identify relatively accurate parameter results. Therefore, with the limited measurement noise in input signal sufficiently accounted by the \mathbf{R} matrix, accurate parameter results could still be obtained. In practice, during pre-processing measured signals, input signal could be de-noised using a low-pass filter. Then the effect of input signal noise is mitigated.

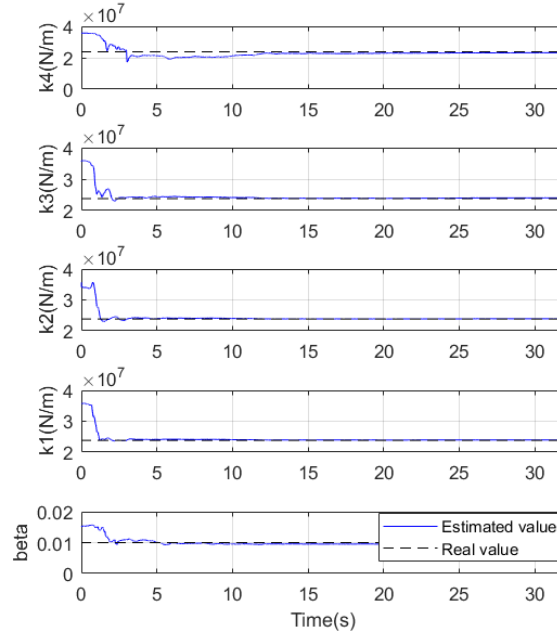
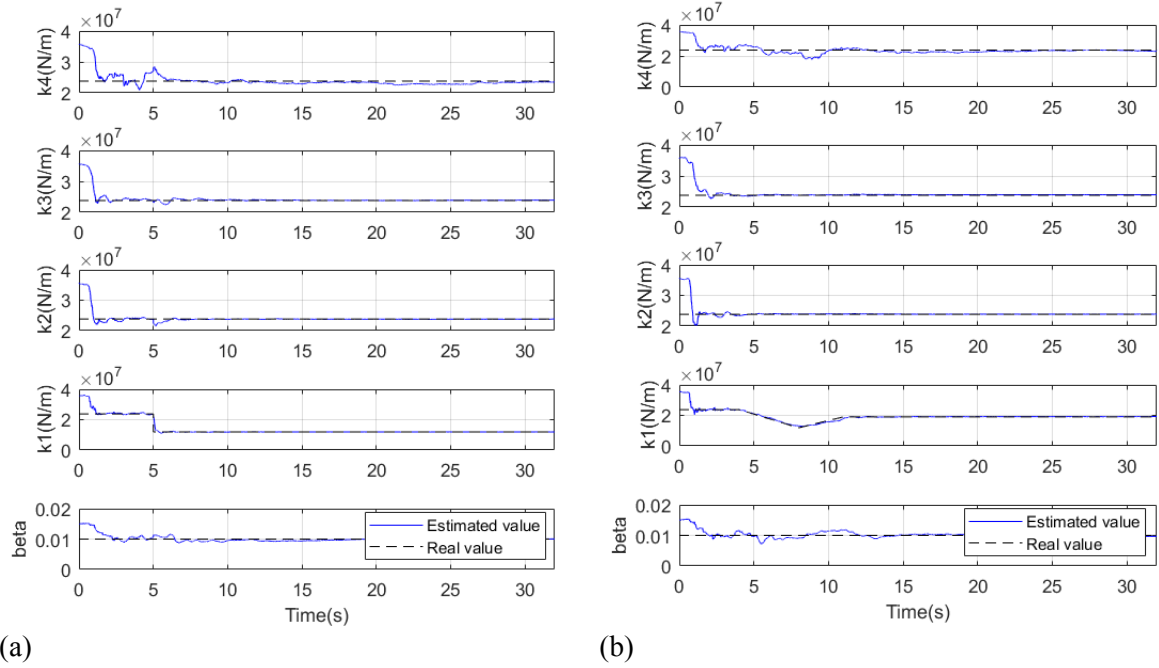


Figure 2.23 time-invariant parameter convergences for lumped mass mode with noisy input excitation



**Figure 2.24 time-variant parameter convergences with noisy input excitation;
(a) stiffness sudden reduction case;(b) stiffness continuous variation case**

2.4 Numerical examples considering inaccurate system models

In the previous chapter, the EKF-RM method is verified by several numerical examples where the system models applied in filter are exactly the same models used in generating signals. However, in reality, such kinds of situations are rare. An assumed system model would never completely describe all of complexities of a real engineering structure. Sometimes, highly simplified models are employed, because, for example, only a limited number of observations are available, or the number

of identified parameters is too large for a delicate system model. In this section, the proposed EKF-RM method is applied to numerical examples where simplified system models, rather than correct models, are applied in filter. Two cases will be demonstrated in this chapter, i.e. one is to estimate a 3D frame building structure based on a 1D lumped mass model, and the other is to estimate a 3D cable stayed bridge structure based on a 2D cable stayed bridge.

2.4.1 A 3D four story frame building model

In this section, the same four story lumped mass building model, as in section 2.3.2 , and its prototype are employed here. At first, a 3D FEM model is extracted from this prototype structure; system responses are then simulated based on this 3D FEM model; finally, system estimation is conducted using these signals based on the 1D lumped mass model.

Some basic information about the prototype structure has already been introduced in section 2.3.2 . For the 3D FEM model, mass distributions for each floor remains same, while cross section stiffness EI for column and floor beam members are purposely tuned, which may not be exactly same as those presented in design drawings, so that the natural frequencies of the FEM model are close to the real structure. 3D Euler-Bernoulli beam elements are used to simulate column and beam members; concentration mass elements are added on floor nodes to compensate mass effects. Rayleigh damping with $\beta=0.01$ is applied here. Forward analysis is conducted using Newmark-beta method with 0.005s time sample considering Takatori earthquakes exciting the model both in X and Y direction simultaneously. Figure 2.25 shows the 3D FEM model and earthquake excitations. The first three modal frequencies of the FEM model in X direction are 1.24Hz, 3.89Hz, and 6.97Hz, while 1.34Hz, 4.14Hz and 7.15Hz in Y direction, as shown in Figure 2.26 and Figure 2.27 respectively.

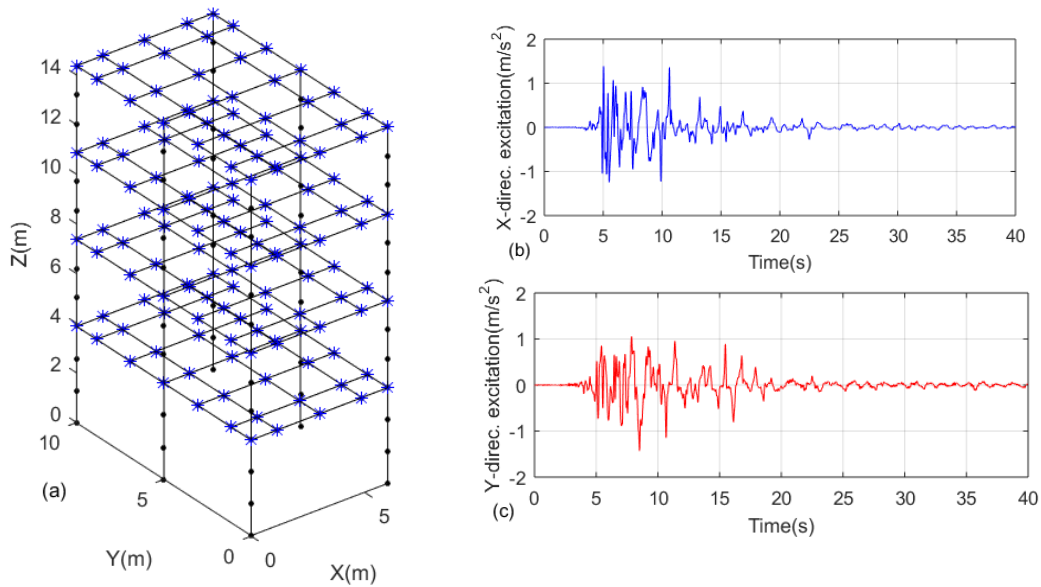


**Figure 2.25 (a) outlook of 3D frame building FEM model;
(b) earthquake excitation in X direction; (c) earthquake excitation in Y direction**

As in the previous case, 5% RMS noise are added to the simulated accelerations and integrated

displacements and accelerations in X and Y directions of central nodes on each floor are measured. Signals from X and Y direction are separately employed to estimate systems in both directions based on 1D lumped mass model. The settings for EKF-RM method here are same as those used in section 2.3.4 but stable mode is used here.

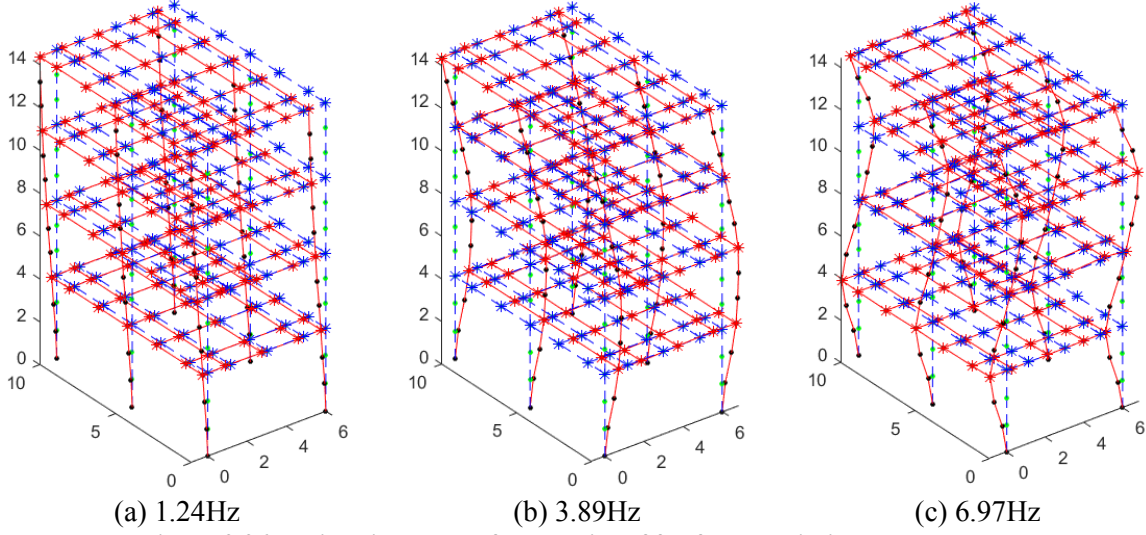


Figure 2.26 X-direction model frequencies of 3D frame building FEM model;
(a) 1st X-direction mode; (b) 2nd X-direction mode; (c) 3rd X-direction mode;

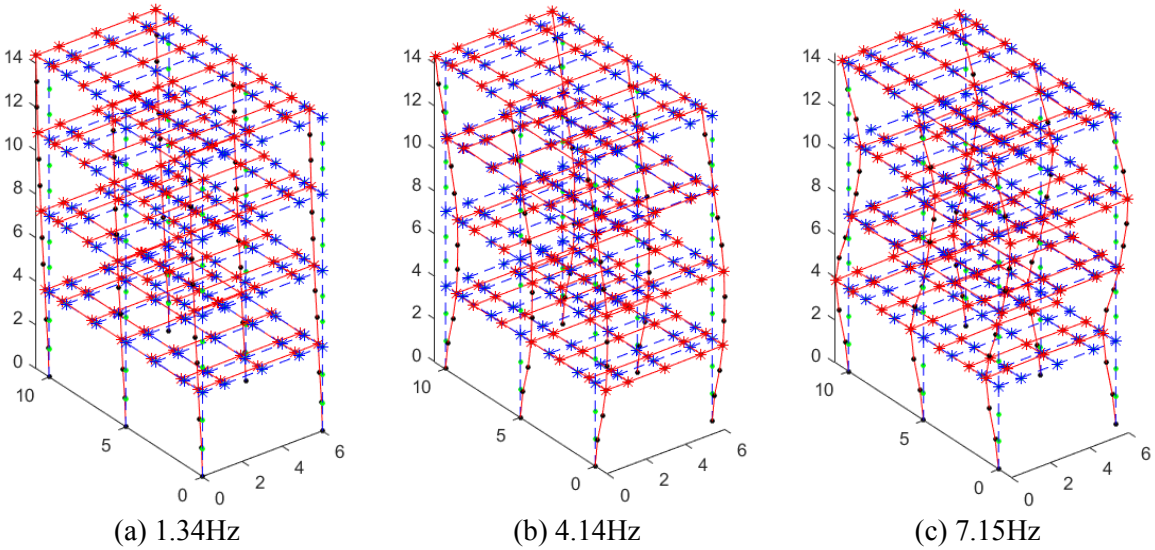


Figure 2.27 Y-direction model frequencies of 3D frame building FEM model;
(a) 1st Y-direction mode; (b) 2nd Y-direction mode; (c) 3rd Y-direction mode;

The parameters convergence in X and Y directions are shown in Figure 2.28. It can be found that β converge to the real value accurately, other parameters also converged quickly. Since no reference value is available for stiffness parameters, the modal frequencies computed using the identified values are compared with those of 3D FEM modal frequencies as well as those obtained from SRIM method as listed in Table 2.2. The first modal frequency of the estimated 1D lumped mass model can coincide with that of 3D FEM model or SRIM method, but other ones are generally lower than the 3D FEM or SRIM case for both X and Y directions. For the second mode, the errors of X and Y

direction are 8% and 5% respectively, while they increase to 20% and 15% for the third mode. This kind of modal frequency discrepancies is due to model inaccuracy because in this case lumped mass models rather than 3D models are assumed in filter.

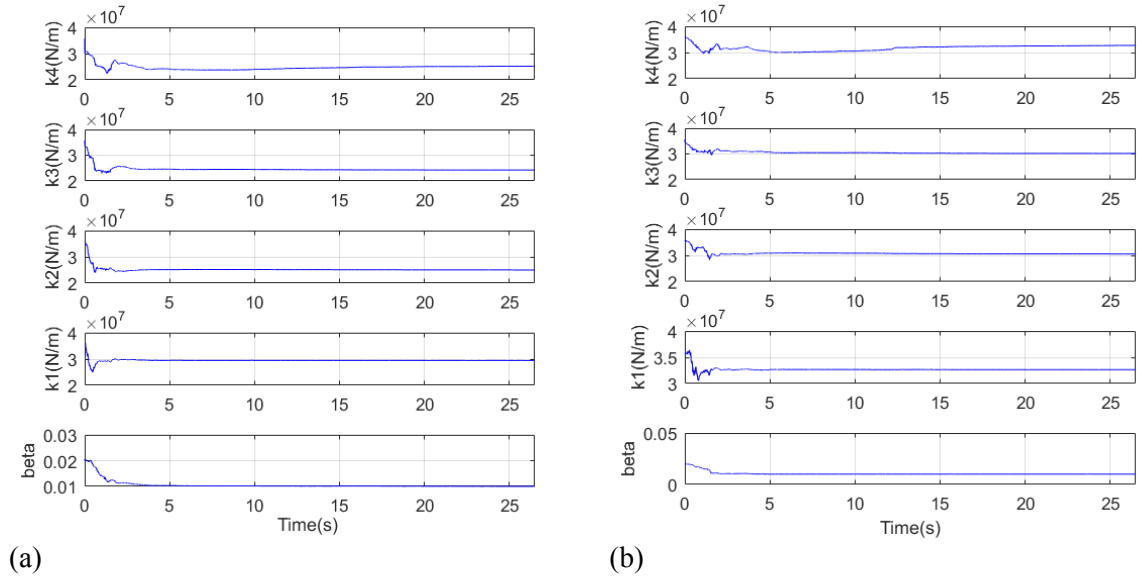


Figure 2.28 parameter convergences based on 1D lumped mass model for original 3D FEM model;
(a) X direction; (b) Y direction

A second 3D FEM model is considered further for higher similarity with 1D lumped mass model. In this 3D model, cross section stiffness of floor beams is amplified 50 times while it reduces to half for column members. The parameter convergences in X and Y directions are shown in and corresponding frequency comparison results are listed in Table 2.2 and Table 2.3. Clearly, the higher order modal frequencies of 1D model become much closer to the 3D one, i.e. the errors of X and Y direction are around 1.5% and 1% for the second mode, 4% and 2% for the third mode respectively.

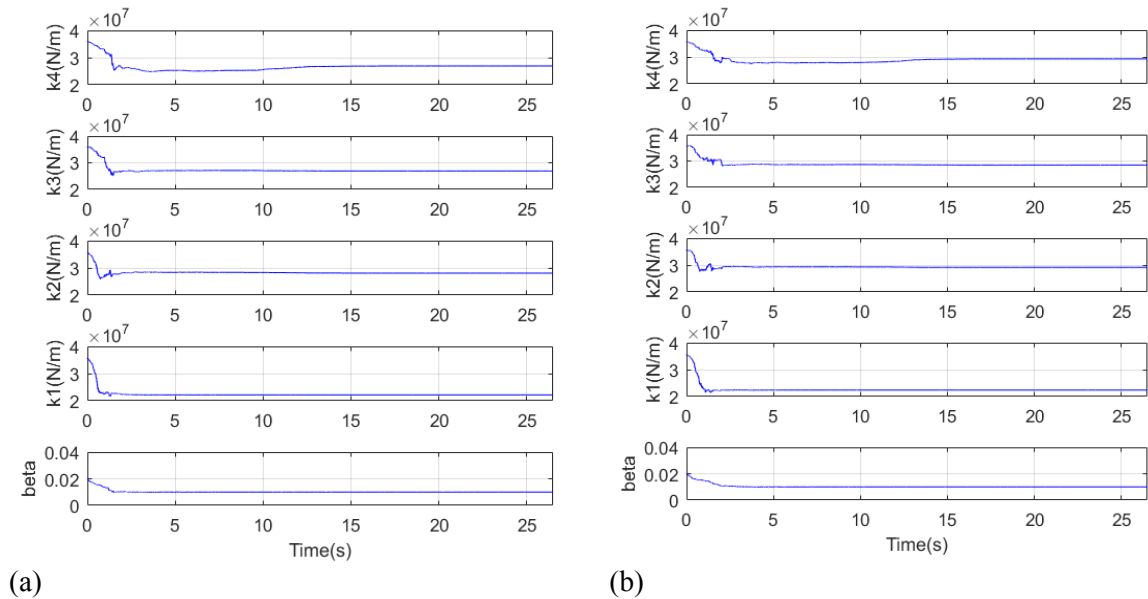


Figure 2.29 parameter convergences based on 1D lumped mass model for modified 3D FEM model;
(a) X-direction; (b) Y-direction

Table 2.2 Comparison of modal frequencies from different models of original 3D FEM model

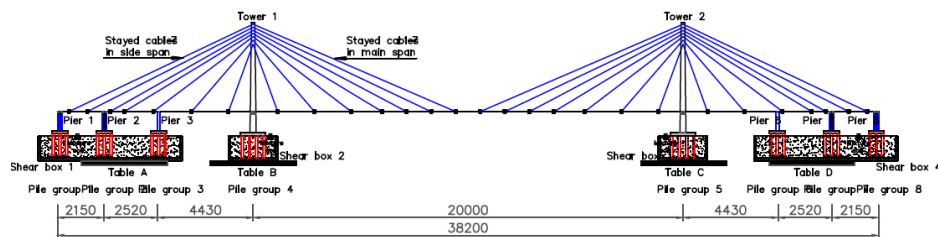
X direction	3D FEM model	1D lumped mass model	SRIM
1 st mode	1.24Hz	1.24Hz	1.24Hz
2 nd mode	3.89Hz	3.57Hz	3.89Hz
3 rd mode	6.97Hz	5.52Hz	N.A.
Y direction			
1 st mode	1.34Hz	1.34Hz	1.34Hz
2 nd mode	4.14Hz	3.93Hz	4.13Hz
3 rd mode	7.15Hz	6.12Hz	N.A.

Table 2.3 Comparison of modal frequencies from different model for modified 3D FEM model

X direction	3D FEM model	1D lumped mass model	SRIM
1 st mode	1.19Hz	1.19Hz	1.19Hz
2 nd mode	3.56Hz	3.50Hz	3.55Hz
3 rd mode	5.85Hz	5.59Hz	N.A.
Y direction			
1 st mode	1.21Hz	1.21Hz	1.21Hz
2 nd mode	3.61Hz	3.58Hz	3.60Hz
3 rd mode	5.87Hz	5.73Hz	N.A.

2.4.2 A 3D cable stayed bridge model case

In this section, the 2D cable stayed bridge and its corresponding prototype structure are studied here. similarly, as last section, a 3D cable stayed bridge FEM model is firstly extract from the prototype structure; then system estimation is conducted based on the 2D cable stayed bridge using simulated signals from 3D model.

**Figure 2.30 elevation view of prototype cable stayed bridge model**

The main geometry differences of the prototype structure from the one used in section 2.3.3 include: 1) the real main towers are ‘A’ type with gradient cross sections along their longitudinal directions, i.e. 115mm×286mm×22mm ~75mm×185mm×22mm box sections for bottom and middle tower parts and 75mm×185mm~65mm×163mm solid section for upper tower part, Accordingly, cables here show space shape rather than plane shape in that 2D model.; 2) the side piers actually consist of multiple columns, i.e. 4 columns for side pier1 or side pier 2 and 2 columns for side pier3; 3) the elements in the 3D model are much denser (461 nodes and 498 elements) than the 2D case (66 nodes and 89 elements). Detailed information about the prototype structure can be referred to[121].

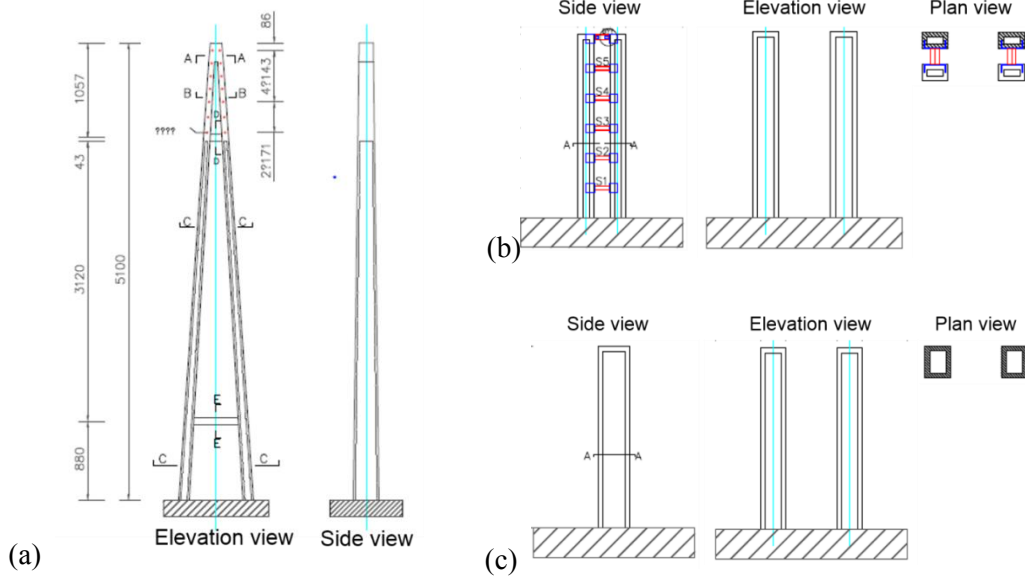
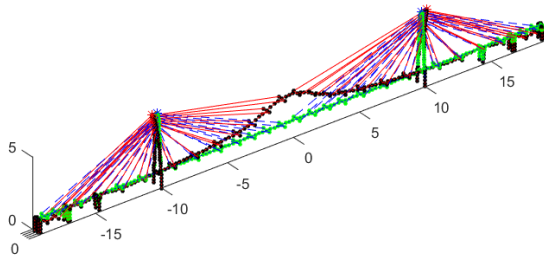
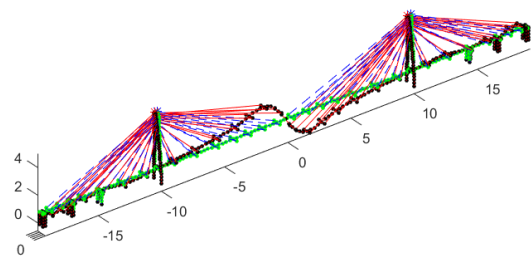


Figure 2.31 (a) tower view; (b) side pier1 and 2 view; (c) side pier3 view

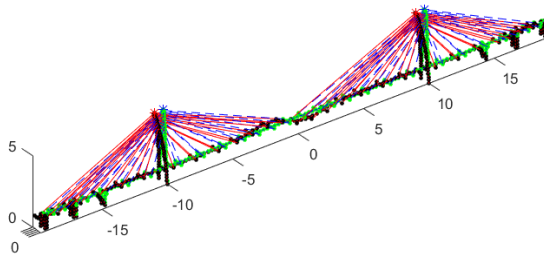
3D Euler-Bernoulli beam elements are used to simulate main tower, pier, and main girder members, while 3D truss elements are for cable members. Rayleigh damping with $\beta=0.01$ is applied here. Forward analysis is conducted using Newmark-beta method with 0.005s time sample considering Takatori earthquake (Figure 2.25(b)) exciting in its longitudinal direction only. The first six modes of the 3D FEM model in vertical direction are shown in figure below, and the corresponding frequencies are: 1.40Hz (1st vertical symmetric mode), 1.64Hz (1st vertical anti-symmetric mode), 1.78Hz (1st longitudinal mode), 2.25Hz (2nd vertical symmetric mode), 2.54Hz (2nd vertical anti-symmetric mode), 2.88Hz (3rd vertical symmetric mode).



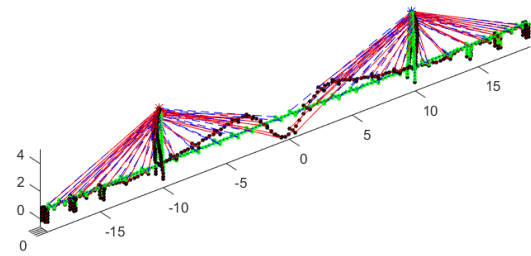
(a) 1.40Hz



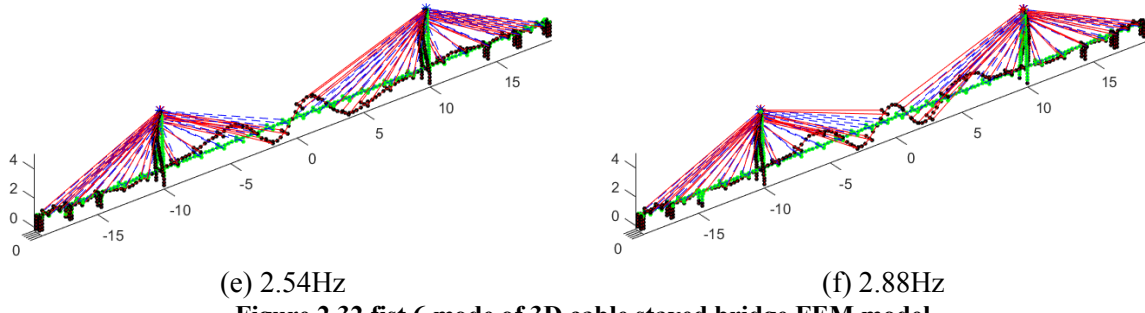
(b) 1.64Hz



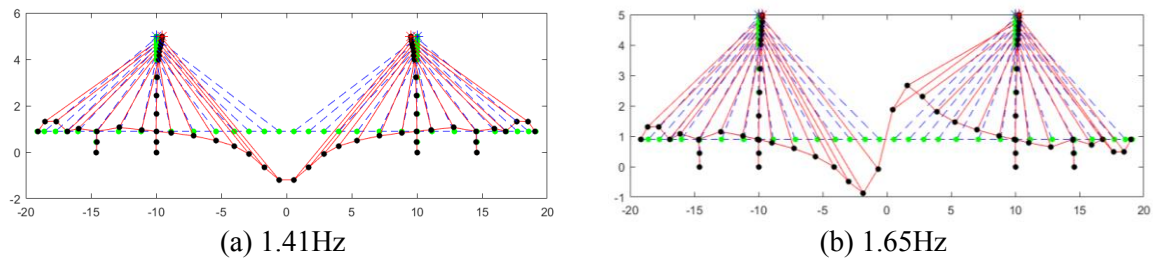
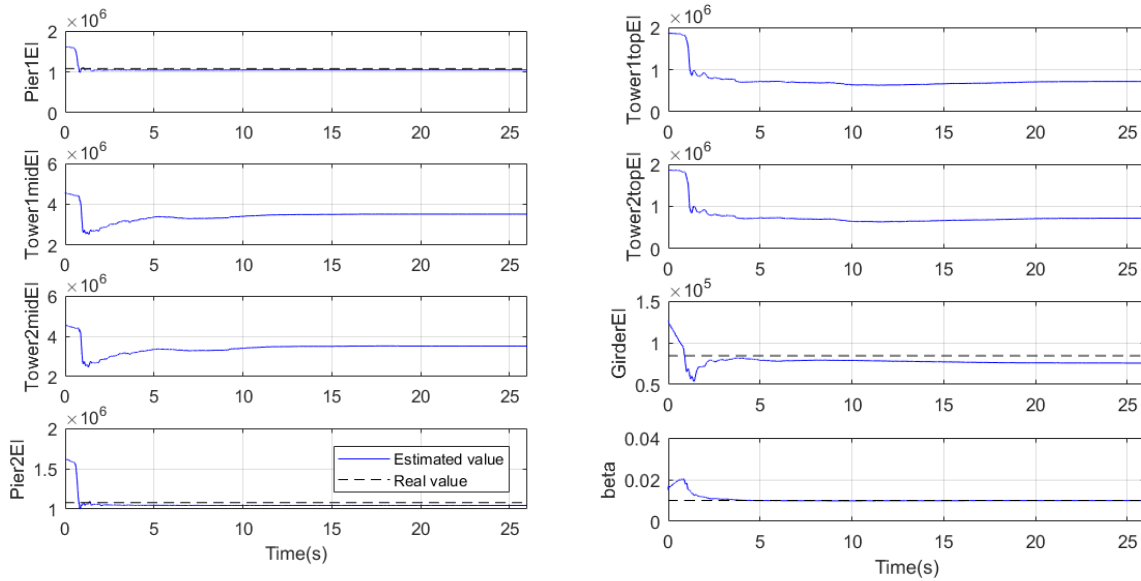
(c) 1.78Hz



(d) 2.25Hz



Similar to previous case, 5% RMS noises are added to the simulated responses. The initial settings, assumptions and observation configurations for EKF-RM method are all same as those in section 2.3.3. Parameter convergences are shown in Figure 2.33. The errors of pier stiffness and β are about 3% and 2%, respectively. The error for main girder stiffness is bit large, i.e. 8%, which might result from the inaccuracy of cable member simulation in the 2D model. Since there is no reference value for middle and top tower stiffness available, the modal frequencies and shapes are computed and compared with those of 3D model. Figure 2.34 shows the modal frequencies and shapes computed from the identified parameters; comparisons of frequency results, including those from SRIM method, are listed in Table 2.4. Similar to previous 3D building model case, low order frequencies are all showing high coincidences, while for high order mode, e.g. 3rd vertical anti-symmetric mode, the error is bit large, i.e. 2%.



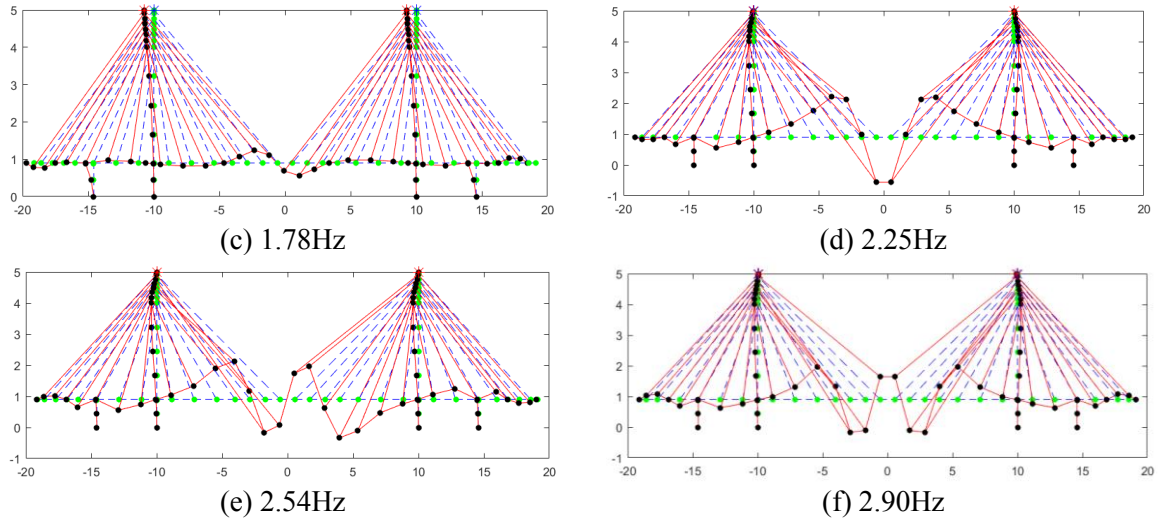


Figure 2.34 modal frequencies computed based on estimated 2D cable stayed bridge model

Table 2.4 Comparison of modal frequencies from different model for 3D cable stayed bridge FEM model

	3D FEM model	2D FEM model	SRIM
1 st vertical symmetric mode	1.40Hz	1.41Hz	N.A.
1 st vertical anti-symmetric mode	1.64Hz	1.65Hz	1.64Hz
1 st longitudinal mode	1.78Hz	1.78Hz	1.78Hz
2 nd vertical symmetric mode	2.25Hz	2.25Hz	N.A.
2 nd vertical anti-symmetric mode	2.54Hz	2.54Hz	2.54Hz
3 rd vertical symmetric mode	2.88Hz	2.90Hz	N.A.
3 rd vertical anti-symmetric mode	3.16Hz	3.23Hz	3.24Hz

2.4.3 Parameter identification consistency

The previous two sections show that reasonable parameter identification results could be obtained using the proposed EKF-RM method even though assumed system model is simplified or inaccurate. This kind of reasonability mainly reflects on modal frequency values. In practical engineering, a structure, during its service period, will experience multiple earthquake excitations, similar parameter values should be identified under various earthquake excitations if no damage or deterioration occurs. Otherwise, if parameter varies significantly among different earthquakes, the parameter identification could result in misleading judgment of the structure. The effect of inaccurate system model on the parameter identification consistency is discussed in this section based on previous numerical models.

45 earthquakes selected from one K-Net station [122], i.e. IBR007, are regarded earthquake inputs here. One of the ground acceleration recorded at the IBR007 station in 2018 is shown in Figure 2.35. The sampling frequency in this case is 100Hz.

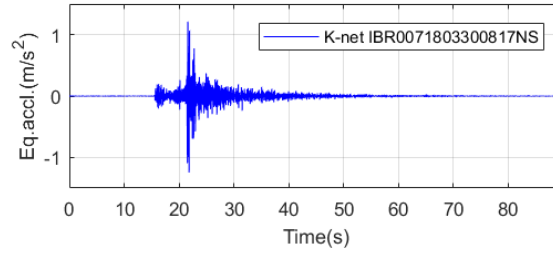


Figure 2.35 recorded ground acceleration at IBR007 station

First of all, the original 3D four story building model is investigated. Forward analyses are conducted using the 45 earthquakes which only exerts on the X direction of the building. For simplicity, 5% RMS noise are added to simulated accelerations and displacements, and signals from the central node of each floor are measured. The 1D lumped mass model is applied to identifying parameters here. The identification results are presented as scattered points here in Figure 2.36.

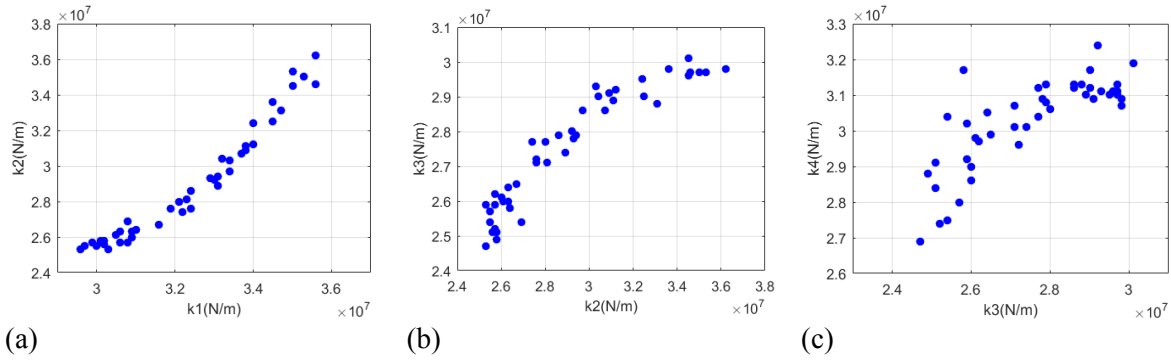


Figure 2.36 identification results for original 3D model using 1D lumped mass model;
(a) $k1$ vs $k2$; (b) $k2$ vs $k3$; (c) $k3$ vs $k4$

Clearly, the parameter identification results are inconsistent and scattered here, indicating that the lumped mass model is not a good candidate for the 3D building. In order to ensure whether the issue comes from the system model rather than the measurement noise, the identification processes were conduct twice. It is found that the identification results of each case have slight differences, but the overall trends are very similar, i.e. a positive correlated trend. In fact, the parameter values with larger values, i.e. points at right-upper part, tend to reproduce the second modal frequency of the original structure accurately, while the points at left-lower part tend to reproduce the first modal frequency accurately. The identified modal frequencies are also scattered as shown in Figure 2.37.

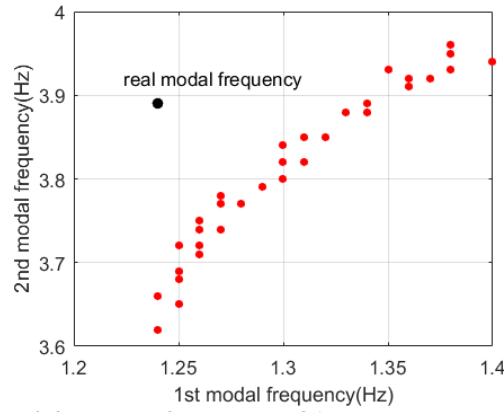


Figure 2.37 modal frequency of 1D lumped mass model

At next, the 3D building model is simplified to a 2D frame model. In this model, the cross section stiffness EI of each floor column is to be identified. Except that, other system parameters are regarded as known values and listed in Table 2.5. On each floor, the translational DOFs of nodes are coupled in order to reduce computation burden. Similarly, in this case, acceleration and displacement of each floor are measured. The EI value identification results are shown in Figure 2.39.

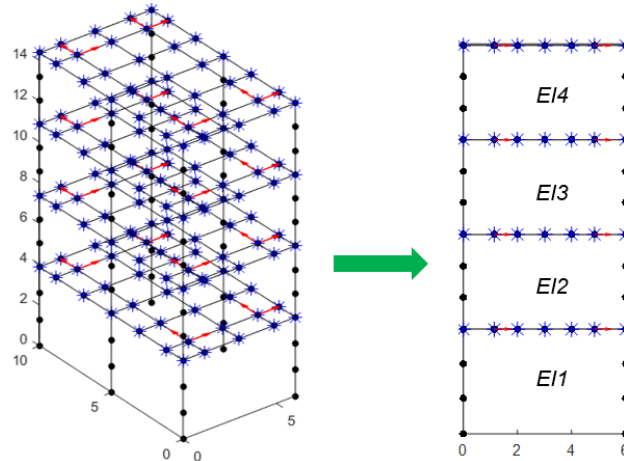


Figure 2.38 simplified 2D model

Table 2.5 known system parameter values of simplified 2D model

	E (N/m ²)	ρ (kg/m ³)	I (m ⁴)	A (m ²)	*C. mass(kg)
Column btw. 1 st ~2 nd floor	2.06×10^{11}	7800	N.A.	0.0398	N.A
Beam of 2 nd floor	2.06×10^{11}	7800	0.0011	0.0250	6844
Column btw. 2 nd ~3 rd floor	2.06×10^{11}	7800	N.A.	0.0398	N.A
Beam of 3 rd floor	2.06×10^{11}	7800	0.0011	0.0250	6800
Column btw. 3 rd ~4 th floor	2.06×10^{11}	7800	N.A.	0.0398	N.A
Beam of 4 th floor	2.06×10^{11}	7800	0.0011	0.0189	6783
Column btw 4 th ~roof floor	2.06×10^{11}	7800	N.A.	0.0398	N.A
Beam of roof floor	2.06×10^{11}	7800	0.0011	0.0157	8451

Obviously, in this case, the parameter identification results are more consistent and concentrated. The modal frequencies computed using the identified parameters are shown in Figure 2.40(a), they are also compared with 1D model case in Figure 2.40(b) in which the parameter consistency can be

readily compared.

In this case, it is shown that the 2D model is a more appropriate model to describe the original 3D building model.

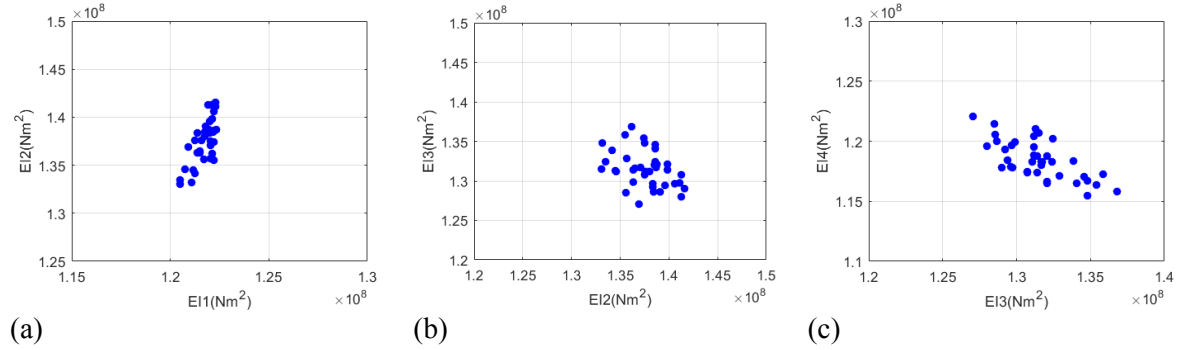


Figure 2.39 identification results for original 3D model using 2D frame model;
(a) EI_1 vs EI_2 ; (b) EI_2 vs EI_3 ; (c) EI_3 vs EI_4

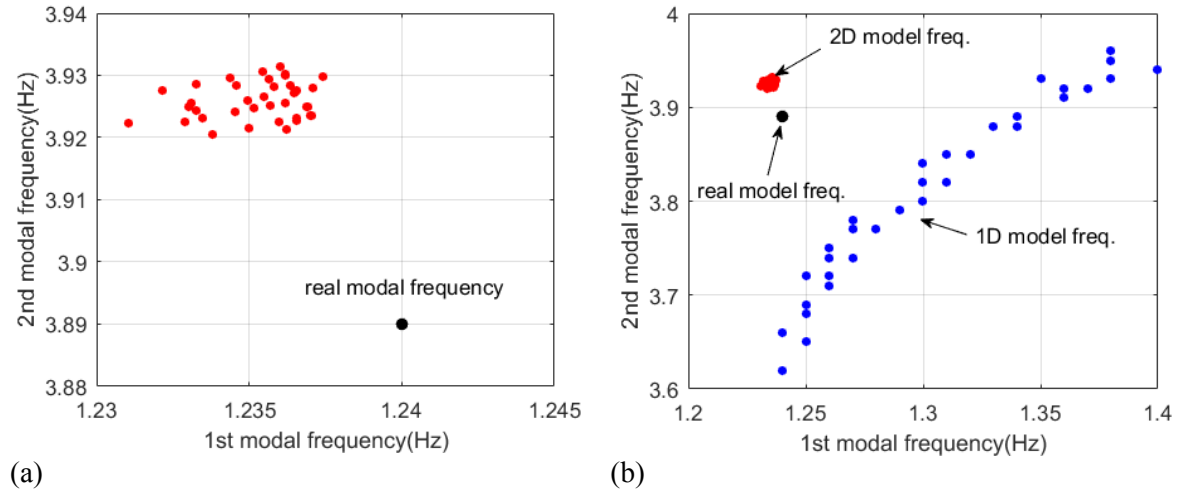
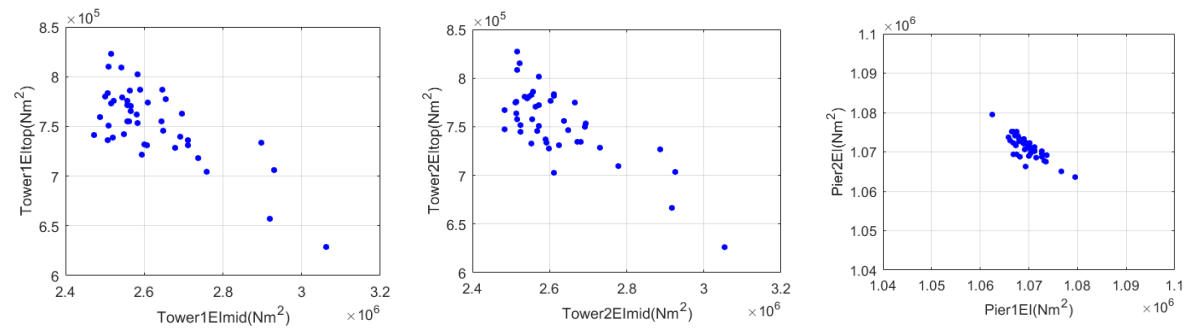


Figure 2.40 (a) modal frequency of 2D frame model; (b) modal frequency comparison

Secondly, the 3D cable stayed bridge model is investigated here. The 2D cable stayed bridge is employed to identify corresponding parameters. 5% RMS noise are added to simulated accelerations and displacements and the general procedure is same as previous case. The identification results are shown in Figure 2.41. Parameter inconsistencies are shown in the tower part EI results while for the pier EI results are quite consistent. Therefore, the pair of piers in 3D model is accurately enough simplified by the single pier in 2D model.



(a) (b) (c)
Figure 2.41 identification results for 3D bridge model using 2D bridge model;
(a) tower1 EI_{mid} vs tower1 EI_{top} ; (b) tower2 EI_{mid} vs tower2 EI_{top} ; (c) pier1 EI vs pier2 EI

Finally, in this section, in order to further verify the performance of beam element, the bridge pier prototype in 2.3.1 is modeled using 3D solid element. 20-node solid element is used here; extra concentration mass elements are added to the top of pier cap to compensate mass of superstructure which is 340 tons here. In order to consider stiffness reduction of the bridge pier, the elastic modulus of bottom 1.0m range is set as 0.6 of the original value ($2.0 \times 10^{10} \text{N/m}^2$). Forward analyses are conducted based on the 3D solid model using the 45 earthquakes; a 1D beam element based model is used to identify EI values of the upper and lower part of the pier model. The measurements are noisy displacements and accelerations at 2.0m, 4.0m and 7.5m as shown in Figure 2.42. The RMS of them are 5% of their corresponding signals' RMS. Figure 2.43 shows the first three modes of the model.

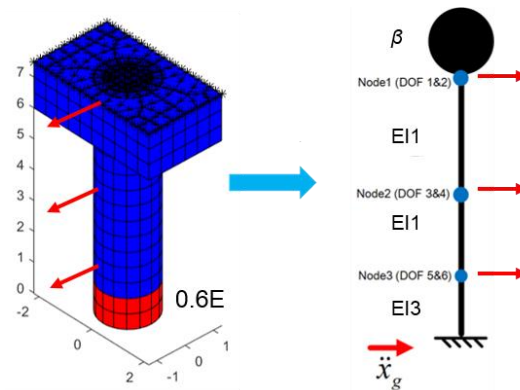
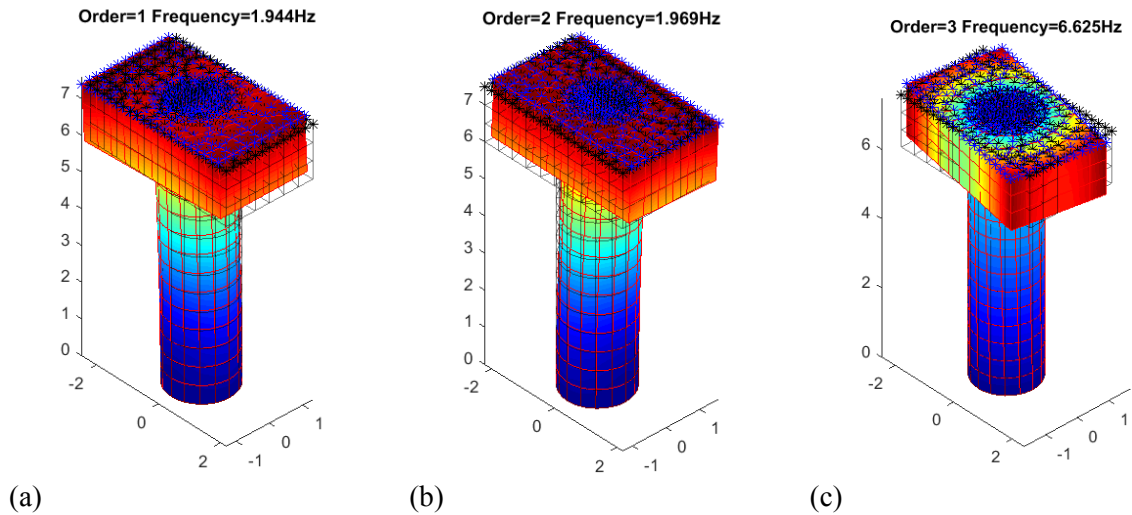


Figure 2.42 simplified bridge pier model



(a) (b) (c)
Figure 2.43 first three modal shape of 3D solid bridge pier model; (a) the 1st mode; (b) the 2nd mode; (c) the 3rd mode

For the simplified 1D beam model, the three elements are 2.0m, 2.0m, 3.5m from the bottom to top with linear density equals to $6.36 \times 10^3 \text{kg/m}$. one concentration mass is added to the top node which is 340 tons. Figure 2.44 shows the identification results. The EI values are quite scattering especially for EI_{II} value; modal frequencies computed using the identified parameters reproduce the real value well. In fact, since the EI_{II} and EI_{III} values are connected together, the negative correlation

trend is reasonable. The structure is also considered to identify its equivalent uniform EI value; the parameter results and corresponding computed mode frequencies are shown in Figure 2.45. In this case, the identified parameters are consistent.

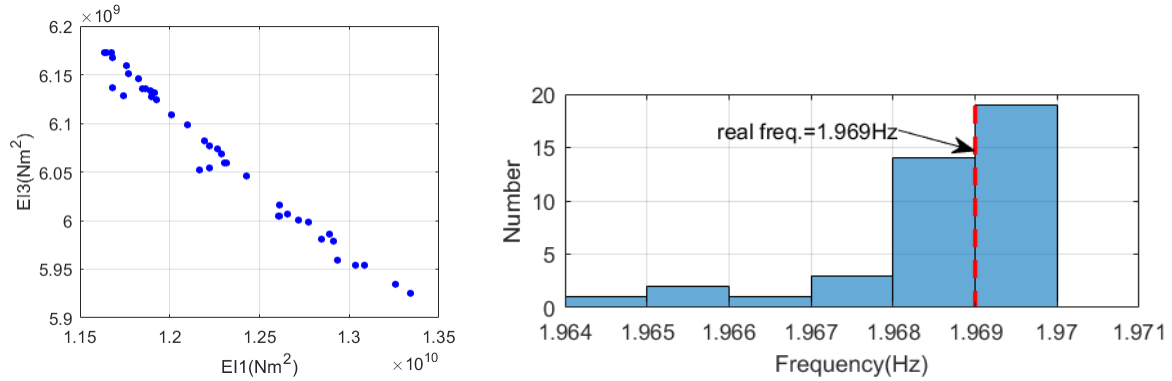


Figure 2.44 identification results based on double EI ; (a) EI_3 vs EI_1 ; (b) mode frequency distribution

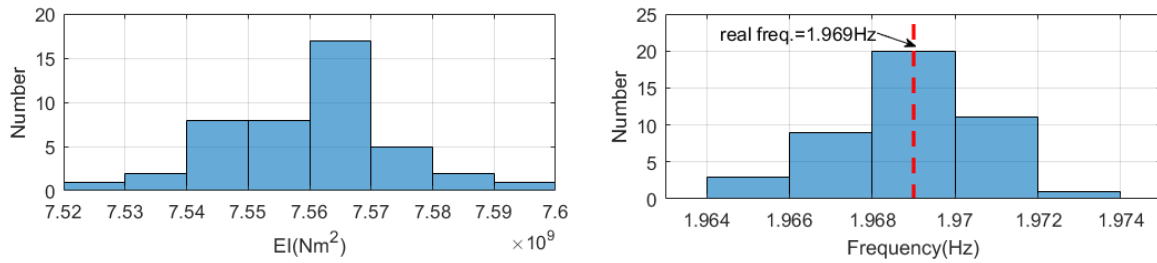


Figure 2.45 identification results based on equivalent uniform EI ; (a) EI value distribution; (b) mode frequency distribution

2.5 Experiment validation of EKF-RM method

In this section, the proposed EKF-RM method is validated through three experiments in E-defense databases, i.e. a full scale bridge pier experiment, a full scale four story frame building and a substructure experiment.

For the first two experiments, time-invariant parameters are supposed to be identified and stable mode is used. Modal frequencies computed using identified parameters are compared with those obtained from SRIM method. Results from different system models applied in filter are discussed. In terms of the substructure experiment, strong nonlinearity exists; therefore, track mode of the proposed method is applied. For all of three experiments, experiments under a series of earthquake excitations are studied.

2.5.1 Full scale bridge pier experiment

The structure in this experiment is the prototype model in section 2.3.1. Some basic information about the experiment model has already introduced in the previous chapter and details can be found in relevant experiment report[103]. The monitoring system is briefly explained here. In total 191 channels of acceleration, 256 channels of strain, 116 channels of displacement were deployed at various locations on the shaking table, the pier and superstructure. In this study, the displacement measurements (relative displacements) and their derivatives (derivative velocities and accelerations), with 200Hz sampling frequency, are mainly used in the EKF-RM method, considering the noise level of measured accelerations is high. Figure 2.46 shows the locations of displacement transducers.

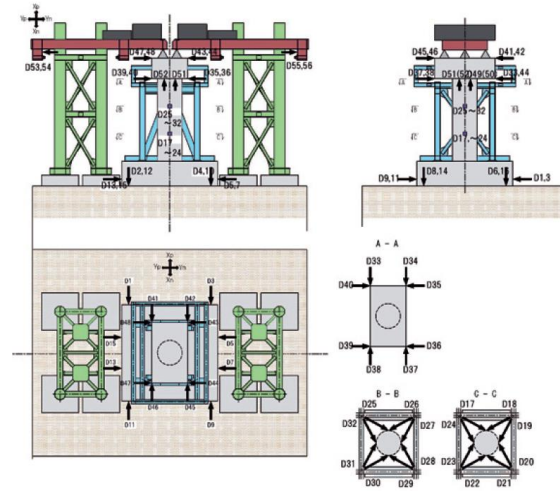


Figure 2.46 location of displacement transducer

The total length of the bridge pier is 7.5m, including 6m of pier itself and 1.5m of bent cap. Multiple displacement transducers of wire type were deployed at 2.0m, 4.0m, 6.0m and 7.5m heights of the pier, as shown in Figure 2.46. At each height, the displacement signals are averaged from the multiple transducers and the signals from north-south direction are analyzed here. In this experiment, a series of Takatori earthquake excitations with various magnitudes were treated as input accelerations. Their ID used in this article and corresponding peak ground acceleration (PGA) are listed in Table 2.6. A typical group of wave forms of displacement signals as well as earthquake excitations (in Takatori20% case) are shown in the Figure 2.47.

Table 2.6 earthquake cases ID and corresponding PGA

ID	PGA(m/s ²)
Takatori20%	1.0
Takatori30%1	1.5
Takatori30%2	1.2
Takatori30%3	1.4
Takatori30%4	1.5
Takatori30%5	1.5
Takatori30%6	1.5

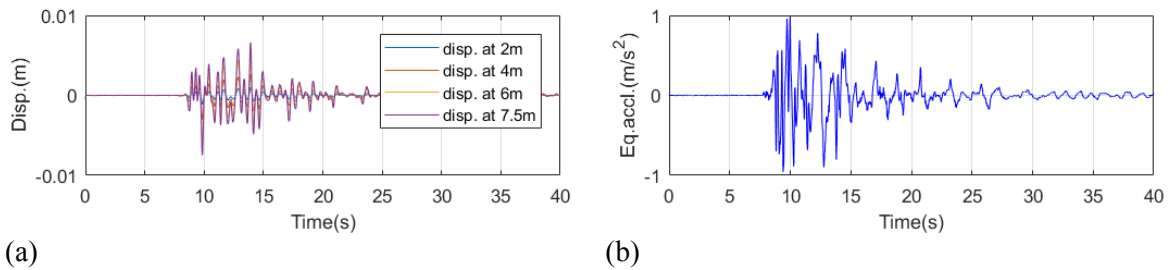


Figure 2.47 Takator20% case; (a) displacement measurements; (b) earthquake excitation

Before conducting the EKF-RM method, SRIM method have been employed to estimate modal frequencies, all four acceleration signals along the pier are used, but only 1st mode is estimated with high confidence. The results are to be compared with those computed using the identified parameters

from the EKF-RM method.

In the first place, a SDOF model is used in filter. The equivalent spring stiffness K and damping factor C are to be identified. The equivalent concentration mass of the SDOF system is 252.5 ton. The displacement at 7.5 m and corresponding derivative acceleration are treated as observations. For all of the cases, initial \mathbf{Q} matrix is set as $\text{diag}([10^{-8}\mathbf{I}, 10^{-6}\mathbf{I}, \mathbf{0}])$; measurement noise $\mathbf{R} = \text{diag}([5 \times 10^{-9}, 10^{-4}])$ (displacement and acceleration respectively).

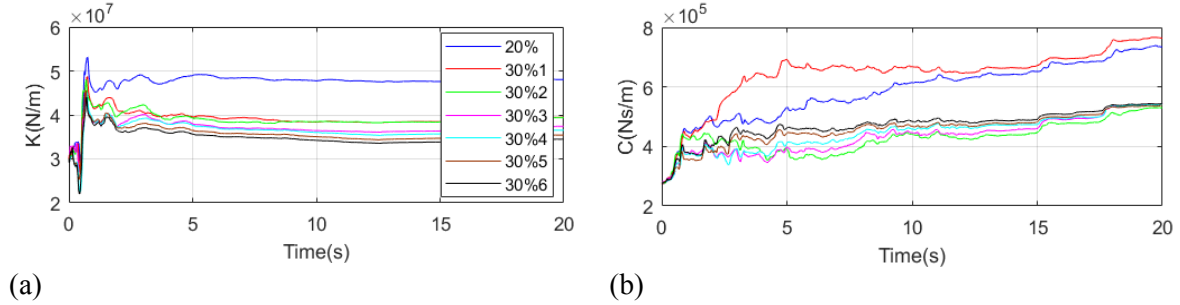


Figure 2.48 parameter identification for SDOF model; (a) stiffness; (b) damping coefficient

Figure 2.48 summarizes the results of parameter identification. Among the series of excitation cases, the stiffness of the equivalent SDOF reduce dramatically at Takatori30%1 case, approximately 20%, and gradually decrease in the following cases. It can be found in Figure 2.49 that relatively large frequency discrepancies exist between the two methods, i.e. the ones from EKF-RM method are quite larger than SRIM. But the tendencies of frequency variations from both methods are similar, i.e. the large reduction at Takatori30%1 case and smooth decrease afterwards. For the SDOF model here, the damping coefficients do not converge to straight lines which indicate relative large model error exists.

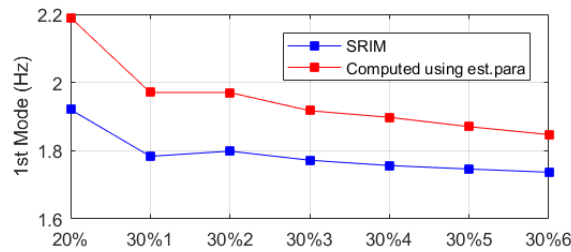


Figure 2.49 comparison of the 1st modal frequency

Since the modal frequencies based on the EKF-RM method cannot match with those of SRIM results, a refined system model is assumed here for the EKF-RM method. The prototype structure is simplified as the FEM model as Figure 2.50. 0~6m part of pier is simulated with 3 FEM beam elements, and a uniform EI is assumed and to be identified here. For the 1.5m height bent cap and superstructure, their effects are all condensed into a concentration mass element with 2 DOFs added on the very top node (NO.1 node) of this model. Specifically, the mass matrix is calculated as $[2.52 \times 10^5, -3.48 \times 10^5; -3.48 \times 10^5, 5.63 \times 10^5]$. The first and second row of this matrix corresponds to translation and rotational DOF of NO.1 node, i.e. 2.52×10^5 and 5.63×10^5 are inertial mass and inertial moment respectively. Besides, the linear density of pier is $6.62 \times 10^3 \text{ kg/m}$. In summary, 6 DOFs are included into the model by ignoring axial deformations, and a uniform EI and Rayleigh damping β are to be identified.

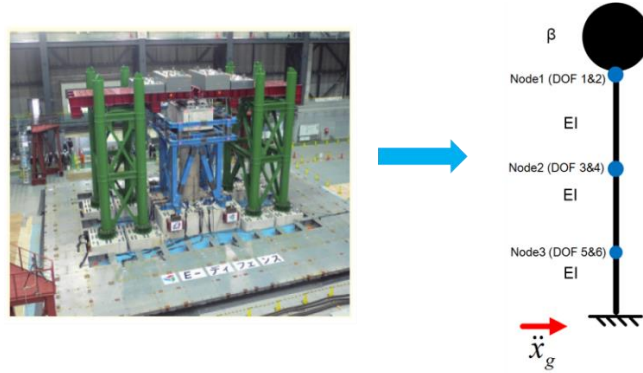


Figure 2.50 FEM model with uniform EI

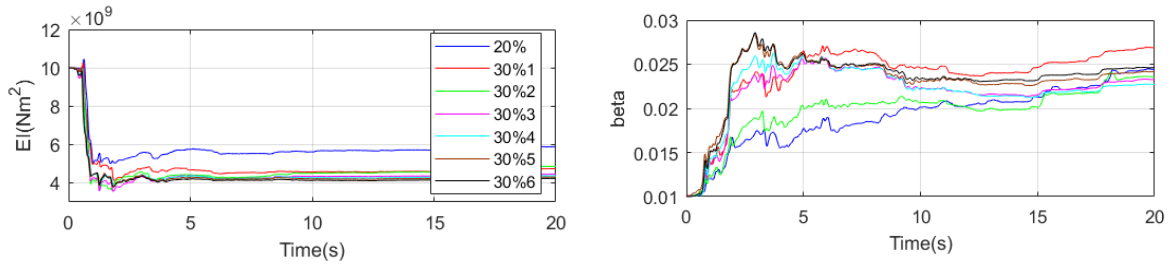


Figure 2.51 parameter identification for uniform EI model; (a) EI value; (b) β value

For all excitation cases, displacements and accelerations at 6.0m (NO.1 node), 4.0m (NO.2 node) and 2.0m (NO.3 node) are treated as observations. \mathbf{R} matrix is set as $\text{diag}([5 \times 10^{-9} \mathbf{I}, 10^{-4} \mathbf{I}])$. Initial \mathbf{Q} matrix is set as $\text{diag}([10^{-8} \mathbf{I}, 10^{-6} \mathbf{I}, 0])$, and α_0 equals to 1/30 is always used. Figure 2.51 shows the EI parameter convergences in a series of earthquake excitation cases. Similar as previous results, significant stiffness reduction, i.e. 20%, occurs at Takatori30%1 case. In the following cases, the decrease of stiffness is gradual and smooth, which is similar as the SDOF case.

The modal frequencies are computed based on the identified parameters and compared with those from SRIM method, as shown in Figure 2.52. Roughly, the tendencies of frequency variation from both methods are similar. For Takatori30%1 and Takatori30%2 cases, the slight stiffness regaining between the two cases in SRIM method is also captured by EKF-RM method. Comparing the modal frequency here with those obtained from SDOF system, the frequency discrepancies with respect to SRIM results actually become smaller. Specifically, the frequency discrepancies of SDOF model are around 0.3Hz~0.15Hz among all cases, while they are 0.13Hz~0.01Hz when applying the uniform EI FEM model. From the perspective of modal frequency, this uniform EI FEM model outperforms the previous SDOF model.

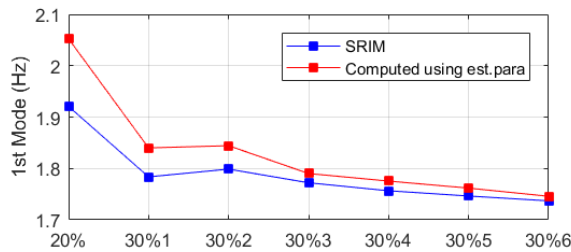


Figure 2.52 comparison of the 1st modal frequency

In order to verify the identified parameters, the system responses are reproduced using the identified parameters based on forward simulation. The constant parameters used for simulations are

the averaged ones over the last 10 seconds of identification histories. Figure 2.53 shows the simulated signals of NO.1 DOF using the identified parameters in Takatori30%1 case. The simulated signals match with the real observed ones fairly. In a series of excitation cases, the errors of the simulated displacements and accelerations of NO.1 DOF are calculated based on equation (2.21), and the results are listed in Table 2.7.

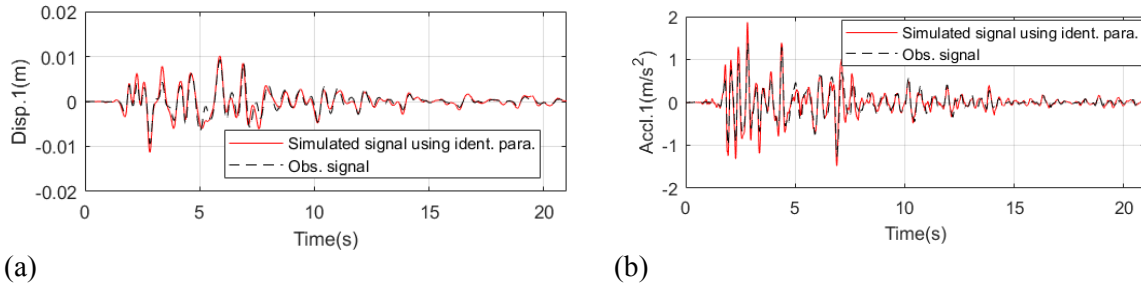


Figure 2.53 simulated signals of NO.1 DOF using identified parameters in Takatori30%1 case: (a) displacement; (b) acceleration

Table 2.7 simulated signal errors of NO.1 DOF using identified parameters

ID	Displacement error	Acceleration error
Takatori20%	47.5%	61.3%
Takatori30%1	43.3%	47.3%
Takatori30%2	44.9%	49.7%
Takatori30%3	39.2%	43.1%
Takatori30%4	35.5%	40.7%
Takatori30%5	37.3%	45.3%
Takatori30%6	34.9%	41.9%

Furthermore, a more refined system model is considered, in which two cross section stiffness EI are estimated, i.e. one for 0~2m part and the other for 2~6m part. Except this point, other system information remains unchanged. In order to obtain reasonable stiffness results, especially for the upper part of the pier, the angular displacement on NO.1 node is also involved into the observation configuration. This response can be calculated from displacement signals at 6.0m and 7.5m assuming the bent cap performs as rigid body. A typical angular displacement wave form is shown in Figure 2.54(b).

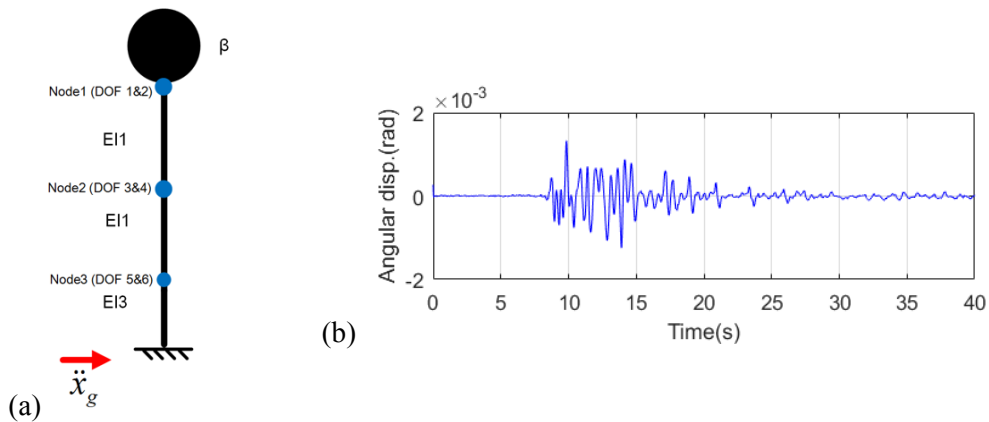


Figure 2.54 (a) FEM model with double EI for C1-1 experiment; (b) Angular displacement in Takatori20% case

To estimate this system, all available displacement and acceleration signals are used, including translational and angular responses at NO.1 node, translational responses at NO.2 and NO. 3 node. The displacement and acceleration measurement noise corresponding to the angular response are 2×10^{-9} and 5×10^{-5} respectively. Other measurement noise values are equal to the previous case. Except the aforementioned information, other settings and system information are exactly same as previous case.

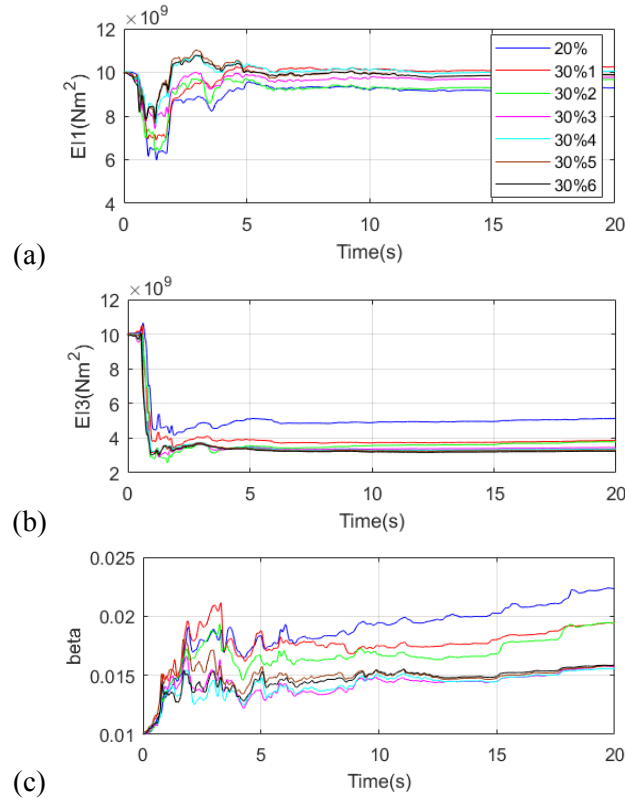


Figure 2.55 parameter identification for double EI model; (a) $EI1$ value; (b) $EI3$ value; (c) β value

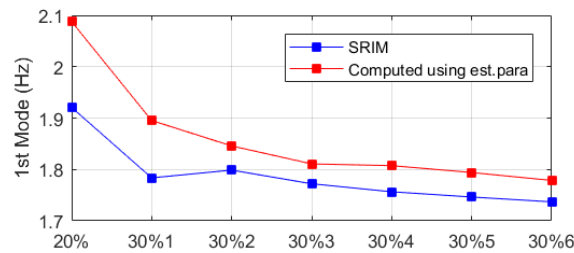


Figure 2.56 comparison of the 1st modal frequency

Figure 2.55 shows the parameter convergences of two EI in a series of excitations cases. In terms of $EI3$ the estimation results are quite similar with that of uniform EI case, i.e. significant stiffness reduction occurs between Takatori20%, Takatori30%1 cases, however the magnitude is bit larger, i.e. the reduction ratios are about 23% in Takatori30%1. While for $EI1$, estimated values are slightly scattering, especially for Takatori20% and Takatori30%2 case which are smaller than other cases, i.e. $EI1=9.2 \times 10^9 \text{ Nm}^2$, but still the values are roughly constant among different cases, i.e. $EI1=9.5 \times 10^9 \text{ Nm}^2$, showing that evident damage might not happened in the upper part of the pier. In fact, from

common sense, it can be predicted with high confidence that damage should exist at the bottom part of the pier, which is also shown here. Figure 2.56 shows the modal frequency comparison between two methods in different cases. The frequency variation trend of the double EI FEM model is similar with that of uniform EI model while the frequency discrepancy values are larger in this case.

In order to test the estimation accuracies of unmeasured system responses, specifically displacement, using limited partial observations, a case where uniform EI of the pier is to be identified. The displacements and accelerations observed at 2.0m and 6.0m are considered only. \mathbf{R} matrix is set as $\text{diag}([5 \times 10^{-9} \mathbf{I}, 10^{-4} \mathbf{I}])$. Other computation settings and system information are same as previous case.

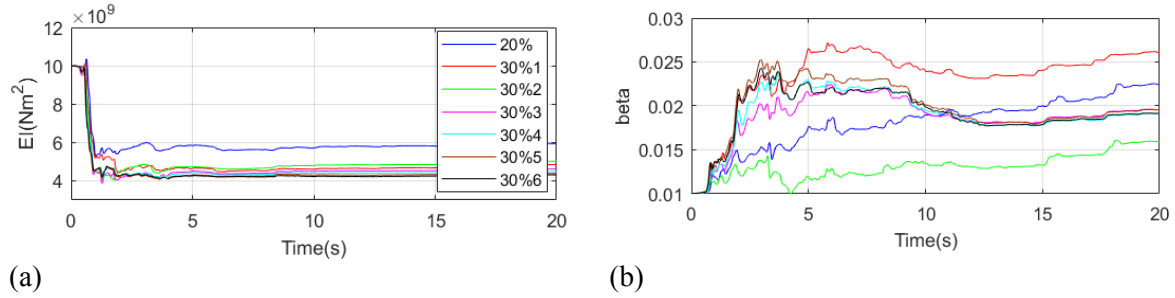


Figure 2.57 parameter identification for uniform EI model with partial observations;
(a) EI value; (b) β value

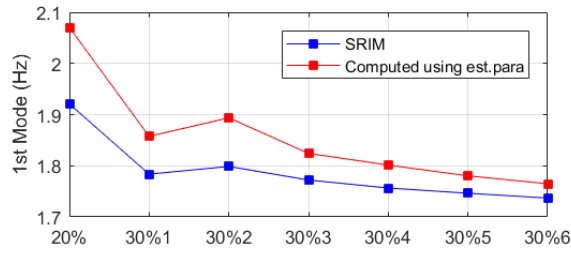


Figure 2.58 comparison of the 1st modal frequency

Figure 2.59 shows the estimated angular displacement at 6.0m (DOF2) and displacement at 4.0m (DOF3) in Takatori20% case. Generally, their wave forms coincide with the real observed signals, for some parts, e.g. at the proximity of 5.0s, however, relatively large error could occur. Table 2.8 lists the estimation errors of this two DOFs in all cases, calculated from equation (2.21). Most of them are less than 20%, and errors of the displacement (DOF3) are generally less than the angular displacement (DOF2).

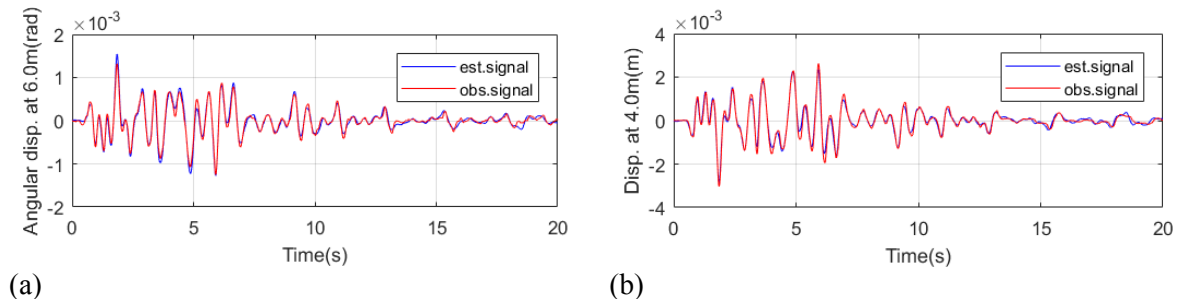


Figure 2.59 estimated displacement in Takatori20% case;
(a) angular displacement at 6.0m(DOF2); (b) displacement at 4.0m (DOF3)

Table 2.8 displacement estimation error

ID	DOF2 error	DOF3error
Takatori20%	19.6%	12.9%
Takatori30%1	23.8%	12.5%
Takatori30%2	18.8%	12.8%
Takatori30%3	19.2%	11.8%
Takatori30%4	19.5%	11.7%
Takatori30%5	19.3%	11.9%
Takatori30%6	18.9%	11.6%

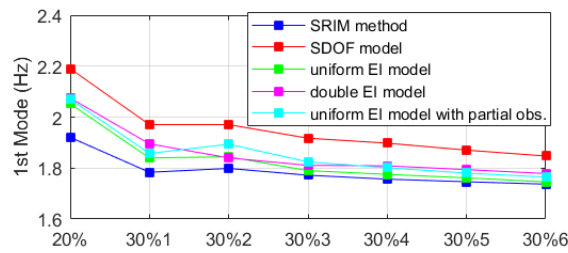


Figure 2.60 comparison of the 1st modal frequency based on different system model

In Figure 2.60, frequency variations based on different system models are summarized. The overall trends are basically similar to each other, even though the frequency values are different. The one based on SDOF model is farthest from the SRIM results, while uniform EI model is the closest. However, all of the system models applied here cannot exactly reproduce the modal frequency results from the SRIM method; the reason might come from that the boundary conditions of the real physical model, e.g. the pier base and the connection with superstructure, cannot be simulated by those models well. It can also be reflected on the bad convergence performances of damping factors in this study.

Finally, for comparison, the damping factor α values are identified along with uniform EI and β values under a series of excitation cases. The displacements and accelerations at NO.1 node, NO.2 node and NO.3 node are treated as observations. The results of damping factor β and α are presented in Figure 2.61. The identified β values here are slightly larger than those in Figure 2.51, while the identified α values even become negative starting from the second excitation case, i.e. Takatori30%1. Damping factors in earthquake engineering are most likely some positive values; negative damping factors may result in computation divergence in forward simulation. Based these facts, only damping factor β values are identified for the experiments here so that the results are more reasonable.

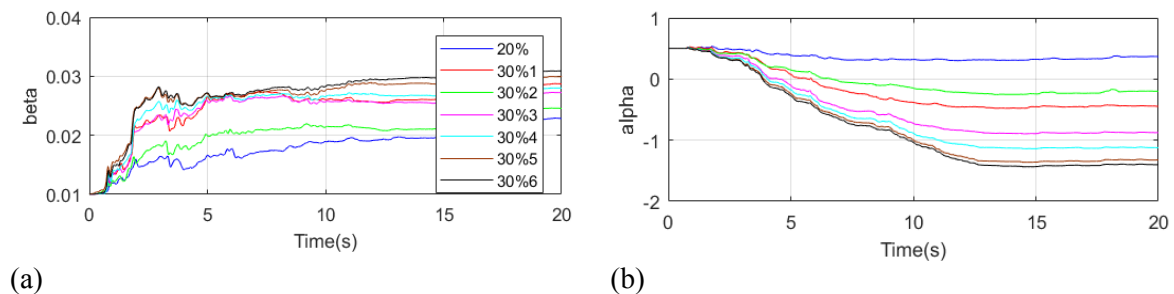


Figure 2.61 parameter identification for uniform EI model; (a) β value; (b) α value

2.5.2 Full scale four story frame building experiment

The target structure in this section is the prototype model introduced in section 2.3.2 . Basic information about the experiment model has been introduced before and details can be found in relevant experiment report [102]. In terms of the monitoring system, there are totally 588 channels of strain, 107 channels of acceleration, and 214 channels of displacement in this building. In fact, inter-story displacements were measured during the experiment, but some of them were broken in certain excitation cases. Accelerometers, on the other hand, always remained intact. Therefore, acceleration measurements on shaking table and each floor of the building, with 200Hz sampling frequency, are mainly used here for system estimation purpose. In this study, displacement and velocity signals are integrated from the accelerations then applied with a high-pass filter of 0.2Hz cutoff frequency.

The locations of accelerometers are deployed in a symmetric manner on each floor in the building, as shown in Figure 2.62. Since multiple sensor measured accelerations on the same floor, the averaged one is used and applied to those integrated displacements and velocities. Signals from two directions i.e. North-south (NS) and West-east (WE), are analyzed here. A series of Takatori earthquakes with increasing magnitudes were input to the system. Their ID used in this paper and corresponding PGA are listed in Table 2.9. Figure 2.63 shows the relative displacement, velocity and acceleration signals as well as earthquake excitation in Takatori12.5% NS case.

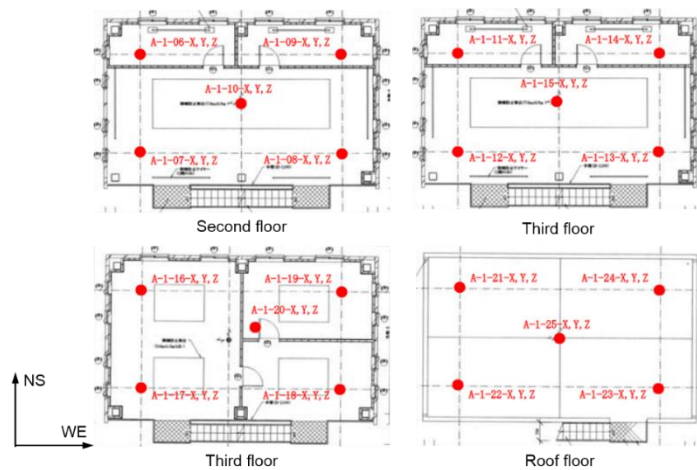


Figure 2.62 location of accelerometers on building

Table 2.9 earthquake ID and corresponding PGA

ID	NS-PGA(m/s^2)	WE-PGA(m/s^2)
Takatori5%	0.25	0.30
Takatori10%	0.60	0.60
Takatori12.5%	0.81	0.84
Takatori13%1	0.74	0.79
Takatori13%2	0.42	0.46
Takatori13%3	0.72	0.79
Takatori13%4	0.82	0.85
Takatori20%	1.39	1.43

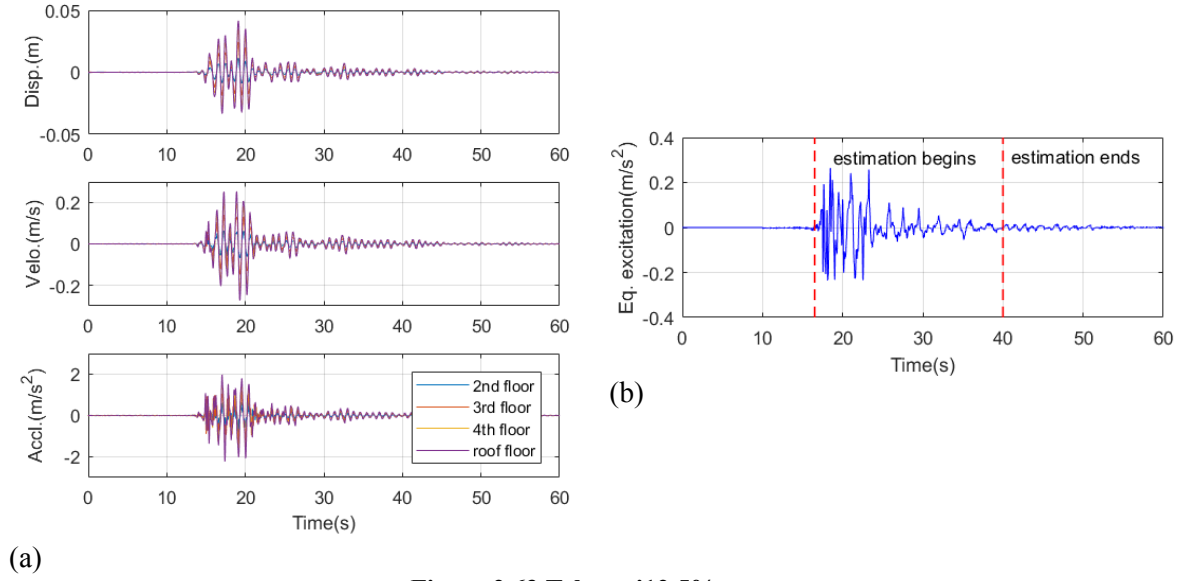


Figure 2.63 Takatori12.5% case;
(a) relative displacement, velocity and acceleration on each floor; (b) earthquake excitation

Similar to the last section, the SRIM method has been applied here to estimate modal frequencies using all four acceleration signals for both directions. First two modes of the structure have been extracted with high reliability. The modal frequency results are to be compared with those based on identified parameters using EKF-RM method.

First of all, the same 4-DOF lumped mass model in section 2.3.2 is assumed as the system model in filter. Stiffness of each floor and Rayleigh damping factor β are to be identified. For both directions, the equivalent concentration masses are 49.1, 48.8, 48.4 and 59.5 ton from 2nd to roof floor. Displacements and accelerations on each floor are observed, regarding as a full observation situation. In terms of \mathbf{R} matrix, 10^{-8} and 10^{-4} are set as displacement and acceleration variance respectively, namely the \mathbf{R} matrix is $diag([10^{-8}\mathbf{I}, 10^{-4}\mathbf{I}])$ for the total 8 cases. For all excitation cases, initial \mathbf{Q} matrix is set as $diag([10^{-8}\mathbf{I}, 10^{-6}\mathbf{I}, \mathbf{0}])$, and α_Q equals to 1/30 is used all the time.

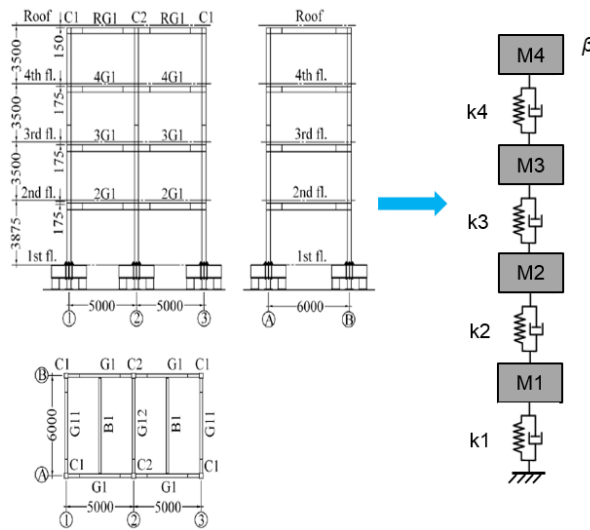


Figure 2.64 simplified 4-DOF system model

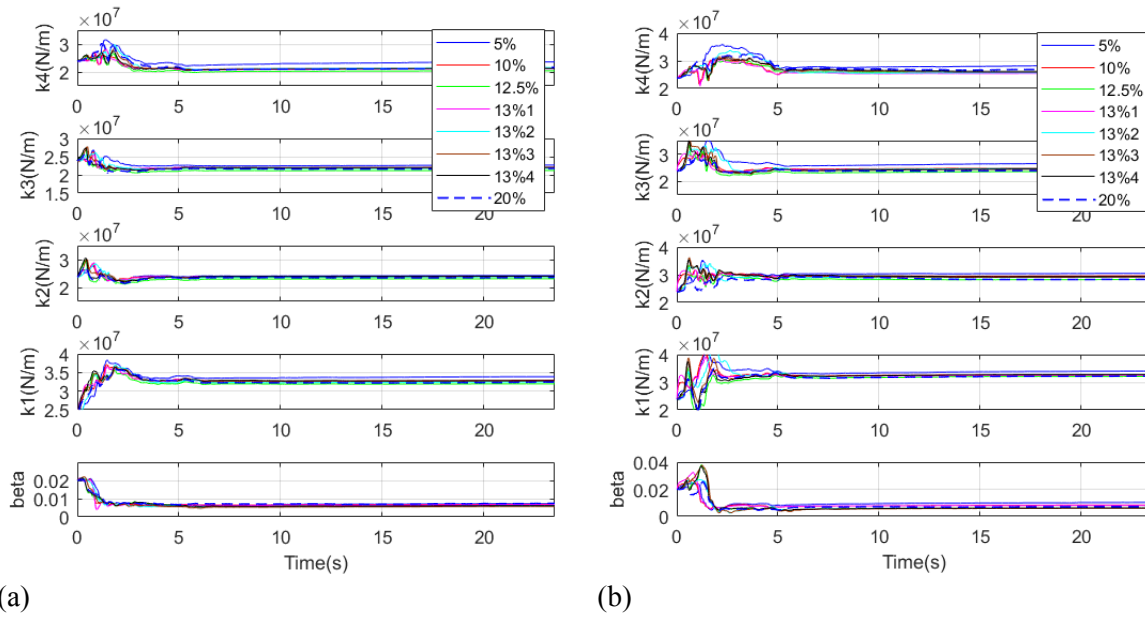


Figure 2.65 stiffness identification of 4-DOF system model; (a) NS direction; (b) WE direction

Figure 2.65 summarizes the stiffness identification results in a series of Takatori earthquake excitation cases for both NS and WE direction. The stiffness identification results from Takatori5% to Takatori20% are all approximately the same.

Figure 2.66 and Figure 2.67 compared the 1st and 2nd modal frequencies obtained from SRIM method and those computed from identified parameters for NS and WE direction respectively. In terms of the 1st mode, the two methods coincide with each other pretty well. It can also be found that slight stiffness reduction appears in the initial parts, i.e. Takatori5%, Takatori10% and Takatori12.5% case. Between Takatori13%1 case and Takatori20% case, modal frequencies roughly remain in a same level, which is 1.22Hz and 1.29Hz for NS and WE direction respectively. However, for the 2nd mode, pretty large frequency discrepancies exist between the two methods, the discrepancy values of NS and WE direction are 0.60Hz and 0.54Hz respectively. Except that, in fact the trends of both methods show same pattern found in the 1st mode case.

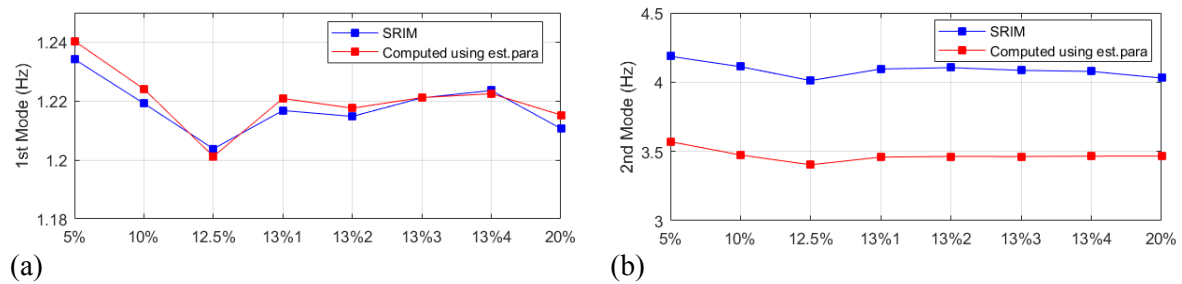


Figure 2.66 comparison of modal frequency in NS direction; (a) the 1st mode; (b) the 2nd mode;

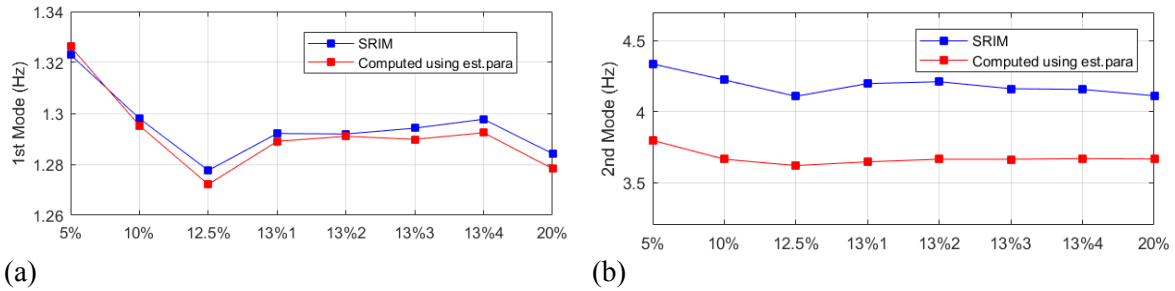


Figure 2.67 comparison of modal frequency in WE direction; (a) the 1st mode; (b) the 2nd mode;

This phenomenon, i.e. accurate reproduction for the 1st modal frequency but large discrepancy for the 2nd modal frequency for frame building model, actually has already been encountered and discussed in section 2.4.1 based on a numerical example. In that case, because of the imperfection of assumed system model, relative large frequency discrepancies are also found in the 2nd mode. A 3D model might be a reasonable improved model in order to match the 2nd modal frequencies, but it could involve too many unknown parameters to be identified or tuned, not to mention that the computation will be extremely time consuming. Therefore, a 2D frame model is considered as a preferable choice here.

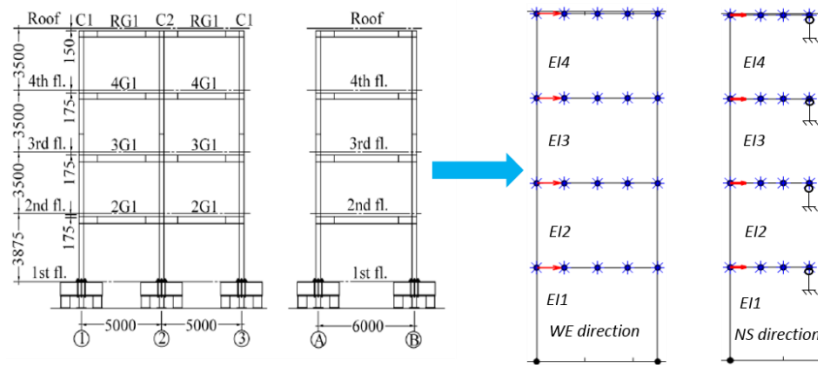


Figure 2.68 simplified 2D frame model

Figure 2.68 shows the simplified 2D model of NS and WE direction for the frame building. In this case, half models of both directions are extracted; the translational DOFs of nodes on each floor are coupled in order to reduce computation burden. The corresponding observations are represented as red arrows in the figures. Cross section stiffness EI of the columns on each floor are assumed as equal values to be identified. Mass effects are compensated with concentration mass elements added on each node of each floor. In these models, besides the column stiffness to be identified, the cross section stiffness EI of floor beams are also unknown parameters, since they involve contributions from both steel H beams and concrete decks of floors, of which equivalent stiffness cannot be defined directly. However, they are not supposed to be identified using EKF-RM, because the vertical vibration signals of the floors are too small and noisy to be employed. The parameters are decided by tuning the EI values of floor beams so that the 1st and 2nd modal frequencies based on EKF-RM method in the Takatori5% case are close enough to the SRIM results. After that, the obtained values of beam stiffness will be remained unchanged and applied to the following cases. Other parameters, such as axial cross section stiffness EA of columns and floor beams, can be readily decided through simple calculations based on design drawings. During the process of parameter tuning, it is found that mass distribution of the model also influenced modal frequencies significantly. By tuning beam stiffness values purely, it is still difficult to match those 2nd modal frequencies. Accordingly, the equivalent concentration mass for each floor are also adjusted along with beam stiffness in Takatori5%

case. Finally, all of the system parameters regarding as known values are listed in Table 2.10. The adjusted equivalent concentration masses are 49.1, 34.2, 38.7, and 68.4 ton from bottom to top floor, which are actually 1.0, 0.7, 0.8 and 1.15 times the original masses. In this 2D model case, displacement and acceleration signals are observed at locations shown in Figure 2.68. Computation parameters for EKF-RM method are all same as previous 4-DOF model case.

Table 2.10 known system parameter values of NS(WE) direction model

	E (N/m ²)	I (m ⁴)	A (m ²)	*C. mass(kg)
Column btw. the 1 st floor	2.06×10^{11}	N.A.	0.0398(0.0265)	N.A
Beam of the 1 st floor		0.0010(0.0065)	0.0250(0.0167)	6844(5309)
Column btw. the 2 nd floor		N.A	0.0398(0.0265)	N.A
Beam of the 2 nd floor		0.0010(0.0065)	0.0250(0.0143)	4710(3670)
Column btw. the 3 rd floor	ρ (kg/m ³)	N.A	0.0398(0.0265)	N.A
Beam of the 3 rd floor	7800	0.0010(0.0065)	0.0189(0.0126)	5401(4190)
Column btw roof floor		N.A	0.0398(0.0265)	N.A
Beam of roof floor		0.0010(0.0065)	0.0157(0.0105)	9735(7563)

*C. mass stands for concentration mass.

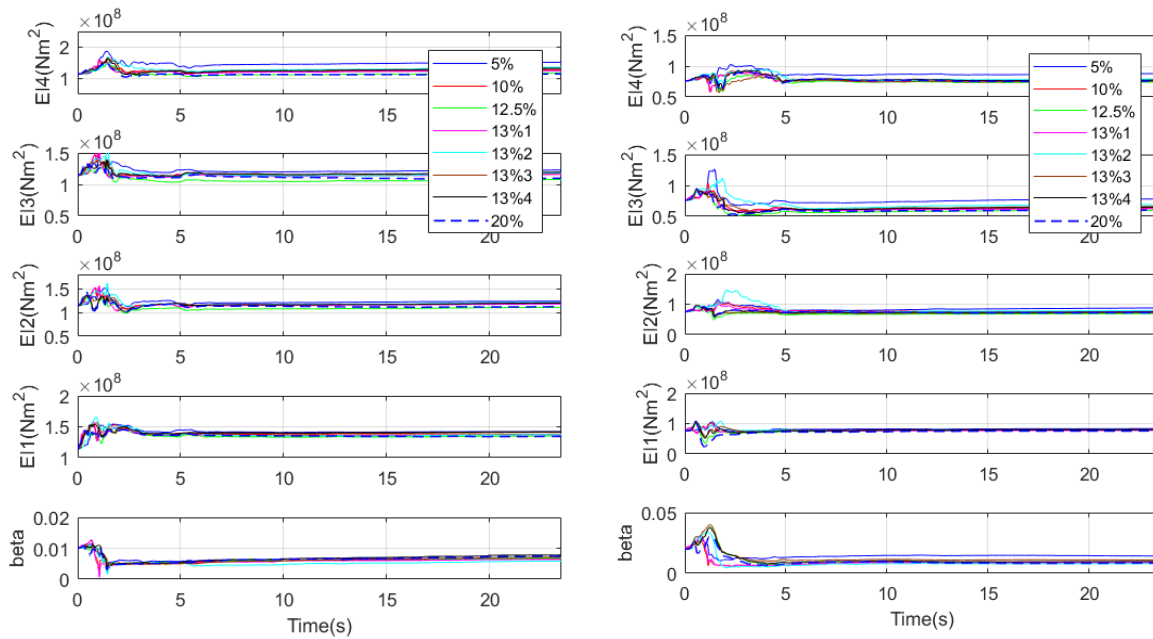
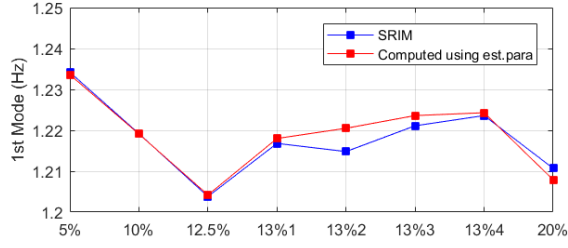
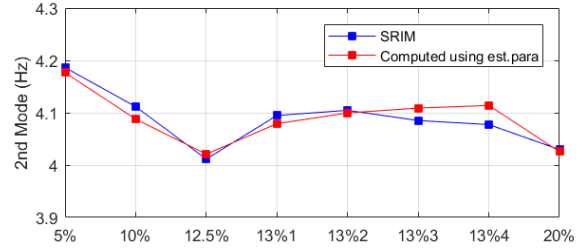


Figure 2.69 stiffness identification of 2D frame model; (a) NS direction; (b) WE direction

Figure 2.69 shows parameter identification results of NS and WE direction in a series of Takatori earthquake excitation cases. Similarly, for the eight cases, most of parameters remain approximately in same levels, but the parameters are slightly more scattering than the previous 4-DOF model case, especially for stiffness of top floor $EI3$ and $EI4$. This is due to that the 2D model possesses more unmeasured DOFs than the 1D model.

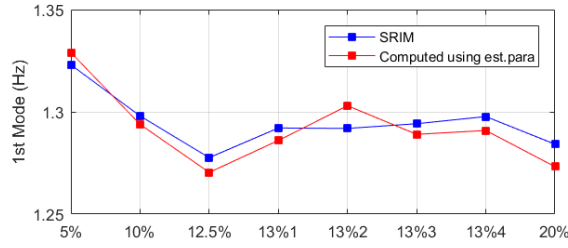


(a)

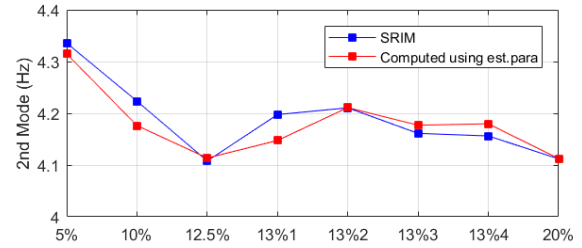


(b)

Figure 2.70 comparison of modal frequency in NS direction; (a) the 1st mode; (2) the 2nd mode

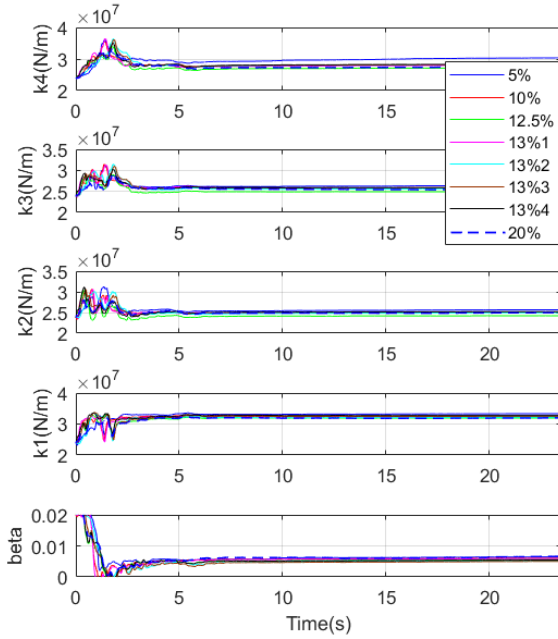


(a)

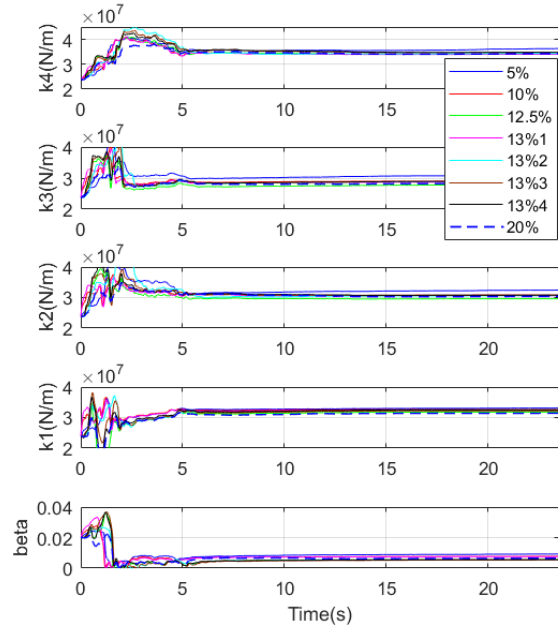


(b)

Figure 2.71 comparison of modal frequency in WE direction; (a) the 1st mode; (2) the 2nd mode



(a)



(b)

Figure 2.72 stiffness identification of mass adjusted 4-DOF model; (a) NS direction; (b) WE direction

Figure 2.70 and Figure 2.71 compare the 1st and 2nd modal frequencies based on the EKF-RM method and the SRIM method for both NS and WE direction. It can be found that both 1st and 2nd frequencies approximately match the SRIM results. The discrepancies of the 2nd modal frequencies are relatively larger than the 1st mode case, and results of NS are slightly better than those of WE direction.

Same as section 2.5.1, to verify the identified parameters, the system responses are reproduced using the identified parameters based on forward simulation. The constant parameters used for

simulations are the averaged ones over the last 10 seconds of identification histories. Figure 2.73 shows the simulated accelerations of the four floors using the identified parameters in Takatori10% case for both directions. The simulated accelerations present good agreements with the real observed ones. The errors of the simulated accelerations on the 4th floor in a series of excitation cases are summarized in Table 2.11. The errors are still calculated based on equation (2.21). In these cases, the accuracies of the NS direction are better than those of the WE direction.

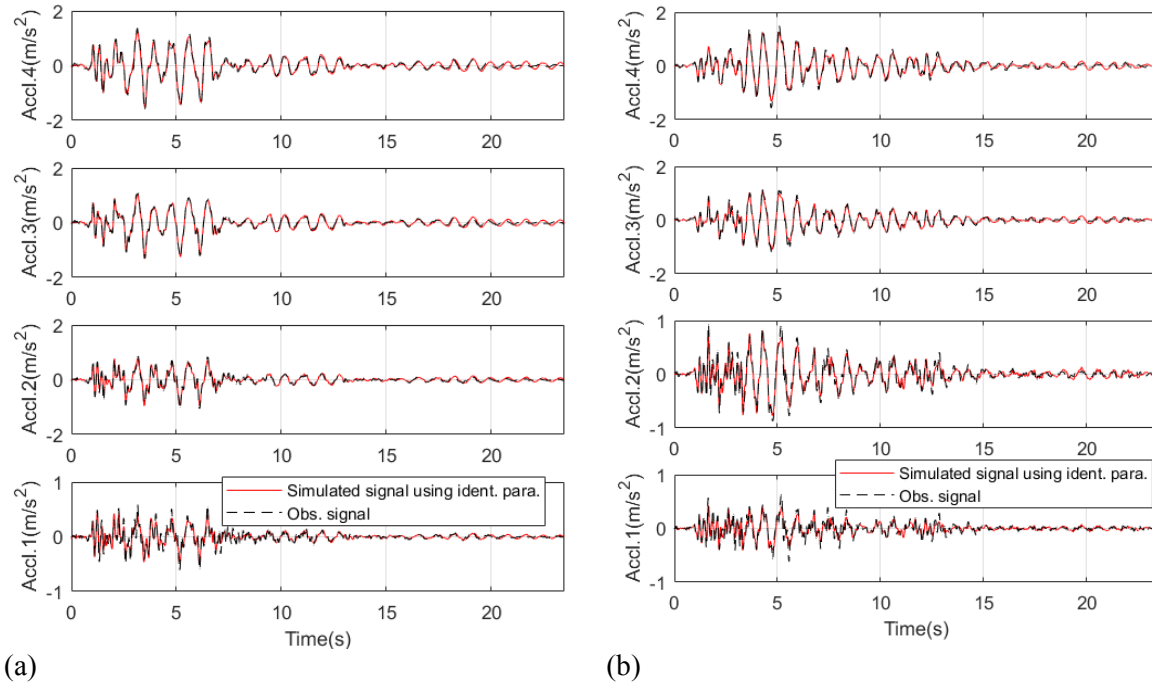


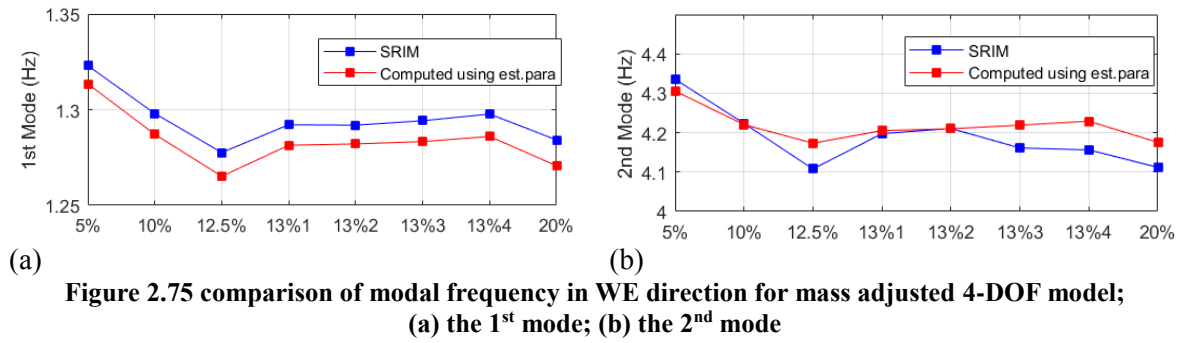
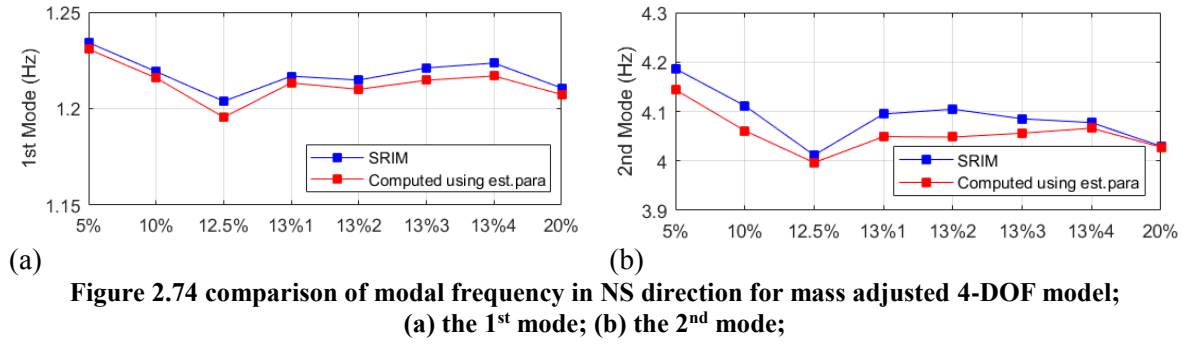
Figure 2.73 simulated accelerations of the four floors using the identified parameters in Takatori10% case: (a) NS direction; (b) WE direction

Table 2.11 errors of simulated accelerations on the 4th floor

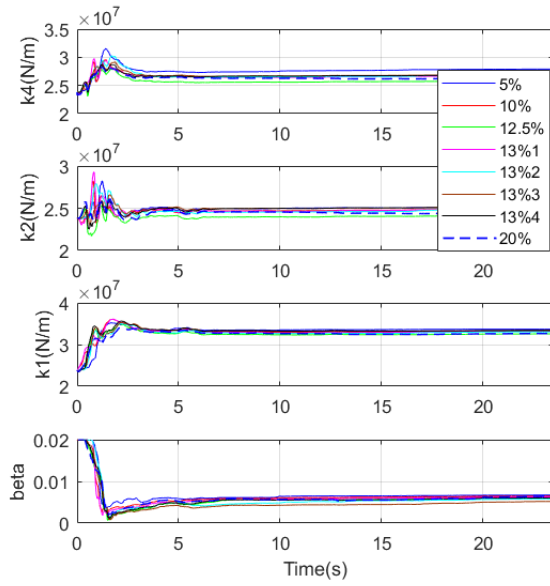
	NS direction	WE direction
Takatori5%	25.5%	35.9%
Takatori10%	18.4%	21.5%
Takatori12.5%	19.4%	29.0%
Takatori13%1	16.3%	19.9%
Takatori13%2	26.9%	25.7%
Takatori13%3	24.2%	34.6%
Takatori13%4	26.2%	29.6%
Takatori20%	17.8%	26.0%

Here, a 4-DOF model with adjusted mass distribution is also considered in order to compare with the 2D frame model. The principle for adjusting mass is same as previous case, i.e. the mass distribution is adjusted so that the 1st and 2nd modal frequency from EKF-RM method in Takatori5% case are close enough to the SRIM results, the adjusted masses remain constant for all following cases. The adjusted equivalent concentration masses are 44.2, 29.3, 43.6, and 80.3 ton from bottom to top floor, which are actually 0.9, 0.6, 0.9 and 1.35 times the original masses. Figure 2.72 shows the parameter identification results in a series of Takatori earthquake cases for NS and WE direction both. Figure 2.74 and Figure 2.75 show the modal frequency results. By using the adjusted masses, the discrepancies of the 2nd modal frequency become smaller but still not accurate, at the same time the

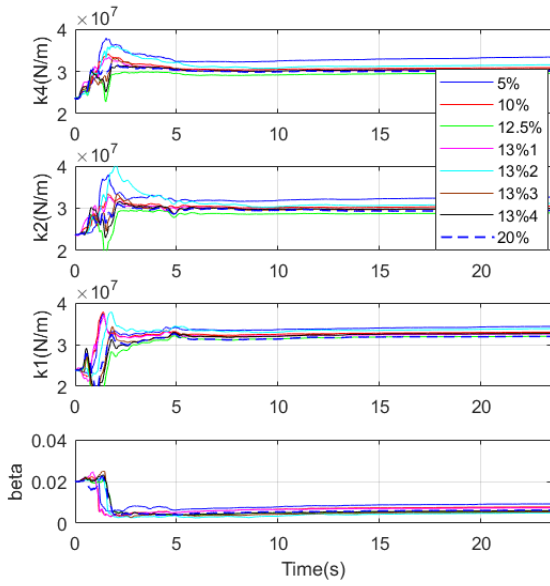
discrepancies of the 1st modal frequency increase a bit comparing the results shown in Figure 2.66 and Figure 2.67. However, comparing the 2nd modal frequency results between the two models, the 2D model still outperforms the 1D model slightly, especially for NS direction. The updated equivalent concentration masses of the second and roof floor for the 1D model are 0.6 and 1.35 times the original mass, while they are 0.7 and 1.15 for the 2D model. The masses of 1D model are quite deviated from the original one. Based on the aforementioned facts, it might not be reasonable to reproduce the 2nd modal frequency accurately based on the 4-DOF lumped mass model.



Finally, in this section, a case with limited partial observations is considered here to test the estimation accuracy of unmeasured system responses based on the 1D mass adjusted model and the 2D frame model. The displacements and accelerations on the 4th floor are ignored and the stiffness of the 4th and roof floor are assumed as uniform. Except that the size of \mathbf{R} matrix should be reduced accordingly, other system and computation information are same as previous case.

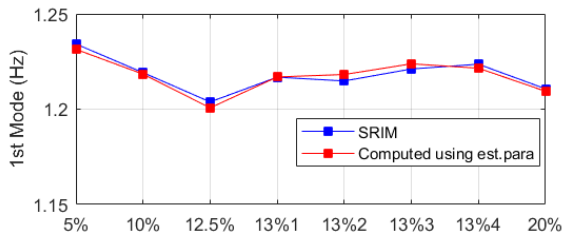


(a)

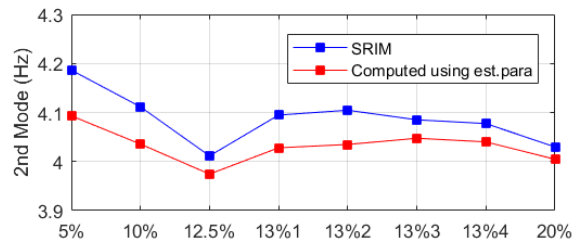


(b)

Figure 2.76 parameter identification of mass adjusted 1D model with partial observations; (a) NS direction; (b) WE direction

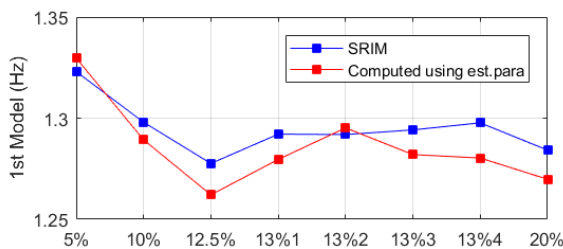


(a)

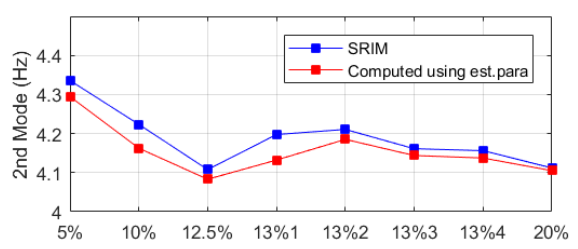


(b)

Figure 2.77 comparison of modal frequency in NS direction for mass adjusted 1D model with partial observations; (a) the 1st mode; (b) the 2nd model

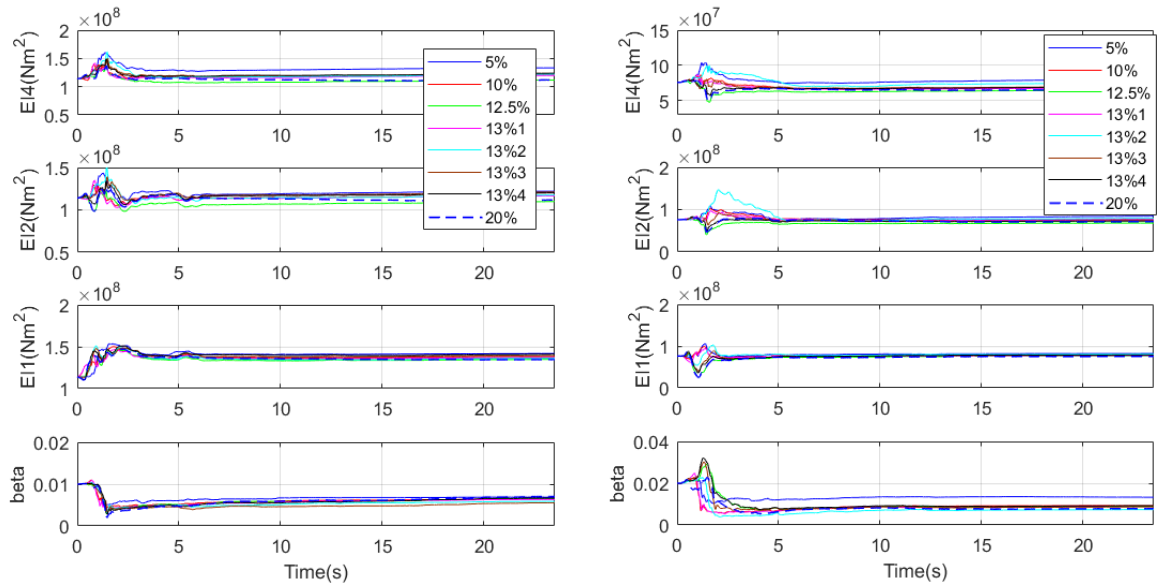


(a)

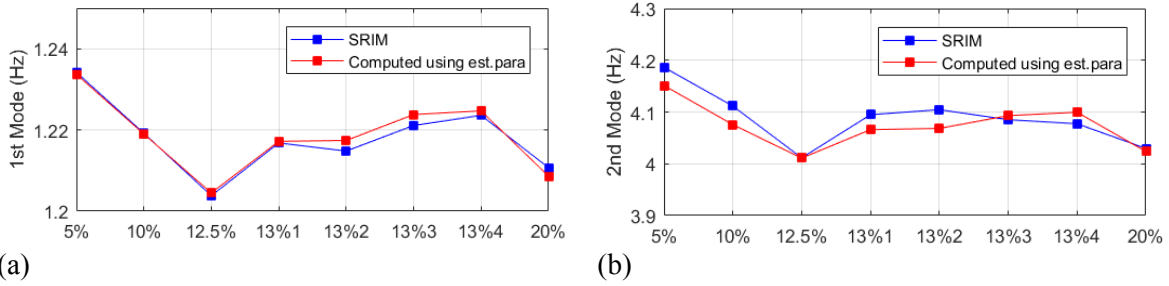


(b)

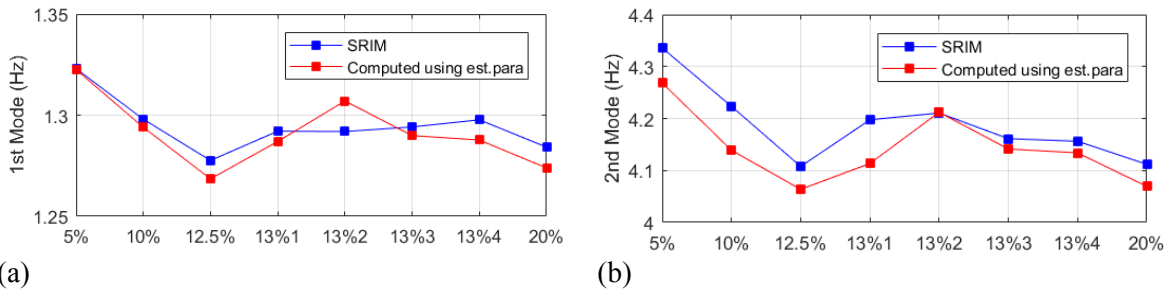
Figure 2.78 comparison of modal frequency in WE direction for mass adjusted 1D model with partial observations; (a) the 1st mode; (b) the 2nd model



(a) (b)
Figure 2.79 parameter identification of 2D frame model with partial observations;
(a) NS direction; (b) WE direction



(a) (b)
Figure 2.80 comparison of modal frequency in NS direction for 2D frame model with partial observations; (a) the 1st mode; (b) the 2nd model



(a) (b)
Figure 2.81 comparison of modal frequency in WE direction for 2D frame model with partial observations; (a) the 1st mode; (b) the 2nd model

Basically, in the partial observation cases, the modal frequencies computed using identified parameters still capture the trend of real frequency variations but the errors become larger. Figure 2.82 and Figure 2.83 shows the estimated displacement on the 4th floor based on the 1D and 2D model respectively. Both show great coincidences. Table 2.12 summaries results of other cases, which again show fair accuracies. In this case, the results from 2D model are slightly better than the

1D model.

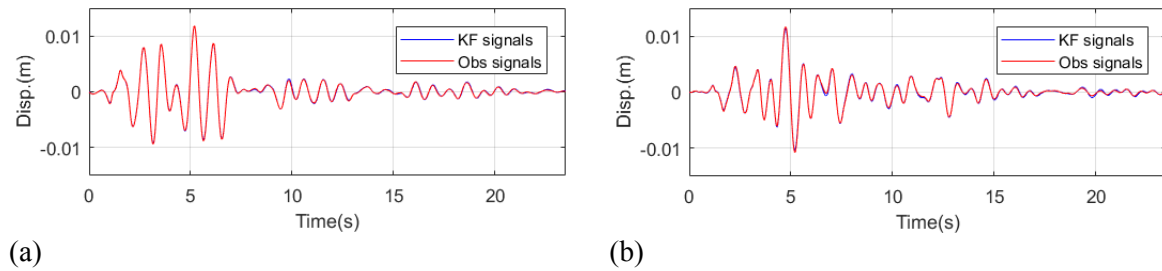


Figure 2.82 estimated displacement on the 4th floor of mass adjusted 1D model in Takatori5% case; (a) NS direction; (b) WE direction

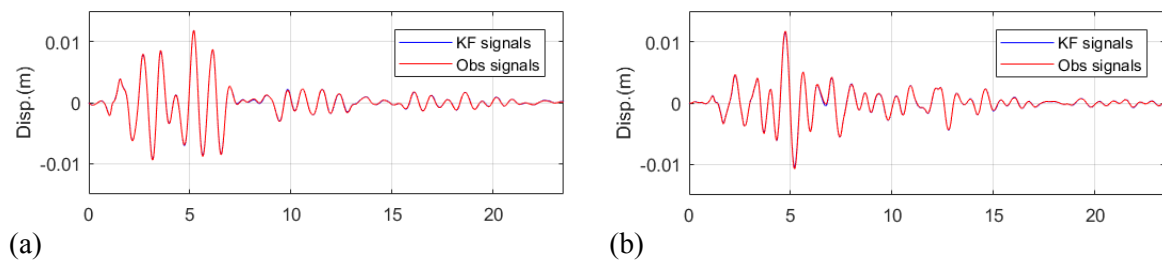


Figure 2.83 estimated displacement on the 4th floor of 2D frame model in Takatori5% case; (a) NS direction; (b) WE direction

Table 2.12 estimated displacement error on the 4th floor

ID	1D model		2D model	
	NS direction	WE direction	NS direction	WE direction
Takatori5%	3.7%	4.5%	2.2%	3.2%
Takatori10%	2.4%	3.0%	1.9%	2.9%
Takatori12.5%	2.3%	3.7%	1.6%	3.2%
Takatori13%1	2.4%	3.0%	1.9%	2.9%
Takatori13%2	2.3%	3.1%	1.7%	3.2%
Takatori13%3	2.2%	3.5%	1.7%	3.1%
Takatori13%4	2.3%	3.5%	1.8%	3.2%
Takatori20%	3.0%	4.2%	1.7%	3.2%

2.5.3 E-defense substructure experiment

A substructure experiment in E-defense database is analyzed here. The purpose of the experiment is development of advanced monitoring system for post-earthquake structure foundation assessment. Figure 2.84 shows the basic setup of the experiment model. The model mainly consists of three parts, i.e. a soil tank of 6.0m depth and 8.0m diameter, a scaled substructure model supported by 6 RC piles, a scaled substructure model supported by 9 steel piles. Two layers of sands are deployed in the soil tank, i.e. silica sand with 60% relative density from -2.0m~0.0m and silica sand with 80% relative density from -6.0m~-2.0m, in order to reproduce compacted multi-layer soil system. In terms of the substructure systems, a rigid steel pile cap with 10ton weight is welded on the top of each pile group assuming a rigid connection between the two members. Mass effect of superstructure in reality is simplified as a 14ton weight steel rigid body which connects with each pile cap through 4 rubber bearings. The RC pile group was supposed to suffer severe damage or even complete collapse during

the experiment for validating the monitoring system. The steel pile group, on the other hand, was expected to remain in elastic field for soil-pile interaction assessment. Detail information about the model can be found in relevant experiment report [104].

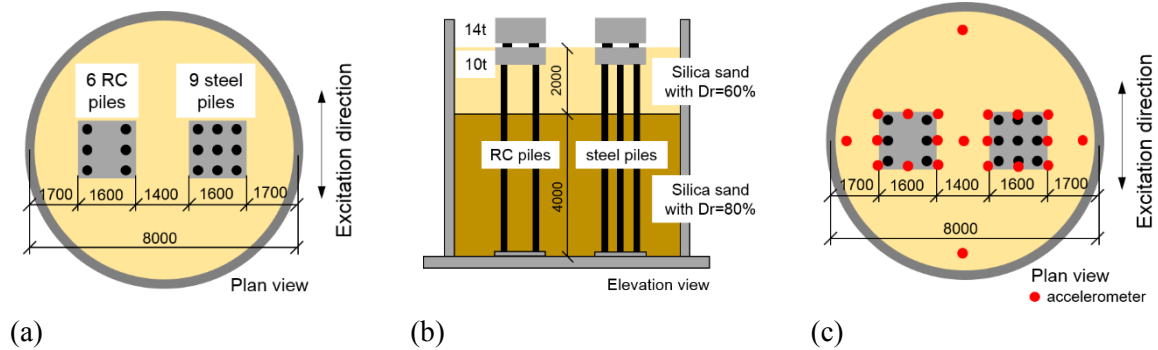


Figure 2.84 basic setup of E-defense substructure experiment model (unit: mm); (a) plan view; (b) elevation view; (c) location of accelerometers

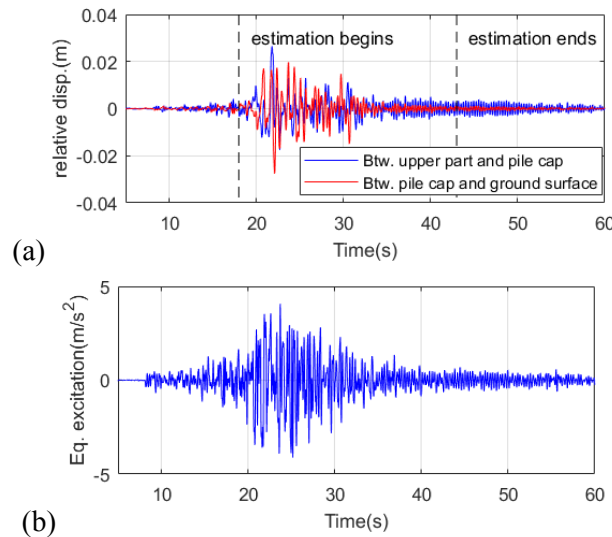


Figure 2.85 RC pile substructure in JMA100% case; (a) relative displacement; (b) surface acceleration

The monitoring system includes various sensor types, including accelerometer, laser displacement transducers, strain gauges, soil pressure sensor, water pressure sensor and etc., so that comprehensive understandings of soil, pile performances and their interaction effect can be obtained. In this study, acceleration measurements, with 200Hz sampling frequency, are mainly used here for system estimation. Accordingly, displacement and velocity signals are integrated from the accelerations then applied with a high-pass filter of 0.4 Hz cutoff frequency. Displacement measurements from laser displacement transducers are either too noisy to be used or not available due to equipment failures, therefore they are not considered here.

Figure 2.84(c) shows the locations of acceleration measurements which are used in this study. In terms of soil tank, five accelerometers are deployed in a symmetric manner on the ground surface; eight points on the top of each pile cap or upper rigid body are measured. The raw acceleration signals are firstly de-noised, and then the averaged one is used and applied to the integrated displacement and velocity for corresponding objects. The experiment model was under a series of JMA earthquake excitations. In the following part, three JMA earthquake excitation cases are analyzed, i.e. JMA100%1, JMA100%2 and JMA150% with PGA equals to 4m/s^2 , 4.7m/s^2 and

5.6m/s² respectively. A typical group of relative displacements and earthquake excitation are shown in Figure 2.85. In this figure, the blue line represents the relative displacement between upper structure and pile cap, while the red line is the relative displacement between pile cap and ground surface.

In this study, each substructure is simplified as two SDOF systems separately, i.e. the upper rigid body part and the substructure part, as shown in Figure 2.86. In terms of the upper rigid body part, input excitation is actually the acceleration on pile cap and system responses are relative ones with respect to pile cap; while for the substructure part, input excitations include both ground surface acceleration and inertial force transferred from the upper rigid body, system responses are relative ones with respect to ground surface. The reason for decomposing the substructure model into two SDOF systems is that strong nonlinearities appear in the experiments, and SDOF system model is considered more advantageous to deal with nonlinear problem. The stiffness of upper part SDOF system comes from the bearing stiffness with design value of $9.36 \times 10^6 \text{ N/m}$. On the other hand, the stiffness of substructure SDOF system can be regarded as the translational part of equivalent sway-rocking (SR) model, of which the design values are calculated as $9.75 \times 10^7 \text{ N/m}$ and $7.12 \times 10^7 \text{ N/m}$ for steel pile group and RC pile group respectively.

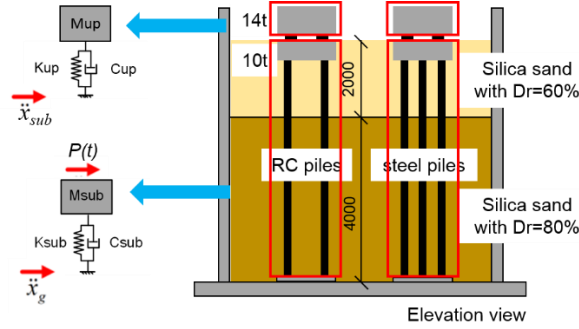


Figure 2.86 simplified SDOF model for substructure experiment

$$m_{up} \ddot{x}_{up} + c_{up} \dot{x}_{up} + k_{up} x_{up} = -m_{up} \ddot{x}_{sub} \quad (2.22)$$

$$m_{sub} \ddot{x}_{sub} + c_{sub} \dot{x}_{sub} + k_{sub} x_{sub} = -m_{sub} \ddot{x}_g - m_{up} (\ddot{x}_g + \ddot{x}_{up}) \quad (2.23)$$

In the estimation process, displacements and accelerations are observed. Measurement noise covariance matrices \mathbf{R} are set as $\text{diag}([10^{-6}, 10^{-1}])$ and $\text{diag}([3 \times 10^{-7}, 3 \times 10^{-2}])$ for upper SDOF system and substructure SDOF system respectively, which correspond to about 15% of displacement RMS 0.007 m, acceleration RMS 2 m/s² for upper part and displacement RMS 0.004 m, acceleration RMS 1.2 m/s² for substructure part respectively. For all excitation cases, initial \mathbf{Q} matrix is set as $\text{diag}([10^{-8}, 10^{-6}, 0, 0])$ and track mode of EKF-RM method with α_Q of 1/30 is used in order to track stiffness variations instantaneously.

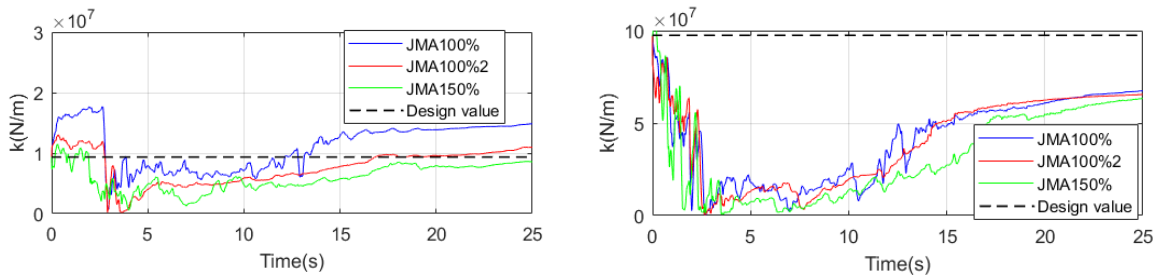


Figure 2.87 stiffness identification of steel pile substructure; (a) bearing stiffness; (b) SR model stiffness

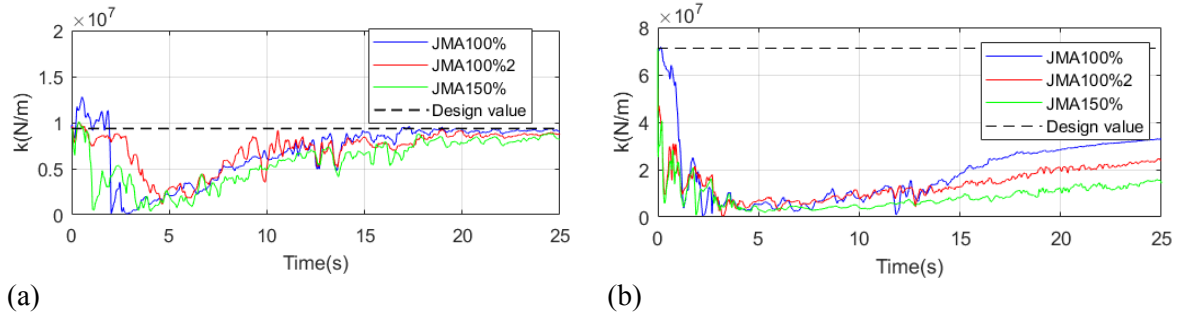


Figure 2.88 stiffness identification of RC pile substructure; (a) bearing stiffness; (b) SR model stiffness

Figure 2.87 and Figure 2.88 show the parameter identification results for steel pile substructure case and RC pile substructure case. In terms of bearing stiffness results, it is clear that significant stiffness degradation occurred between 3 s and 10 s approximately for both cases, showing as a concave shape during the period of time. From 10s to 20s, the bearing regains its stiffness and roughly remains as a constant value afterwards, most of which are close to the design value of $9.36 \times 10^6 \text{ Nm}^{-1}$. This phenomenon reflects that the bearings might not suffer severe damage during the earthquake excitations since residual stiffness (20s~25s) of all cases, except the JMA100% steel pile case, are at the same level. The part presenting evident stiffness reduction may come from the inherent nonlinearity of bearing itself.

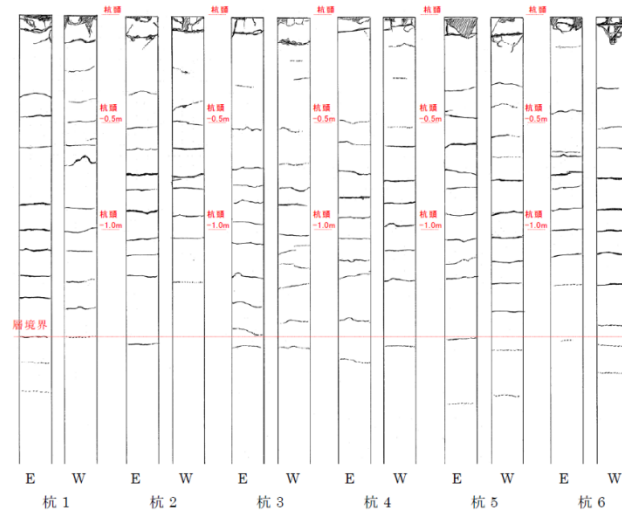


Figure 2.89 crack sketch of RC pile [104]

In terms of the SR model stiffness, similar stiffness variation pattern is found, i.e. from 3s to 15s stiffness is much smaller than corresponding design value while SR model spring regains its stiffness afterwards. For the steel pile substructure case, the residual stiffness (20s~25s) part approximately remains same trend and value among different excitation cases. It might be regarded as the proof that the conditions of steel piles are intact, which is confirmed by experiment report. Additionally, the residual stiffness is generally below the design value. It is natural because both soil and pile group contribute to the stiffness of SR model, and the reduction of soil stiffness under earthquake excitation could result in overall reduction of SR model stiffness. As it will be shown later, by considering the soil stiffness reduction, the SR model stiffness could reduce to 0.2~0.3 of the design value. If nonlinearity, e.g. local plasticity between soil and pile, is further account, the value could be smaller. For the RC pile substructure case, the residual stiffness is not only far away from design value, but

also decreases continually along with the series of excitations. This continuous stiffness degradation reflects the damage development of RC piles. Figure 2.89 shows the crack sketch of the RC piles after excitations. Obviously extensive damages happened.

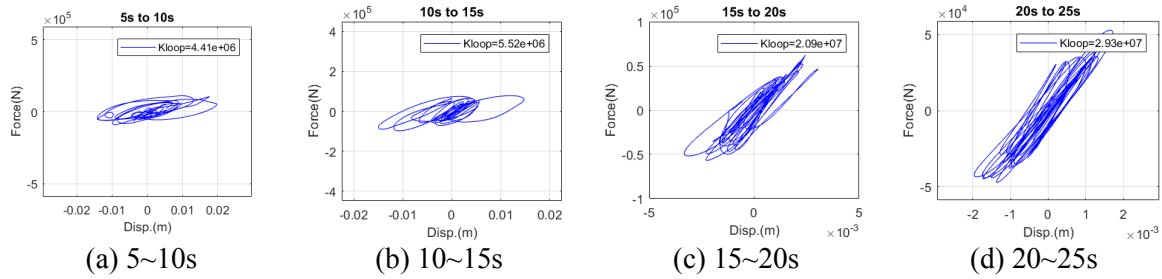


Figure 2.90 hysteresis loop of pile cap of RC pile substructure in JMA100% case

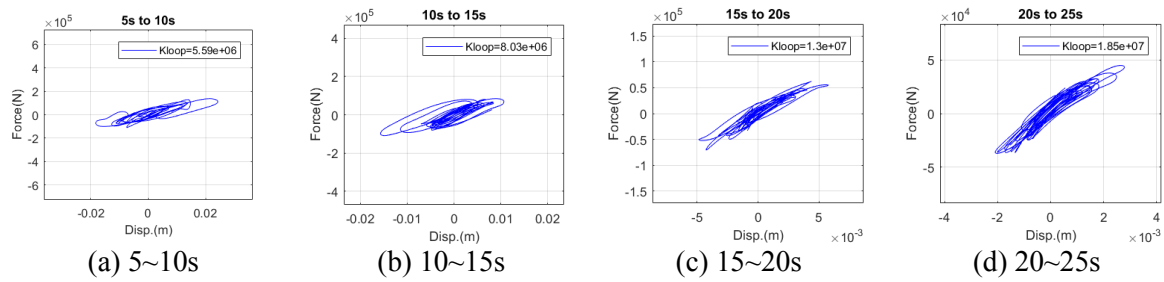


Figure 2.91 hysteresis loop of pile cap of RC pile substructure in JMA100% 2 case

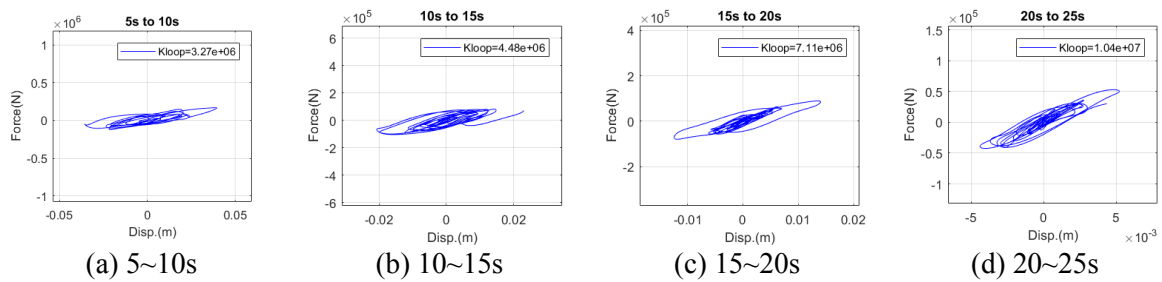


Figure 2.92 hysteresis loop of pile cap of RC pile substructure in JMA150% case

Since no real reference value of stiffness is available in this study, the estimated stiffness from EKF-RM method is further compared with the slope of measured hysteresis loop of each SDOF model. The force of hysteresis loop is inertial force exerted on each concentration mass. Figure 2.90 ~ Figure 2.92 show the measured hysteresis loops of pile cap of RC pile substructure between different time intervals for the three excitation cases, in which 'Kloop' represents slope value (linear fit value) of a measured hysteresis loop. It clearly shows that the slopes of hysteresis loops become larger in a same row, especially for the JMA100% case, which reflects the stiffness regaining process. Table 2.13 compares the slope values with the estimated stiffness value for each time interval. It is clear they show good consistencies even though the values are not rigorously same. The hysteresis loops are also consistent with corresponding identification results for the bearing in the RC pile substructure. The hysteresis loops and identified stiffness results are shown from Figure 2.93 ~ Figure 2.95 and listed in Table 2.14. Due to limited space, results from other cases are not presented here.

Table 2.13 comparison of slopes of hysteresis loop and estimated stiffness for SR model in RC pile subs.

JMA100%	Slope of hysteresis loop	Range of estimated stiffness
---------	--------------------------	------------------------------

	(N/m)	(N/m)
5s~10s	4.41×10^6	$2.39 \times 10^6 \sim 1.20 \times 10^7$
10s~15s	5.52×10^6	$4.63 \times 10^6 \sim 1.82 \times 10^7$
15s~20s	2.09×10^7	$1.80 \times 10^7 \sim 2.81 \times 10^7$
20s~25s	2.93×10^7	$2.81 \times 10^7 \sim 3.33 \times 10^7$
JMA100%2		
5s~10s	5.59×10^6	$2.63 \times 10^6 \sim 1.14 \times 10^7$
10s~15s	8.03×10^6	$4.29 \times 10^6 \sim 1.30 \times 10^7$
15s~20s	1.30×10^7	$1.30 \times 10^7 \sim 2.11 \times 10^7$
20s~25s	1.85×10^7	$1.89 \times 10^7 \sim 2.42 \times 10^7$
JMA150%		
5~10s	3.27×10^6	$1.99 \times 10^6 \sim 5.19 \times 10^6$
10s~15s	4.48×10^6	$3.41 \times 10^6 \sim 8.34 \times 10^6$
15s~20s	7.11×10^6	$6.38 \times 10^6 \sim 1.22 \times 10^7$
20s~25s	1.04×10^7	$1.01 \times 10^7 \sim 1.63 \times 10^7$

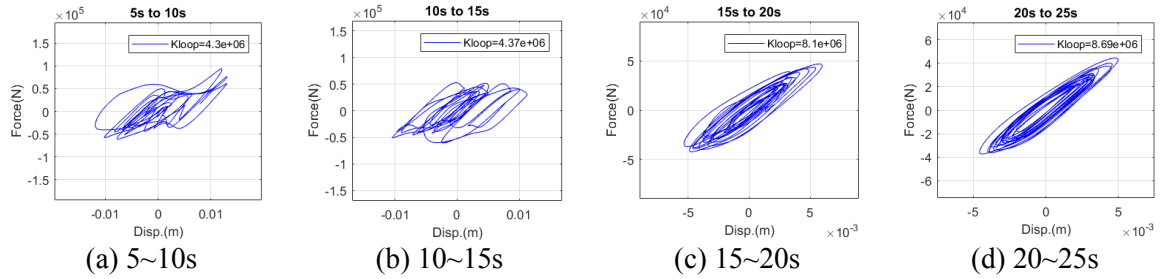


Figure 2.93 hysteresis loop of bearing of RC pile substructure in JMA100% case

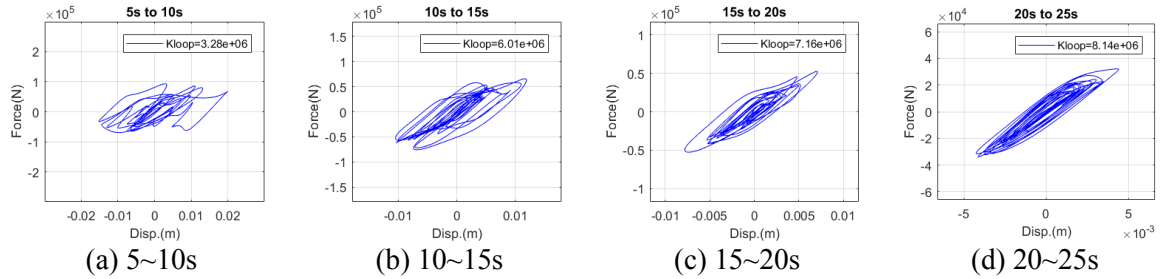


Figure 2.94 hysteresis loop of bearing of RC pile substructure in JMA100%2 case

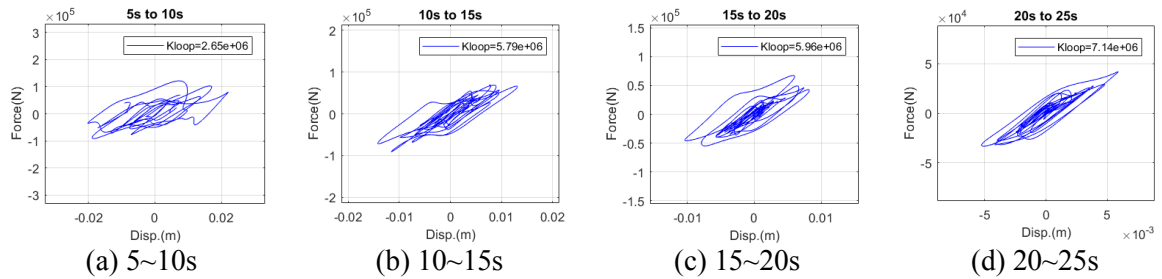


Figure 2.95 hysteresis loop of bearing of RC pile substructure in JMA150% case

Table 2.14 comparison of slopes of hysteresis loop and estimated stiffness for bearing in RC pile subs.

JMA100%	Slope of hysteresis loop (N/m)	Range of estimated stiffness (N/m)
---------	-----------------------------------	---------------------------------------

5s~10s	4.30×10^6	$2.12 \times 10^6 \sim 6.99 \times 10^6$
10s~15s	4.37×10^6	$4.81 \times 10^6 \sim 8.96 \times 10^6$
15s~20s	8.10×10^6	$7.57 \times 10^6 \sim 9.61 \times 10^6$
20s~25s	8.69×10^6	$8.68 \times 10^6 \sim 9.31 \times 10^6$
JMA100%2		
5s~10s	3.28×10^6	$2.82 \times 10^6 \sim 8.41 \times 10^6$
10s~15s	6.01×10^6	$3.54 \times 10^6 \sim 9.18 \times 10^6$
15s~20s	7.16×10^6	$6.98 \times 10^6 \sim 9.31 \times 10^6$
20s~25s	8.14×10^6	$8.35 \times 10^6 \sim 9.11 \times 10^6$
JMA150%		
5~10s	2.65×10^6	$7.82 \times 10^5 \sim 4.86 \times 10^6$
10s~15s	5.79×10^6	$4.12 \times 10^6 \sim 7.37 \times 10^6$
15s~20s	5.96×10^6	$5.31 \times 10^6 \sim 8.78 \times 10^6$
20s~25s	7.14×10^6	$7.47 \times 10^6 \sim 8.81 \times 10^6$

It is worth noting here that the tracked stiffness values in Figure 2.87 and Figure 2.88 almost reach zero sometimes, e.g. 3.0~5.0s which is not that reasonable. In the proposed method of track mode, in fact secant stiffness of system is identified, which is accurate for the numerical example in 2.3.4 where the secant stiffness at each time instant is defined as shown in Figure 2.18. However, in this experiment, the equivalent secant stiffness is identified for hysteresis loop. Unavoidably, there are identification errors involved, especially during hysteresis loop is large and not close to a linear lightly damped loop trajectory. Therefore, those large fluctuations, i.e. 3~10s, and unreasonable stiffness values close to zero do not accurately represent the physical stiffness values. For the latter part of the estimations, i.e. 15~25s, the hysteresis loops resemble those of linear lightly damped systems as shown in Figure 2.90 ~ Figure 2.92, and the stiffness identification results are smoother and more accurate. Therefore, an identified value at certain time instant might not be accurate but the overall stiffness variation trends captured by the proposed method actually reflect system nonlinearity.

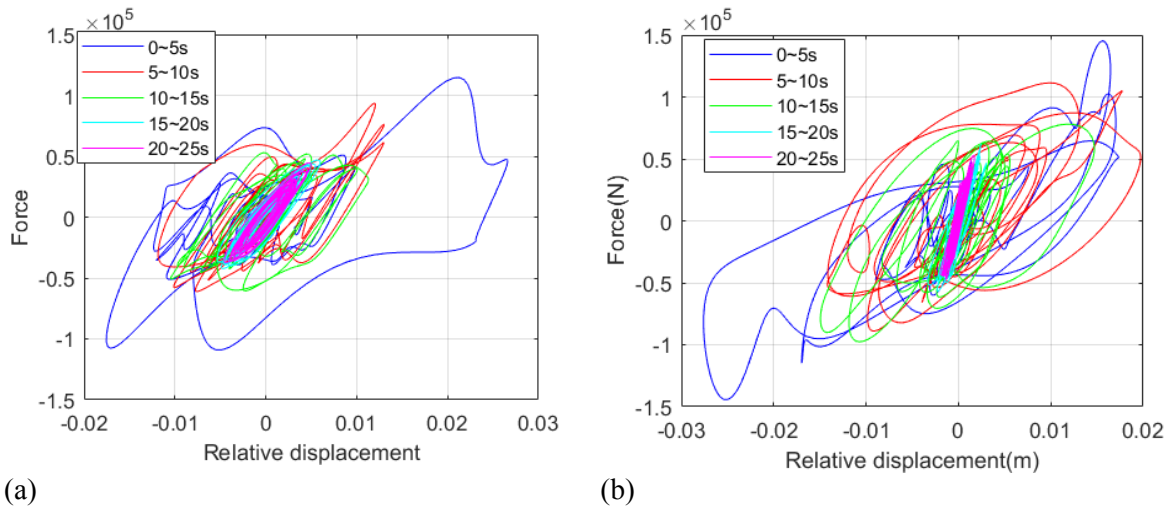


Figure 2.96 hysteresis loop of (a) bearing; (b) pile cap of RC pile substructure in JMA100% case

Figure 2.96 shows the hysteresis loop of pile cap and bearing of RC pile substructure in JMA100% case for different time interval. As shown in the figure, during 0~10s, actually the hysteresis loop is large, i.e. blue line for 0~5s and 5~10s for red line; while for 15~25s the behaviors of hysteresis loops

are more in linear shapes, i.e. cyan line for 15~20s and magenta line for 20~25s.

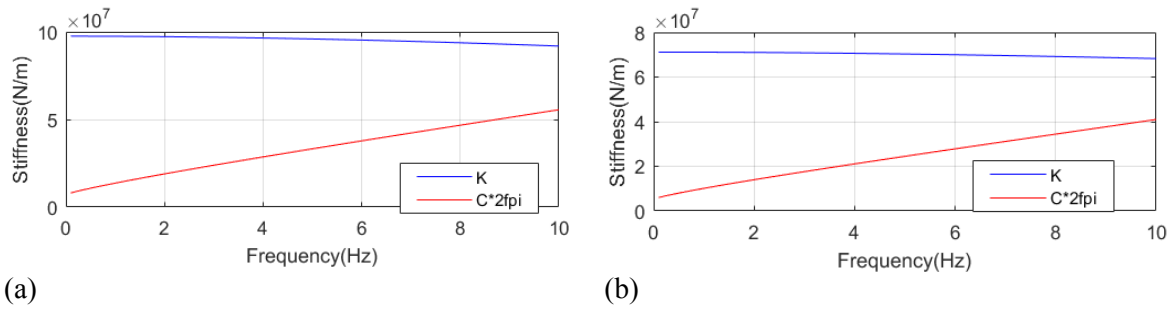


Figure 2.97 calculation of SR model stiffness reduction considering no material reduction;
(a) steel pile case; (b) RC pile case

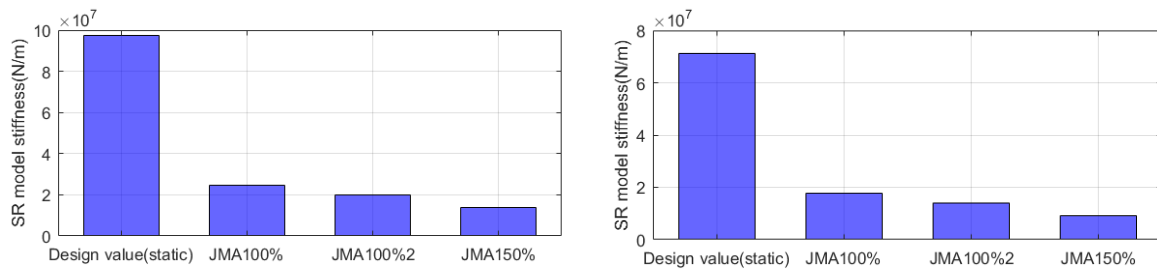


Figure 2.98 calculation of SR model stiffness considering soil stiffness reduction (at 0 Hz);
(a) steel pile case; (b) RC pile case

As aforementioned, for the steel/RC pile part, actually the stiffness is calculated as SR model stiffness, specifically translational stiffness, using the method proposed in [123, 124]. The design values shown in Figure 2.87 and Figure 2.88 are calculated using soil and pile material properties in static condition, i.e. no stiffness reduction is considered. The results in steel pile and RC pile are shown in the Figure 2.97. Since the value is actually frequency dependent, the value at 0 Hz is used according to some design codes suggest. If soil stiffness reduction is considered by calculating equivalent soil stiffness under seismic excitation based on SHAKE algorithm [125], the equivalent SR model stiffness considering seismic effect can be calculated under a series of earthquake excitations and are shown in Figure 2.98. Because of soil stiffness reduction, the SR model stiffness decrease significantly. If some local soil nonlinearities (e.g. contact between soil and pile) are accounted, which are not considered in the SHAKE algorithm and SR model, the SR model stiffness could be smaller. The method of SR model stiffness computation and SHAKE algorithm are presented in Appendix A and B in detail. Specifically, using the SHAKE algorithm, the calculated soil properties in a series excitation cases are listed in Table 2.15. Based on these values, the corresponding SR model stiffness values are listed in Table 2.16 which are also shown in Figure 2.98.

In Table 2.15, ρ , ν , C_s , and β stand for soil density, poison's ratio, shear wave velocity and damping factor respectively.

Table 2.15 soil properties for SR model stiffness computation

Layer(m)	$\rho(\text{kg/m}^3)$	ν	Static		JMA100%1		JMA100%2		JMA150%	
			$C_s(\text{m/s})$	β	$C_s(\text{m/s})$	β	$C_s(\text{m/s})$	β	$C_s(\text{m/s})$	β
0~1	1430	0.26	103.2	0.05	39.9	0.18	33.8	0.20	25.3	0.21
-1~-2	1430	0.26	135.8	0.05	46.3	0.19	39.6	0.20	28.7	0.21
-2~-3	1720	0.44	185.5	0.05	113.8	0.12	106.7	0.13	90.4	0.15
-3~-4	1720	0.44	204.0	0.05	121.6	0.12	115.0	0.13	90.4	0.16
-4~-5	1720	0.44	218.5	0.05	128.6	0.12	124.9	0.13	94.8	0.16

-5~-6	1720	0.44	230.6	0.05	129.4	0.13	129.8	0.13	95.0	0.17
-------	------	------	-------	------	-------	------	-------	------	------	------

Table 2.16 summary of calculated SR model stiffness values		
	Steel pile case (N/m)	RC pile case (N/m)
Static	9.75×10^7	7.12×10^7
JMA100%1	2.46×10^7	1.77×10^7
JMA100%2	1.98×10^7	1.40×10^7
JMA150%	1.37×10^7	0.92×10^7

2.5.4 Discussion about the application of EKF-RM method

The EKF-RM method was validated through the E-defense experiments in previous section. For the first and second experiment, stable mode was used, while track mode was applied to the substructure experiment due to its strong nonlinearity. As mentioned previously, appropriate application of different computation mode of the proposed method is important.

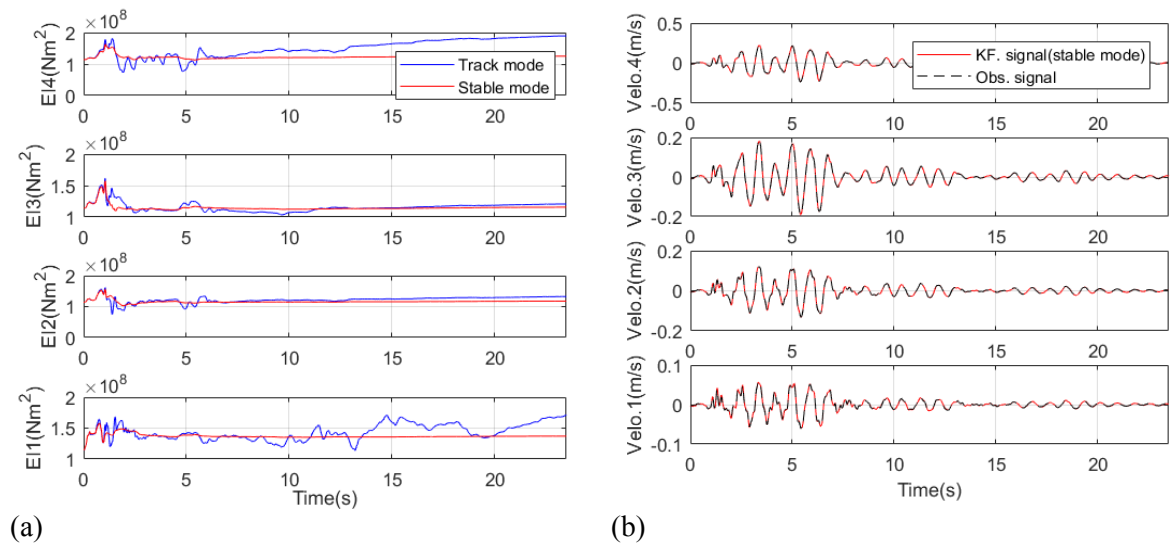
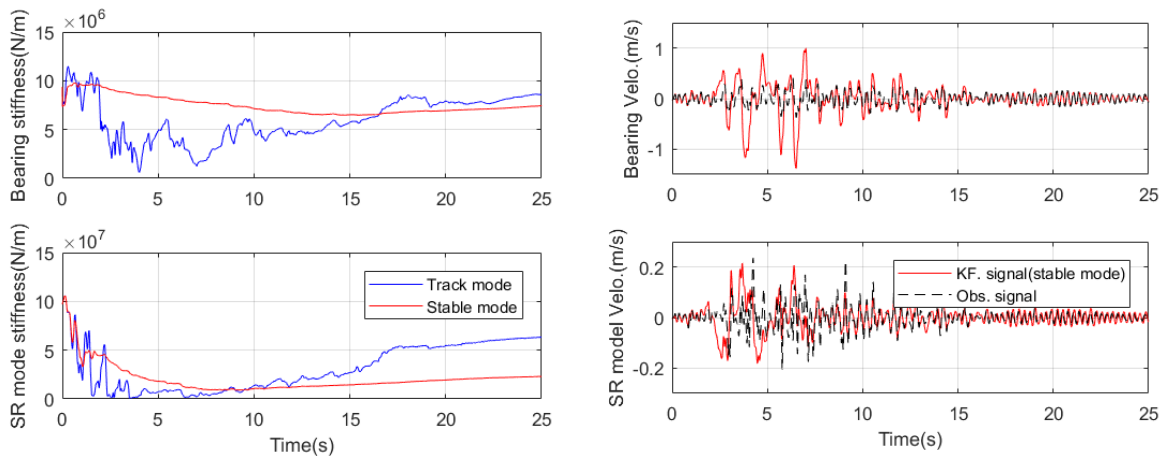


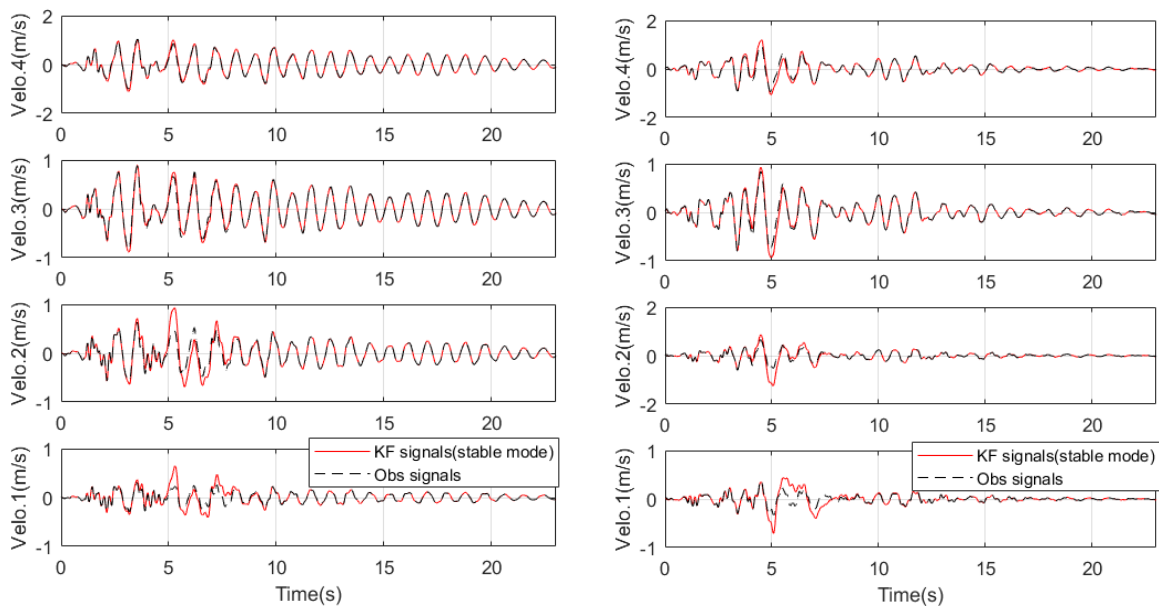
Figure 2.99 comparison of stable and track mode results using 2D model for building experiment in Takatori13% NS case;(a) stiffness identification comparison; (b) comparison of estimated velocities using stable mode and observed ones



(a) (b)
Figure 2.100 comparison of stable and track mode result for substructure experiment in steel pile JMA150% case; (a) stiffness identification comparison; (b) estimated velocity comparison

Figure 2.99(a) compares the parameter identification results of track mode and stable mode based on the 2D model for the four story building experiment in Takatori13% case. By using the track mode, unreasonable fluctuations appear in the estimation history especially for the bottom floor stiffness; while for stable mode, the results are clear and stable. Figure 2.99(b) compares the estimated velocities based on stable mode and the ones observed (i.e. integrated using accelerations) for the same case. The estimated velocities almost coincide with the observed one. The good coincidence shows that the system performs mainly in linear phase and it is reasonable to employ the stable mode.

In terms of the substructure experiments, Figure 2.100 presents comparisons of the two computation modes for RC pile JMA150% case. Obviously, by using the stable mode, some of the important stiffness variation parts are totally ignored as in Figure 2.100(a), e.g. 5~15 s in bearing stiffness case and 15~25 s in SR model stiffness case. Figure 2.100(b) shows that estimated velocities possess significant discrepancies comparing to the observed ones, therefore strong nonlinearities are supposed to be in the systems which is actually confirmed by the parameter estimation results using track mode.



(a) (b)
Figure 2.101 estimated velocity comparison using 2D model for building experiment in Takatori60% case; (a) NS direction; (b) WE direction

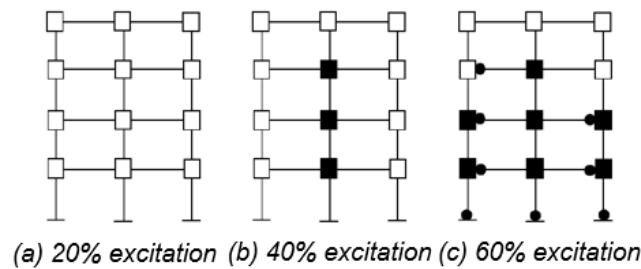


Figure 2.102 plastic area

In fact, for the subsequent cases of four story building experiments, the structure experienced certain level of nonlinearities. The experiment report shows that at Takatori40% and Takatori60% case, plastic hinges already formed in the structure, as shown in Figure 2.102. The estimated velocity using stable model of the proposed method are compared with those observed ones in Figure 2.101. Clearly, the estimated velocity distortions reflect the nonlinearities. Figure 2.103 shows the parameter identification results based on 2D model in the Takatori60% case as the blue lines. It shows that the nonlinearity of the structure is not as strong as the substructure experiment, i.e. no significant stiffness reduction occurs in extensive period of time as in Figure 2.87~Figure 2.88. The stiffness variations mainly happen between 5~10s. The identified stiffness values become roughly constants after 10.0s, but some instability still exist during the part especially for E_{II} parameter. The parameter results can be improved by combing track mode and stable mode. By applying the stable mode for 0.0s to 1.0s and 10.0s to end time interval, and the track mode for 1.0s to 10.0s time interval, the parameters are identified again and are shown as red lines in Figure 2.103. In this case, the identified parameters become stable after 10.0s.

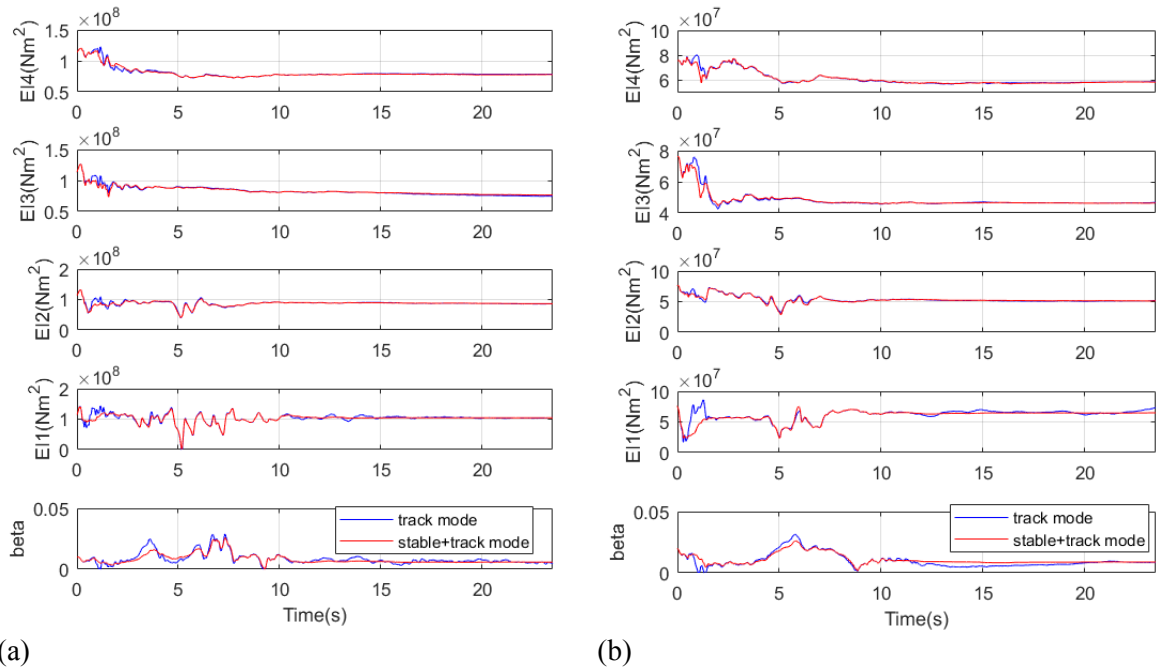


Figure 2.103 2D model parameter identification results using track mode for building experiment in Takatori60% case; (a) NS direction; (b) WE direction

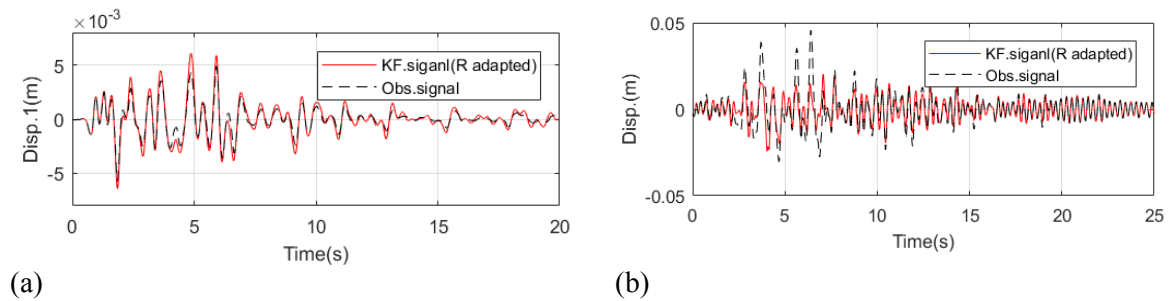
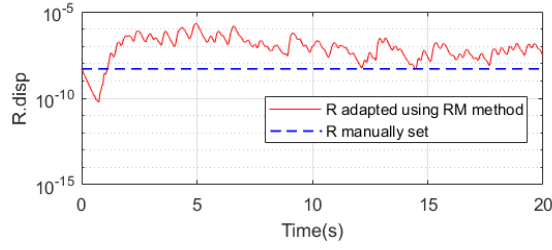
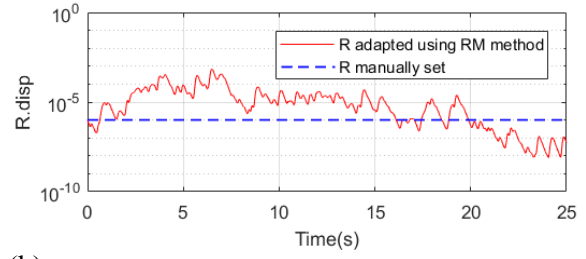


Figure 2.104 estimated displacement with R adaption; (a) bridge pier case; (b) substructure case



(a)



(b)

Figure 2.105 R adapted using RM method; (a) bridge pier case; (b) substructure case

Finally, as mentioned earlier, theoretically speaking, the measurement noise \mathbf{R} could be adapted based on the RM method, which is also shown by some other similar studies. However, it is found that by adapting the \mathbf{R} matrix automatically, the estimated signals probably deviate from the observed ones, as the displacement signals shown in Figure 2.104. It becomes more severe for the time-variant parameter identification case, i.e. the displacement discrepancies are large in Figure 2.104(b). In this situations, usually the \mathbf{R} adapted are much larger than the reasonable values decided beforehand as shown in Figure 2.105. This phenomenon is unreasonable because the observed signals are usually regarded more reliable than assumed system model in filter. Of course, if system model in filter is accurate enough, \mathbf{Q} and \mathbf{R} can be adapted simultaneously. However, this is not the case in the current experiments, therefore \mathbf{R} matrix adaption is cancelled in this study and further study on robust \mathbf{R} are expected to conduct.

Chapter 3 Displacement estimation of nonlinear SDOF system under seismic excitation

3.1 Chapter outline

In this chapter, an EKF based displacement estimation method of nonlinear SDOF system under seismic excitation is proposed. In this method, track model of EKF-RM method is firstly employed to distinguish time interval with or without significant system nonlinearity. For time period when system is in elastic phase, e.g. initial and ending part of time history, observations in EKF are acceleration and displacement which is obtained by combining double integrated displacement and residual displacement value. During time period with significant nonlinearity, acceleration is only employed and two EKF schemes can be applied, i.e. one assuming a bi-linear system model with optimized model parameters and the other using an augmented state vector with time-variant stiffness parameter estimation in EKF. The results are further smoothed by EKS after EKF which is found to be more accurate than filter results. In the following part of the chapter, the dynamic displacement estimation method is firstly presented in section 2 in detail. In section 3, the proposed method is numerically verified with three different SDOF models, i.e. bi-linear model, tri-linear model and Bouc-Wen model, excited by earthquakes of various type and amplitudes. In section 4, two shaking table experiments from E-defense database [102, 103], i.e. a full scale bridge pier and full scale four story building experiments, are employed to validate the method.

3.2 Dynamic displacement estimation method

3.2.1 Equation of motion and acceleration-augmented state space model

The equation of motion (EOM) of a nonlinear SDOF system under seismic excitation in relative coordinate can be written as

$$m\ddot{x} + c\dot{x} + f(x, \dot{x}) = -m\ddot{u}_g \quad (3.1)$$

in which x , \dot{x} and \ddot{x} are vectors of displacement, velocity and acceleration respectively; m and c are mass and damping coefficient which could be regarded as constant value in normal forward nonlinear dynamic analysis; $f(\bullet)$ represents nonlinear restoring force with respect to $x(t)$ and $\dot{x}(t)$, which involve hysteretic rule of loading and unloading; \ddot{u}_g is input ground acceleration. In case where a multistory building is simplified as a lumped mass structure, a specific story in it can be extracted as a SDOF model, the right hand side of the equation should also incorporate inertial forces transformed from above floors, namely

$$m\ddot{x}_i + c\dot{x}_i + f(x, \dot{x}) = -\sum_{j=i+1}^N m_j (\ddot{x}_j + \ddot{u}_g) - m_i (\ddot{u}_g + \ddot{x}_{i-1}) \quad (3.2)$$

in which i stands for i th story and N is the total number of DOF of the lumped mass structure. Assuming that accelerations are measured at all story of a multistory building, equation.(3.1) and (3.2) are actually equivalent, in the following part equation (3.1) will be used for simplicity. A more frequently used form of equation (3.1) is in incremental formulation as

$$m\Delta\ddot{x} + c\Delta\dot{x} + k_T\Delta x = -m\Delta\ddot{u}_g \quad (3.3)$$

in which Δ stands for incremental value and k_T is tangential stiffness for each time instance.

Usually, equation (3.3) is solved by numerical integration algorithms in a step by step manner, e.g. incremental Newmark-beta method, as

$$\Delta x = k_d^{-1} p_d \quad (3.4)$$

$$\Delta \dot{x} = \frac{\delta}{\beta \Delta t} \Delta x - \frac{\delta}{\beta} \dot{x} + \left(1 - \frac{\delta}{2\beta}\right) \Delta t \ddot{x} \quad (3.5)$$

$$\Delta \ddot{x} = \frac{1}{\beta \Delta t^2} \Delta x - \frac{1}{\beta \Delta t} \dot{x} - \frac{1}{2\beta} \ddot{x} \quad (3.6)$$

in which Δt is time interval; β and δ are integration parameters of the algorithms which are set as 1/6 and 0.5 in this study; k_d and p_d are equivalent dynamic stiffness and load defined as

$$k_d = \frac{1}{\beta \Delta t^2} m + \frac{\delta}{\beta \Delta t} c + k_T \quad (3.7)$$

$$p_d = m \Delta \ddot{u}_g + \left(\frac{1}{\beta \Delta t} \dot{x} + \frac{1}{2\beta} \ddot{x} \right) m + \left[\frac{\delta}{\beta} \dot{x} + \left(\frac{\delta}{2\beta} - 1 \right) \Delta t \ddot{x} \right] c \quad (3.8)$$

The above incremental Newmark-beta numerical integration algorithms can be transformed into discrete state space model as below

$$\begin{bmatrix} x(k+1) \\ \dot{x}(k+1) \\ \ddot{x}(k+1) \end{bmatrix} = \left\{ \mathbf{I} + \begin{bmatrix} 1 \\ \delta/\beta \Delta t \\ 1/\beta \Delta t^2 \end{bmatrix} \mathbf{L} + \begin{bmatrix} 0 & 0 & 0 \\ 0 & -\delta/\beta & (1-\delta/2\beta)\Delta t \\ 0 & -1/\beta \Delta t & -1/2\beta \end{bmatrix} \right\} \begin{bmatrix} x(k) \\ \dot{x}(k) \\ \ddot{x}(k) \end{bmatrix} + \begin{bmatrix} 1 \\ \delta/\beta \Delta t \\ 1/\beta \Delta t^2 \end{bmatrix} k_d^{-1} m \Delta \ddot{u}_g \quad (3.9)$$

in which \mathbf{I} is the unit matrix; k stands for a specific time instant, \mathbf{L} matrix is defined as below

$$\mathbf{L} = \left\{ 0 \quad k_d^{-1} \left(\frac{m}{\beta \Delta t} + \frac{\delta c}{\beta} \right) \quad k_d^{-1} \left[\frac{m}{2\beta} + c \left(\frac{\delta}{2\beta} - 1 \right) \Delta t \right] \right\} \quad (3.10)$$

The state space model based on incremental Newmark-beta method is different from normally used one [28, 30, 31, 38] where only displacement and velocity variables are included into state vector. It is also different from the one with acceleration-augmented based on Wilson-theta [126] or Generalized-alpha method [127], because dynamic equilibrium is not enforced in this state space model rather than the aforementioned ones. In these state space models, considering representing restoring force as $f(x) = kx$, dynamic equilibrium is exerted implicitly on the initial point or some internal point according to integration algorithms. And because of that, they can only be applied to linear elastic system. It is also worth noting that if only acceleration is observed in the state space model of equation (3.9), the displacement variable is actually unobservable, i.e. the rank of corresponding observability matrix [128] is 2. The unobservability comes from that if $x(t)$ is the solution to the problem, then $x(t) + C$ (C is a constant) is also the solution of it. However, if appropriate assumption about displacement time history is applied, e.g. zero displacement value at beginning point, this unobservability is not an issue. In fact, the same phenomenon also occurs to plenty of Bouc-Wen model studies [30, 34, 79] where post-yielding stiffness ratio α is set as 0.

In this study, parameters can also be identified along with dynamic displacement by augmenting them into state vector, which is same as previous chapters. Except the incremental Newmark-beta state-space model is used in the chapter, other information is all the same. Specially, the augmented state vector, system equation and observation equation are presented as below

$$\mathbf{X}_a = \begin{bmatrix} \mathbf{x}(t)^T & \dot{\mathbf{x}}(t)^T & \ddot{\mathbf{x}}(t)^T & \boldsymbol{\theta}^T \end{bmatrix}^T \quad (3.11)$$

$$\mathbf{X}_a(k+1) = \mathbf{f}(\mathbf{X}_a(k), \Delta \ddot{\mathbf{u}}_g) + \mathbf{w}(k) \quad (3.12)$$

$$\mathbf{y}(k+1) = \mathbf{h}(\mathbf{X}_a(k+1)) + \mathbf{v}(k+1) \quad (3.13)$$

In terms of process noise adaption, the RM algorithm is employed here.

3.2.2 Observation schemes

In the practical engineering, as mentioned earlier, accelerations are the most easily accessible system responses. Based on the acceleration measurement, dynamic displacement without low frequency drift can be obtained by double integration and high-pass filtering as mentioned earlier. Namely, the true dynamic displacement can be regarded as the combination of double integrated displacement and a low frequency drift component. Figure 3.1 shows the dynamic displacement decomposition.

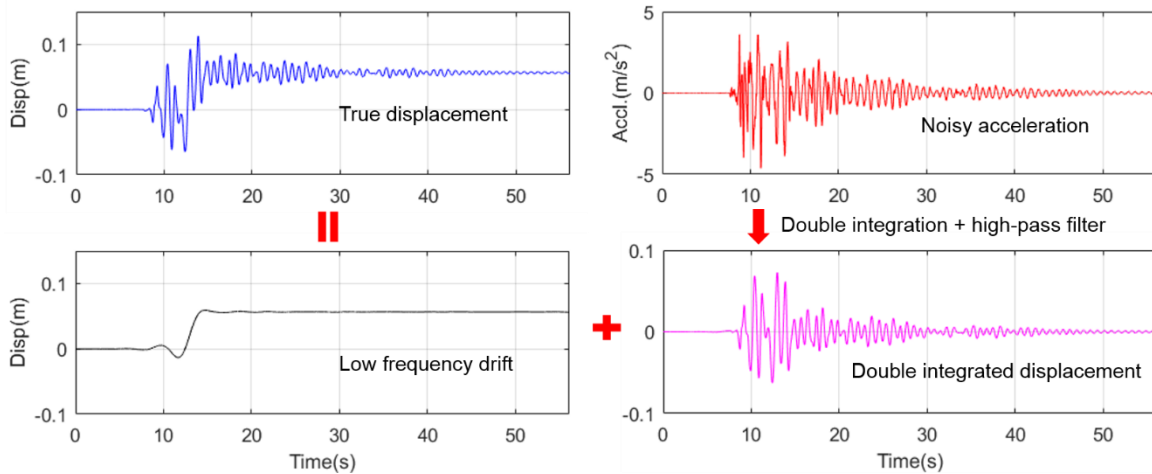


Figure 3.1 dynamic displacement decomposition

It can be found that except the residual displacement value, the initial and ending part of the double integrated displacement can reproduce the corresponding part of true dynamic displacement, which means that at least these part of double integrated displacement information can contribute to the true displacement estimation. In the middle part, e.g. 10~20s in the figure above, because of employment of high-pass filter, double integrated displacement differs from the true one significantly.

In terms of residual displacement, in practical engineering, it can be measured by inclinometer indirectly. From a forward simulation point of view, however residual displacement value is sensitive to nonlinear system parameters, e.g. bi-linear model studied in [129, 130]. It indicates that estimation of residual displacement through identifying relevant parameters accurately may not be implemented easily, not to mention probable large model error between system and real hysteretic model. Considering above discussion, the residual displacement value in this study is assumed as known.

Therefore, upon to this point, the available measurement information for true displacement estimation includes acceleration signal, initial and ending part of displacement which is obtained by combining double integrated and residual displacement information. In order to complement the missing middle part of displacement measurement, a virtual displacement measurement as shown in Figure 3.2, i.e. a straight line connecting the two sides, is applied. The virtual displacement should possess large measurement noise since actually it does not really exist. This method was firstly proposed by Chatzi et al. [131] for linear dynamic displacement estimation using acceleration only, which was found to be able to suppress displacement divergence. Naets et al. [132] employed this method in displacement estimation with unknown input using acceleration only, which helped to improve unobservability issue. Both of the studies considered the virtual displacement as artificial white noise with zero mean. Figure 3.2 shows the available observation information in this study.

Upon to this point, one issue is still left, i.e. how to define the time interval where the virtual displacement should be applied. As previously studies, this can be achieved by identifying the time-variant parameters of the system using track mode of EKF-RM method based on double integrated displacement. The time interval where significant stiffness reduction occurs would be defined as the part with virtual displacement measurement. It will be demonstrated with numerical examples in the following sections.

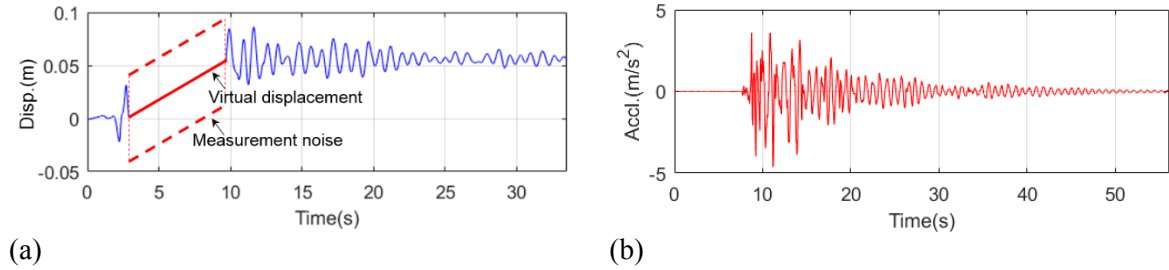


Figure 3.2 available observations (a) displacement; (b) acceleration

3.2.3 Estimation schemes during virtual displacement measurement part

As mentioned earlier, the time interval with virtual displacement actually corresponds to the period when system experience strong nonlinearity, i.e. stiffness parameter is changing.

Intuitively, in order to consider the nonlinearity, the first proposal is to identify the time-variant stiffness value along with system response as shown in equation (3.11). In this case, the track model of EKF-RM method will be used. By applying the incremental Newmark-beta state space model (3.9), the stiffness identified is actually tangential stiffness rather than equivalent secant stiffness value. In terms of damping coefficient, they can be identified in the previous step, i.e. when time interval with virtual displacement is defined. Specifically, the identified values in the ending part, i.e. elastic phase, could be used. Alternatively, values from previous tiny earthquake and ambient vibration results in practical engineering could also be reasonable one. This is based on the assumption that if system performs strong hysteretic behaviors, this type of viscous damping does not play significant role in it.

The other proposal is that a specific hysteretic model can be assumed during this time interval, e.g. bi-linear model. If, in ideal case, the hysteresis model as well as its corresponding parameters is accurate, dynamic displacement could be accurately estimated using acceleration measurements only. In case the assumed hysteresis model is different from real model, an approximate one close to the real model could be found by optimized parameters of the assumed hysteresis model. In this study, bi-linear model is employed considering it only possesses a few model parameters. In terms of the elastic stiffness and damping coefficient, appropriate values could be determined from previous step, i.e. when time interval with virtual displacement is defined. Therefore, only yielding displacement Δy

and post-yielding stiffness ratio α need to be identified. It is proposed to optimize these parameters by minimizing the fitness function below

$$F_{fitness}(dy, \alpha) = \left(\frac{1}{k_{t1} - k_{t0} + 1} \right) \sum_{k=k_{t0}}^{k_{t1}} Q_{accl}(k|dy, \alpha) \quad (3.14)$$

in which $Q_{accl}(k|dy, \alpha)$ stands for acceleration process noise in time instant k given parameters dy and α ; k_{t0} and k_{t1} are starting and ending point of the time interval with virtual displacement. Thus, the basic idea is to find appropriate parameters by minimizing the acceleration process noise which indicates model error. During this step, the stable mode of EKF-RM is applied from which acceleration process noise can be obtained. Actually observations include both acceleration and displacement here, but the process noise of displacement will not be used because it is from the virtual displacement. After obtaining the optimized parameter, they will be put into the EKF-RM with the incremental Newmark-beta based state space model (3.9) to estimate dynamic displacement. In this proposal, the incremental Newmark-beta state vector contains system responses only, i.e. dy and α parameters are decoupled and not identified along with responses state variables. For simplicity reason, the aforementioned methods are denoted as method 1 and method 2 in following.

3.2.4 Extended Kalman smoother

As mentioned in the last section, $\hat{X}_a(k/k)$ is the estimated value of state vector based on measurement information up to k instant, i.e. $\mathbf{y}_{1:k}$. In order to involve measurements of all time instants, especially the signals in the latter parts including residual displacements, into estimation results, EKS based on Rauch-Tung-Striebel smoothing [133] is applied to results from EKF further. With the estimated value and error-covariance of state vector at ending point, i.e. $\hat{X}_a(N/N)$ and $P(N/N)$, smoothed results at k instant ($k=N-1, N-2, \dots, 1$) can be written as

$$\mathbf{J}_{k-1} = \mathbf{P}(k-1/k-1) \mathbf{F}^T(k) / \mathbf{P}(k/k-1) \quad (3.15)$$

$$\hat{X}_a(k-1/N) = \hat{X}_a(k-1/k-1) + \mathbf{J}_{k-1} [\hat{X}_a(k/N) - \hat{X}_a(k/k-1)] \quad (3.16)$$

$$\mathbf{P}(k-1/N) = \mathbf{P}(k-1/k-1) + \mathbf{J}_{k-1} [\mathbf{P}(k/N) - \mathbf{P}(k/k-1)] \mathbf{J}_{k-1}^T \quad (3.17)$$

in which N stands for the total number of time samples; \mathbf{J} is called gain matrix of the Kalman smoother; all of other symbols possess same meaning as last chapter.

It is found that results from smoother are more accurate than those from filter, which will be shown in following part. For both of the methods, after applying EKF-RM, the estimated result will be further smoothed by EKS. Overall, Figure 3.3 shows the flow chart of the dynamic displacement estimation method.

In this study, actually the method 2 is actually an improved version of the method proposed in [53], in which only acceleration observation and EKF-RM method are applied, i.e. the displacement observation and EKS are ignored.

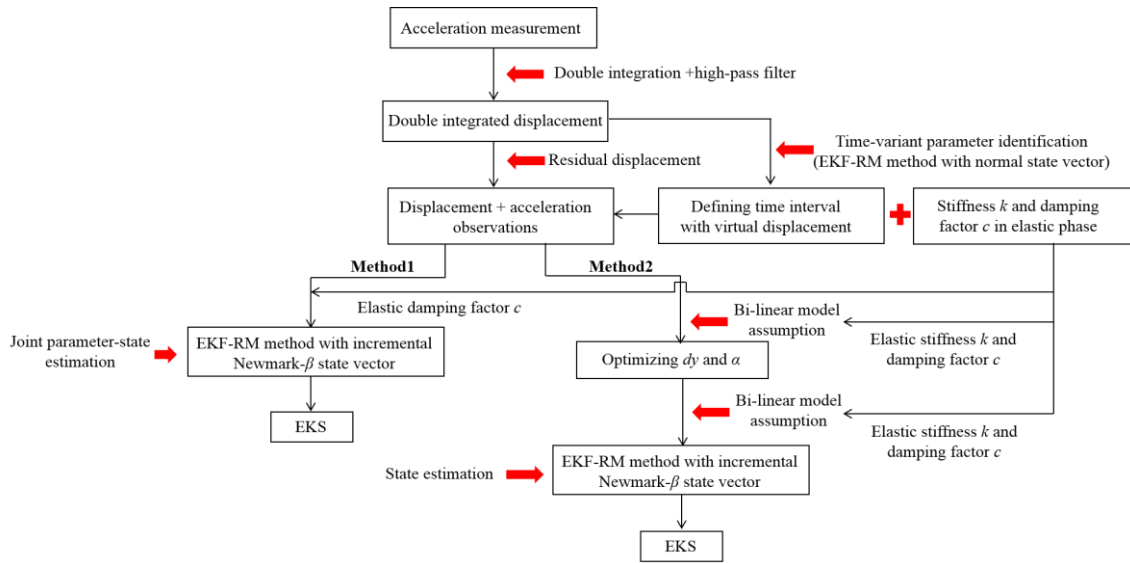


Figure 3.3 flow chart of dynamic displacement estimation method

3.3 Numerical verification of the dynamic displacement estimation method

In this section, the effectiveness of the proposed methods is demonstrated with numerical models, including three SDOF model with different hysteretic rules, i.e. bi-linear model, tri-linear model, Bouc-Wen model, under various earthquake excitations. As previously mentioned, acceleration measurements and residual displacement information are assumed available. In the beginning, the application of the method is presented and discussed in detail based on a bi-linear and a Bouc-Wen model, while results under a series of conditions are summarized in following.

3.3.1 Application to a bi-linear SDOF model

The illustrative model considered here is a SDOF model with bi-linear hysteretic rule. The prototype of the model is simplified from a full scale bridge pier experiment, called C-1-1 experiment in E-defense shaking database, as shown in the figure below. The basic parameters of the SDOF model includes mass $m=252.5$ ton, elastic stiffness $k=1.625 \times 10^7$ N/m, damping coefficient $c=4.05 \times 10^4$ Ns/m, post-yielding stiffness ratio $\alpha=0.05$, and yielding displacement $\Delta y=0.05$ m.

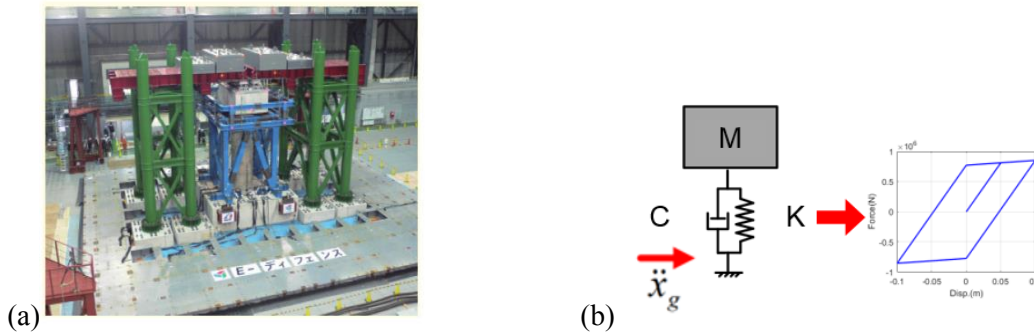


Figure 3.4 (a) C1-1 prototype experiment structure; (b) simplified bi-linear SDOF model

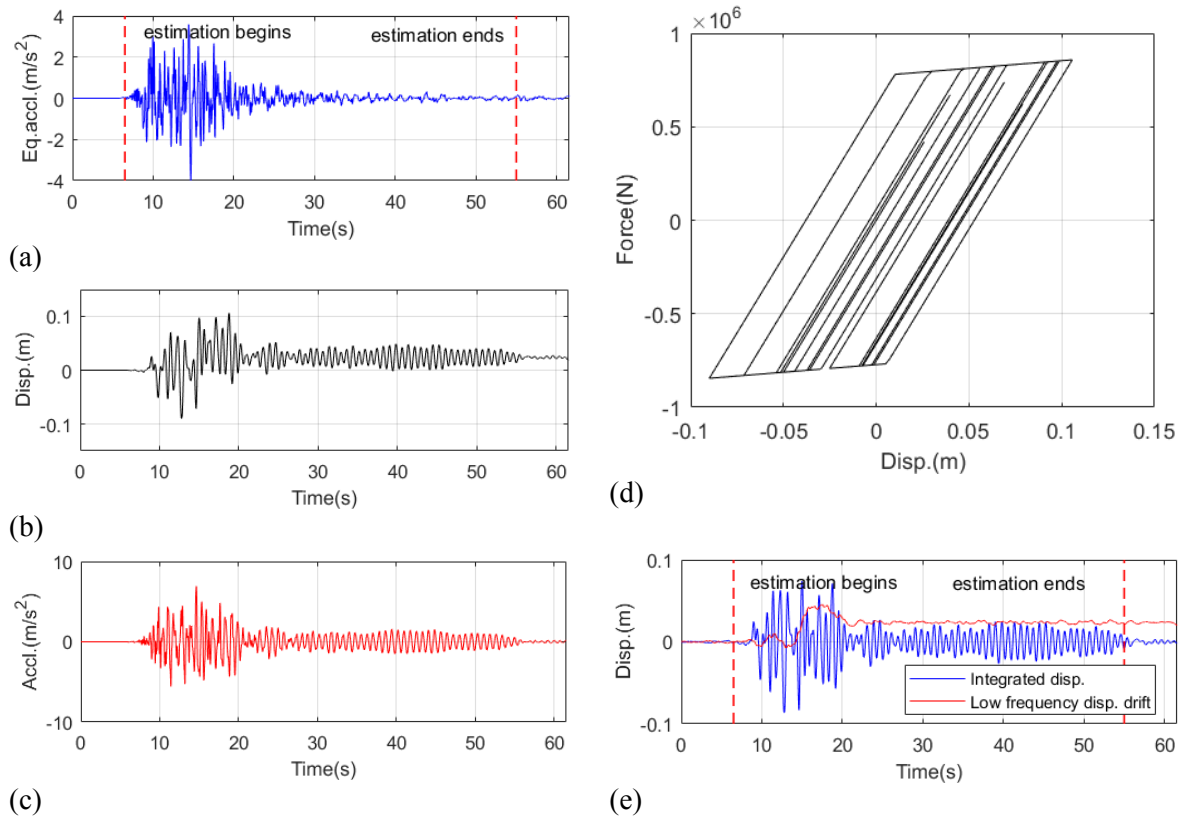
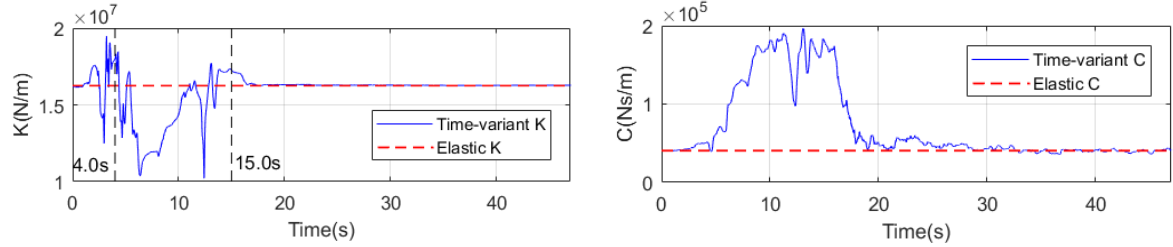


Figure 3.5 bi-linear model simulation response;
(a) earthquake acceleration; (b) displacement; (c) acceleration; (d) hysteretic loop; (e) double integrated displacement and low frequency displacement drift

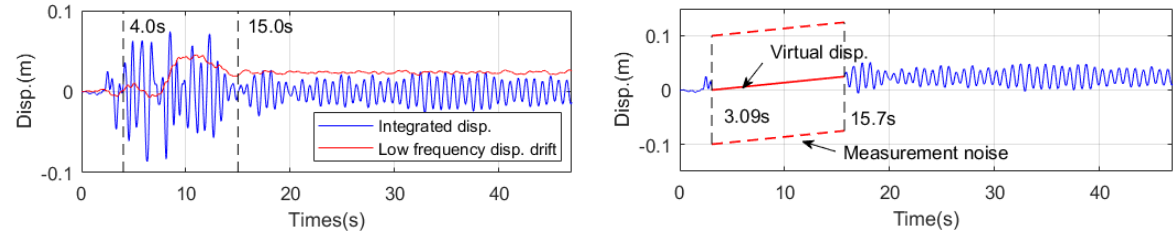
The forward analysis is conducted using incremental Newmark-beta method with $\beta=1/6$ and time sample equals to 0.005s. Northridge earthquake acceleration is treated as excitations. The simulated displacement, acceleration, hysteretic loop as well as the earthquake signals are shown in Figure 3.5. The simulated acceleration signal is then added with white noise process whose RMS equals to 5% of signal's RMS (1.2m/s^2) to consider practical measurement noise. Based on the noisy acceleration, as mentioned earlier, double integrated displacement is obtained by using a high-pass filter with 0.2Hz cutoff frequency. Figure 3.5(e) shows the double integrated displacement and low frequency displacement drift, i.e. difference between integrated and true displacement. In this case, the residual displacement occurs from about 22s with 2.3cm. Subsequently time-variant stiffness value can be identified using the integrated displacement and acceleration. \mathbf{R} matrix and initial \mathbf{Q} is set as $\mathbf{R}=\text{diag}([10^{-5}, 5 \times 10^{-3}])$ and $\mathbf{Q}=\text{diag}([10^{-6}, 10^{-4}, 0, 0])$; initial parameter value and error covariance matrix are set $1.0\theta_{real}$ and $\text{diag}([0.1\theta_{real}]^2)$ where θ_{real} stands for real elastic parameter value. Besides, the α_Q coefficient of RM algorithm is set as 1/15. Here, the \mathbf{R} matrix value for displacement is set as 15% of the integrated displacement's RMS, i.e. 0.02m. The period of time of estimation is shown in Figure 3.5 (a). The identified time-variant parameter time histories are shown in Figure 3.6. It is worth noting here that by using the integrated displacement, the time-variant parameters are identified based on state-space model of elastic system, i.e. equivalent secant stiffness and damping coefficient of nonlinear system are identified rather than tangential ones. It can be observed that except the fluctuation during the initial time, significant stiffness reduction occurs between 4~15s which matches with the time interval of significant low frequency drift well as shown in Figure 3.7(a). For the latter part of the identification, e.g. after 15s, the identified parameters coincide with those real elastic parameter values well, because the system is in elastic phase during this period of

time.

Based on the time-variant stiffness identification results, the time interval with virtual displacement is defined from 3.09s to 15.7s. The latter part of integrated displacement is summed with residual displacement, i.e. 2.3cm. The displacement measurement is shown in Figure 3.7(b). Specifically, the time instants, i.e. 3.09s and 15.7s, should be selected so that corresponding integrated displacements cross zero for displacement smoothness concern. In terms of the measurement noise of virtual displacement, as studied in [131] [132], a wide range of values could be applicable as long as they are above some lower threshold. When the measurement noise value is too small, the filter will force the estimated displacement to adhere to the virtual one which is not expectable. In this study, the measurement noise value is selected based on the maximum absolute value of integrated displacement. Specifically, 0.10m is employed in this case because the maximum absolute value of integrated displacement is about 0.09m as shown in Figure 3.7(b). For the integrated displacement part, the measurement noise used in time-variant parameter estimation could be applied. If the displacement error of integrated displacement is expected to be suppressed further, a relative large noise value could be employed for the integrated displacement. In this case, it is selected as 0.01m.



(a) (b)
Figure 3.6 Time-variant parameter estimation time history; (a) stiffness; (b) damping coefficient



(a) (b)
Figure 3.7 (a) integrated displacement; (b) displacement observation

In the first place, the method 1 which is based on joint parameter-state estimation is applied here. As discussed above, the displacement and acceleration measurements are that of Figure 3.7(a) and Figure 3.5(c). \mathbf{R} matrix is set as $\text{diag}([10^{-2}, 5 \times 10^{-3}])$ and $\text{diag}([10^{-4}, 5 \times 10^{-3}])$ for virtual displacement and integrated displacement part respectively. Initial \mathbf{Q} matrix is set as $\text{diag}([10^{-6}, 10^{-4}, 10^{-2}, 0])$ corresponding to displacement, velocity, acceleration and stiffness value. Note that damping coefficient is regarded as a known value from the time-variant parameter estimation result. Except these, other computation information is unchanged.

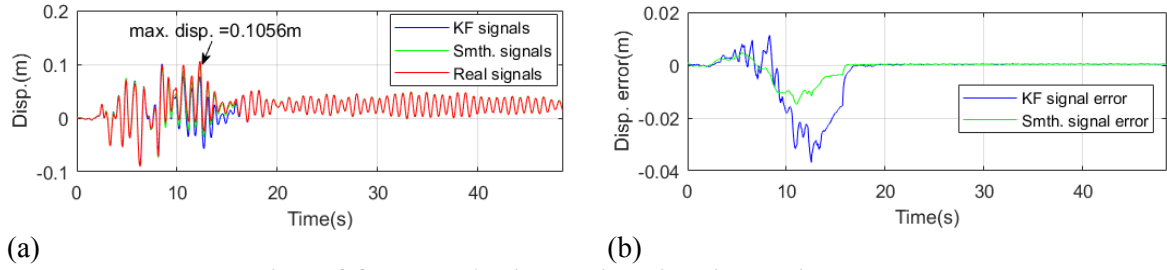


Figure 3.8 method 1 using straight line virtual displacement
(a) comparison between estimated and real displacement; (b) estimation error comparison

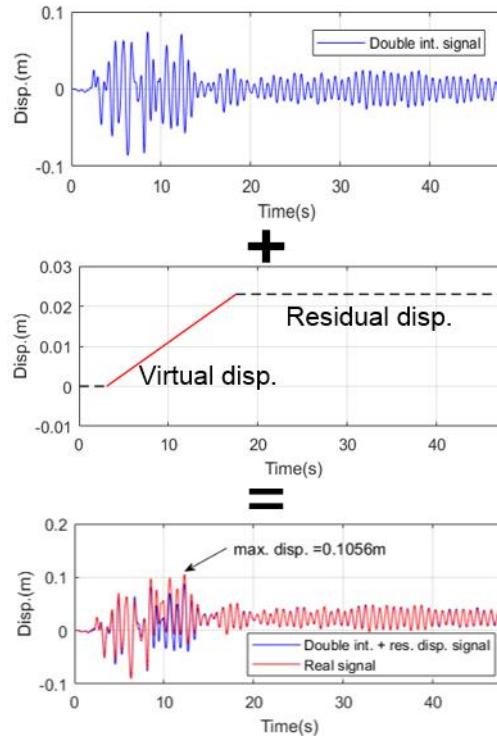


Figure 3.9 comparison of double integrated and true displacement

Figure 3.8(a) shows the estimated displacement from EKF and EKS as well as real displacement signal, while Figure 3.8(b) shows the estimation error of EKF and EKS results. It can be observed that the EKS result is closer to real displacement of which the maximum error is about 1.5cm comparing to about 3.7cm of EKF result. The maximum absolute displacement occurs at 12.28s with 0.1056m. The error corresponding to this point is 0.98cm and 2.89cm with respect to EKS and EKF result. For comparison, the double integrated displacement is also presented here in Figure 3.9. However, the double integrated displacement here also combines the residual and virtual displacement information. The error at the maximum displacement is 1.8cm. In this case, it shows that by incorporating the information of latter residual displacement part based on EKS, estimation accuracy of virtual displacement part can be improved. This is intuitive and obvious, since EKF estimation is only taking advantage of information up till the current point. In this example, the virtual displacement is initially assumed a straight line as shown in Figure 3.7(b). If the low frequency drift component is extracted from the former EKS result, it can be regarded as the virtual displacement, and the update displacement measurement is shown in Figure 3.10.

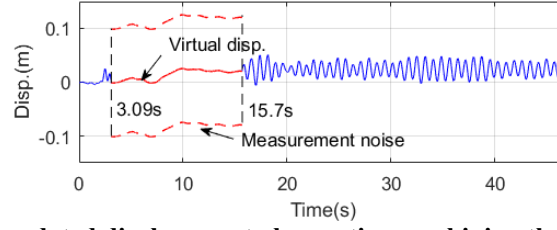


Figure 3.10 updated displacement observation combining the 1st EKS result

Based on the updated displacement observation, the estimated displacement results are shown in Figure 3.11.

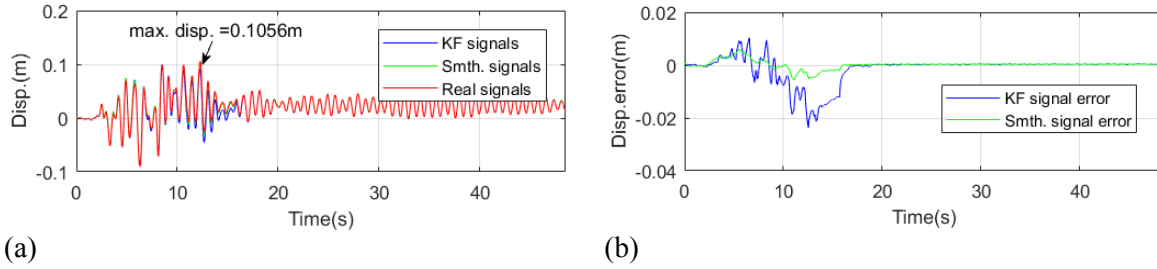


Figure 3.11 method 2 using updated displacement measurement
(a) comparison between estimated and real displacement; (b) estimation error comparison

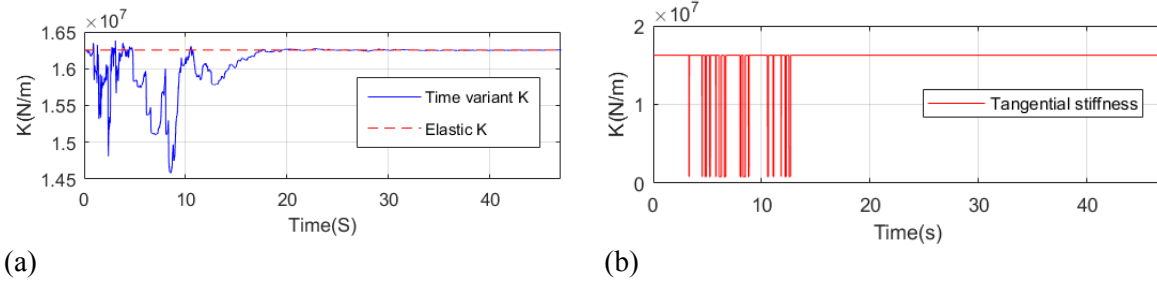


Figure 3.12 (a) time variant stiffness estimation time history; (b) real tangential stiffness

It can be observed that the estimation result based on the update displacement measurement is more accurate than previous case for both EKF and EKS case. Specifically, the maximum error is about 0.5cm and 2.4cm for EKS and EKF respectively. In terms of the maximum displacement, the error is 0.25cm and 1.56cm. The improvement is due to that the updated virtual displacement is more like the real low frequency displacement drift. For example, from 8~15s, the real low frequency displacement drift and the update virtual displacement both present upward curves while it is firstly assumed as a straight line. This is also the reason that displacement is underestimated between 8~15s as shown in Figure 3.8(b). Intuitively, it seems that by consecutive iterations, the estimated displacement will be much closer to the real one. Unfortunately, this is not the case. Situation where some parts are closer but other parts are more deviate from the real displacement is often encountered. Besides that, it is difficult to find an index indicating when the iteration should stop based on the current available measurement. Therefore, this 2 iteration computation scheme is designated here empirically. In the following part, it shows this empirical way works well.

As mentioned earlier, along with the displacement, time-variant stiffness, specifically tangential stiffness, is also identified in this method because of the incremental Newmark-beta state space model used. However, this stiffness is not expected to be identified accurately since only acceleration measurement is mainly functioning for parameter identification during time interval with significant nonlinearity. Figure 3.12(a) shows the identified time-variant stiffness while Figure 3.12(b) presents

the real time history of the tangential stiffness. Large discrepancy exists between the two. In fact, if accurate tangential stiffness is expected to be obtained, displacement observation is suggested to be included [40]. And in this field, some multi-resolution analysis methods, e.g. wavelet method [65, 134], have been studied, but this is out of the scope of this paper. Therefore, by identifying the time-variant stiffness here based on acceleration measurement, the inherent nonlinearity of the system is intended to be considered as much as possible.

In the second place of the section, the method 2 which is based on bi-linear model assumption is applied here. In this case, the displacement and acceleration observations are first determined with the same procedures as method 1. The elastic stiffness and damping coefficient should be regarded as known here. They can be identified based on time-variant parameter estimation using the integrated displacement as shown in Figure 3.6. Note that equivalent secant parameters are identified here based on state space model of elastic system and the latter part of the estimation value should be used, i.e. $k=1.625 \times 10^7$ N/m, $c=4.05 \times 10^4$ Ns/m. The parameters to be determined is yielding displacement d_y and post-yielding stiffness ratio α . In terms of the fitness function equation (3.14), the computation interval is set same as virtual displacement interval, i.e. 3.09s~15.7s. The genetic algorithm (GA) is applied here to find optimized values which minimize the fitness function. The EKF works here so that its Jacobian matrix is recalculated once the system is estimated with phase alteration, i.e. elastic to plastic phase or vice versa.

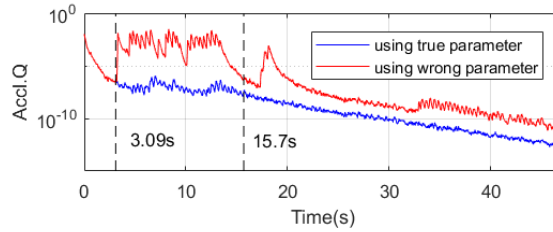


Figure 3.13 comparison of acceleration process noise

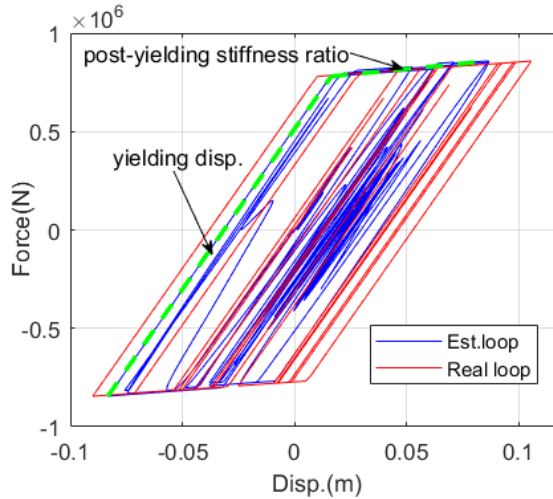


Figure 3.14 comparison between real and hysteresis loop of double integrated displacement

First of all, acceleration process noise Q_{acc} computed using true d_y and α value ($d_y=0.05$, $\alpha=0.05$) and a set of wrong values ($d_y=0.03$, $\alpha=0.03$) are compared in the Figure 3.13. The computation information here is same as previous case. It can be found that the acceleration process noise corresponding to true parameter value is truly smaller than that of wrong parameters especially during the time interval with virtual displacement. It is thus proved that the Q_{acc} is sensitive to the two parameters, and it is reasonable to regard Q_{acc} as fitness function for GA.

Before conducting GA, it is required to set bounding information of the parameters. Here it is proposed to define them based on the double integrated displacement. The hysteresis loop is plot in Figure 3.14. Since the real hysteresis loop here is a bi-linear model, the estimated one is pretty clear and close to the real loop and parameter $d\gamma$ and α can be easily determined from the green lines in the figure. However, a relatively wide range of parameter bounding is defined as $0.01 \leq d\gamma \leq 0.10$ and $0.03 \leq \alpha \leq 0.08$ based on them so as to consider more uncertain condition in practical engineering. In the GA computation, 20 generations with 30 populations of each are employed. The total computation time is about 20 minutes in a standard laptop PC and Figure 3.15 shows the convergence plot of GA. The optimized $d\gamma$ and α value are 0.050 and 0.0449 respectively. Based on the optimized values, the estimated dynamic displacement is shown in Figure 3.16.

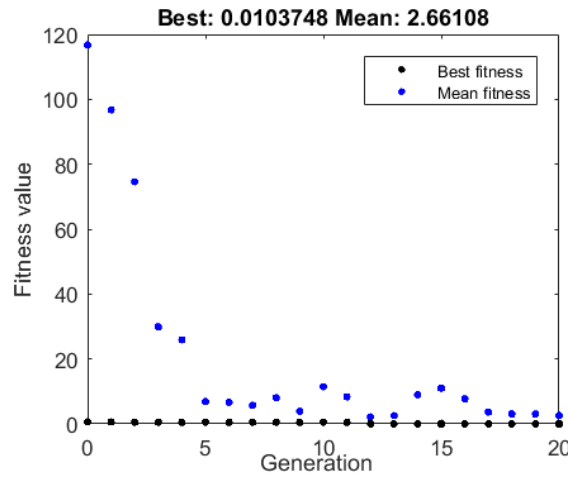


Figure 3.15 convergence plot of GA

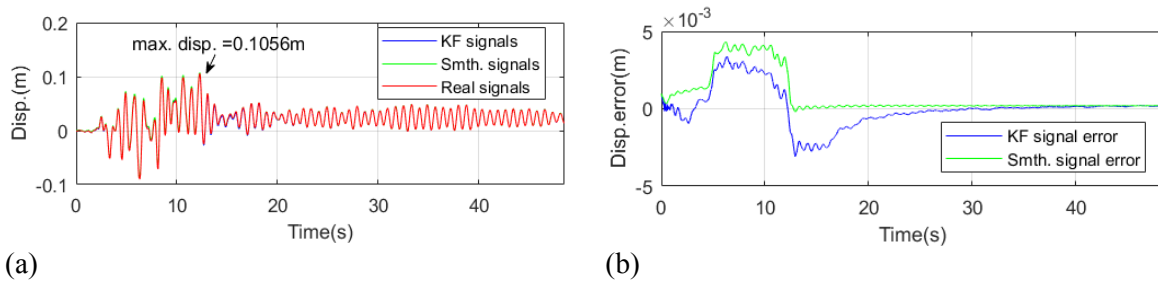


Figure 3.16 estimated displacement based on method 2;

(a) comparison between estimated and real displacement; (b) estimation error comparison

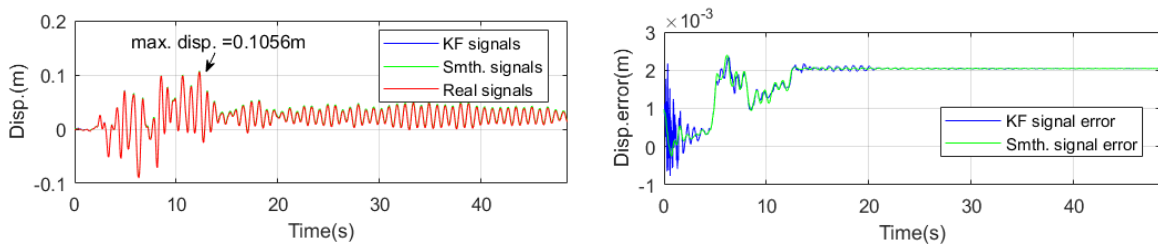


Figure 3.17 estimated displacement based on method 2 using acceleration only;

(a) comparison between estimated and real displacement; (b) estimation error comparison

In this case, both the EKF and EKS give accurate estimation results. The maximum errors of them are smaller than 5mm and the errors at maximum absolute displacement are 0.5mm and 2mm

for EKF and EKS respectively. Since in this case, the system model in EKF is same as real physical model and relatively accurate parameters are identified, the EKF result already possesses high estimation accuracy and result from EKS does not improve it a lot. Actually, if only acceleration is used here which is similar to the method proposed in [53], good result can also be obtained which is shown in Figure 3.17.

3.3.2 Application to a Bouc-Wen SDOF model

The example considered here is a SDOF with Bouc-Wen hysteresis rule. With the application of the Bouc-Wen model, the restoring force could be written as [135]

$$f(x, \dot{x}) = \alpha kx + (1 - \alpha)kw \quad (3.18)$$

$$\dot{w} = \frac{\dot{x} - \nu(\beta|\dot{x}|w|^{n-1}w + \gamma\dot{x}|w|^n)}{\eta} \quad (3.19)$$

in which k , α are elastic stiffness and post-yielding stiffness ratio as mentioned earlier; w is hysteresis displacement; β, γ and n are loop parameters which control the shape of hysteresis loop, e.g. β and γ control the concavity/convexity of loop, n control the sharpness of transition area of loop [136]; ν and η are stiffness and strength degradation shape functions respectively, they are defined as

$$\nu(\varepsilon) = 1 + \delta_\nu \varepsilon \quad (3.20)$$

$$\eta(\varepsilon) = 1 + \delta_\eta \varepsilon \quad (3.21)$$

$$\varepsilon(t) = \int_0^t w \dot{x} dt \quad (3.22)$$

in which ε is dissipated energy of hysteresis loop; δ_ν and δ_η are stiffness and strength degradation ratios respectively. In fact, yielding displacement dy possesses following relations with β , γ and n

$$\beta = \frac{1}{dy^n(1 + \mu)} \quad (3.23)$$

$$\mu = \gamma / \beta \quad (3.24)$$

The basic parameters of the Bouc-Wen SDOF model and their corresponding values applied in this example are listed in Table 3.1.

Table 3.1 basic parameters of Bouc-Wen SDOF model

Parameter	Value
Mass m (ton)	252.5
Elastic stiffness k (N/m)	1.625×10^7
Elastic damping coefficient c (Ns/m)	4.05×10^4
Post-yielding displacement dy (m)	0.05
Post-yielding stiffness ratio α	0.05
Loop parameter n	5

Loop parameter μ	1
Stiffness degradation parameter δ_b	20
Strength degradation parameter δ_η	20

San Fernando earthquake is used in this example and the forward analysis is conducted by fourth-order Runge-Kutta method with 0.005s time sample. System responses and hysteresis loop are shown in Figure 3.18. Same as previous case, 5% RMS white noise is added to the acceleration (its RMS is approximately 1.4m/s^2) and double integrated displacement is obtained with high-pass filter of 0.2Hz cutoff frequency as shown in Figure 3.18(e). It is also observed that the residual displacement occurs from about 11s with 3.7cm. Time-variant parameters are identified using the integrated displacement and acceleration during the time interval shown in Figure 3.18 (a). The computation information is same as previous case and estimation history is shown in Figure 3.19. It can be observed that stiffness variation mainly occurs during about 2.5~11s which matches with the time interval of low frequency drift well as shown in Figure 3.20(a). Since in this Bouc-Wen model stiffness and strength degradation effects are considered, for the latter part of the identification, i.e. after 11s, the identified stiffness converges to a smaller value, i.e. 1.45×10^7 which is about 0.90 of the real elastic stiffness value. Based on the identified time-variant stiffness value, the time interval with virtual displacement is defined from 2.56s to 11.05s. The displacement measurement is shown in Figure 3.20(b) in which the measurement noise of virtual displacement is set as 0.10m.

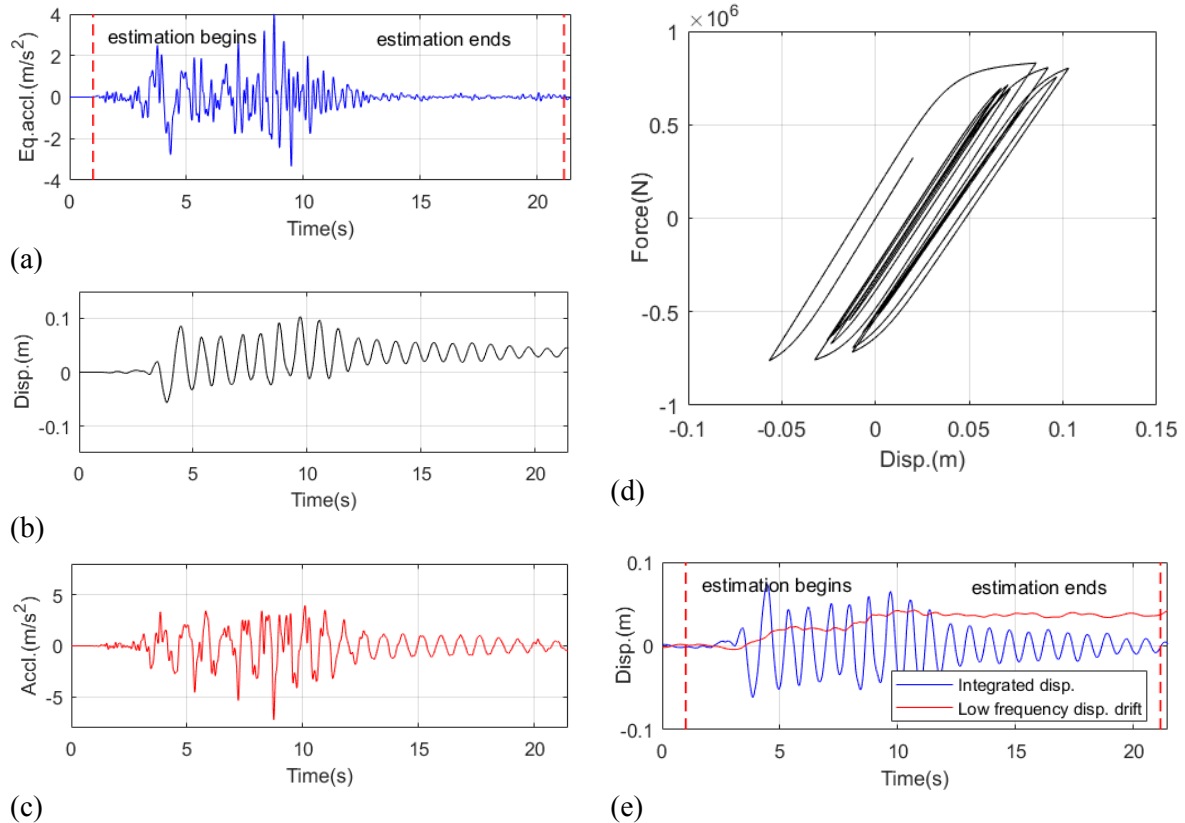


Figure 3.18 Bouc-Wen model simulation response;
(a) earthquake acceleration; (b) displacement; (c) acceleration; (d) hysteretic loop; (e) double integrated displacement and low frequency displacement drift

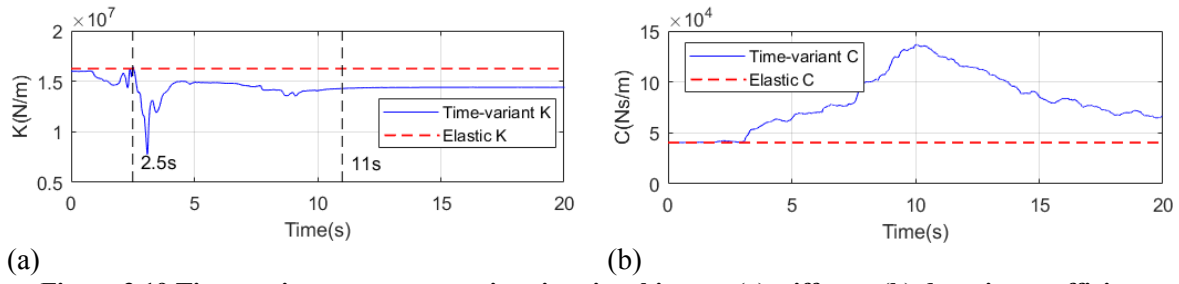


Figure 3.19 Time-variant parameter estimation time history; (a) stiffness; (b) damping coefficient

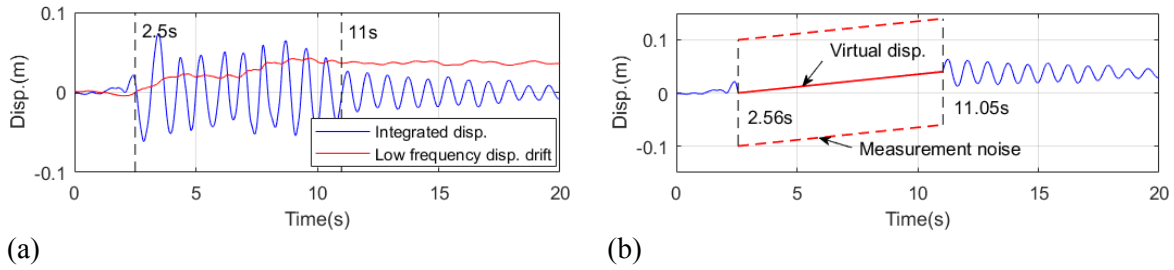


Figure 3.20 (a) integrated displacement; (b) displacement measurement

Method 1 is applied here firstly. The computation information is same as previous case. From the Figure 3.19(b), it can be observed that the damping coefficient does not converge to a stable value finally. Here the real elastic value, i.e. 4.05×10^4 , is firstly employed as known parameter for displacement estimation. The displacement estimation results at the 1st and 2nd iteration are shown in Figure 3.21 and Figure 3.22 respectively. Both of the smoothed signals present relatively high accuracies. The maximum displacement error and error at maximum absolute displacement are 5mm and 3.7 mm respectively for the 1st iteration while they are 7mm and 0.8mm for the 2nd iteration. As mentioned earlier, the iteration computation does not ensure displacement error minimized everywhere during the virtual displacement part. By comparing the result, improvement of error at maximum absolute displacement is achieved along with deterioration of the maximum error, but overall, performance of the 2nd iteration is still satisfying. Additionally, a few more cases are analyzed here considering various damping coefficients are used. Figure 3.23 shows the estimated displacements and estimation errors with $1.0c$, $2.0c$ and $3.0c$ used. No big difference is found among the estimation errors which are beneficial to practical usage.

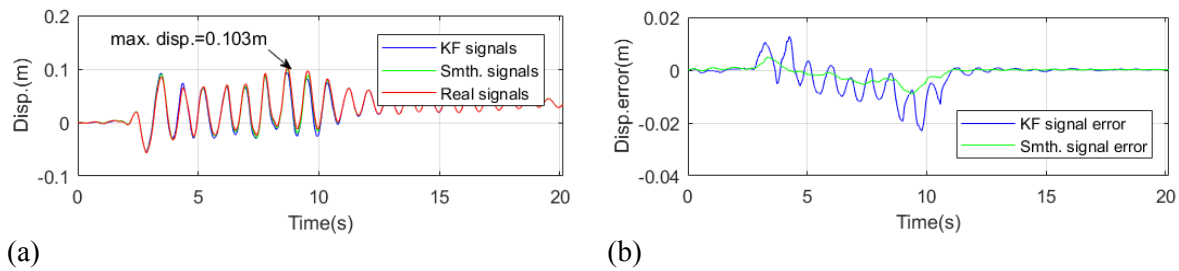


Figure 3.21 estimation at the 1st iteration of method 1;
(a) comparison between estimated and real displacement; (b) estimation error comparison

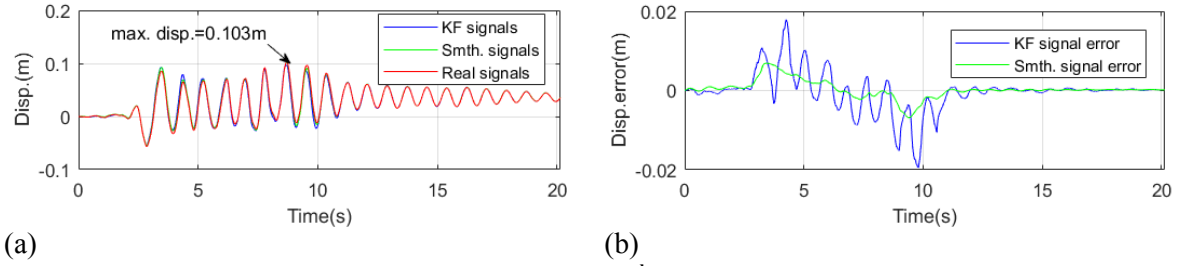


Figure 3.22 estimation at the 2nd iteration of method 1;
(a) comparison between estimated and real displacement; (b) estimation error comparison

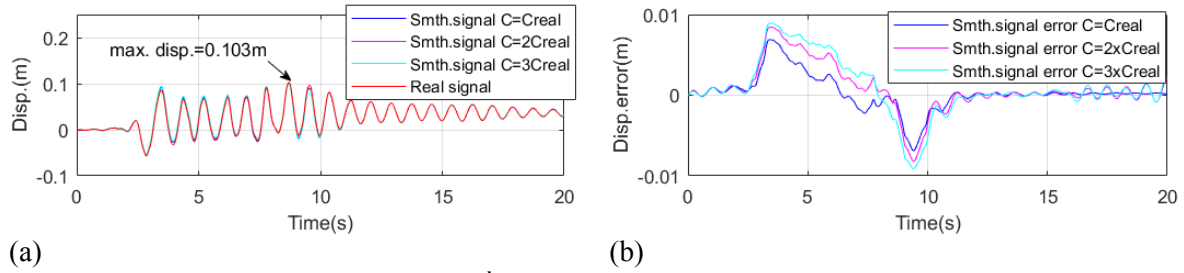


Figure 3.23 estimation at the 2nd iteration of method 1 considering various c value;
(a) comparison between estimated and real displacement; (b) estimation error comparison

Subsequently, the method 2 is applied. The elastic stiffness and damping coefficient employed here is 1.45×10^7 and 8×10^4 . The hysteresis loop estimated from the double integrated displacement can help to find the appropriate range of yielding displacement d_y and post-yielding stiffness ratio α . Rough values can be determined from the green lines shown in Figure 3.24, and the parameter range is defined as $0.01 \leq d_y \leq 0.10$ and $0.03 \leq \alpha \leq 0.08$ based on that. The GA computation calculated 20 generations with 30 populations of each. Convergence plot of GA is shown in Figure 3.25. The optimized d_y and α value are 0.0503 and 0.095 respectively. Based on the optimized values, the dynamic displacement is estimated and shown in Figure 3.26. In this case, the EKS gives accurate results with maximum error 7mm and error at maximum absolute displacement 1.5mm. In this case, the displacement is also estimated using acceleration measurement only (similar to method in [53]), which is shown in Figure 3.27. Obviously, because of lack of displacement information in the latter part, the estimated residual displacement is incorrect, i.e. 0.9cm larger than the real value. It indicates that residual displacement estimation become unreliable when only acceleration measurement is employed and system model is inaccurate, frequently encountered situations in practice. Considering measuring residual displacement is available in real engineering, it is necessary and preferable to incorporate it into displacement estimation.

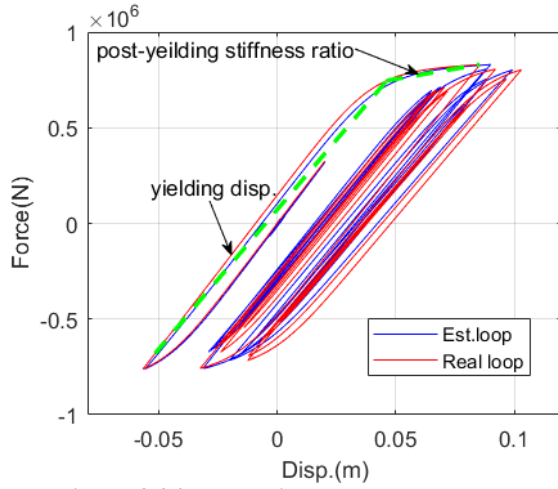


Figure 3.24 comparison between real and estimated hysteresis loop of double integrated displacement

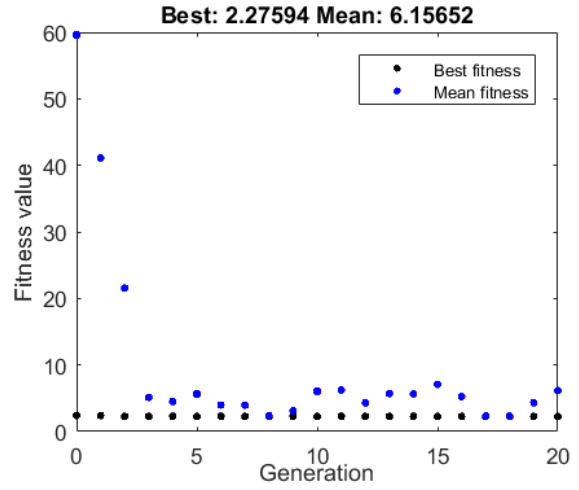
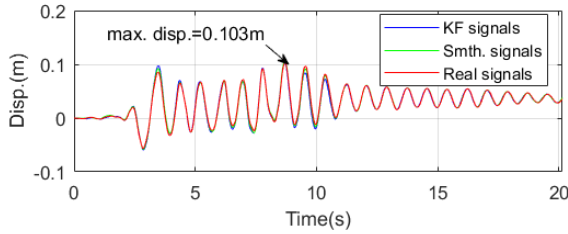
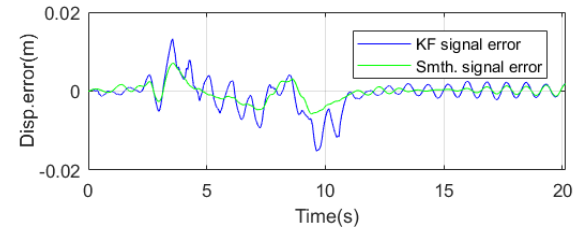


Figure 3.25 convergence plot of GA



(a)



(b)

Figure 3.26 estimated displacement based on method 2;

(a) comparison between estimated and real displacement; (b) estimation error comparison

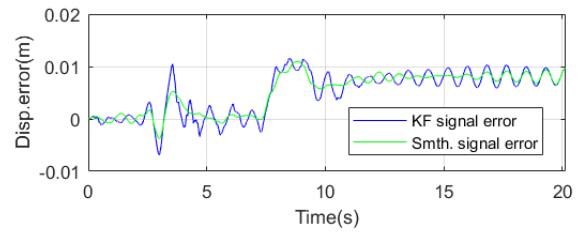
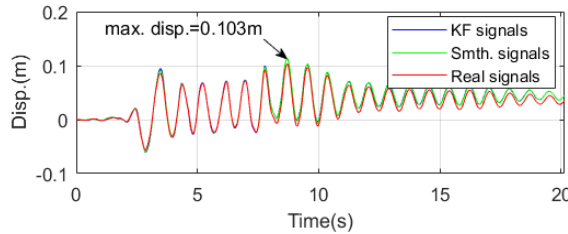


Figure 3.27 estimated displacement based on method 2 only using acceleration measurement;

(a) comparison between estimated and real displacement; (b) estimated error comparison

3.3.3 Effect of input signal noise

Similar to last chapter, the effect of measurement noise in input signal is also investigated in the section. The Bouc-Wen model used in section 3.3.2 is also investigated here except that white noise process is added to the input acceleration signal as Figure 3.28. The RMS of the measurement noise in the input signal is 0.03m/s^2 .

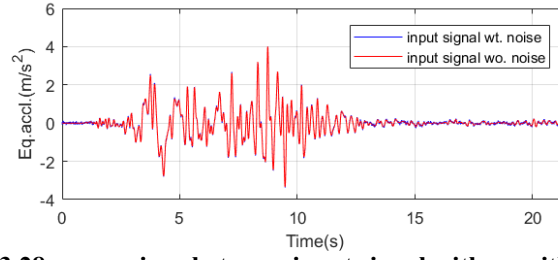


Figure 3.28 comparison between input signal with or without noise

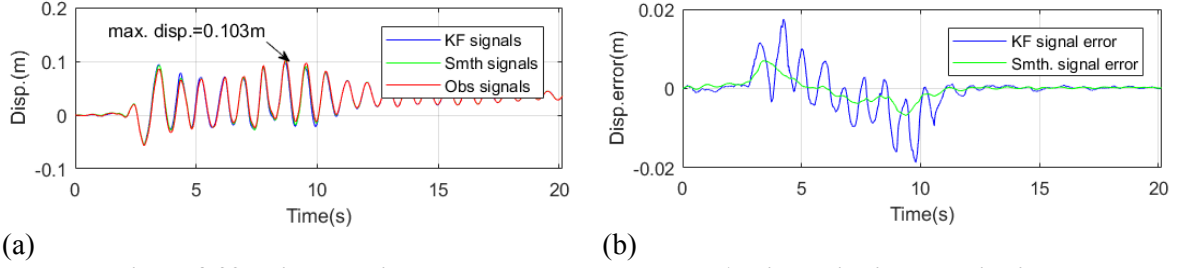


Figure 3.29 estimated displacement based on method 1 using noisy input excitation; (a) comparison between estimated and real displacement; (b) estimation error comparison

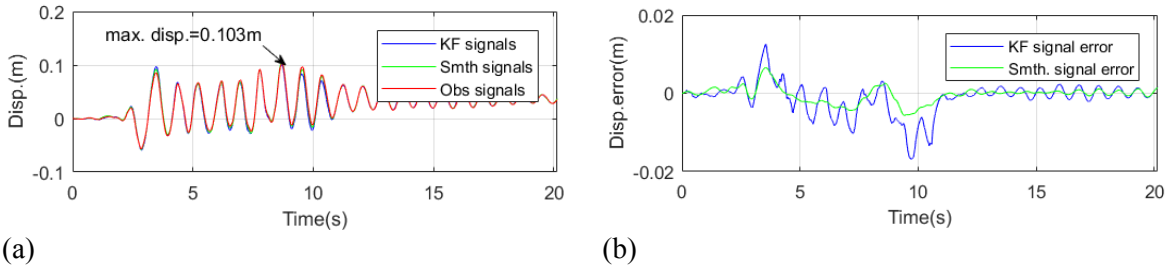


Figure 3.30 estimated displacement based on method 2 using noisy input excitation; (a) comparison between estimated and real displacement; (b) estimation error comparison

Based on the noisy input signal, the displacement is estimated again using both method 1 and method 2. The computation parameters are all same as in section 3.3.2 . For the method 2, the optimized δy and α parameters are 0.0509 and 0.0995 respectively using the noisy input signal. The final estimated displacements as well as their errors are shown in Figure 3.29 and Figure 3.30, in which the 2nd iteration result of method 1 is presented. Compared to the previous results, no significant deterioration of accuracy is found. As discussed in last chapter, in practice the effect of input signal noise can be mitigated by de-noising the input signal in advance.

3.3.4 Application to various hysteresis model and earthquake excitations

In this section, the proposed methods are further numerically investigated using various hysteresis models and earthquake excitations. Specifically, three hysteresis models including bi-linear model, tri-linear model and Bouc-Wen model are considered with four earthquake excitations, i.e. Takatori, Northridge, Imperial valley and San Fernando earthquakes. Additionally, two levels of peak ground acceleration (PGA) are employed here, i.e. 400gal and 800gal. The basic parameter values of these hysteresis models and earthquake accelerations are summarized in Table 3.2 and Figure 3.31 respectively. The hysteresis loops of the three models under 400gal Northridge earthquake excitations are shown in Figure 3.32.

Table 3.2 summary of basic parameters of three hysteresis models

Parameter	Bi-linear	Tri-linear	Bouc-Wen
Mass m (ton)	252.5	252.5	252.5
Elastic stiffness k (N/m)	1.625×10^7	1.625×10^7	1.625×10^7
Elastic damping coefficient c (Ns/m)	4.05×10^4	4.05×10^4	4.05×10^4
The 1 st post-yielding displacement dy_1 (m)	0.05	0.03	0.05
The 2 nd post-yielding displacement dy_2 (m)	N.A.	0.05	N.A.
The 1 st post-yielding stiffness ratio α_1	0.05	0.20	0.05
The 2 nd post-yielding stiffness ratio α_2	N.A.	0.067	N.A.
Loop parameter n	N.A.	N.A.	5
Loop parameter μ	N.A.	N.A.	1
Stiffness degradation parameter δ_v	N.A.	N.A.	20
Strength degradation parameter δ_η	N.A.	N.A.	20

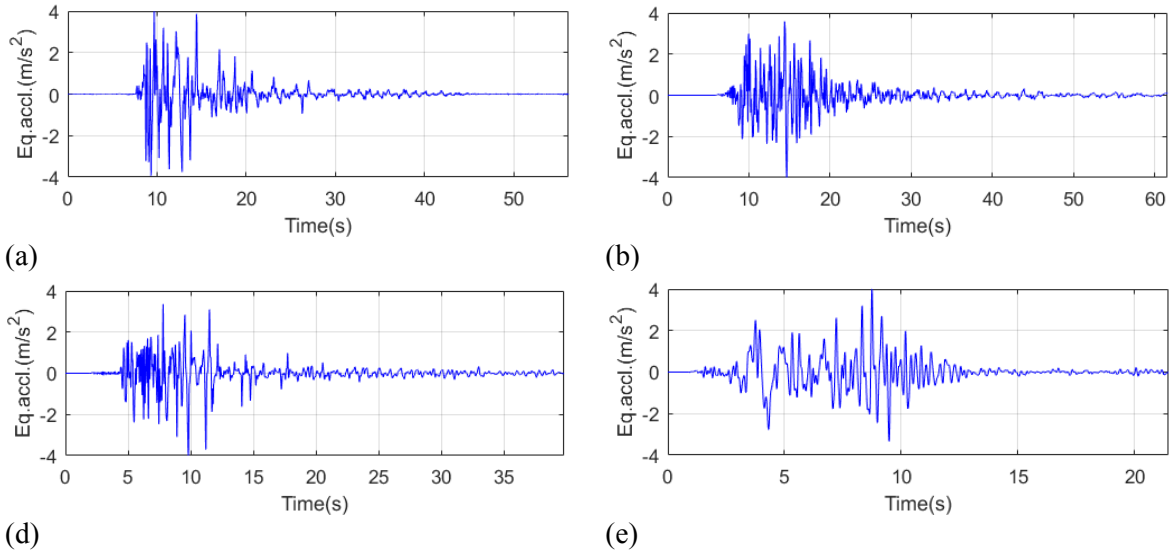


Figure 3.31 earthquake excitations; (a) Takatori; (b) Northridge; (c) Imperial valley; (d) San Fernando

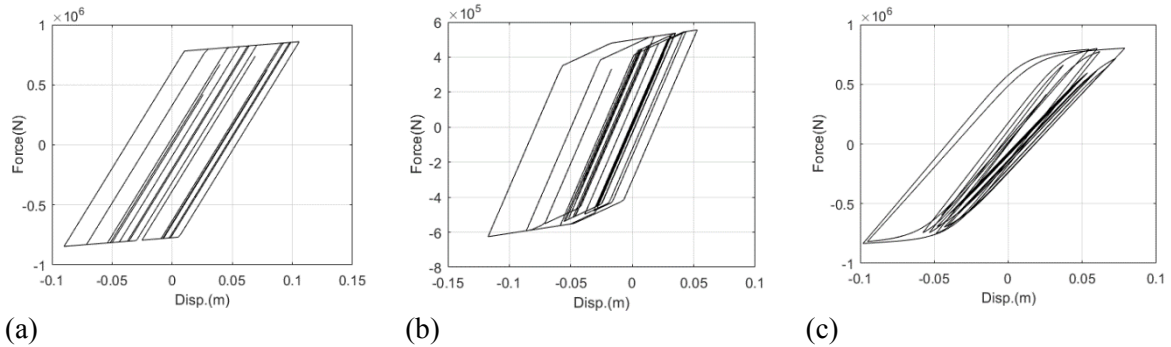


Figure 3.32 hysteresis loops under 400gal Northridge earthquake excitation; (a) bi-linear model; (b) tri-linear model; (c) Bouc-Wen model

In all of the simulations, the forward analyses are conduct with 0.005s time sample. 5% RMS white noises are added to the simulated accelerations. Besides displacement estimated from method

1 and method 2, double integrated displacements from the noisy accelerations are also compared with aforementioned methods in this section in order to present the effectiveness of the proposed methods. The double integrated displacements are construct based on the approach shown in Figure 3.9. In terms of method 1, only the 2nd iteration result of each case is considered, while for method 2 the whole optimized parameter dy and α values are summarized in Table 3.3.

Table 3.3 summary of optimized parameters

	400gal		800gal	
Bi-linear model	$dy(m)$	α	$dy(m)$	α
Takatori	0.0498	0.0554	0.0503	0.0500
Northridge	0.0500	0.0449	0.0500	0.0548
Imperial valley	0.0499	0.0548	0.0504	0.0512
San Fernando	0.0500	0.0553	0.0501	0.0514
Tri-linear model				
Takatori	0.0310	0.1284	0.0313	0.0786
Northridge	0.0311	0.1173	0.0321	0.0761
Imperial valley	0.0310	0.1350	0.0321	0.0689
San Fernando	0.0313	0.0995	0.0321	0.0656
Bouc-Wen model				
Takatori	0.0524	0.0686	0.0623	0.0680
Northridge	0.0529	0.0965	0.0698	0.0680
Imperial valley	0.0531	0.0949	0.0700	0.0700
San Fernando	0.0503	0.0950	0.0700	0.0416

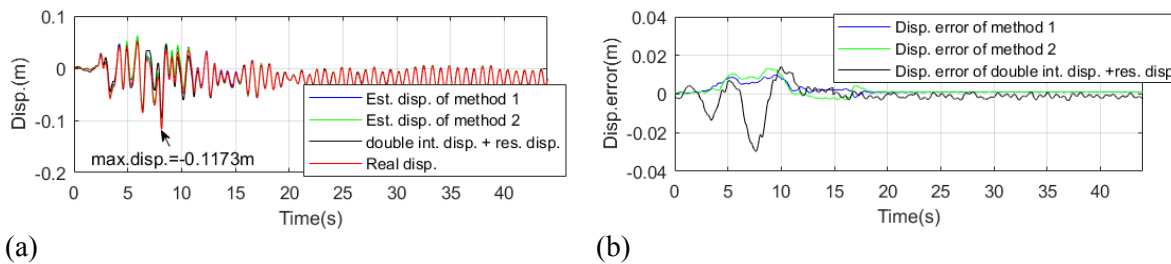
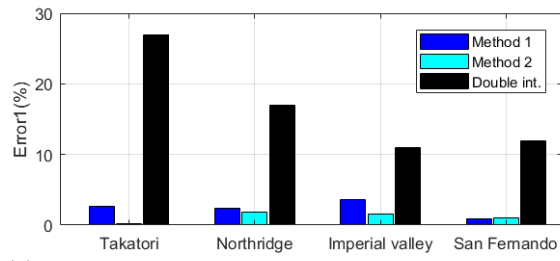
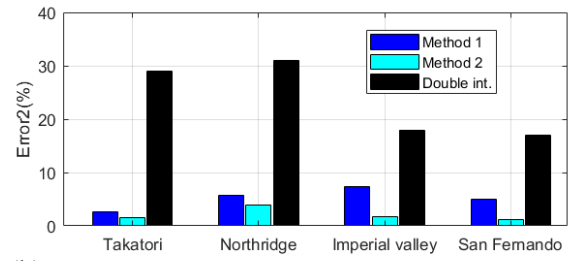


Figure 3.33 estimated displacement of tri-linear model in 400gal Northridge earthquake case; (a) comparison between estimated and real displacement; (b) estimation error comparison

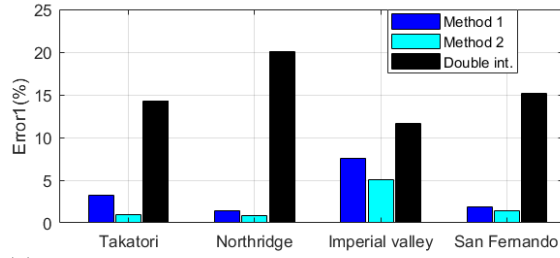
Two errors based on EKS result, i.e. error at maximum absolute displacement and maximum error, normalized by maximum absolute displacement are employed here to represent the estimation accuracy quantitatively. In the following part, they are referred as error1 and error2 respectively for simplicity. The estimation results of tri-linear model in 400gal Northridge earthquake case is shown in Figure 3.33, where smoothed displacement results using method 1 (the 2nd iteration) and 2 are compared with the integrated displacement. Obviously, the proposed methods outperform double integrated displacement significantly. Error 1 of the three type results are 6.4%, 8.3% and 18.5%, while they are 8.5%, 11.1% and 25.6% for error 2. The bar Figure 3.34 to Figure 3.36 show the results of all cases studied in the section.



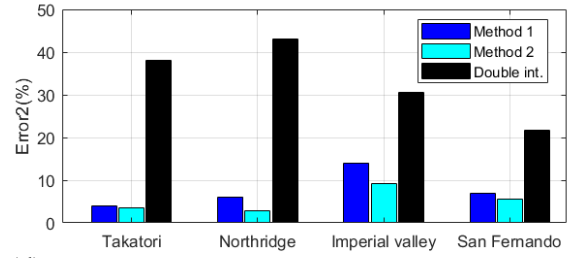
(a)



(b)



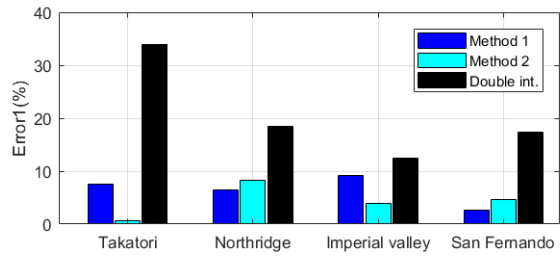
(c)



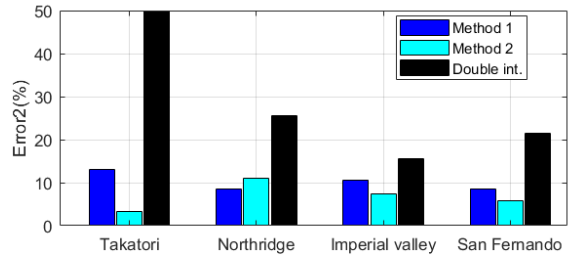
(d)

Figure 3.34 estimation errors of bi-linear model;

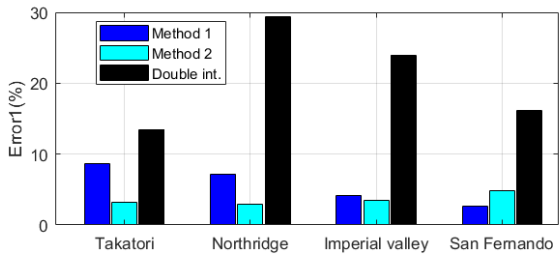
(a) error1 of 400gal case; (b) error2 of 400gal case; (c) error1 of 800gal case; (d) error2 of 800gal case



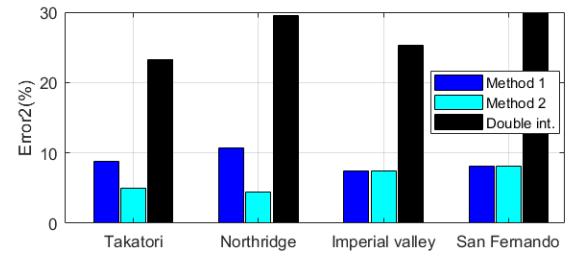
(a)



(b)



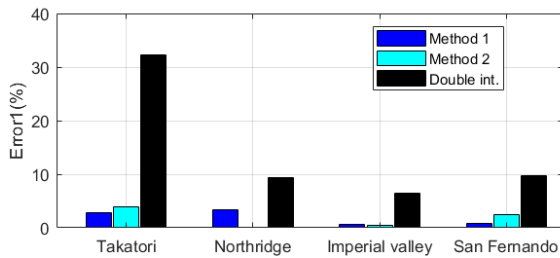
(c)



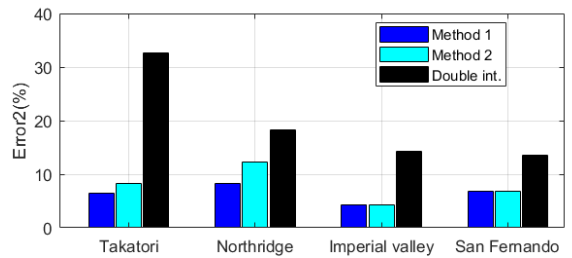
(d)

Figure 3.35 estimation errors of tri-linear model;

(a) error1 of 400gal case; (b) error2 of 400gal case; (c) error1 of 800gal case; (d) error2 of 800gal case



(a)



(b)

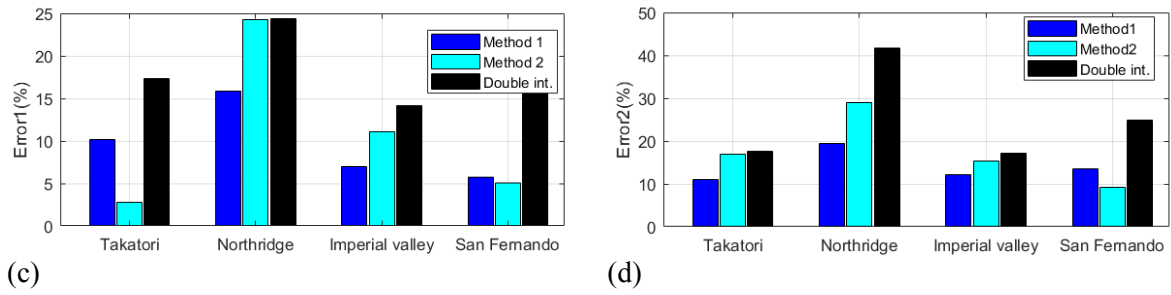


Figure 3.36 estimation errors of Bouc-Wen model;
(a) error1 of 400gal case; (b) error2 of 400gal case; (c) error1 of 800gal case; (d) error2 of 800gal case

Generally, the proposed methods present good performance and outperform double integrated displacement significantly. In terms of the maximum absolute displacement estimation, error1 usually is more accurate than error2, i.e. most of error1 values are below 10% while error2 values are generally lower than 20%.

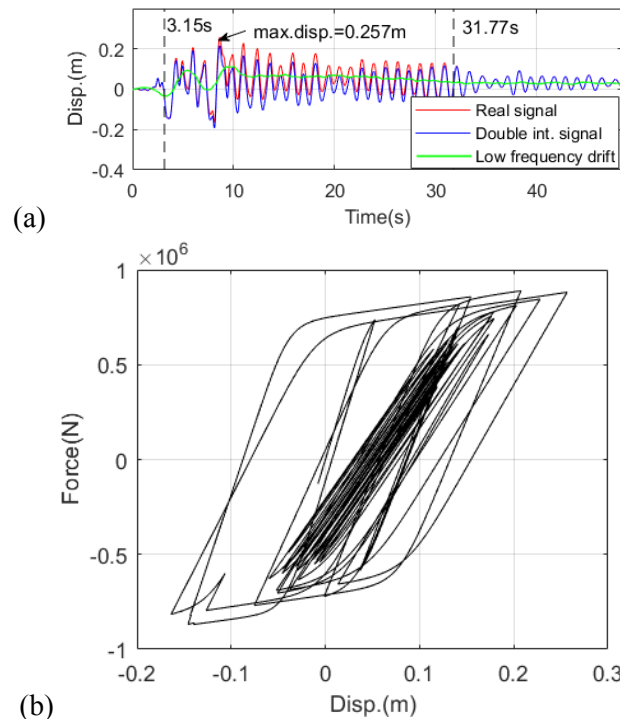
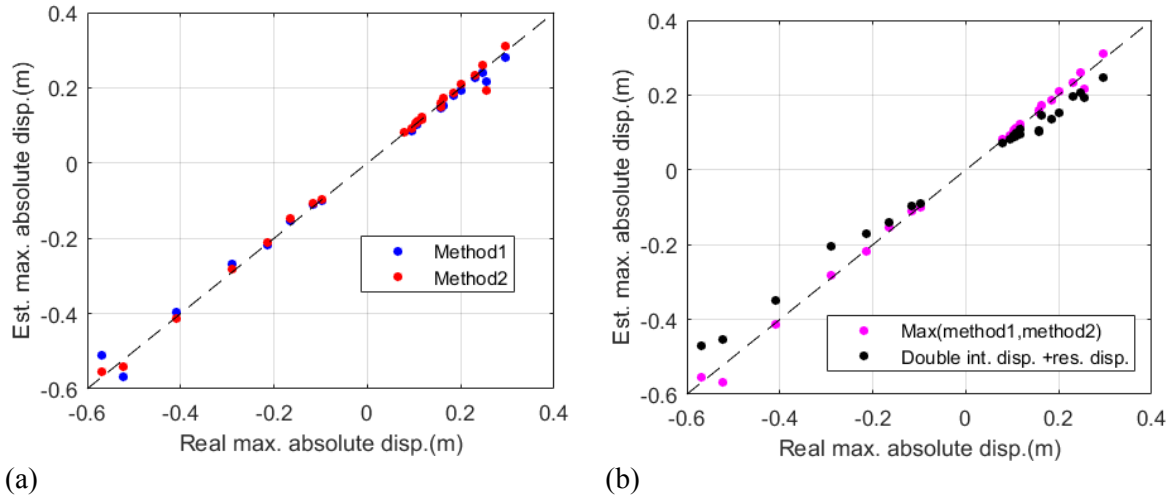


Figure 3.37 Bouc-Wen model responses under 800gal Northridge earthquake excitation;
(a) displacement; (b) hysteresis loop

One exception is the case of Bouc-Wen model under 800gal Northridge earthquake excitation. Error1 values are about 15% and 25% for method 1 and method 2 respectively while corresponding error2 values are about 20% and 30%. The 25% error1 value of method 2 is even larger than the error of integrated displacement 22%. Figure 3.37 shows the system response of this case. One reason of the poor performance is that the time interval with virtual displacement here is much longer, i.e. almost 30s, comparing to other cases which are within 20s or even shorter. The long time interval is due to strong nonlinearity of the Bouc-Wen model in which system strength and stiffness decrease successively and significantly as shown in Figure 3.37 (b).

Since in practical engineering, maximum absolute displacement is more of interest. Finally, the

estimated maximum absolute displacement values are compared with those real ones as shown in Figure 3.38 for all of the earthquake cases. Generally, results from the proposed method reproduce real values well, i.e. most of points do not deviate from the $y=x$ line too much. In practical engineering, the maximum value from the two methods could be selected, as shown in Figure 3.38 (b), to avoid underestimation of displacement as much as possible.



**Figure 3.38 (a) estimated maximum absolute displacement of two methods;
(b) maximum values among the two methods**

3.4 Experiment validation of the dynamic displacement estimation method

In this section, the proposed dynamic displacement estimation method is validated through two experiments in E-defense database, i.e. a full scale bridge pier experiment and a full scale four story frame experiment.

The cases where the experimental models experience strong earthquake excitations and present nonlinearity are selected. Both of the real models are simplified to SDOF systems for displacement estimation.

3.4.1 Full scale bridge pier experiment

The C1-1 bridge pier experiment is used here. Some of the detailed information about the experiment has already been given before. As mentioned earlier, since the acceleration measurements are noisy in this case, the displacement signals measured at the top of pier cap are employed here. Acceleration and velocity signals can be derivative from the displacement. Additionally, 5% RMS white noises are added to the acceleration signals to simulate measurement noise manually in this case. The sampling frequency is 200Hz. The north-south (NS) and west-east (WE) directions of the experiment are analyzed under a series of Takatori earthquake excitations. Their ID used in this paper and corresponding peak ground acceleration (PGA) are listed in Table 3.4. A group of wave forms of earthquake excitations as well as relative displacement and relative acceleration in Takatori100%1 NS case are shown in Table 3.4. Since SDOF system is used here, only the concentration mass is regarded as known parameter, i.e. $m=252.5$ ton for NS direction and 340 ton for WE direction according to experiment report. In the flowing part, the Takatori100%1 NS direction case will be presented in detail.

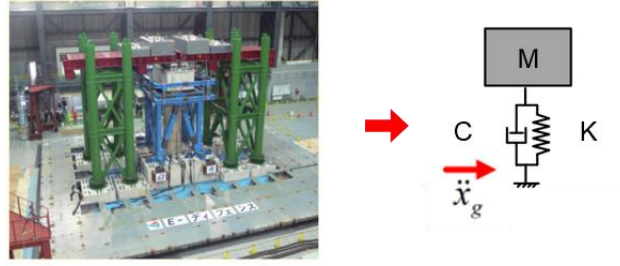


Figure 3.39 C1-1 prototype experiment model

Table 3.4 earthquake case ID and corresponding PGA

ID	NS-PGA(m/s^2)	WE-PGA(m/s^2)
Takatori100%1	5.76	7.83
Takatori100%2	6.25	6.11

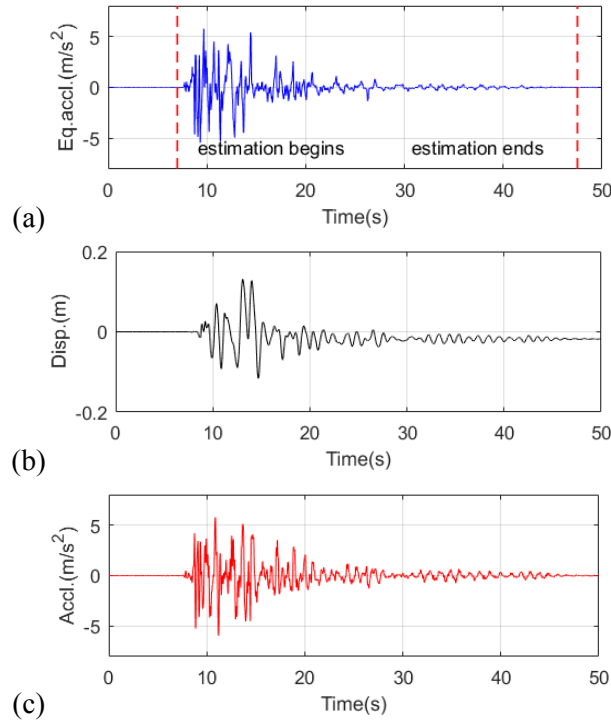
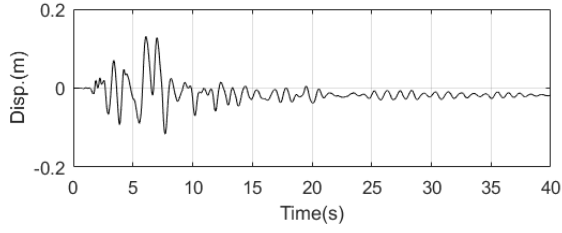


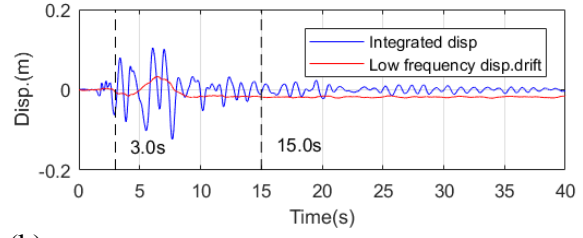
Figure 3.40 Takatori100%1 NS case;

(a) earthquake acceleration; (b) relative displacement; (c) relative acceleration

In the first place, according to the procedures discussed as above, the acceleration is used to obtain double integrated displacement; the integrate displacement as well as corresponding low frequency drift part is presented in Figure 3.41 for the estimation time interval as shown in Figure 3.40(a). Based on the integrated displacement and acceleration, time-variant parameter of the SDOF system can be identified. In this step, the \mathbf{R} matrix and initial \mathbf{Q} matrix is set as $\mathbf{R} = \text{diag}([5 \times 10^{-6}, 10^{-2}])$ (corresponding to displacement and acceleration measurement noise) and $\mathbf{Q} = \text{diag}([10^{-6}, 10^{-4}, 0, 0])$; besides, the α_Q value of RM algorithm is set as 1/15. The time-variant parameter results are shown in Figure 3.42. It can be observed that stiffness reduction period mainly occurs between 3~15s which matches well with the significant low frequency drift part in Figure 3.41(b). For the latter part of the identification, i.e. after 15s, the stiffness and damping coefficient are stable which are about $1.28 \times 10^7 \text{N/m}$ and $3 \times 10^5 \text{Ns/m}$ respectively.

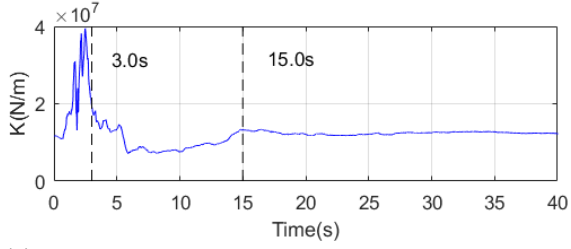


(a)

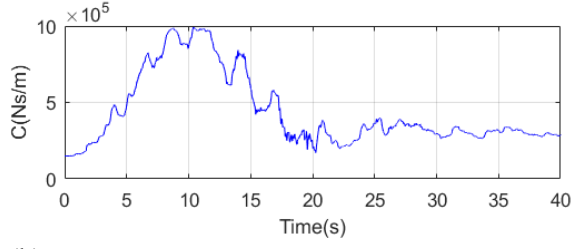


(b)

Figure 3.41 (a) true displacement; (b) double integrated displacement and low frequency drift



(a)



(b)

Figure 3.42 (a) time-variant stiffness value; (b) time-variant damping coefficient value

Based on the time-variant stiffness identification results, the time interval with virtual displacement is defined from 2.66s to 15.61s at which the integrated displacement cross zero. Combining with residual displacement -1.8cm in the latter part, the displacement measurement is established and shown in Figure 3.43. Based on the maximum absolute value of integrated displacement, the measurement noise for the virtual displacement is set as 0.15m.

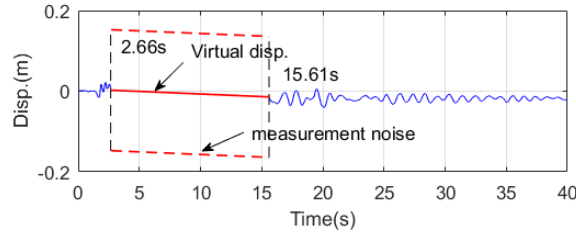
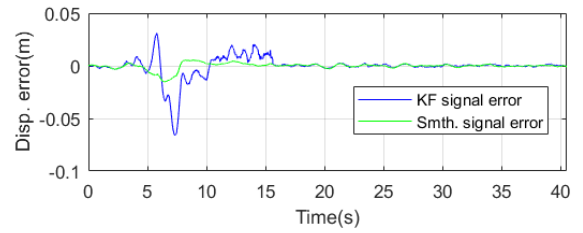
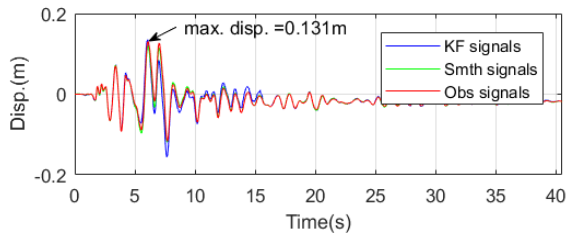
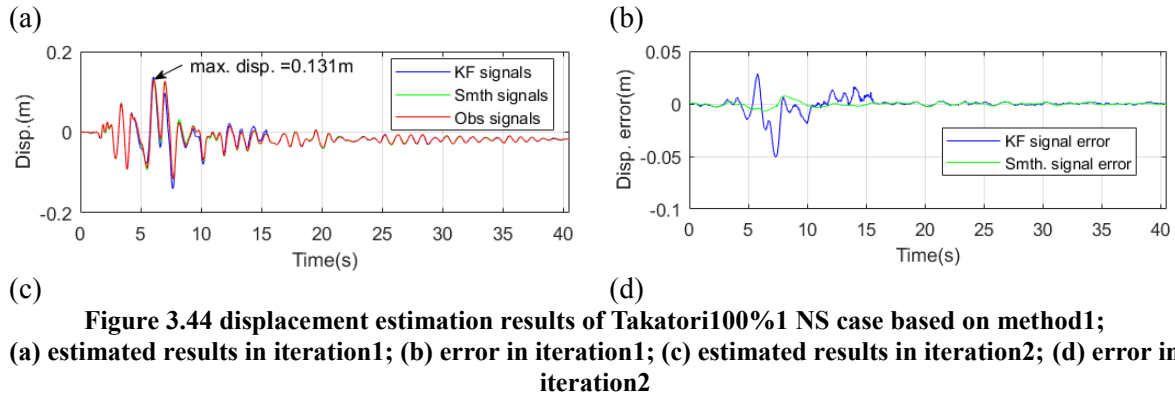


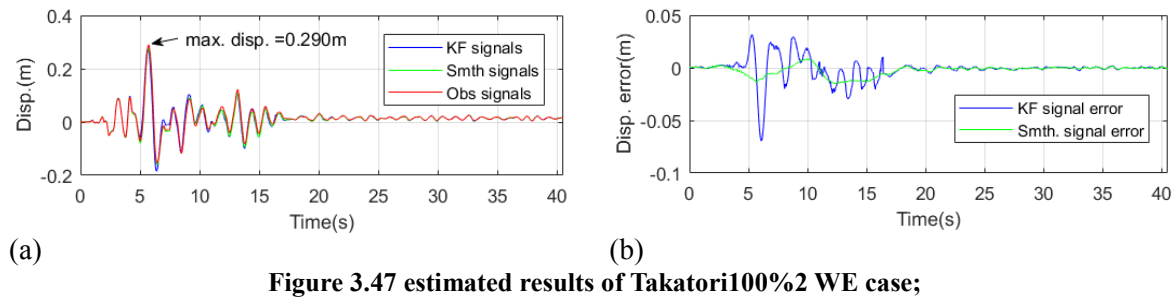
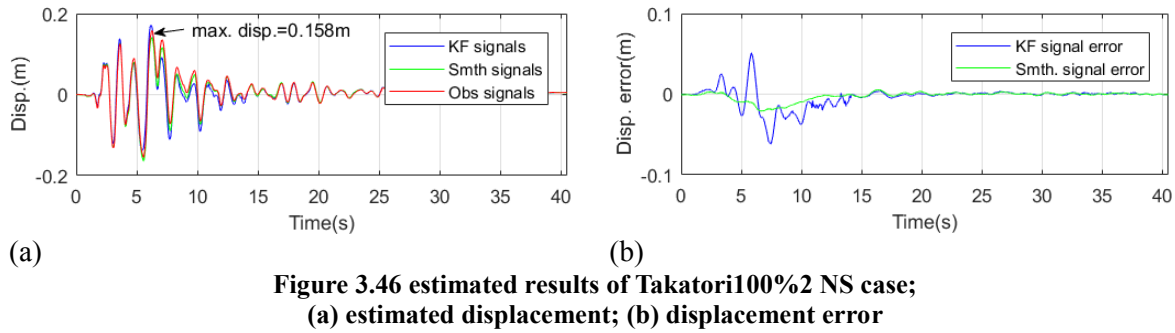
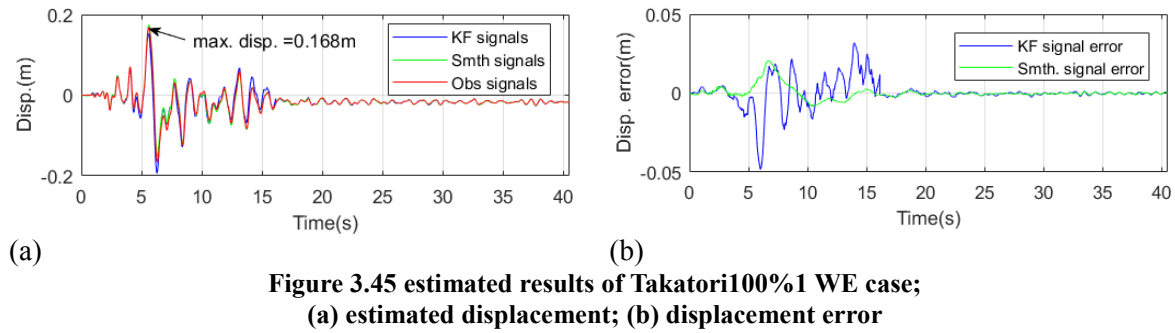
Figure 3.43 displacement measurement

Based on the above displacement measurement and acceleration in Figure 3.40, the displacement is firstly estimated using method1. In this case, the \mathbf{R} matrix in this case is set as $\text{diag}([0.0225, 10^{-2}])$ and $\text{diag}([5 \times 10^{-5}, 10^{-2}])$ for the virtual displacement and integrated displacement part respectively. Initial \mathbf{Q} matrix is set as $\text{diag}([10^{-6}, 10^{-4}, 10^{-2}, 0])$ corresponding to displacement, velocity, acceleration and stiffness value. The damping coefficient $c=3 \times 10^5 \text{Ns/m}$ is applied as known parameter in this estimation.





The results of the first and second iteration in method1 are shown in Figure 3.44. The maximum absolute displacement occurs at 6.09s with 0.131m. The error1 values of EKS signals corresponding to this point are about 8.9% and 4.3% respectively for the 1st and 2nd iteration. The error2 values are 11.5% and 5.8% respectively. Here, the 2nd iteration results outperform the 1st one. This is also true for other cases discussed in this section and their results in the 2nd iteration are shown in Figure 3.45 to Figure 3.47.



(a) estimated displacement; (b) displacement error

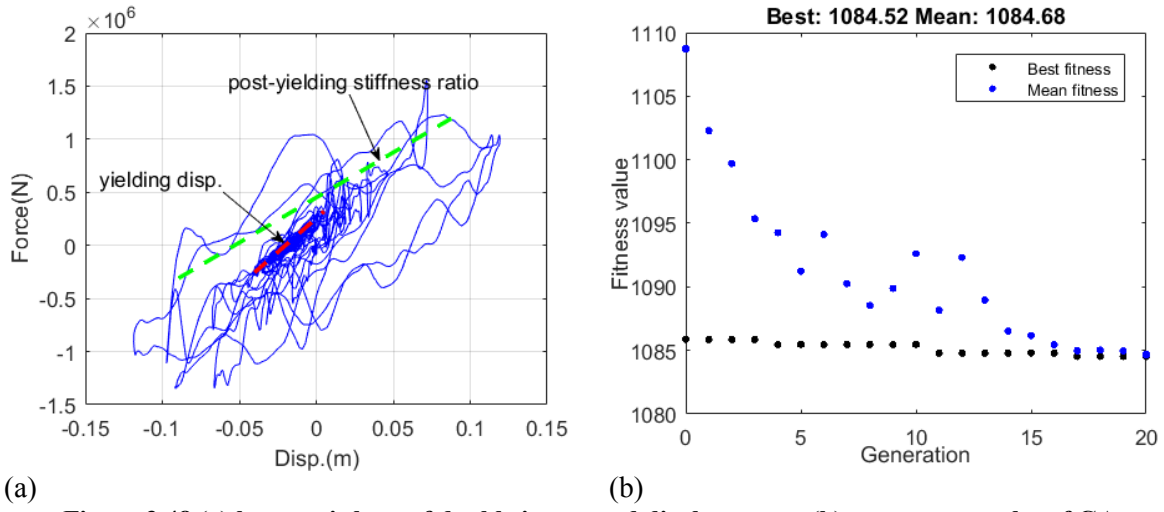


Figure 3.48 (a) hysteresis loop of double integrated displacement; (b) convergence plot of GA

In the second place, the method2 is applied here. As discussed earlier, the elastic stiffness and damping coefficient, i.e. $k=1.28 \times 10^7 \text{N/m}$ and $c=3 \times 10^5 \text{Ns/m}$, are regarded as known parameters. Bi-linear model parameter d_y and α are optimized using GA. The range of d_y and α is defined based on the red and green dashed line in Figure 3.48(a). The hysteresis loop shown is based on the double integrated displacement. Here, the range is defined as $0.02 \leq d_y \leq 0.05$ and $0.3 \leq \alpha \leq 0.8$. In the GA computation, 20 generations with 30 populations of each are employed. Figure 3.48(b) shows the convergence plot. The optimized d_y and α values are 0.0492 and 0.5136 respectively. Based on these values, the dynamic displacement is estimated based on bi-linear model which is shown in Figure 3.49. In this case, the error1 and error2 are 5.7% and 6.8% respectively. Results of other cases are also shown in Figure 3.50 ~Figure 3.52. The optimized values of d_y and α are listed in Table 3.5.

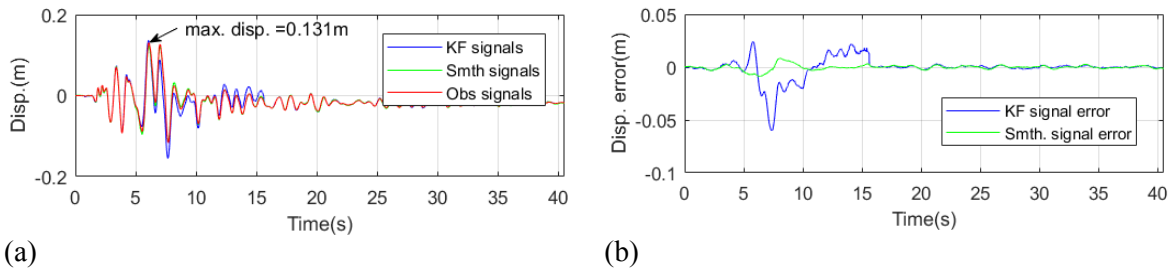


Figure 3.49 displacement estimation results of Takatori100%1 NS case based on method 2;
(a) estimated displacement; (b) displacement error

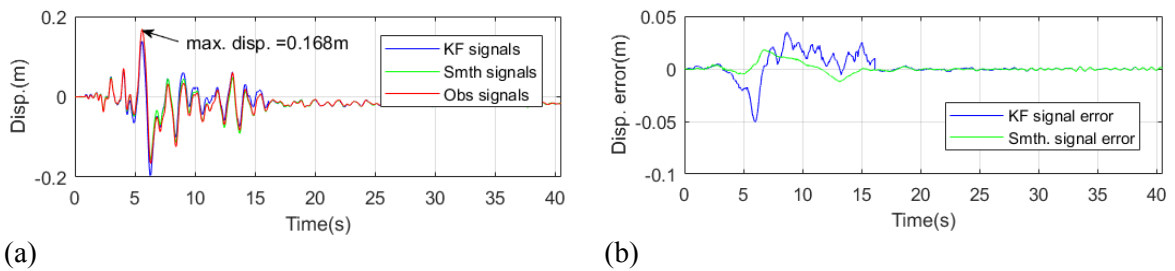


Figure 3.50 estimated results of Takatori100%1 WE case;
(a) estimated displacement; (b) displacement error

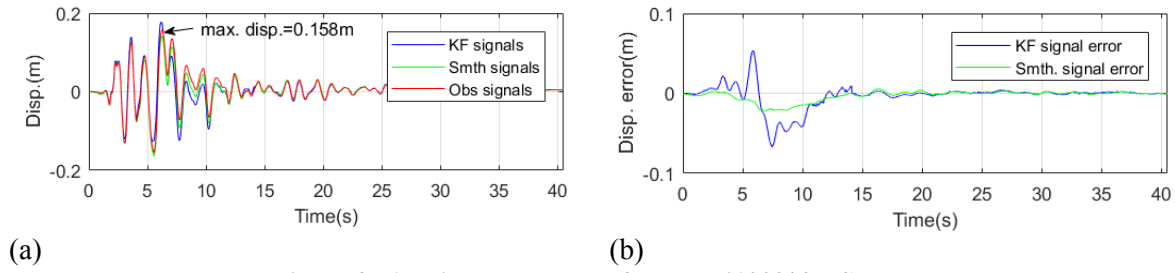


Figure 3.51 estimated results of Takatori100%2 NS case;
(a) estimated displacement; (b) displacement error

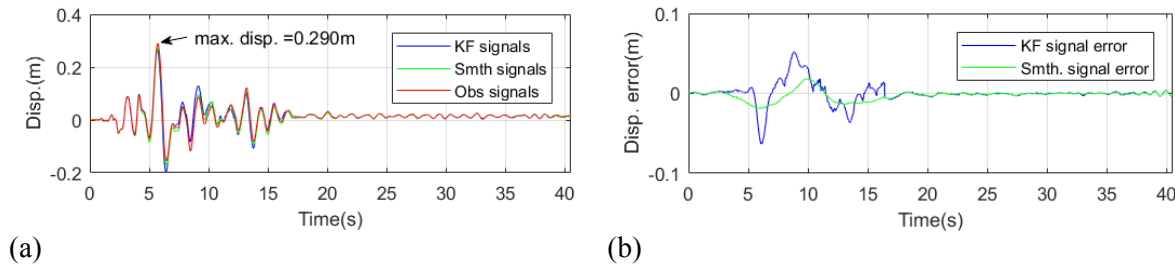


Figure 3.52 estimated results of Takatori100%2 WE case;
(a) estimated displacement; (b) displacement error

Table 3.5 results of optimized values

ID	NS direction		WE direction	
	$dy(m)$	α	$dy(m)$	α
Takatori100%1	0.0492	0.5136	0.0305	0.401
Takatori100%2	0.0327	0.5528	0.0246	0.3320

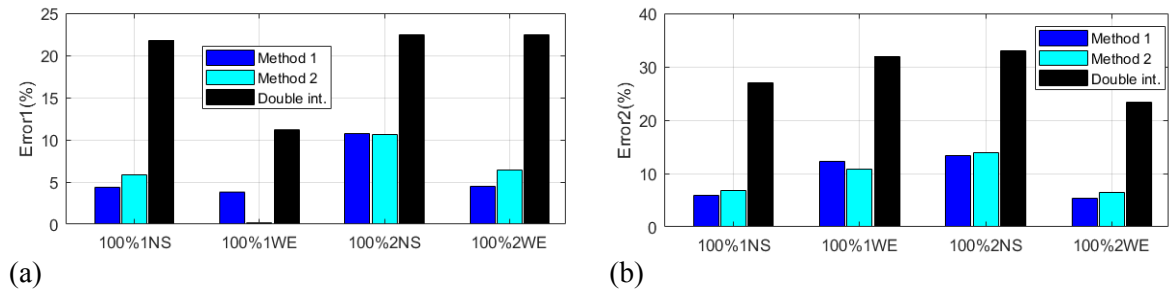


Figure 3.53 estimation error; (a) error1; (b) error2

Finally, the errors from the two methods are compared with double integration method as shown in Figure 3.53. Both methods perform similarly and outperform double integration displacement significantly.

3.4.2 Full scale four story building experiment

The full scale four story building experiment data are applied here. The building model is simplified as 4-DOF lumped mass model with equivalent concentration mass for each floor are 44.2, 29.3, 43.6 and 80.3 ton from bottom to top floor which are the update values used in section 2.5.2 . Accelerometer and laser displacement transducer for each floor are available in the Takatori60% case. Also, relative large system nonlinearity happens in the case for the 1st and 2nd floor. Thus they

will be analyzed here for both NS and WE direction. The earthquake accelerations, inter-story displacements and accelerations are shown in Figure 3.55~Figure 3.57 respectively. The PGA of NS and WE direction earthquakes are 5.24m/s^2 and 4.38m/s^2 respectively.

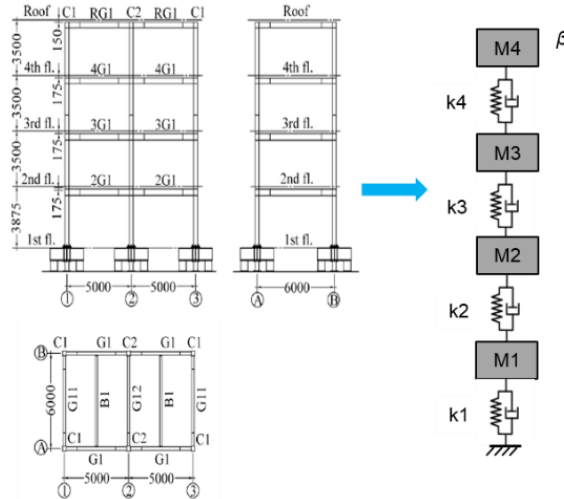


Figure 3.54 simplified 4-DOF system model

In these experiments, the nonlinearity is not that significant and the residual displacement is relatively small, but it is still assumed that they are known after earthquake. The information is summarized in Table 3.6. In the flowing part, the first floor of WE direction case will be presented in detail.

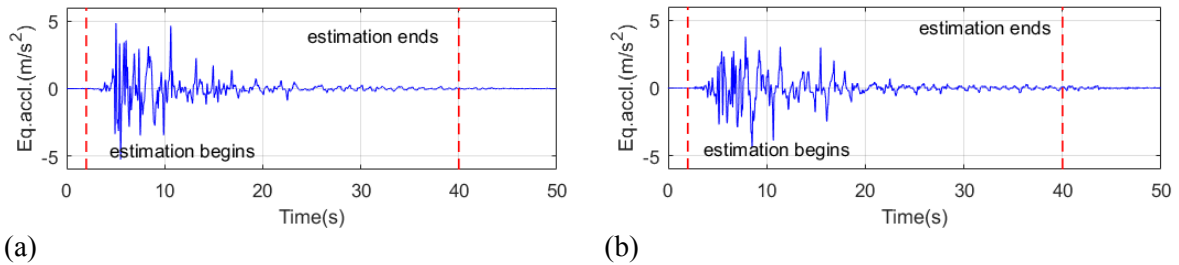


Figure 3.55 earthquake acceleration; (a) NS direction; (b) WE direction

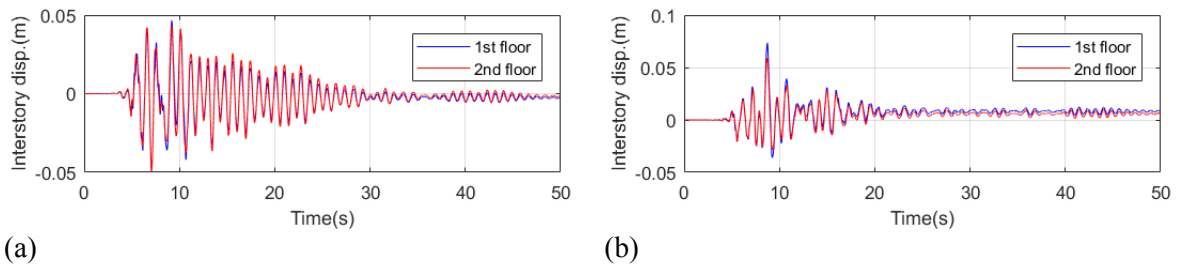


Figure 3.56 inter-story displacement; (a) NS direction; (b) WE direction

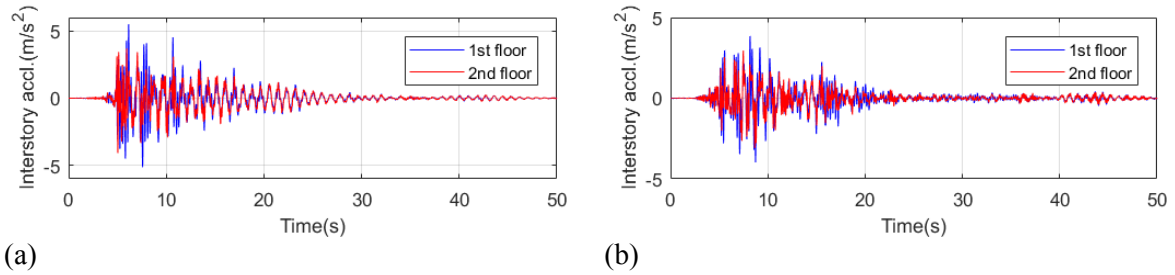


Figure 3.57 inter-story acceleration; (a) NS direction; (b) WE direction

Table 3.6 basic information summary

	NS direction	WE direction
Ground PGA	5.24m/s ²	4.38m/s ²
The 1 st floor residual displacement	-3mm	8mm
The 2 nd floor residual displacement	-2mm	6mm

Same as before, the double integrated displacement is firstly obtained based on measured acceleration. The true displacement and the integrated one for the estimation interval in Figure 3.55 are shown in Figure 3.58. In this case, the EOM of SDOF is written as equation (3.2), i.e. the inertial force comes from not only ground acceleration but also force transferred from floors above. Based on the integrated displacement and acceleration, time-variant stiffness and damping coefficient are identified. The \mathbf{R} matrix is set as $\mathbf{R} = \text{diag}([10^{-6}, 10^{-3}])$, other computation information is same as previous case. Figure 3.59 shows the time-variant parameter identification results. Except the fluctuation during the initial time, stiffness variation part mainly occurs from 5.0s to 15.0s. Comparing with the low frequency drift part in Figure 3.58(b), it overestimates the time interval, i.e. low frequency drift mainly occurs from 5.0s to 10.0s. However, in the following this time interval will still be employed. In this case, the stiffness and damping coefficient presents stable values in the latter part, i.e. $k=2.65 \times 10^7 \text{N/m}$ and $c=5 \times 10^5 \text{Ns/m}$. Based on the information, the virtual displacement is defined from 3.27s to 15.08s, and corresponding displacement measurement is shown in Figure 3.60. Here the measurement noise for the virtual displacement is set as 0.09m based on maximum value of double integrated displacement.

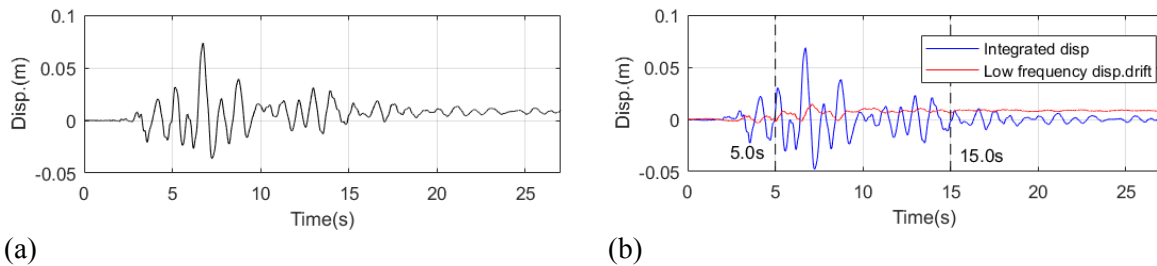


Figure 3.58 (a) true displacement; (b) double integrated displacement and low frequency drift

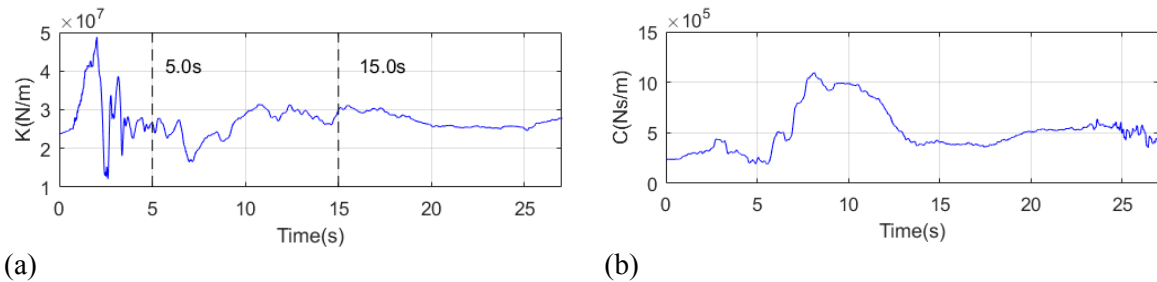


Figure 3.59 (a) time variant stiffness value; (b) time variant damping coefficient value

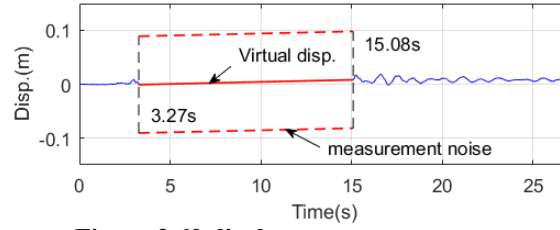


Figure 3.60 displacement measurement

Using method1, the dynamic displacement is firstly estimated based on the displacement and acceleration measurement. Even though the damping coefficient identified previously roughly converge to a stable value, in order to consider the effect of it on the estimation results, three damping coefficient values, i.e. $c=2.50 \times 10^5 \text{Ns/m}$, $5.00 \times 10^5 \text{Ns/m}$, $7.50 \times 10^5 \text{Ns/m}$, are applied here for comparison. The R matrix used here is $\text{diag}(10^{-5}, 10^{-3})$ and $\text{diag}([0.0036, 10^{-3}])$ for the integrated and virtual displacement part respectively.

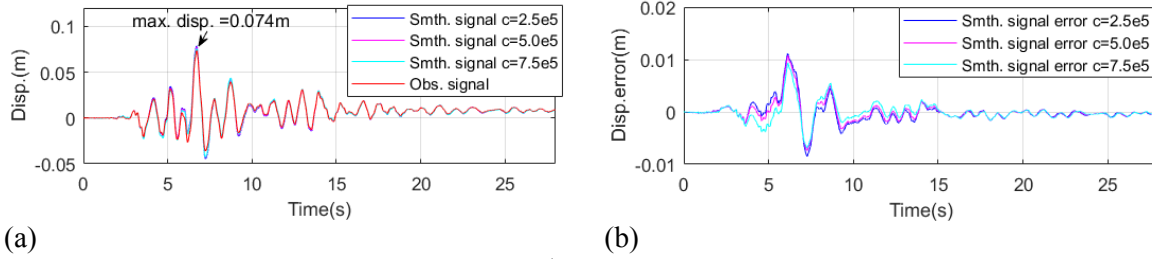


Figure 3.61 estimated results of the 1st floor WE direction case based on method 1;
(a) estimated displacement; (b) displacement error

Figure 3.61 compares the estimated displacement results using the three damping coefficients as well as their errors. There is no significant difference between them in terms of the errors. The estimated maximum absolute values are 7.86cm, 7.75cm and 7.58cm while the real maximum absolute displacement occurs at 6.72s with 7.4cm. In terms of the maximum error, they are 11.1mm, 10.7mm and 9.3mm respectively. The above discussion shows the insensitivity of displacement estimation to damping coefficient from the perspective of experiment data. In fact, it is also investigated based on numerical simulation in section 3.3.2 . Results from other cases are shown from Figure 3.62 to Figure 3.64.

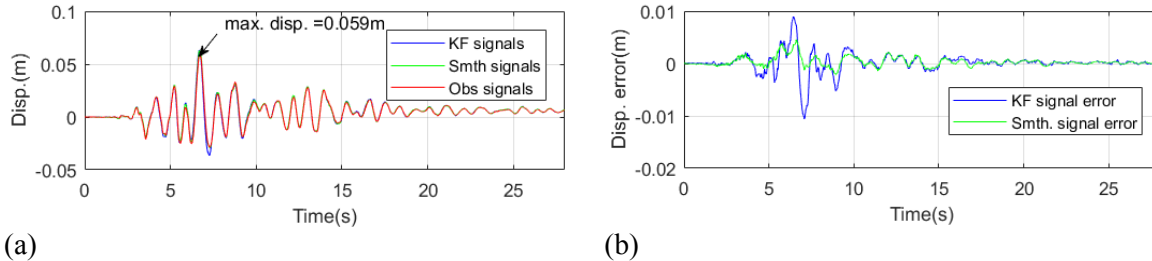


Figure 3.62 estimated results of the 2nd floor WE direction;
(a) estimated displacement; (b) displacement error

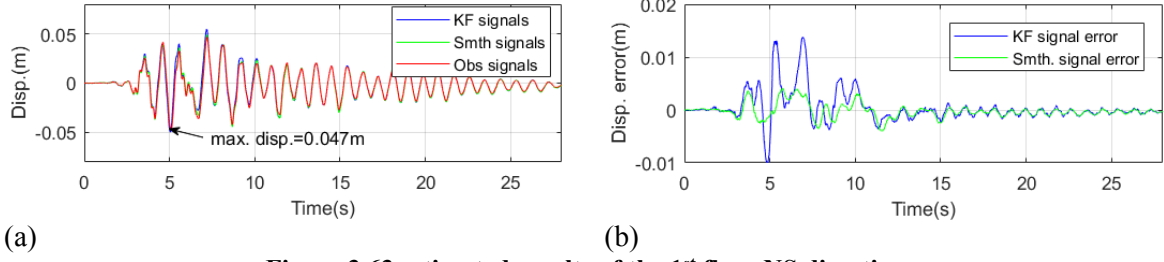


Figure 3.63 estimated results of the 1st floor NS direction;
(a) estimated displacement; (b) displacement error

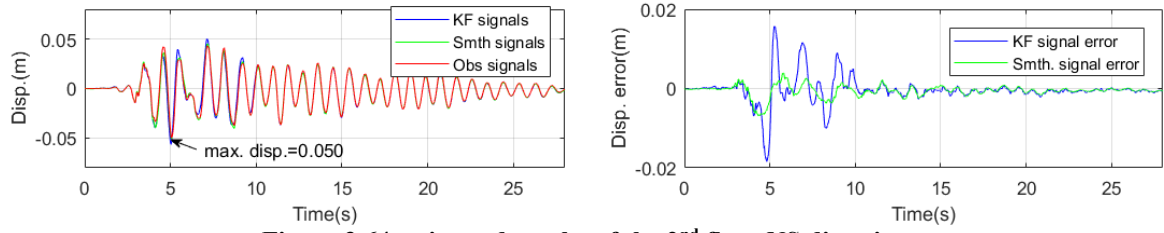


Figure 3.64 estimated results of the 2nd floor NS direction;
(a) estimated displacement; (b) displacement error

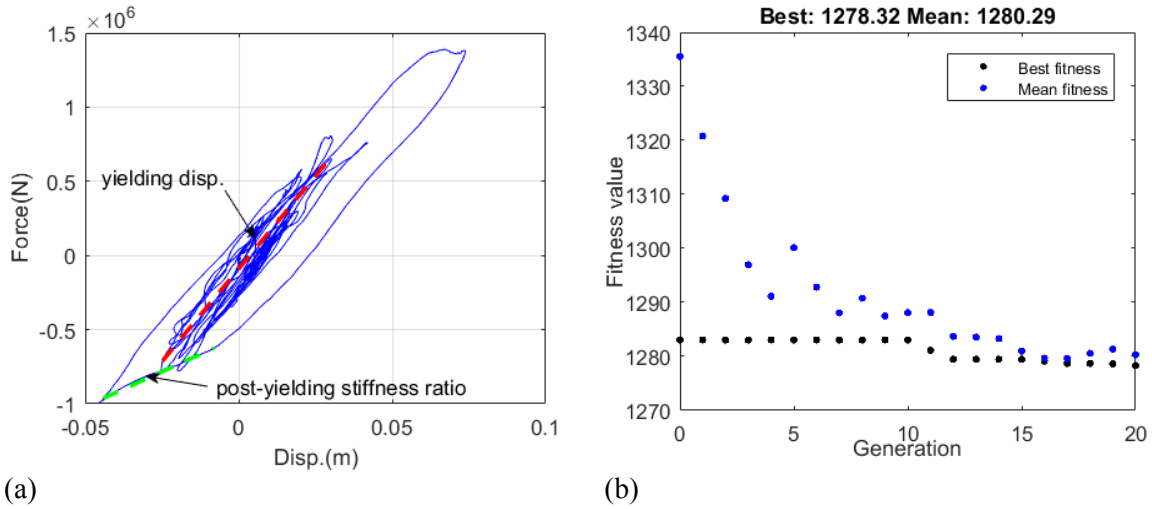
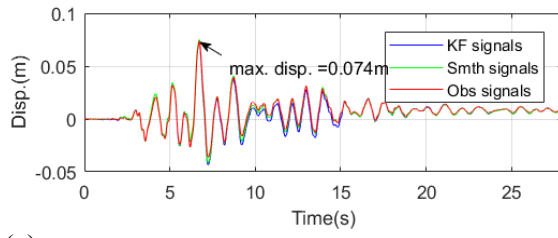
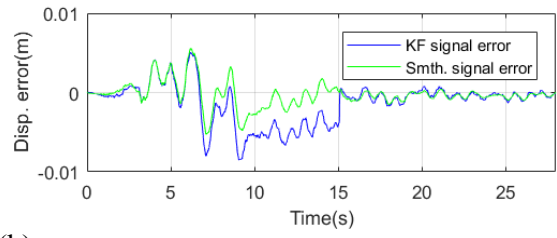


Figure 3.65 (a) hysteresis loop of double integrated displacement; (b) convergence plot of GA

Secondly, the method2 is applied here and the elastic stiffness and damping coefficient, i.e. $k=2.65 \times 10^7 \text{N/m}$ and $c=5 \times 10^5 \text{Ns/m}$, are regarded as known parameters. The range of d_y and α for bi-linear model is decided based on the red and green dashed line in Figure 3.65(a). The range is defined as $0.03 \leq d_y \leq 0.04$ and $0.3 \leq \alpha \leq 0.5$. The computation information of GA is same as previous case, and the optimized d_y and α are 0.0356 and 0.49 respectively. Based on the values, the displacement estimation results are shown in Figure 3.66. Results of other cases as well as optimized values of d_y and α are presented in following.



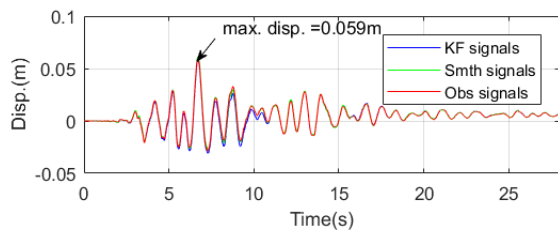
(a)



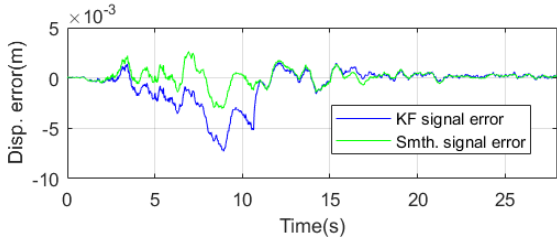
(b)

Figure 3.66 estimated results of the 1st floor WE direction case based on method 2;

(a) estimated displacement; (b) displacement error



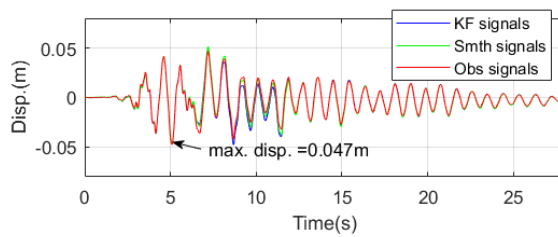
(a)



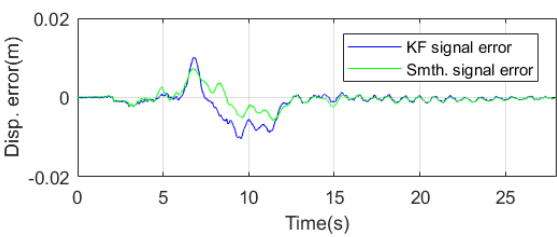
(b)

Figure 3.67 estimated results of the 2nd floor WE direction;

(a) estimated displacement; (b) displacement error



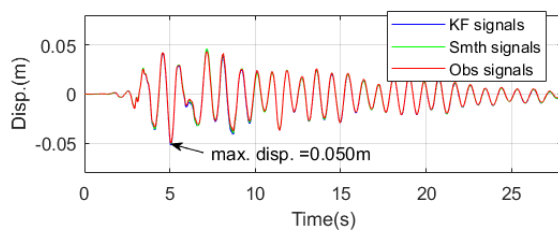
(a)



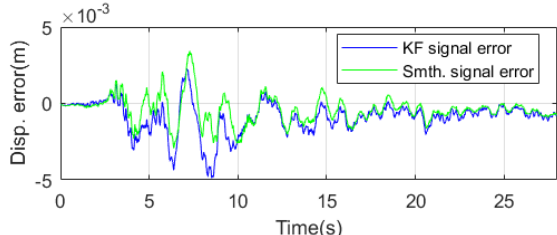
(b)

Figure 3.68 estimated results of the 1st floor NS direction;

(a) estimated displacement; (b) displacement error



(a)



(b)

Figure 3.69 estimated results of the 2nd floor NS direction;

(a) estimated displacement; (b) displacement error

Table 3.7 results of optimized values

	NS direction		WE direction	
	$dy(m)$	α	$dy(m)$	α
The 1 st floor	0.0281	0.399	0.0356	0.490
The 2 nd floor	0.0396	0.668	0.0337	0.499

The estimation errors of the two methods are compared with double integration method as

shown in Figure 3.70. the superiority of the proposed methods is not that evident because the nonlinearity is not that strong in this case. But the displacement estimation accuracies are still satisfying, i.e. error1 values are generally below 6% for method 1 and below 4% for method 2.

Finally, in Figure 3.71 the estimated maximum absolute displacement values of all the experiments presented based on the two methods are compared with real ones. Good coincidence can be found.

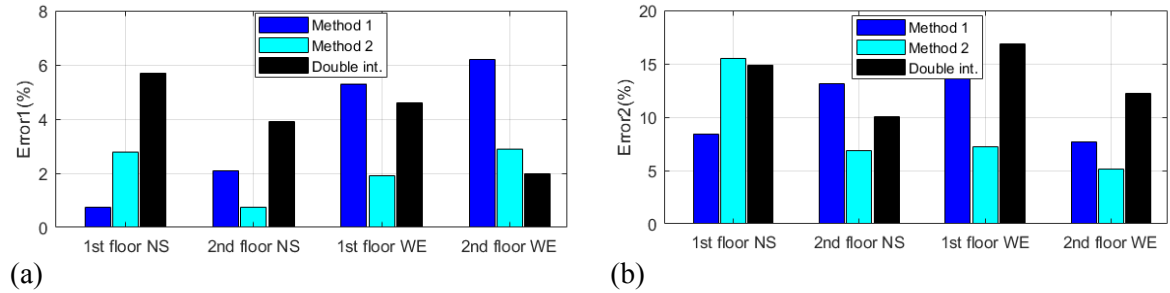


Figure 3.70 estimation error; (a) error1; (b) error2

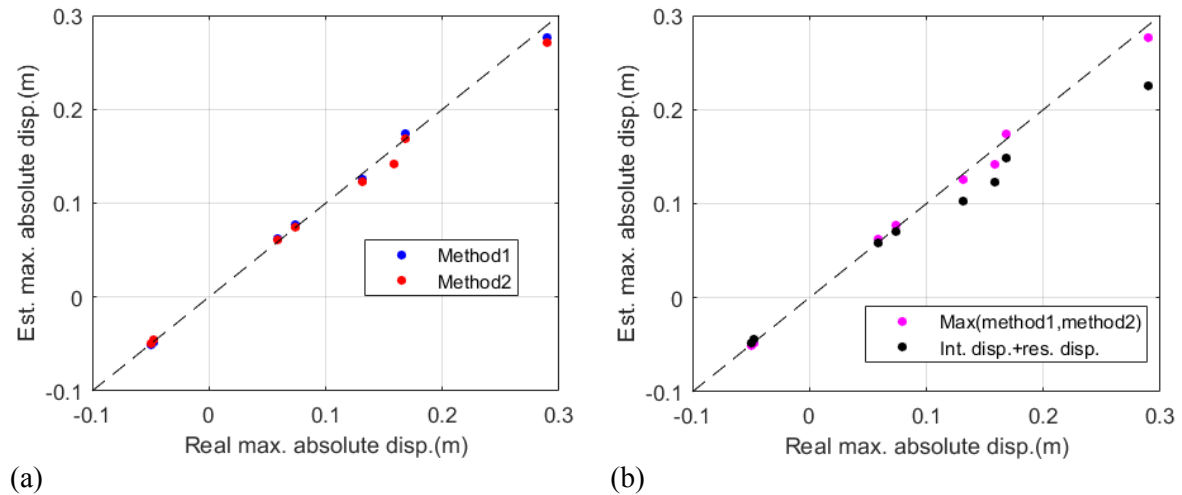


Figure 3.71 (a) estimated maximum absolute displacement of two methods; (b) maximum values among the two methods

Chapter 4 Parameter identification under unknown seismic excitation

4.1 Chapter outline

In this chapter, an augmented state vector involving all system response, parameters and inputs is employed to conduct system estimation considering unknown input based on EKF method. An offline process noise estimation method is combined with EKF to adjust the \mathbf{Q} matrix automatically. Firstly, the normal EKF with the augmented state vector is conducted with assumed \mathbf{Q} matrix; then extended Kalman smoother (EKS) is employed to smooth the results and updated the \mathbf{Q} matrix using state innovation information; the updated \mathbf{Q} is regarded as known and put into next iteration computation. The whole process stops when parameter estimation results converge. Moreover, it is found that normal state vector including displacements and velocities is prone to diverge in case of distributed mass system. In order to enhance filter stability, accelerations are also augmented into state vector based on Generalized-alpha numerical integration method. The proposed adaptive EKF-UI method is validated both numerically and experimentally using shaking table experiment data from E-defense database [102, 103]. For the following parts of the chapter, the adaptive EKF-UI method is firstly proposed in section 2. Some criteria about joint input-state-parameter estimation problem are also discussed in the section. In section 3, the proposed method is numerically verified through two models simplified from real engineering problems, including a bridge pier model and 2D four story frame structure model. The adaptive EKF-UI method is also studied combining with substructure method based on the bridge pier model and a 3D cable stayed bridge model numerically in section 4. Furthermore, in section 5, two shaking table experiments from E-defense database, i.e. a full scale bridge pier experiment and a full scale four story building experiment are employed to demonstrate the effectiveness of the method.

4.2 Parameter identification under unknown seismic excitation based on adaptive EKF-UI method

4.2.1 Equation of motion and EKF system equation

Normally, the equation of motion (EOM) of structure system under seismic excitation is written in a relative coordinate, in which ground accelerations are regarded as input excitations and system responses computed based on the EOM are relative value with respect to ground motion. In practical engineering, actually signals of absolute values, e.g. accelerations, are measured. Therefore, it is more natural and convenient to employ the EOM in absolute coordinate so that the two parts can match each other well. The EOM of a multi support structure system can be written in sub-matrix form as below

$$\begin{bmatrix} \mathbf{K}_{ss} & \mathbf{K}_{sg} \\ \mathbf{K}_{gs} & \mathbf{K}_{gg} \end{bmatrix} \begin{bmatrix} \mathbf{x}_s \\ \mathbf{x}_g \end{bmatrix} + \begin{bmatrix} \mathbf{C}_{ss} & \mathbf{C}_{sg} \\ \mathbf{C}_{gs} & \mathbf{C}_{gg} \end{bmatrix} \begin{bmatrix} \dot{\mathbf{x}}_s \\ \dot{\mathbf{x}}_g \end{bmatrix} + \begin{bmatrix} \mathbf{M}_{ss} & \mathbf{M}_{sg} \\ \mathbf{M}_{gs} & \mathbf{M}_{gg} \end{bmatrix} \begin{bmatrix} \ddot{\mathbf{x}}_s \\ \ddot{\mathbf{x}}_g \end{bmatrix} = \begin{bmatrix} \mathbf{0} \\ \mathbf{P}_g \end{bmatrix} \quad (4.1)$$

in which $\mathbf{x}(t)$, $\dot{\mathbf{x}}(t)$ and $\ddot{\mathbf{x}}(t)$ are vectors of displacement, velocity and acceleration respectively; \mathbf{M} , \mathbf{C} and \mathbf{K} are mass, damping and stiffness matrix respectively which are all constant if linear elastic assumption is considered; subscript ss and gg stands for structural and ground DOFs while sg and gs corresponds to coupling terms between structural and ground DOFs; \mathbf{P}_g is the boundary reaction force vector of the ground DOFs. Subsequently, if the first line of equation (4.1) is extracted, the EOM corresponding to non-supporting DOFs can be written as

$$\mathbf{K}_{ss}\mathbf{x}_s + \mathbf{C}_{ss}\dot{\mathbf{x}}_s + \mathbf{M}_{ss}\ddot{\mathbf{x}}_s = -(\mathbf{K}_{sg}\mathbf{x}_g + \mathbf{C}_{sg}\dot{\mathbf{x}}_g + \mathbf{M}_{sg}\ddot{\mathbf{x}}_g) \quad (4.2)$$

The right hand of the equation can be regarded as equivalent external load terms due to ground displacements, velocities and accelerations. They might be exerted on multiple boundary DOFs with different values. Furthermore, assuming Rayleigh damping, the equation (4.2) can be written as

$$\mathbf{K}_{ss}\mathbf{x}_s + \mathbf{C}_{ss}\dot{\mathbf{x}}_s + \mathbf{M}_{ss}\ddot{\mathbf{x}}_s = -\mathbf{K}_{sg}\mathbf{x}_g - \beta\mathbf{K}_{sg}\dot{\mathbf{x}}_g - \alpha\mathbf{M}_{sg}\dot{\mathbf{x}}_g - \mathbf{M}_{sg}\ddot{\mathbf{x}}_g \quad (4.3)$$

Assuming that the mass matrix term \mathbf{M}_{sg} does not play significant role in the right hand side of the equation, and they can be ignored. The equation (4.3) can be simplified as

$$\mathbf{K}_{ss}\mathbf{x}_s + \mathbf{C}_{ss}\dot{\mathbf{x}}_s + \mathbf{M}_{ss}\ddot{\mathbf{x}}_s = -\mathbf{K}_{sg}\bar{\mathbf{x}}_g \quad (4.4)$$

in which $\bar{\mathbf{x}}_g = \mathbf{x}_g + \beta\dot{\mathbf{x}}_g$ can be regarded as equivalent earthquake displacement input. In convention, the mass matrix \mathbf{M}_{ss} can be determined with accuracy using geometry and material information from design drawings; the mass matrix is thus regarded as known in this study. The objective of system estimation with unknown seismic input here is to identify system parameters, i.e. stiffness and damping coefficient corresponding to \mathbf{K}_{ss} and \mathbf{C}_{ss} , unmeasured system responses as well as unknown input $\bar{\mathbf{x}}_g$ based on known partially measured system responses. The real earthquake displacements, velocities input can be solved as a first order differential equation (4.5) with identified β value,

$$\mathbf{x}_g(t) + \beta \frac{d\dot{\mathbf{x}}_g(t)}{dt} = \bar{\mathbf{x}}_g(t) \quad (4.5)$$

Finally, accelerations could also be obtained by differentiating the displacement or velocity signals.

In order to estimate system parameters and inputs simultaneously, the parameter and input vector can both be augmented into the state vector as

$$\mathbf{X}_a = \begin{bmatrix} \mathbf{x}(t)^T & \dot{\mathbf{x}}(t)^T & \boldsymbol{\theta}^T & \bar{\mathbf{x}}_g^T \end{bmatrix}^T \quad (4.6)$$

In the aforementioned state vector, displacements and velocities are involved into the state vector, the system equation in EKF with the augmented state vector in the situation can be written as follow

$$\frac{d\mathbf{X}_a(t)}{dt} = \frac{d}{dt} \begin{bmatrix} \mathbf{x}(t) \\ \dot{\mathbf{x}}(t) \\ \boldsymbol{\theta} \\ \bar{\mathbf{x}}_g \end{bmatrix} = \begin{bmatrix} \dot{\mathbf{x}}(t) \\ \mathbf{M}_{ss}^{-1} [-\mathbf{K}_{sg}(\boldsymbol{\theta})\bar{\mathbf{x}}_g - \mathbf{K}_{ss}(\boldsymbol{\theta})\mathbf{x}_s - \mathbf{C}_{ss}(\boldsymbol{\theta})\dot{\mathbf{x}}_s] \\ \mathbf{0} \\ \dot{\bar{\mathbf{x}}}_g \end{bmatrix} \quad (4.7)$$

If the system equation in continuous form is transformed into a discrete form, the nonlinear system equation (4.7) can be written as

$$\mathbf{X}_a(k+1) = \mathbf{f}(\mathbf{X}_a(k)) + \mathbf{w}(k) \quad (4.8)$$

In this formula, $\mathbf{w}(k)$ is the process noise vector but represents different meaning for each

component here; i.e. in terms of displacements and velocities, $\mathbf{w}(k)$ stands for model error of the system which is usually treated as uncorrelated zero mean noise as last chapter; in terms of system parameters, they should be zero or some tiny values because only time-invariant parameter estimation is considered in this study; in terms of unknown inputs, it actually represents a random walk model for describing the input signals in discrete form.

$$\bar{\mathbf{x}}_g(k+1) = \bar{\mathbf{x}}_g(k) + \mathbf{w}_g \quad (4.9)$$

Thus \mathbf{w}_g can be understood as dynamic changes of unknown inputs in two consecutive time instants. Usually the variances of them are set as some constant values in computation. Some researchers defined them by L-curve method as in their dynamic load estimation researches [61, 86].

The rest part of EKF formula in this part is the same as last chapter; therefore, it is not repeated here.

4.2.2 Offline process noise adaption method

By assuming some constant value of \mathbf{Q} matrix, the system could be estimated based on that using EKF. Similar to previous study on nonlinear displacement in section 3.2, the estimated results from EKF could be smoothed further using EKS. Based on the smoothed state vector which involves measurement information of all time instants, the \mathbf{Q} matrix can be estimated as

$$\hat{\mathbf{Q}} = 1/(N-1) \sum_{i=1}^{N-1} \mathbf{d}(k+1) \mathbf{d}(k+1)^T \quad (4.10)$$

$$\mathbf{d}(k+1) = \hat{\mathbf{X}}_a(k+1/N) - \mathbf{f}(\hat{\mathbf{X}}_a(k/N)) \quad (4.11)$$

in which $\mathbf{d}(k+1)$ is the so called innovation vector based on the smoothed state vectors of two consecutive time instants. The \mathbf{Q} matrix is further constrained to have a diagonal form, since the process noise is assumed uncorrelated as mentioned above. Besides, the \mathbf{Q} matrix estimated here is only focused on system response variables in the state vector; process noise corresponding parameters and unknown inputs should remain constants due to their meanings discussed earlier. The noise adaption method applied here is similar to the Expectation Maximization (EM) method in [92, 93], of which the formulas are presented below:

$$\hat{\mathbf{Q}} = 1/(N-1) \sum_{i=1}^{N-1} [\mathbf{B}_1(k+1) + \mathbf{B}_3(k+1) - \mathbf{B}_2(k+1) - \mathbf{B}_2^T(k+1)] \quad (4.12)$$

$$\mathbf{B}_1(k+1) = \mathbf{P}(k+1/N) + \hat{\mathbf{X}}_a(k+1/N) \hat{\mathbf{X}}_a^T(k+1/N) \quad (4.13)$$

$$\mathbf{B}_2(k+1) = \mathbf{P}(k+1/N) \mathbf{J}_k^T \mathbf{F}_{\mathbf{X}_a=\hat{\mathbf{X}}_a(k/N)}^T + \hat{\mathbf{X}}_a(k+1/N) \mathbf{f}^T(\hat{\mathbf{X}}_a(k/N)) \quad (4.14)$$

$$\mathbf{B}_3(k+1) = \mathbf{F}_{\mathbf{X}_a=\hat{\mathbf{X}}_a(k/N)} \mathbf{P}(k/N) \mathbf{F}_{\mathbf{X}_a=\hat{\mathbf{X}}_a(k/N)}^T + \mathbf{f}(\hat{\mathbf{X}}_a(k/N)) \mathbf{f}^T(\hat{\mathbf{X}}_a(k/N)) \quad (4.15)$$

in which

$$\mathbf{F}_{\mathbf{X}_a=\hat{\mathbf{X}}_a(k/N)} = \left. \frac{\partial \mathbf{f}(\mathbf{X}_a)}{\partial \mathbf{X}_a} \right|_{\mathbf{X}_a=\hat{\mathbf{X}}_a(k/N)} \quad (4.16)$$

Meanings of other symbols in the equations above are same as previous chapters. In the EM-based method, the innovation vector term $\mathbf{d}(k+1)$ is actually implicitly included in the equations above. Besides that, some auto and cross error covariance matrix terms are also included in the formulas,

which is the main difference from the proposed method. The proposed method can also be regarded as an offline version of the online noise adaption methods in [119, 120], i.e. RM method, which are also based on innovation vectors. Similar to Chapter 2, the R matrix adaption is not considered here.

The estimation process starts with normal EKF as discussed in section 4.2.1 using an assumed constant Q matrix; results from EKF are further smoothed with EKS and the Q matrix is updated based on formula introduced in section 4.2.2; then the updated Q matrix is regarded as known and put into next iteration computation. During the iteration process, process noise corresponding to parameter and input vector should remain unchanged. Specifically, θ is set in Q for parameter vector, while some constant values based on the RMS of displacement on the bottom part of structure are employed for input vector component in Q . The estimation stops when parameter results converge in several consecutive iterations. In this chapter, the total iteration number is defined in advance in a trial and error manner. More than 5 times are recommended. Figure 4.1 shows the flow chart of the adaptive EKF-UI method. It is worth noting that the values corresponding to parameters in the error covariance matrix P remain unchanged at the beginning of each iteration so as to avoid parameters converge to inaccurate values too early.

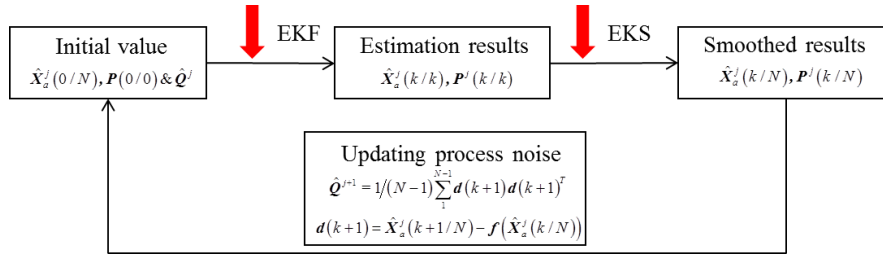


Figure 4.1 flow chart of adaptive EKF-UI method

4.2.3 Acceleration augmented state vector

In most of previous work about KF based system estimation, displacements and velocities are included into state vector, because the EOM is actually a second order differential equation. It is natural to transform it to a state-space model in continuous form where time derivatives of displacement and velocity are velocity and acceleration respectively as shown in equation (4.7). The discrete form of the system equation can be achieved by numerical integration method, e.g. Newmark-beta method or simple Euler method. Additionally, in the discrete form of system equation, accelerations can also be augmented into the state vector using integration method like Wilson-theta method or Generalized-alpha[137] method of which the formula are introduced below,

$$x(k+1) = x(k) + \Delta t \dot{x}(k) + \Delta t^2 \left[(0.5 - \beta_g) \ddot{x}(k) + \beta_g \ddot{x}(k+1) \right] \quad (4.17)$$

$$\dot{x}(k+1) = \dot{x}(k) + \Delta t \left[(1 - \gamma_g) \ddot{x}(k) + \gamma_g \ddot{x}(k+1) \right] \quad (4.18)$$

$$M \ddot{x}_{k+1-\alpha_m} + C \dot{x}_{k+1-\alpha_f} + K x_{k+1-\alpha_f} = F(t_{k+1-\alpha_f}) \quad (4.19)$$

where

$$x_{k+1-\alpha_f} = (1 - \alpha_f) x(k+1) + \alpha_f x(k) \quad (4.20)$$

$$\dot{x}_{k+1-\alpha_f} = (1 - \alpha_f) \dot{x}(k+1) + \alpha_f \dot{x}(k) \quad (4.21)$$

$$\ddot{x}_{k+1-\alpha_m} = (1 - \alpha_m) \ddot{x}(k+1) + \alpha_m \ddot{x}(k) \quad (4.22)$$

$$t_{k+1-\alpha_f} = (1 - \alpha_f) t(k+1) + \alpha_f t(k) \quad (4.23)$$

in the above formula, Δt is time interval; $\beta_g, \gamma_g, \alpha_f$ and α_m are computation parameters of the algorithms, the integration scheme becomes unconditionally stable and second-order accurate when the parameters are calculated as

$$\alpha_m = \frac{2\rho - 1}{\rho + 1} \quad \alpha_f = \frac{\rho}{\rho + 1} \quad (4.24)$$

$$\beta_g = 0.25(1 - \alpha_m + \alpha_f)^2 \quad \gamma_g = 0.5 - \alpha_m + \alpha_f \quad (4.25)$$

in which $0 < \rho < 1$. Considering zero-hold order assumption for external force \mathbf{F} , the above numerical integration algorithms can be transformed into discrete state space model as below,

$$\begin{bmatrix} \mathbf{x}(k+1) \\ \dot{\mathbf{x}}(k+1) \\ \ddot{\mathbf{x}}(k+1) \end{bmatrix} = \begin{bmatrix} \mathbf{I} & \Delta t \mathbf{I} & \Delta t^2(0.5 - \beta_g) \mathbf{I} \\ \mathbf{0} & \mathbf{I} & \Delta t(1 - \gamma_g) \mathbf{I} \\ \mathbf{0} & \mathbf{0} & \mathbf{0} \end{bmatrix} + \begin{bmatrix} \Delta t^2 \beta_g \mathbf{I} \\ \Delta t \gamma_g \mathbf{I} \\ \mathbf{I} \end{bmatrix} \mathbf{L} \begin{bmatrix} \mathbf{x}(k) \\ \dot{\mathbf{x}}(k) \\ \ddot{\mathbf{x}}(k) \end{bmatrix} + \begin{bmatrix} \Delta t^2 \beta_g \mathbf{I} \\ \Delta t \gamma_g \mathbf{I} \\ \mathbf{I} \end{bmatrix} \mathbf{M}_d^{-1} \mathbf{F}(k) \quad (4.26)$$

in which \mathbf{I} is the unity matrix, \mathbf{M}_d and \mathbf{L} matrix are defined as below

$$\mathbf{M}_d = (1 - \alpha_m) \mathbf{M} + (1 - \alpha_f) \gamma_g \Delta t \mathbf{C} + (1 - \alpha_f) \beta_g \Delta t^2 \mathbf{K} \quad (4.27)$$

$$\mathbf{L} = \mathbf{M}_d^{-1} \begin{bmatrix} -\mathbf{K} & -(1 - \alpha_f) \Delta t \mathbf{K} - \mathbf{C} & \mathbf{M}_d - \mathbf{M} - (1 - \alpha_f) \Delta t \mathbf{C} - 0.5(1 - \alpha_f) \Delta t^2 \mathbf{K} \end{bmatrix} \quad (4.28)$$

With the acceleration-augmented state vector, accelerations become linear observations in KF rather than nonlinear ones in normal state vector cases. The similar type of state vector was also used in Lee et al [126] for parameter identification with known input based on Wilson-theta method. The acceleration-augmented state vector will be employed in the following part of the study without particular notation. In fact, the acceleration-augmented state vector could also be employed to the study of last chapter as an alternative of the standard state vector, but since no stability problem occurs there, the advantage of the state vector is not clear.

4.2.4 Discussion about observability of joint-input-state-parameter estimation problem

Observability is an important concept in KF based system estimation. A system is observable when system state variables can be uniquely defined by measured output information. In terms of time-invariant linear system, it was well explored in [138]. Its nonlinear counterpart, i.e. system estimation including parameter estimation, was also studied widely in [139-141]. In this section, A SDOF system is firstly used to discuss the observability problem of system estimation with unknown seismic excitations. After simple algebra manipulation, the EOM of SDOF can be written as

$$c\dot{x} + m\ddot{x} = k(\bar{x}_g - x) \quad (4.29)$$

Suppose damping and mass are known and all responses are measured for the system, the left hand side of above equation is totally known. However, in this case the right hand of the equation is still indistinguishable because unknown stiffness k and input \bar{x}_g are presented in a product form. Each arbitrary k value can correspond to an input signal, for example, if k is estimated as αk , the

corresponding input is $1/\alpha \bar{x}_g + (1-1/\alpha)x$. Therefore, the uniqueness of solution is lost. The basic idea can be extended to multi-story like structure because substructure of each floor can be regarded as a SDOF system [142].

Additionally, displacement or displacement-like signals, e.g. strain, have to be measured to ensure the observability condition. Taking example of the SDOF system as well but with known system parameters, if only acceleration is measured, $(x', \bar{x}'_g) = (x + a, \bar{x}_g + a)$ are also the solution satisfying Eq.(4.29). Here a is an arbitrary constant. However, they will be shown as some low frequency divergence in estimated signals when measured acceleration is noisy. A comprehensive study about the observability problem of dynamic load estimation can be found in [62]. Basically, the number of displacement or displacement-like measurements should not be less than the number of unknown inputs.

For the theoretical observability analysis of nonlinear system with unknown input, to the best knowledge of the author, problems still exist, even though some researchers gave their method [81, 132]. The observability of parameters and inputs are analyzed separately based on a dual UKF in [81]. Based on the method, the SDOF system with unknown input could be observable with only one acceleration measurement, which of course is not the real case. While based on the method proposed in [80], the observable condition could only be achieved with displacement measurements even in known input condition. It is not true either, because the system is observable when acceleration and input are measured like most of the joint state-parameter estimation problems. Considering the discussion above and combining experience in following numerical simulations, at least two measurement points are required for structural element directly connecting ground in this study. Displacement measurements have to be included. In practice, accelerometers are mostly commonly used sensors, dynamic displacement and velocity, if not measured directly, can be obtained by integrating measured accelerations and conducting proper high-pass filter in sequence. In fact, in order to obtain accurate and consistent parameter estimation results, especially stiffness, displacements are recommended to be included in observation as reported by Chatzi et al [40].

4.3 Numerical verification of adaptive EKF-UI method

In this section, the effectiveness of the proposed EKF-UI method is demonstrated with two numerical models simplified from experimental models in E-defense database [102, 103], i.e. a full scale bridge pier model and a 2D four story frame structure model. In order to reproduce the conditions in practical engineering, all displacement measurements are obtained as the double integrated ones from noisy acceleration signals. Nonlinear residual displacement is out of scope in this study. In the first numerical example, the exact accurate system model will be used; the second numerical example is also exact accurate but possesses large DOFs; inaccurate system model will be applied in the third numerical example.

4.3.1 A bridge pier model case

This model is the beam model already employed in 2.5.2, i.e. C1-1 experiment in E-defense shaking table laboratory, as shown in the Figure 4.2. The geometric and mass information about the model is exactly same as that used in section 2.5.2. Except that, 0~6m part of pier is assumed with 3 same FEM beam elements with an EI value equal to 4.55×10^9 here. The damping effect is considered by Rayleigh damping stiffness coefficient $\beta=0.02$. In summary, 6 DOFs are included into the model ignoring axial deformations; a uniform EI , damping coefficient β as well as unknown earthquake input are to be identified in this simulation.

The forward analysis is conducted using Generalized-alpha method with $\rho=1/6$ and time sample equals to 0.005s. Takatori earthquake displacement and velocity shown in Figure 4.3 are treated as

excitations. White noise process whose root-mean-square (RMS) is 3% of signals' RMS are added. Double integrated displacement signals of the three translational DOFs as well as corresponding accelerations, as shown in Figure 4.4(a), are firstly employed. The process noise for displacement, velocity and unknown input are set as 10^{-6} , 10^{-4} and 10^{-4} , namely $\mathbf{Q} = \text{diag}([10^{-6}\mathbf{I}, 10^{-4}\mathbf{I}, 10^{-2}\mathbf{I}, \mathbf{0}, 10^{-4}\mathbf{I}])$. The process noise of displacement and velocity here is intentionally set as relatively large values so that the capability of noise adaption of the proposed method could be presented. The \mathbf{R} matrix is set as $\text{diag}([10^{-6}\mathbf{I}_{3 \times 1}, 5 \times 10^{-4}\mathbf{I}_{3 \times 1}])$. As a matter of fact, since the system model in filter is same as the model for forward analysis in the simulation, process noise should be some tiny values. The filter starts working with initial parameter values as $1.5\theta_{real}$ and error covariance matrix as $\text{diag}([0.1\theta_{real}]^2)$. The period of estimation is shown in Figure 4.3(a) specifically.

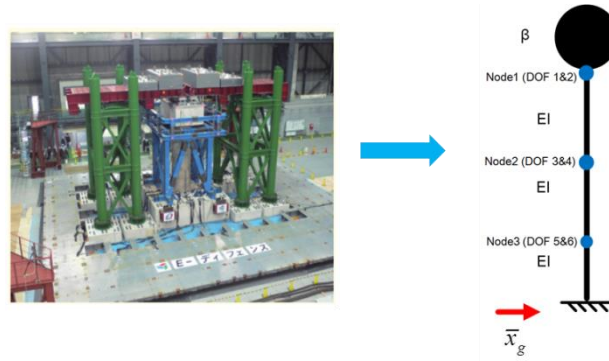


Figure 4.2 simplified bridge pier model

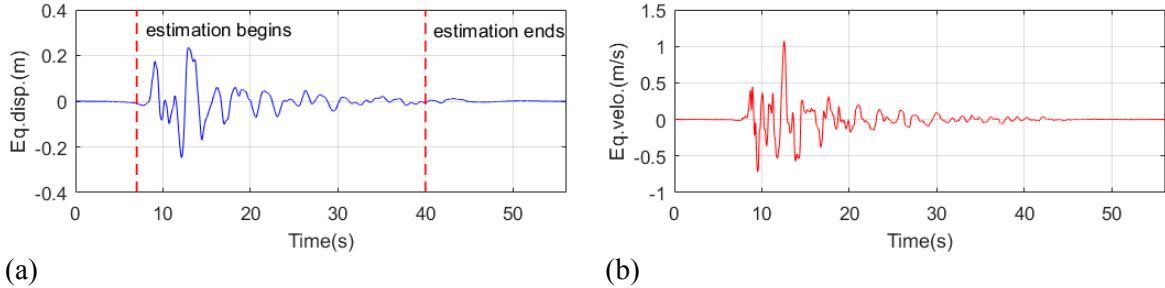


Figure 4.3 Takatori earthquake; (a) displacement input; (b) velocity input

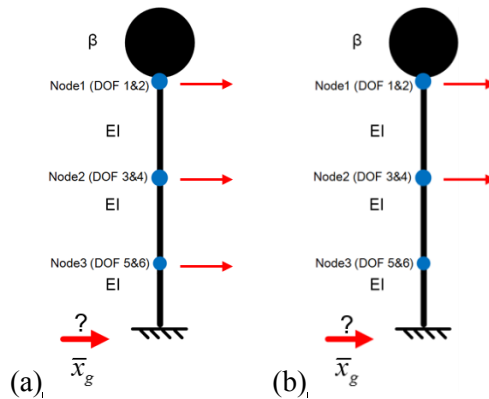


Figure 4.4 measurement scheme; (a) 3-DOF case; (b) 2-DOF case;

In this case, 9 iterations are employed and the parameter identification results at each iteration are shown in Figure 4.5. By applying the adaptive EKF-UI method, parameters converge to real values after about 5 iterations in this case, while parameters of the 1st iteration converge to incorrect

values because inappropriate \mathbf{Q} matrix is applied. Figure 4.6 shows the parameter identification history at the last iteration, it can be observed the identified parameters almost coincide with the true values except some fluctuations occur during the very initial time. This is due to the large error covariance of parameters ($\text{diag}([0.1\theta_{real}]^2)$) at the beginning of each iteration.

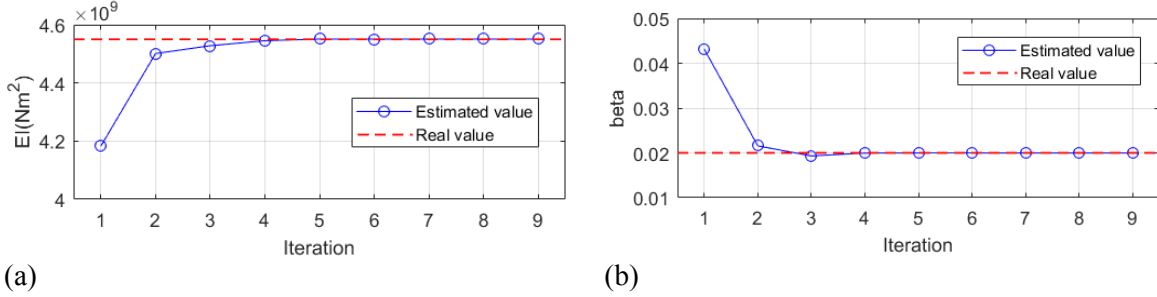


Figure 4.5 parameter identification at each iteration using 3-DOF measurement; (a) EI ; (b) β

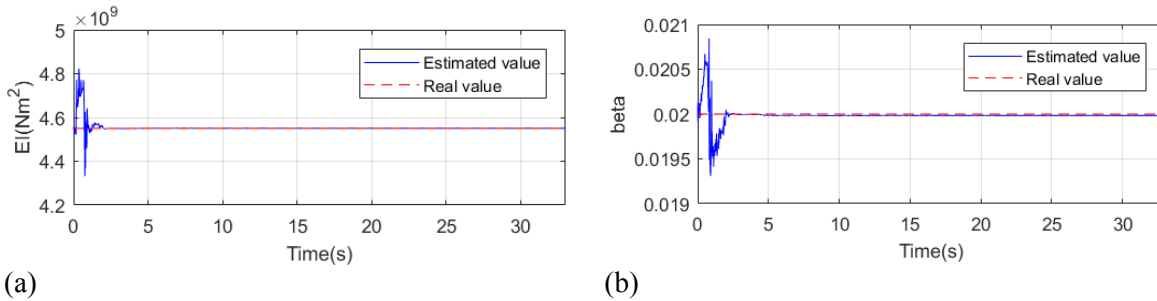


Figure 4.6 parameter convergence at the last iteration using 3-DOF measurement; (a) EI ; (b) β

Figure 4.7 shows the displacement process noise adapted using the proposed method. In this case, after 5 iterations, the adapted process noises also become stable corresponding to the convergence of parameters. Obviously, the adaptive EKF-UI method possesses robust ability to find appropriate process noise value automatically. Figure 4.8 shows the comparison of estimated earthquake signals and real ones. The smoothed earthquake displacement is presented here along with the acceleration, i.e. double derivative of displacement. Both signals coincide with real ones well indicating the effectiveness of the proposed method.

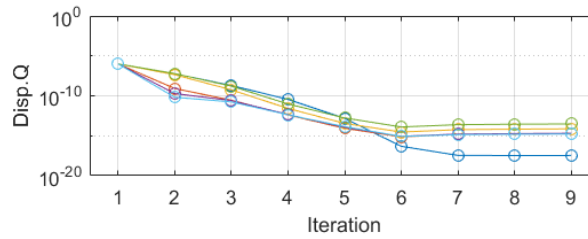


Figure 4.7 displacement process noise at each iteration

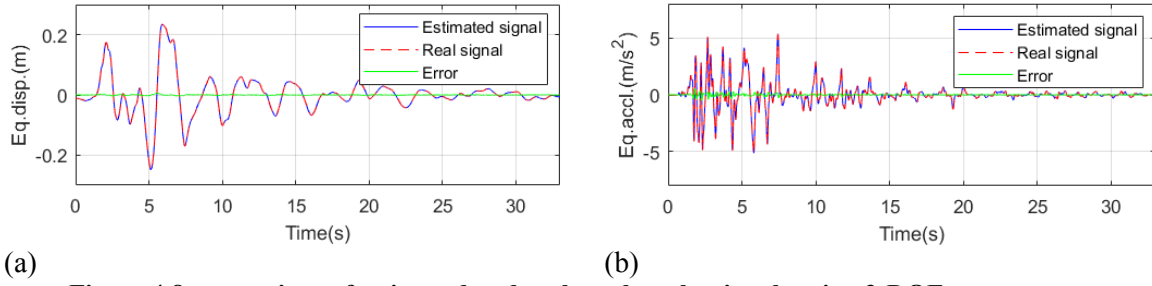


Figure 4.8 comparison of estimated and real earthquake signals using 3-DOF measurement; (a) displacement; (b) acceleration

In the second place, the measurement scheme containing only top two translational DOFs, as shown in Figure 4.4(b), is also considered here. Corresponding double integrated displacement and accelerations are set as observation variables here; other computation information is the same as previous case. Figure 4.9 compares the results at each iteration based on two measurement scheme. By using the 2-DOF measurement scheme, convergence of parameters, especially stiffness, is slower than the previous case, i.e. EI convergences after around 6 iterations. Since earthquake input can be regarded as equivalent loads exerting on NO.3 node, without measurement on the DOFs, the input estimation becomes more difficult than previous case which further influences the convergence of parameters. However, if those methods [71-73, 81, 82] based on direct feedback of accelerations are applied here, the problem cannot be solved because corresponding gain matrix for load estimation is singular. Figure 4.10 shows the estimated earthquake displacement and corresponding acceleration, good coincidence is still observed in the case.

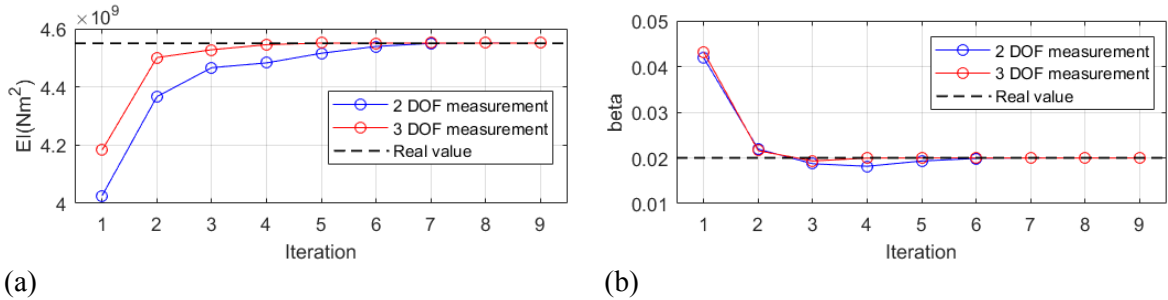


Figure 4.9 comparison of parameter identification results at each iteration; (a) EI ; (b) β

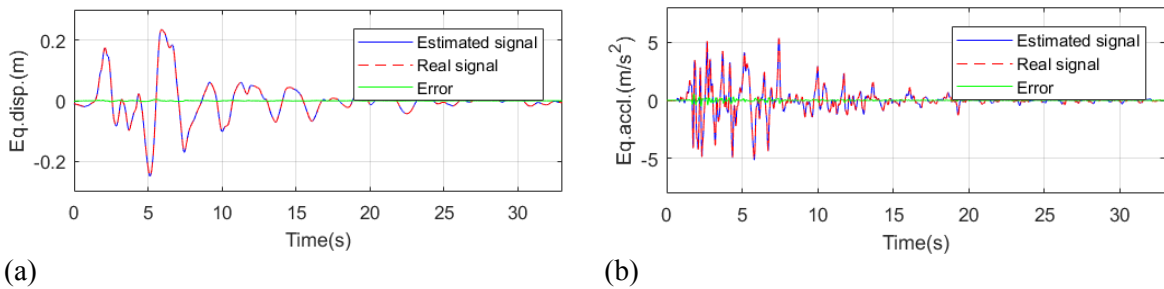


Figure 4.10 comparison of estimated and real earthquake signals using 2-DOF measurement; (a) displacement; (b) acceleration

As discussed in section 4.2.2, the proposed offline process noise adaption method starts from some empirically set \mathbf{Q} matrix initially. In order to investigate the sensitivity to the initial \mathbf{Q} matrix, identifications are conduct from three different \mathbf{Q} matrix, i.e. $\mathbf{Q}_I = \text{diag}([10^{-5}\mathbf{I}, 10^{-3}\mathbf{I}, 10^{-1}\mathbf{I}, 0, 10^{-4}\mathbf{I}])$,

$\mathbf{Q}_2 = \text{diag}([10^{-6}\mathbf{I}, 10^{-4}\mathbf{I}, 10^{-2}\mathbf{I}, \mathbf{0}, 10^{-4}\mathbf{I}])$, $\mathbf{Q}_3 = \text{diag}([10^{-7}\mathbf{I}, 10^{-5}\mathbf{I}, 10^{-3}\mathbf{I}, \mathbf{0}, 10^{-4}\mathbf{I}])$. They are based on the bridge pier model using the 3-DOF measurement scheme; other computation information remain unchanged. The identification results at each iteration are presented in Figure 4.11. All of three cases converge to accurate parameters after about 4 iterations, which reflects the sensitivity to initial \mathbf{Q} matrix is not significant. With the \mathbf{Q} becoming smaller which is closer to real \mathbf{Q} matrix, the convergences become faster, e.g. the identified parameters based on \mathbf{Q}_3 almost reach to the true parameter values at the first iteration.

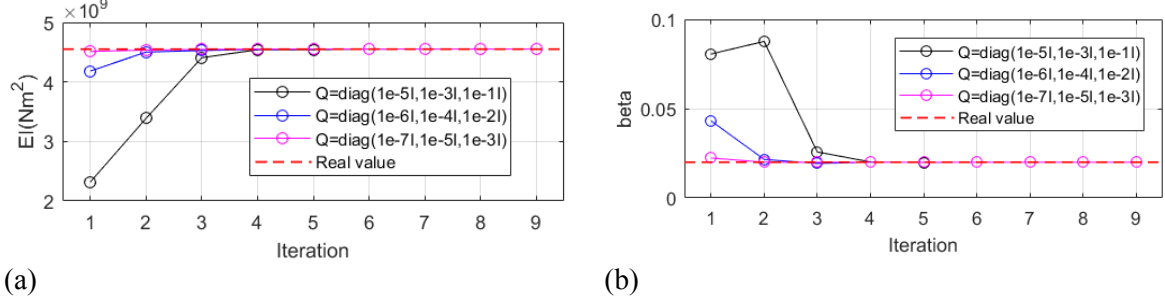


Figure 4.11 parameter identification at each iteration using 3-DOF measurement scheme from different initial \mathbf{Q} matrices; (a) EI ; (b) β

For comparison, the identification is also conducted in this case using the stable mode of EKF-RM method proposed in Chapter 2. Similarly, the unknown input is augmented into the state vector and Generalized-alpha method is applied in system equation. In this case, the RM method is used to adapt the \mathbf{Q} matrix in an online manner rather than the offline method proposed here. Figure 4.12 shows the parameter results comparison between the two methods. The 3-DOF measurement scheme is used here. It can be found that based on the EKF-RM method accurate parameter values cannot be obtained. Using EKF-RM method, the estimated earthquake acceleration signals shown in Figure 4.13 are noisier than its counterpart in Figure 4.10. Due to the relatively poor performance of EKF-RM method it cannot estimate process noise correctly in the case of unknown input, i.e. the process noise in Figure 4.8(b) is much larger than that in Figure 4.7.

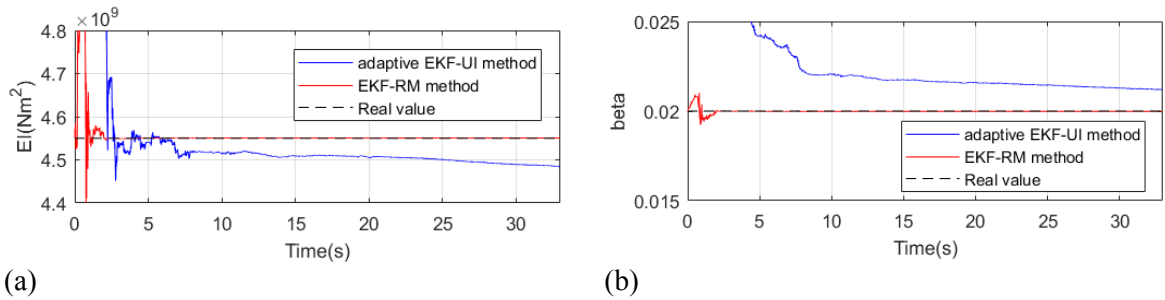


Figure 4.12 comparison between adaptive EKF-UI and EKF-RM method; (a) EI ; (b) β

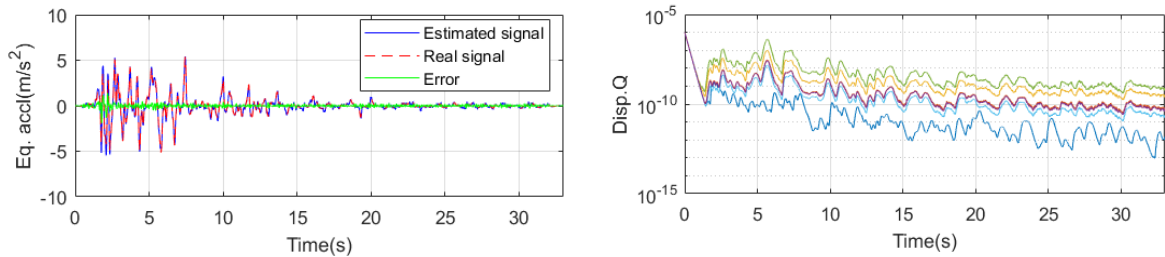


Figure 4.13 using EKF-RM method (a) estimated earthquake acceleration; (b) estimated displacement process noise of 6 DOFs

In the previous cases, the acceleration-augmented state vector based on Generalized-alpha method is used. For comparison, the parameters are identified using the normal state vector based on Newmark-beta method and the 2-DOF measurement scheme here. The forward simulation is also conduct using Newmark-beta method in this case. Unfortunately, the computation diverges at the first iteration. The parameter and the input estimation histories are shown in Figure 4.14 and Figure 4.15 respectively. This problem is discussed here taking example of the bridge pier model as well. When the normal state vector method is employed, estimated acceleration is actually calculated based on EOM, i.e. $\ddot{x}(k) = \mathbf{M}^{-1}[\mathbf{F}(k) - \mathbf{C}\dot{x}(k) - \mathbf{K}x(k)]$. For distributed mass system, e.g. beam element, tiny errors e of displacements could result in large error of stiffness force, i.e. $\mathbf{K}e$; errors of accelerations due to it will be further enlarged when magnitude of \mathbf{M} matrix is much smaller than \mathbf{K} matrix, e.g. in this case the magnitude of \mathbf{K} is 10^4 times larger than that of \mathbf{M} . Suppose white noises corresponding to 1% of signals' RMS are added on the relative displacements and all of other system values are corrects, Figure 4.16 shows the comparisons of accelerations calculated based on the real and noisy displacements in one arbitrary time instant (9.0s). It can be observed that the differences in real and noisy displacements are negligible at all DOFs; however, the calculated accelerations based on them differ from each other significantly which will present as some consecutive high frequency fluctuations in time domain. For normal state vector case, since accelerations are actually calculated in system equation stage, the instability makes filter prone to diverge. By using the Generalized-alpha method, EOM is not strictly established on each time instant point as seen in equation (4.19), and it introduces numerical damping to suppress those high-frequency fluctuations. Therefore, filter divergence could be avoided.

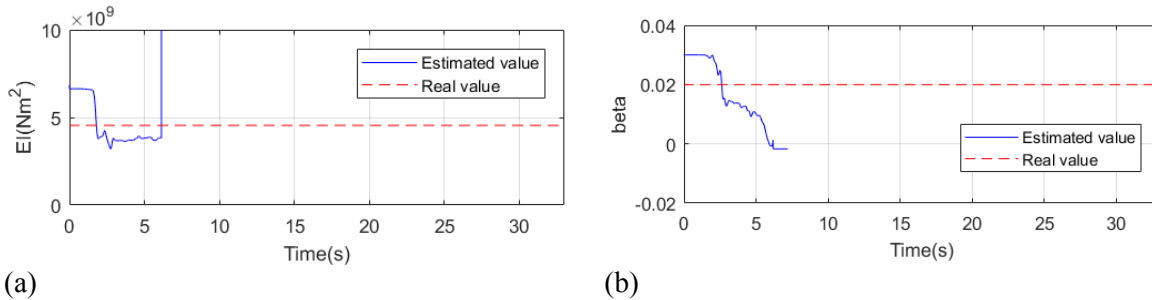


Figure 4.14 parameter estimation history using 2-DOF measurement based on normal Newmark-beta state vector; (a) EI ; (b) β

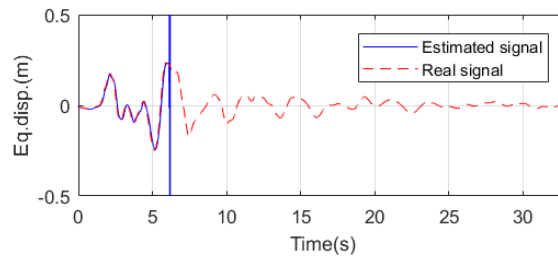


Figure 4.15 estimated earthquake displacement using 2-DOF measurement based on normal Newmark-beta state vector

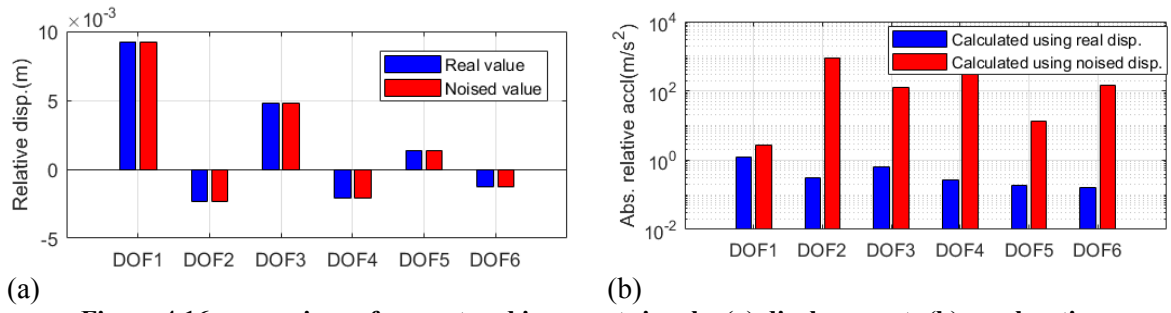


Figure 4.16 comparison of correct and incorrect signals; (a) displacement; (b) acceleration

4.3.2 A 2D four story frame structure case

The 2D four story frame structure model employed in section 2.5.2 is studied here. NS direction of the prototype building is extracted and simplified into a 2D FEM model as shown in Figure 4.17 (b). A half structure is employed here in order to reduce computation burdens. Cross section stiffness EI of columns on each floor and stiffness damping coefficient β are unknown parameters to be identified. Except these parameters, other structural parameters, e.g. floor beam EI , axial stiffness EA and mass information, are regarded as known values based on design drawings of the experiment model. Both of them are listed in Table 4.1. The true stiffness EI of each floor column is $1.141 \times 10^8 \text{ Nm}^2$; β equals to 0.01; the equivalent concentration mass for each floor are 49.1, 34.2, 38.7, and 68.4 ton from bottom to top. The mass values applied here are the adjusted ones used in section 2.5.2.

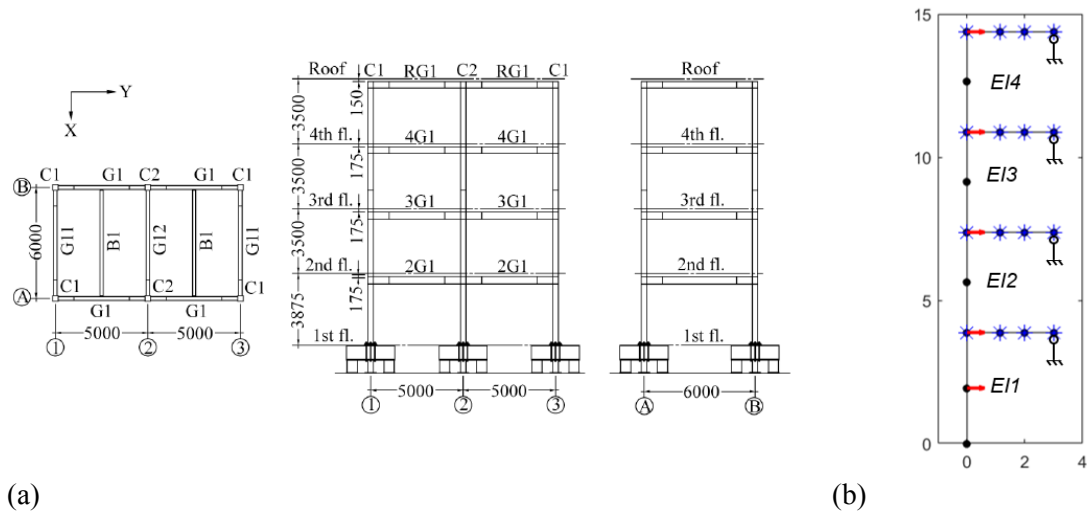


Figure 4.17 (a) frame structure of four story building model; (b) simplified FEM model

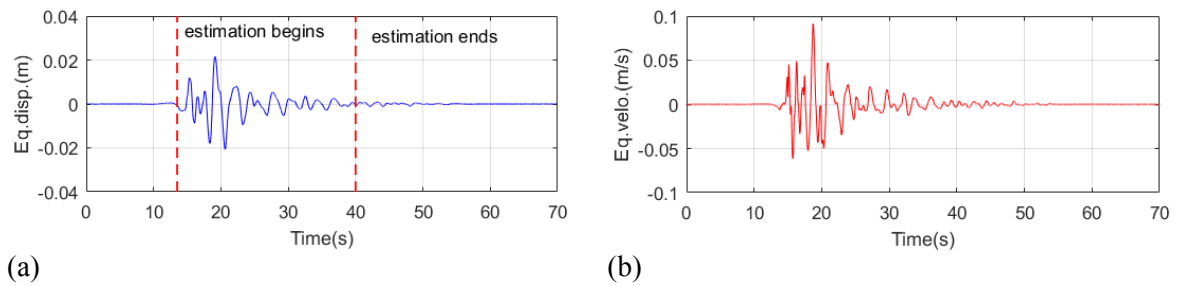


Figure 4.18 earthquake input; (a) displacement; (b) velocity

Table 4.1 system parameter values of 2D FEM model

	E (N/m ²)	I (m ⁴)	A (m ²)	* C_{mass} (kg)
Column of. the 1 st floor	2.06×10^{11}	0.000554	0.0398	N.A
Beam of the 1 st floor		0.0011	0.0250	6844
Column of the 2 nd floor	ρ (kg/m ³)	0.000554	0.0398	N.A
Beam of the 2 nd floor	7800	0.0011	0.0250	4710
Column of. the 3 rd floor		0.000554	0.0398	N.A
Beam of the 3 rd floor	β	0.0011	0.0189	5401
Column of roof floor	0.01	0.000554	0.0398	N.A
Beam of roof floor		0.0011	0.0157	9735

Firstly, signals are generated using Generalized-alpha method with the same computation parameters as last case. The earthquake input signals used here are shown in Figure 4.18. White noise whose RMS are 3% of signals' RMS are added to accelerations while displacements are double integrated based on them. The collocated displacement and acceleration measurements are represented as red arrows in Figure 4.17(b), where two measurement points locates on the first floor based on the principle discussed in section 4.2.4 and one on each of other floors. The initial process noise covariance matrix is set as $\mathbf{Q} = \text{diag}([10^{-6}\mathbf{I}, 10^{-4}\mathbf{I}, 10^{-2}\mathbf{I}, \mathbf{0}, 10^{-5}\mathbf{I}])$; the \mathbf{R} matrix is set as $\text{diag}([10^{-8}\mathbf{I}_{4 \times 1}, 10^{-6}\mathbf{I}_{4 \times 1}])$. $1.5\theta_{real}$ and $\text{diag}([0.1\theta_{real}]^2)$ are for initial parameter vector and error covariance values.

Figure 4.19 shows the parameter estimation results at each iteration. It can be observed that the parameter values converge after about 3 iterations here; the estimated values show good accuracy with respect to true ones as shown in Figure 4.19(b), i.e. the errors are less than 0.5%. Also, the estimated earthquake acceleration coincides with real signal well which is shown in Figure 4.20(b). Along with that, the adapted displacement process noise at each iteration is shown in Figure 4.20(a).

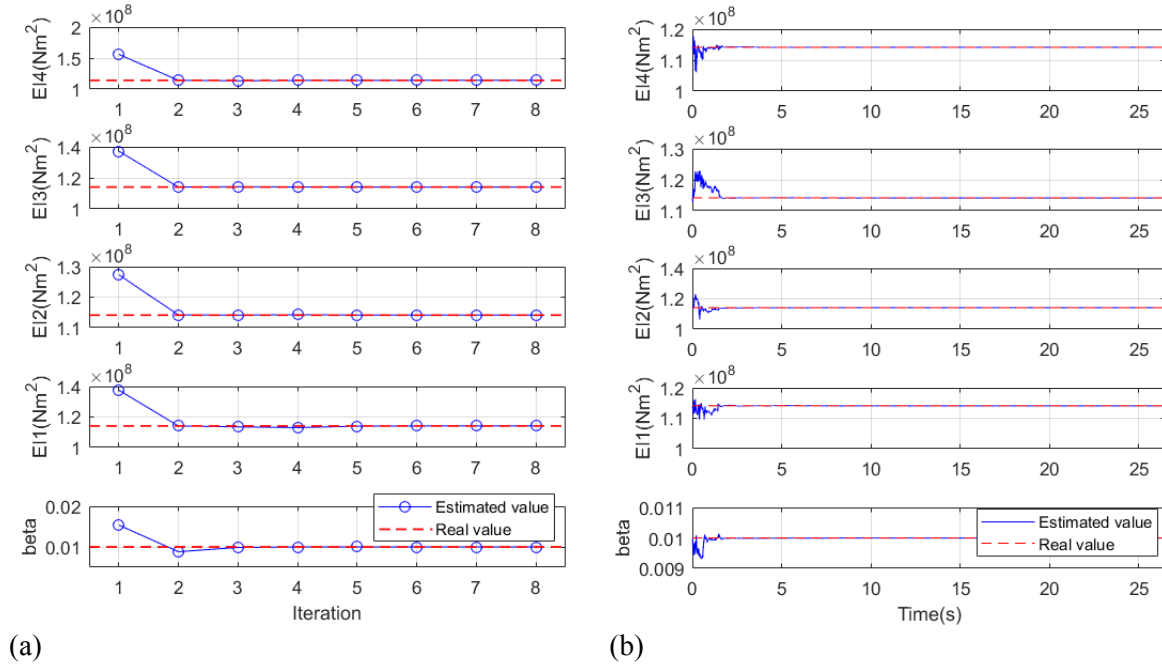


Figure 4.19 identification results of 2D frame structure model;
(a) parameter results at each iteration; (b) parameter convergence at last iteration

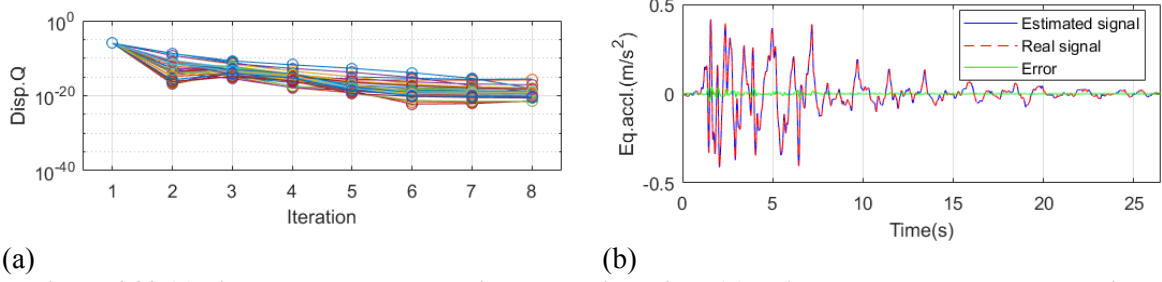


Figure 4.20 (a) displacement process noise at each iteration; (b) estimated earthquake acceleration

Similar to previous numerical case, the sensitivity of initial \mathbf{Q} matrix is also studied here based on the four story building model. $\mathbf{Q}_1 = \text{diag}([10^{-5}\mathbf{I}, 10^{-3}\mathbf{I}, 10^{-1}\mathbf{I}, \mathbf{0}, 10^{-4}\mathbf{I}])$, $\mathbf{Q}_2 = \text{diag}([10^{-6}\mathbf{I}, 10^{-4}\mathbf{I}, 10^{-2}\mathbf{I}, \mathbf{0}, 10^{-4}\mathbf{I}])$, $\mathbf{Q}_3 = \text{diag}([10^{-7}\mathbf{I}, 10^{-5}\mathbf{I}, 10^{-3}\mathbf{I}, \mathbf{0}, 10^{-4}\mathbf{I}])$ are used here for the initial \mathbf{Q} matrices, and other computation information remain unchanged. The identified $EI4$ and β values at each iteration are shown in Figure 4.21. Clearly, even with the three different initial \mathbf{Q} matrices, based on the proposed method, accurate parameters are identified after about 3 iterations.

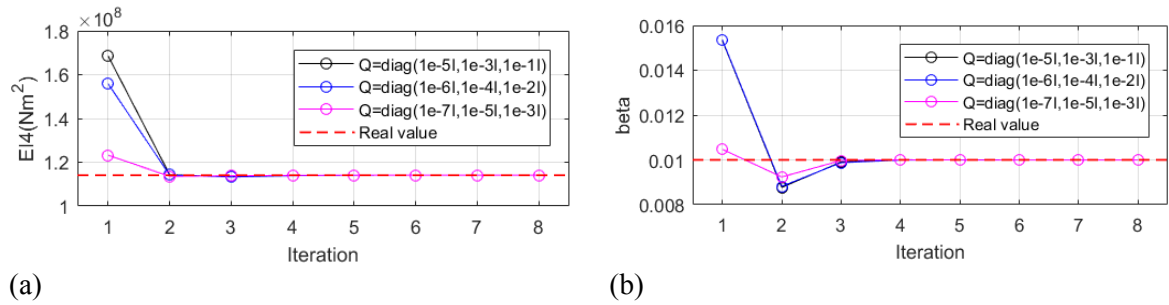


Figure 4.21 parameter identification at each iteration from different initial \mathbf{Q} matrices; (a) $EI4$; (b) β

Finally, in this section, a more complex numerical case is considered in which the Rayleigh mass damping factor $\alpha=0.3$ is involved. The damping ratios of the first two modes of the four story building model in this case are $\zeta_1=0.058$ and $\zeta_2=0.132$ respectively. Consequently, in forward simulation, the input term in equation (4.2) is actually $-\mathbf{K}_{sg}\mathbf{x}_g - \beta\mathbf{K}_{sg}\dot{\mathbf{x}}_g - \alpha\mathbf{M}_{sg}\dot{\mathbf{x}}_g$, i.e. the mass damping term is included. During the estimation, however, the unknown input is still estimated as $\mathbf{x}_g + \beta\dot{\mathbf{x}}_g$. The initial process noise covariance matrix is set as $\mathbf{Q} = \text{diag}([10^{-6}\mathbf{I}, 10^{-4}\mathbf{I}, 10^{-2}\mathbf{I}, \mathbf{0}, 10^{-5}\mathbf{I}])$, and other computation information remain unchanged. The identified parameter and input results are shown in Figure 4.22 and Figure 4.23 respectively. Good accuracies are obtained.

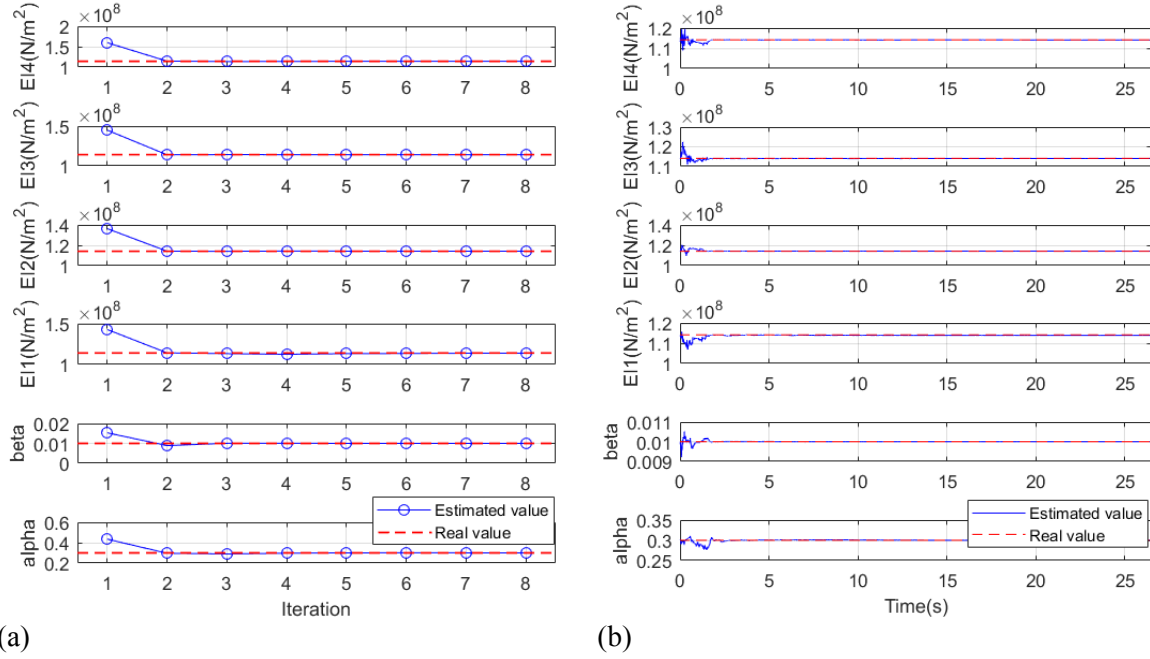


Figure 4.22 identification results of 2D frame structure model with damping factor α ;
(a) parameter results at each iteration; (b) parameter convergence at last iteration

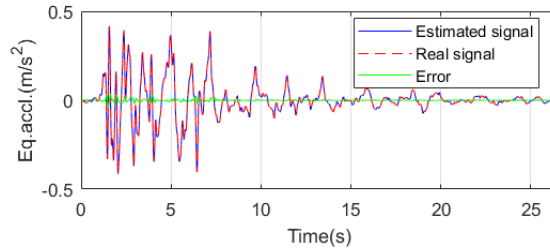


Figure 4.23 estimated earthquake acceleration for 2D frame structure model with damping factor α

As mentioned earlier, w_g , i.e. process noises corresponding to inputs, were defined based on a L-curve method in previous research [61, 86]. In the L-curve method, w_g of values with different magnitudes are tried; the one corresponding to tiny mean-square value of signal estimation errors is chosen to be appropriate w_g values, which actually locate in a wide range. In this study, since the earthquake displacement input is analogous to structural translational displacement in its bottom part, the root mean square (RMS) of latter ones can be good references for selection of w_g . Values comparable to RMS of displacement responses are reasonable. For example, in the bridge pier numerical case, RMS of translation displacement is about 0.05m and w_g equals to 0.01m is employed; in the four story building numerical case, RMS of translation displacement is about 0.004m and w_g equals to 0.003m is employed.

4.3.3 Bridge pier model of variant cross section stiffness with foundation

In the previous two numerical simulations, accurate system models are employed in the filter. However, in practical engineering, the assumed system model in filter is not exactly same as real physical model. In order to check the performance of the proposed method with respect to inaccurate system model, a more complex and realistic bridge pier model based on the one in section 4.3.1 is considered as shown in Figure 4.24. The cross section stiffness EI values are $1.2 \times 4.55 \times 10^9$ Nm²,

$1.0 \times 4.55 \times 10^9 \text{ Nm}^2$ and $0.5 \times 4.55 \times 10^9 \text{ Nm}^2$ from top to bottom element in order to consider damage occurring in the bottom of pier; β equals to 0.02. Additionally, a sway-rocking (SR) model based foundation is also included in the model. In terms of the SR model, the stiffness, damping and mass matrix are $[1.8 \times 10^9, 4.6 \times 10^9; 4.6 \times 10^9, 9.7 \times 10^{10}]$, $[6.36 \times 10^7, 9.9 \times 10^7; 9.9 \times 10^7, 5.94 \times 10^8]$ and $\text{diag}([6.12 \times 10^5, 2.82 \times 10^6])$, respectively. The SR model value is calculated based on a concrete pile foundation and geological data of a real bridge structure. The basic geometrical information of the concrete pile foundation is shown in Figure 4.25. The material information employed for the SR model computation is listed in Table 4.2 while the computation method of the SR model is presented in Appendix B. The symbols in Table 4.2 represent the same meanings as Table 2.15.

System model which is same as that of section 4.3.1 is still applied here, i.e. an equivalent uniform EI is expected to be identified. The measurement scheme includes accelerations at DOF 1 and 5 as well as corresponding double integrated displacements which is shown in Figure 4.24.

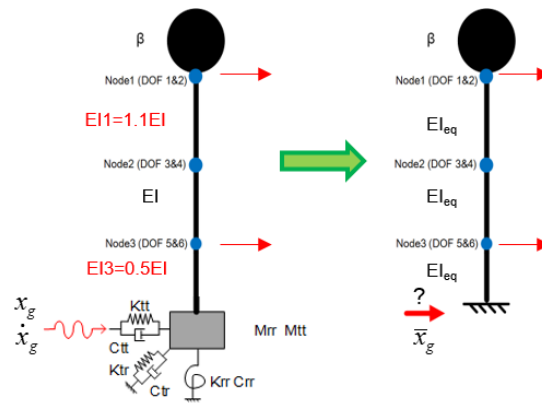


Figure 4.24 bridge pier model with variant EI and substructure

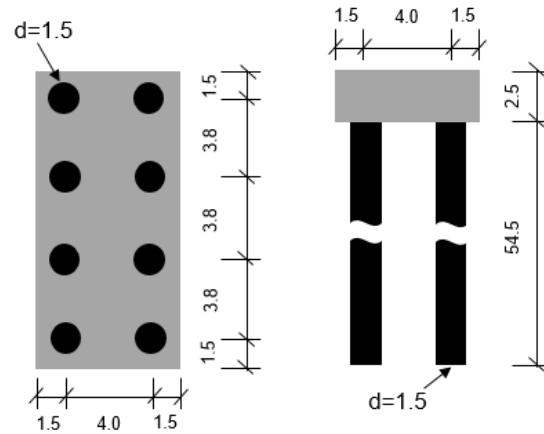


Figure 4.25 plan and side view of pile foundation (unit:m)

Table 4.2 material information for SR model computation

Soil properties				
Layer(m)	$\rho(\text{kg/m}^3)$	ν	$C_s(\text{m/s})$	β
0~5.92	1735	0.40	168	0.05
-5.92~-9.72	1735	0.40	145	0.05
-9.72~-37.47	1633	0.40	159	0.05
-37.47~-39.27	1735	0.40	161	0.05
-39.27~-52.57	1633	0.40	191	0.05

-52.57~-54.50	1735	0.40	294	0.05
Concrete properties				
$E_c(\text{Nm}^2)$	3×10^{10}	$\rho_c(\text{kg/m}^3)$	2500	

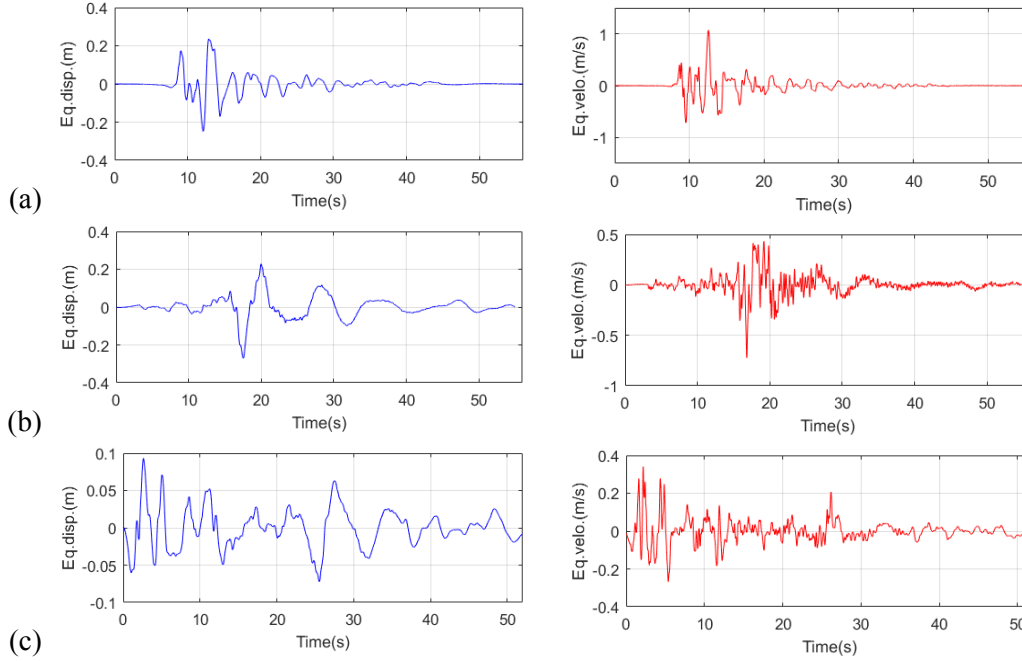


Figure 4.26 earthquake inputs; (a) Takatori; (b) JMA; (c) El centro

As discussed in Chapter 2, consistent results of identified parameters are helpful in practical engineering; if the identified parameters of same structure show large scattering characteristic under different excitations, assessment of structural damage condition will become confusing and difficult. Three different earthquake inputs, including Takatori, JMA and El centro earthquake as shown in Figure 4.26, are considered in the numerical example to confirm the consistency of the identified results. Figure 4.27 and Figure 4.28 show the parameter and earthquake acceleration identification results respectively using the proposed method. It can be found that the parameters in the three excitation cases all converged to the similar values after 4 iterations, i.e. EI equals to around 2.98×10^9 while β equals to 0.02.

Here, the parameters are also identified considering known earthquake inputs based on EKF-RM method, which are plotted as black dashed lines in Figure 4.27. The difference of stiffness value is about 5% while damping values are close to each other. It is natural since the system model employed here is inaccurate; in fact, the earthquake inputs estimated also show observable discrepancies with respect to real signals, as green lines in Figure 4.28.

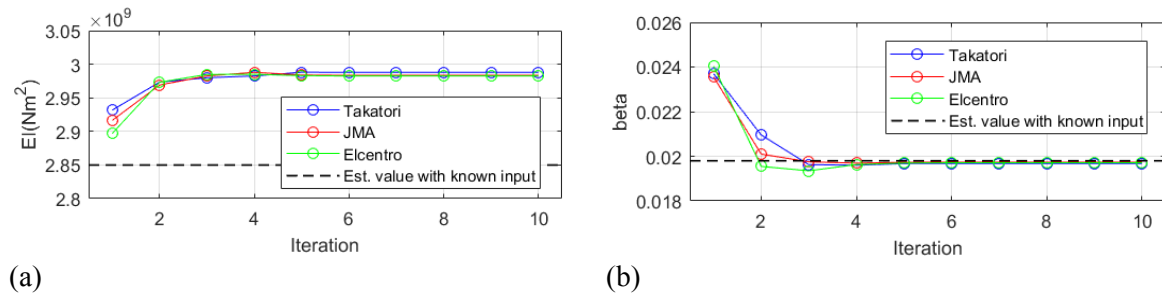


Figure 4.27 comparison of parameter identification results under different earthquake inputs;

(a) EI ; (b) β

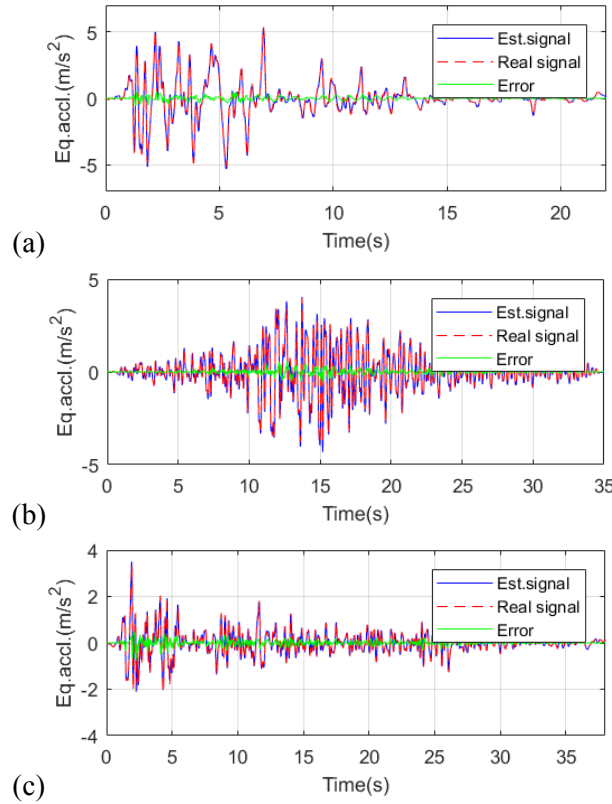


Figure 4.28 estimated earthquake accelerations; (a) Takatori; (b) JMA; (c) El centro

For comparison, assuming the bridge pier is in healthy condition and EI value of it is $1.2 \times 4.55 \times 10^9 \text{ Nm}^2$ uniformly; the parameters are identified with unknown input here again. The results are shown in Figure 4.29. Similarly, consistent parameter results are obtained under different input excitations, i.e. EI equals to 5.41×10^9 while β equals to 0.02. The values are close to the real ones of the structure. Comparing the results in Figure 4.27 and Figure 4.29, the variation of identified EI value is evident. Therefore, even though identification discrepancies exist between unknown and known input cases, structural damage is still reflected by identified parameters with unknown input.

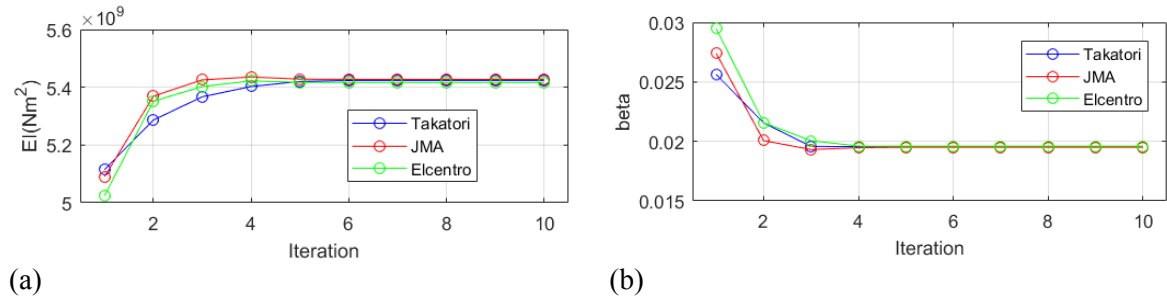


Figure 4.29 comparison of parameter identification results under different earthquake inputs; (a) EI ; (b) β

4.4 Numerical verification of adaptive EKF-UI method with substructure

In the last section, the proposed adaptive EKF-UI method is verified numerically in which

earthquake excitations are regarded as unknown inputs and whole structures are analyzed. For large DOF complex structures, KF formulation becomes time consuming and uncertainties of many structural parameters and modeling errors need to be considered. Inappropriate model results in poor KF performance. Thus if we can split large complex structure into small substructures (note: substructures in section 2.5.3 refer to soil-pile foundations), uncertainties in modeling of structural elements away from the target element are not needed. KF become practical.

In fact, system responses could also be treated as inputs when substructures extracted from whole structures are considered. Equation (4.1), (4.2) and (4.4) could still be employed, i.e. subscript s and g stand for interior DOFs of substructures and exterior DOFs connecting with rest of structure members respectively in this case. In this section, the bridge pier model employed in last section and a 3D cable-stayed bridge model are discussed based on the method.

4.4.1 Bridge pier model with substructure

The top two elements of bridge pier model in section 4.3.1 are extracted as substructure in this section. NO.1~4 are regarded as interior DOFs while DOF5 and DOF6 are regarded as those exterior DOFs. Two situations are considered here, i.e. translational displacement of DOF5 is known while angular displacement of DOF6 is unknown and vice versa. For both of the two cases, accelerations on DOF1 and 3 as well as their collocated double integrated displacements are observed. Additionally, DOF2 is also assumed observed here because it has been shown in the experiment of section 2.5.1 that the angular responses are beneficial to reasonable stiffness identification of the upper part of pier. The uniform cross section EI and damping coefficient β are to be identified. Specifically, in practical engineering, angular displacement can be obtained from integrating angular velocity measured by gyroscope. Figure 4.30 shows the schemes of the two substructures.

Three levels of acceleration measurement noise are considered here, 0%, 3% and 8% of signals' RMS. The process noise variance matrix for the two substructure cases are $\mathbf{Q}=\text{diag}([10^{-6}\mathbf{I}, 10^{-4}\mathbf{I}, 10^{-2}\mathbf{I}, \mathbf{0}, 5 \times 10^{-6}\mathbf{I}])$ and $\mathbf{Q}=\text{diag}([10^{-6}\mathbf{I}, 10^{-4}\mathbf{I}, 10^{-2}\mathbf{I}, \mathbf{0}, 10^{-4}\mathbf{I}])$, respectively. Specifically, for the first substructure, a virtual angular displacement can be calculated using the difference of two translational displacement signals, i.e. $x_{rot}=(x_1-x_5)/l$. Process noise corresponding to unknown angular input can be defined based on the value. Except this information, other computation information in the section is same as those in section 4.3.1 .

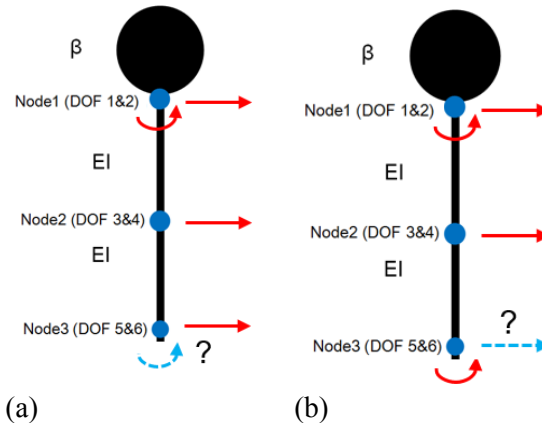
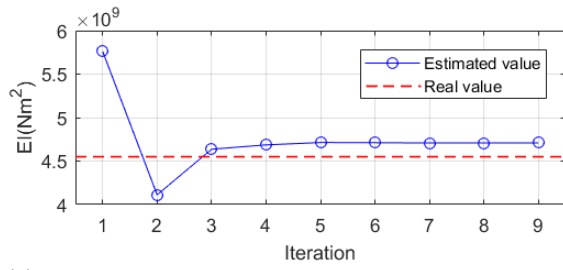
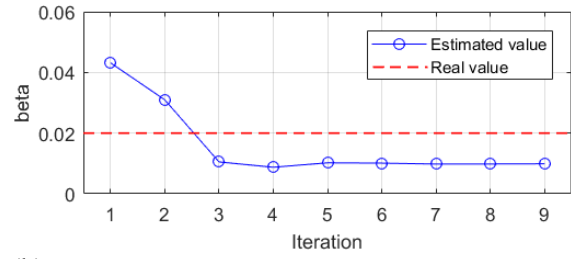


Figure 4.30 bridge pier substructures; (a) substructure 1 unknown bottom rotation input; (b) substructure 2 unknown bottom translation input

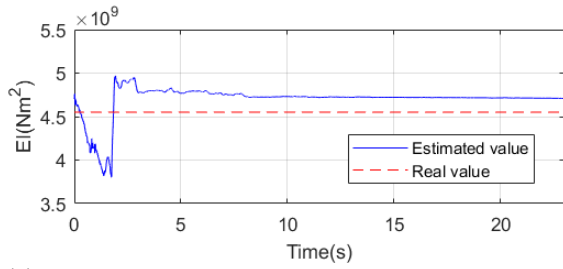


(a)

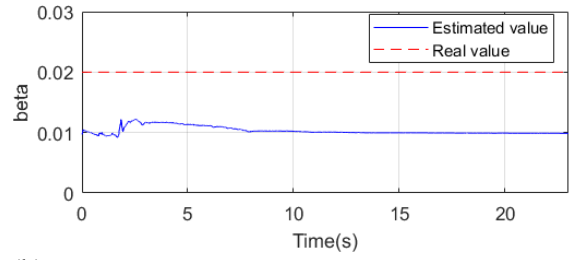


(b)

Figure 4.31 parameter identification results at each iteration of substructure 1 with 3% measurement noise; (a) EI ; (b) β

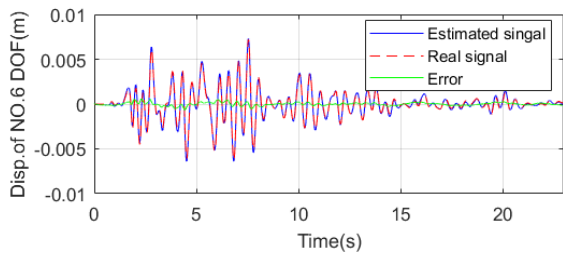


(a)

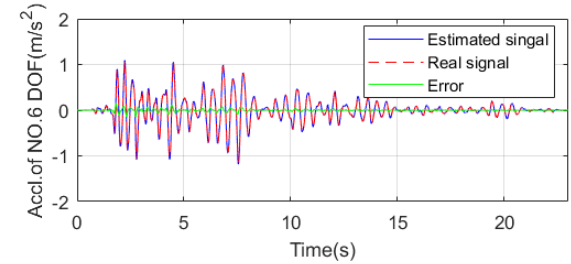


(b)

Figure 4.32 parameter convergence at later iteration of substructure 1 with 3% measurement noise; (a) EI ; (b) β

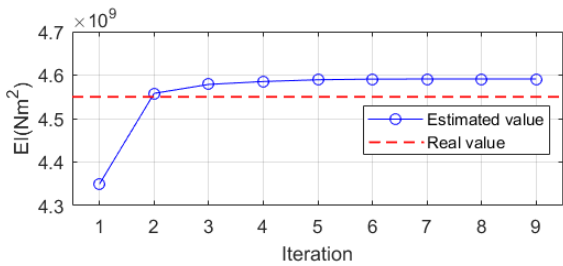


(a)

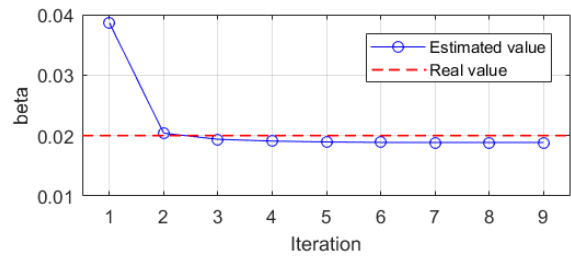


(b)

Figure 4.33 estimated system input of NO. 6 DOF with 3% measurement noise; (a) angular displacement; (b) angular acceleration



(a)



(b)

Figure 4.34 parameter identification results at each iteration of substructure 2 with 3% measurement noise; (a) EI ; (b) β

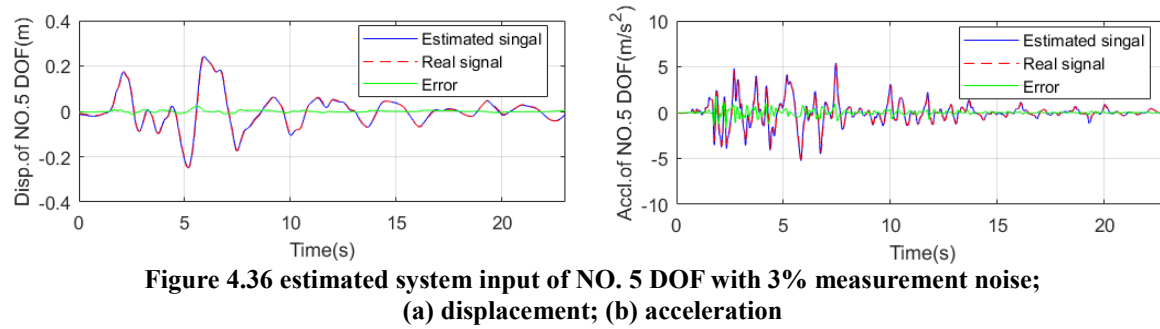
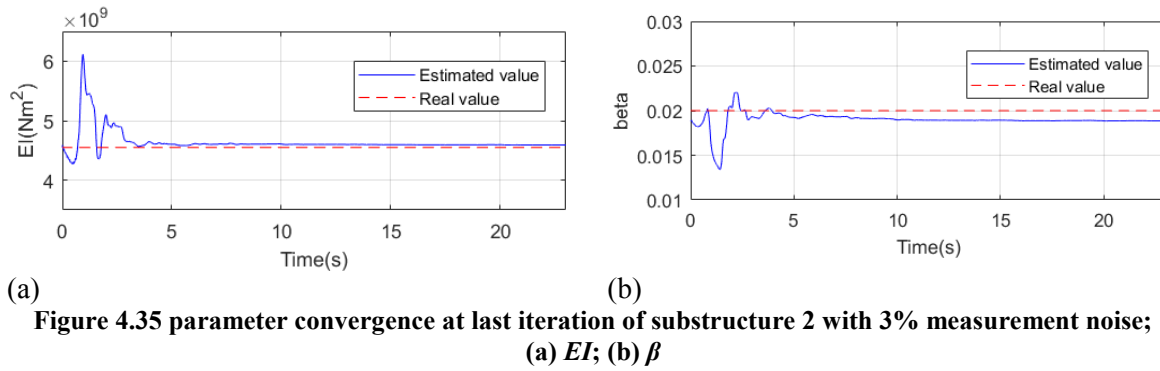


Figure 4.31~Figure 4.33 shows the parameter and unknown input estimation results of substructure 1 in the case of 3% measurement noise; Figure 4.34~Figure 4.36 shows the results of substructure 2 in the same conditions. For both cases, parameter converge after 4 iterations, however, the estimation accuracy is relatively low comparing to case of whole structure in section 4.3.1. Here, the known input of each substructure, i.e. NO.5 DOF displacement in substructure 1 and NO.6 displacement in substructure 2, is also obtained from the noisy measurement signals; since they are regarded as system inputs, the errors of themselves cannot be compensate by the filter and directly influence parameter estimation accuracies. Table 4.3 compares the parameter identification accuracies of the two substructures under three measurement noise levels. When there is no measurement noise, accurate parameter can be identified; however, as long as measurement noise exists, parameter values with high precisions cannot be achieved. Besides, if the DOF2 is not observed, the parameters are also identified and the results are shown in Table 4.4. The similar conclusion is drawn. Generally speaking, the accuracies of EI values are more stable than β , since most of EI errors are below 5% in these cases while the errors of β reach to 50%.

Table 4.3 parameter accuracies under difference measurement noise levels

Measurement noise	Error of EI		Error of β	
	Substructure 1	Substructure 2	Substructure 1	Substructure 2
0%	0.1%	0.1%	1%	1%
3%	3.5%	0.9%	50%	5.8%
8%	5.1%	2.3%	25%	7.7%

Table 4.4 parameter accuracies under different measurement noise levels without DOF2 observation

Measurement noise	Error of EI		Error of β	
	Substructure 1	Substructure 2	Substructure 1	Substructure 2
0%	0.1%	0.1%	1%	1%

3%	3.8%	5.3%	1%	50%
8%	4.4%	4.4%	2.7%	7.4%

4.4.2 A 3D cable stayed bridge case

In this section, the 3D cable stayed bridge employed in the last chapter is studied here to evaluate the performance of the proposed method when inaccurate system model with large DOFs is assumed in the KF. Detailed information about the prototype structure can be referred to Xie and Sun [121].

For the 3D bridge model, forward analysis is conducted with Generalized-alpha method with $\rho=1/6$ in this case. First of all, the same 2D cable-stayed bridge model as last chapter is employed in KF to identify cross section stiffness EI of auxiliary piers, middle and upper parts of bridge towers, damping coefficient β as well as four earthquake inputs. Except the aforementioned parameters, others are treated as known information. The simplified 2D cable stayed bridge model, parameters to be identified as well as corresponding observation configuration is shown in Figure 4.37(a). In this numerical case, only those members with lateral vibration are focused; three earthquake inputs, i.e. Takatori, JMA and El centro, are applied to here to confirm parameter identification consistency.

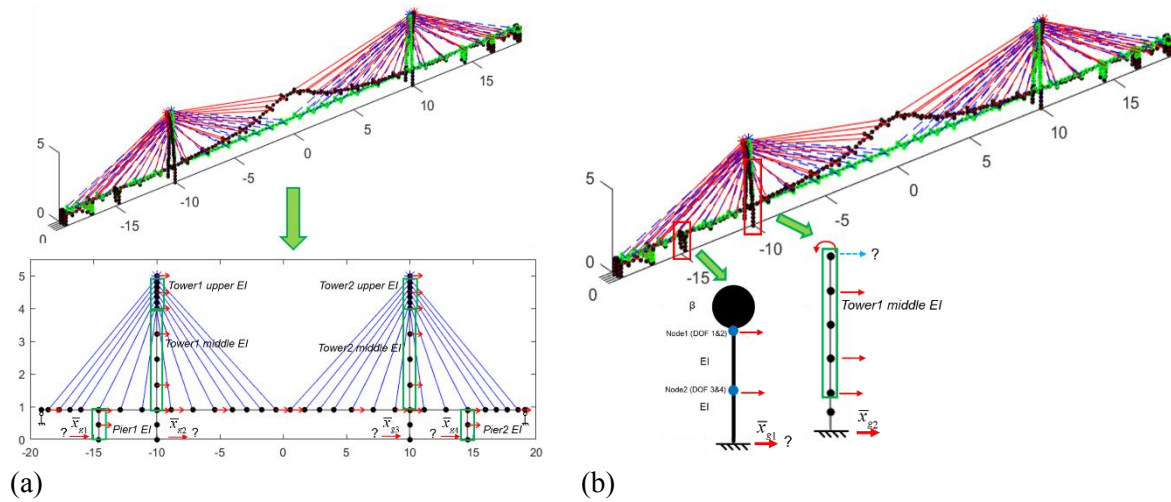


Figure 4.37 (a) simplified 2D cable stayed bridge model; (b) substructure model

Figure 4.38 shows the identification results of pier 1, middle and top part of tower1 under the different earthquake inputs. Clearly, the tower EI values identified are inconsistent among the three earthquakes, while pier 1 EI values show good consistency, since it is accurately modeled in the 2D model. (Note: in the 2D/3D model, the pier 1 is connected with the main girder above only in translation DOF) To solve the problem, substructure method can be applied to members of a whole complex structure. Figure 4.37(b) shows the two substructures extracted from the 3D bridge model, corresponding to pier 1 and middle to bottom part of tower 1. In the pier substructure, two translational responses are measured, while an angular response is measured on the top of the tower substructure besides other three translational displacement measurements. EI of pier 1 and middle part of tower 1 are to be identified.

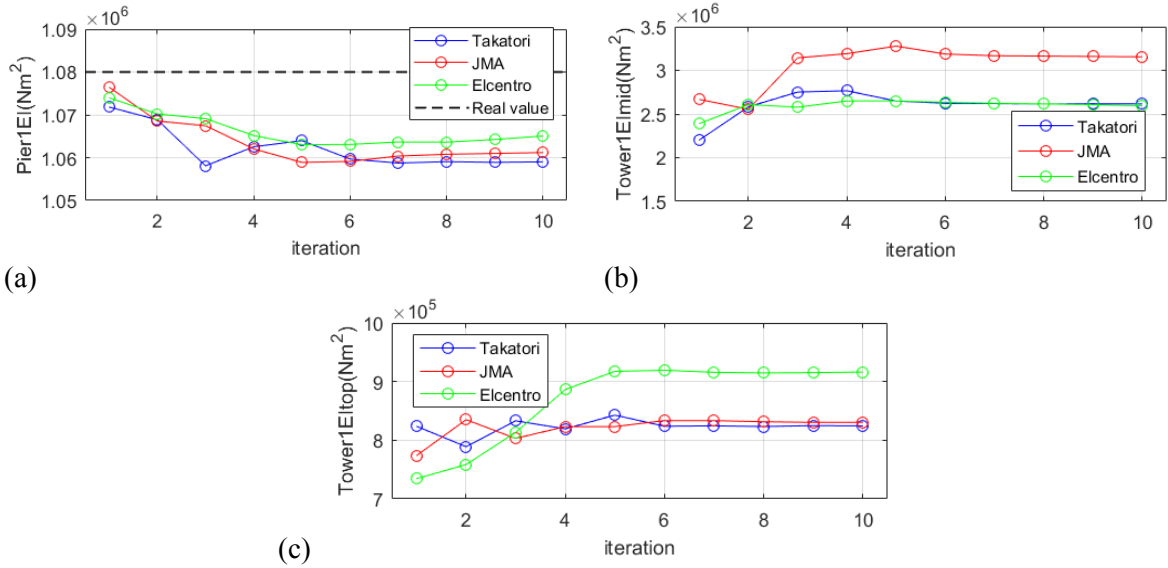


Figure 4.38 parameter identification at each iteration of 2D bridge model;
(a) pier 1; (b) middle part of tower1; (c) top part of tower1

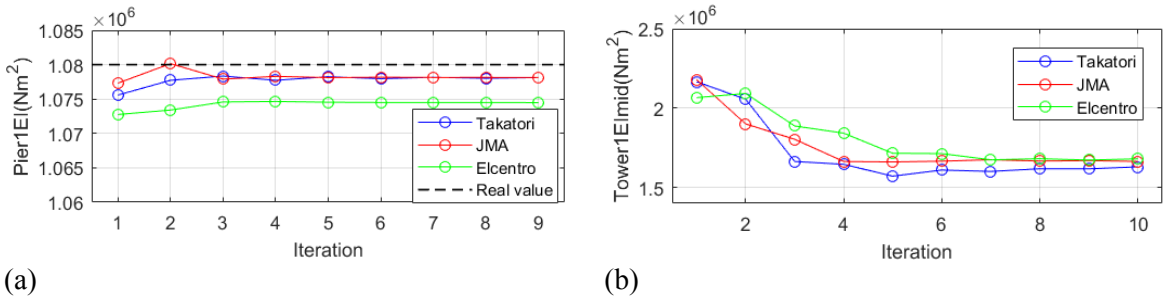


Figure 4.39 parameter estimation at each iteration of substructure case;
(a) pier 1; (b) middle part of tower1

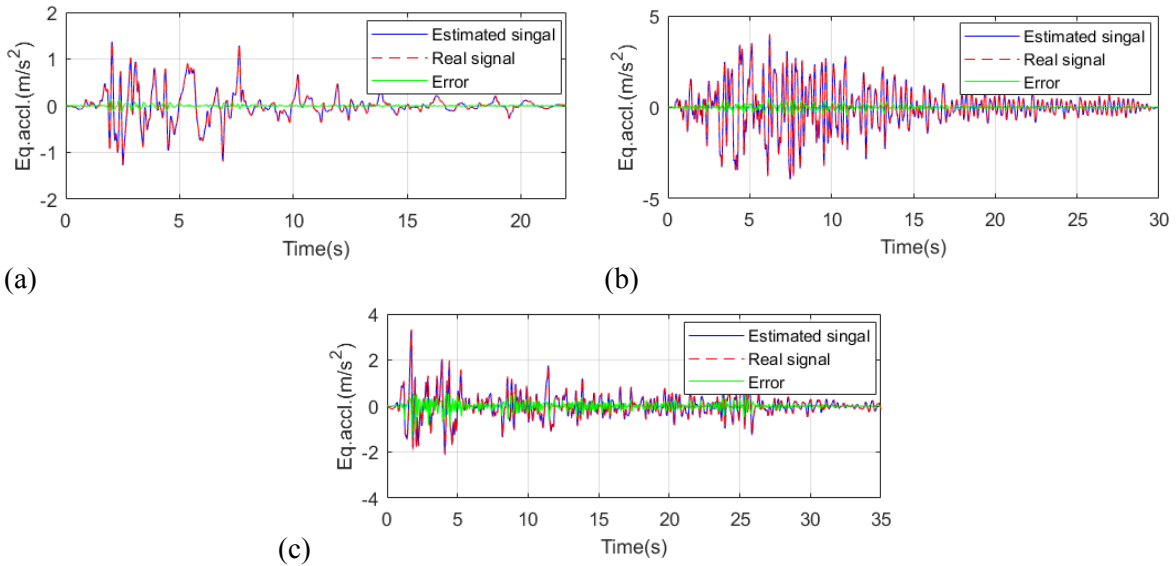


Figure 4.40 estimated earthquake accelerations; (a) Takatori; (b) JMA; (c) El centro

Figure 4.39 and Figure 4.40 shows the estimated parameters and earthquake accelerations

respectively. Obviously, based on the substructures, good identification consistencies are shown comparing to previous 2D structure case. In terms of the pier 1 substructure, the pier top mass is actually tuned based on the Takatori case so that the identified stiffness value could be close to the real one. The same mass value is then used in other two cases. In practical engineering, it can be achieved by taking advantage of small earthquakes. In the tower substructure, regarding the top translation response as known input and the angular response as unknown one, the parameters are also tried to be identified. But the performance is not as good as the original one, i.e. parameter consistencies are not ideal. Additionally, tower substructure without the bottom part has also been applied but the parameter results are inconsistent. Thus, selection of substructure is also a crucial part of applying the substructure method; in practical engineering, it can be investigated in advance based on numerical models before analyzing in-site measurement signals.

In this section, the proposed adaptive EKF-UI method is validated through two experiments in E-defense database, i.e. a full scale bridge pier experiment and a full scale four story frame experiment. Parameter identification results based on the adaptive EKF-UI method is compared with those obtained considering known input conditions. For both of the experiments, experiments under a series of earthquake excitations are studied.

The experiment model is the one used in section 2.5.1 . The detailed information about the experiment model and monitoring system has been introduced before. Therefore, they will not be repeated here. In this study, the displacement measurements (relative displacements), with 200Hz sampling frequency, are mainly used, considering the noise level of acceleration measurements on the structure is high. Reasonable velocity and acceleration signals can be obtained as derivatives of the measured displacement signals.

Figure 4.41 location of displacement transducer

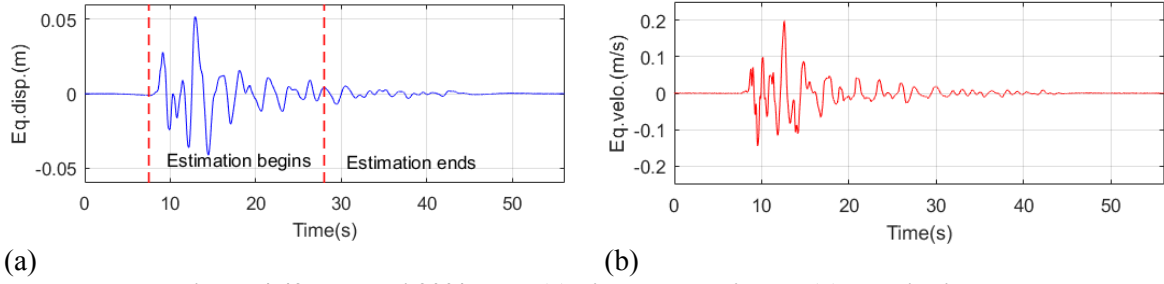


Figure 4.42 Takatori 20% case; (a) displacement input; (b) velocity input

In the first place, the same system model in section 2.5.1 is employed here. The equivalent uniform cross section stiffness EI and stiffness damping coefficient β are to be identified. Four measurement schemes are compared in this case. In the first 3 schemes, accelerations and displacements of DOF1 and 5, DOF1 and 3, DOF3 and 5 are observed, while all of three translational DOFs are employed in the last scheme. They are shown in Figure 4.43. For all of the measurement and excitation cases, process noise covariance matrix \mathbf{Q} is initially set as $\text{diag}([10^{-8}\mathbf{I}, 10^{-6}\mathbf{I}, 10^{-4}\mathbf{I}, 0, 10^{-4}\mathbf{I}])$; measurement noise covariance matrix \mathbf{R} is set as $\text{diag}([5 \times 10^{-9}\mathbf{I}, 10^{-4}\mathbf{I}])$, i.e. noises variances are 5×10^{-9} and 10^{-4} for displacements and accelerations respectively, which correspond to around 8% RMS of relative displacement and acceleration signal on NO.1 DOF in Takatori 20% case.

Figure 4.44 and Figure 4.45 shows the stiffness and damping coefficient identification results at each iteration and the convergence history at the last iteration based on the four measurement schemes for Takatori 20% case. Generally, the parameters converge to stable values after about 4 iterations for each measurement scheme; however, they are not exactly the same with each other. For measurement scheme of DOF 1 and 3, i.e. the upper part of pier is observed, the identified stiffness is about $6.4 \times 10^9 \text{Nm}^2$ which is the maximum value among the four schemes; the minimum identified value is about $6.0 \times 10^9 \text{Nm}^2$ when DOF 3 and 5 are measured, i.e. the lower part of bridge pier is observed. For the rest of two measurement schemes, the identified stiffness values are roughly same, $6.3 \times 10^9 \text{Nm}^2$.

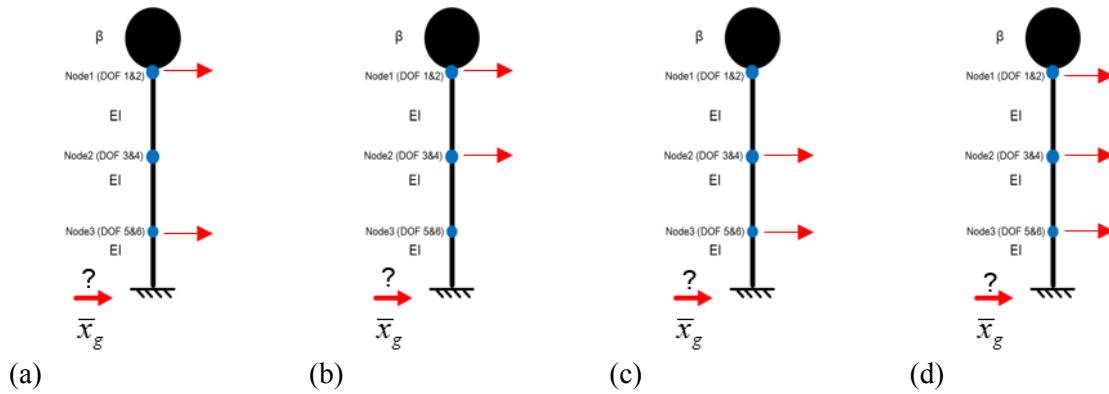


Figure 4.43 measurement configurations; (a) DOF1&5; (b) DOF1&3; (c) DOF3&5; (d) DOF1,3&5

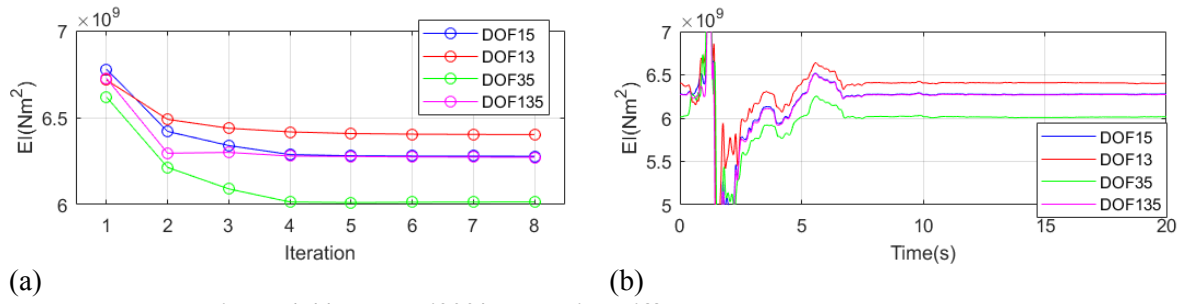


Figure 4.44 Takatori20% case using different measurement schemes;
(a) EI value at each iteration; (b) EI convergence at the last iteration

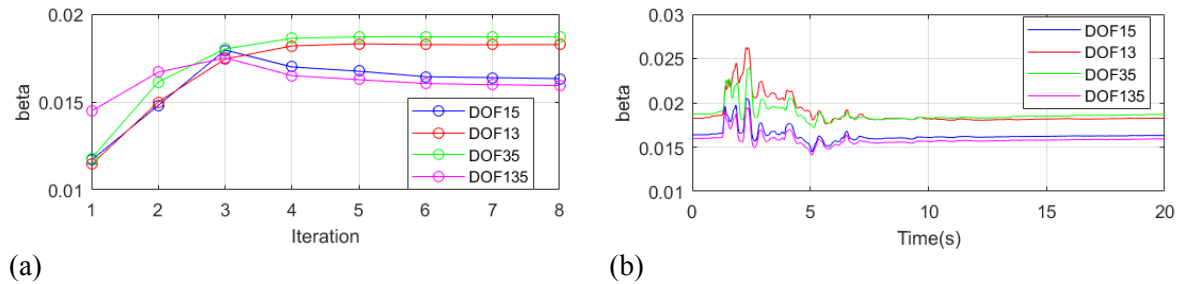


Figure 4.45 Takatori20% case using different measurement schemes;
(a) beta value at each iteration; (b) beta convergence at the last iteration

Figure 4.46 and Figure 4.47 shows the input estimation results of Takatori 20% case using the first and second measurement scheme in Figure 4.43. In terms of earthquake displacements, both schemes give good results which coincide with real measured one; while for accelerations, the first scheme is evidently better than the second scheme, i.e. the estimated acceleration in second scheme is noisier and larger errors are presented. It is due to that the bottom DOFs are unobserved in the case. Besides, other two measurement schemes present similar accuracies of estimated inputs as the first one. Table 4.5 shows the earthquake acceleration estimation errors under a series of Takatori excitations using the four measurement scheme. The errors in the table are calculated as ratios of RMS of signal discrepancies to RMS of real signals.

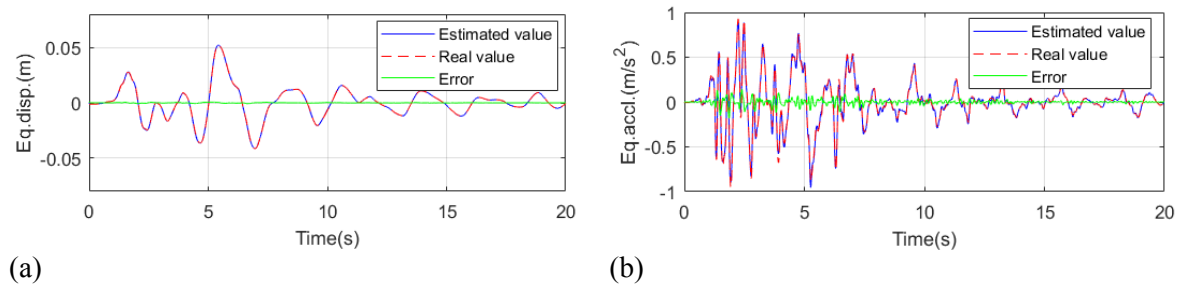


Figure 4.46 Takatori 20% case using measurement scheme of DOF 1&5;
(a) comparison of earthquake displacement; (b) comparison of earthquake acceleration

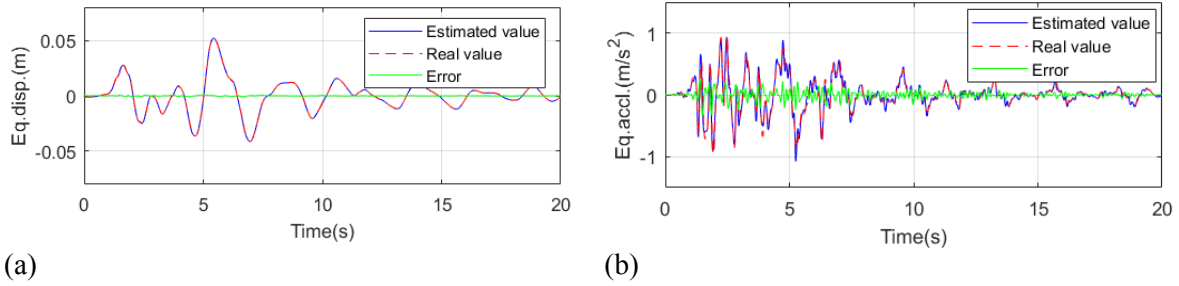
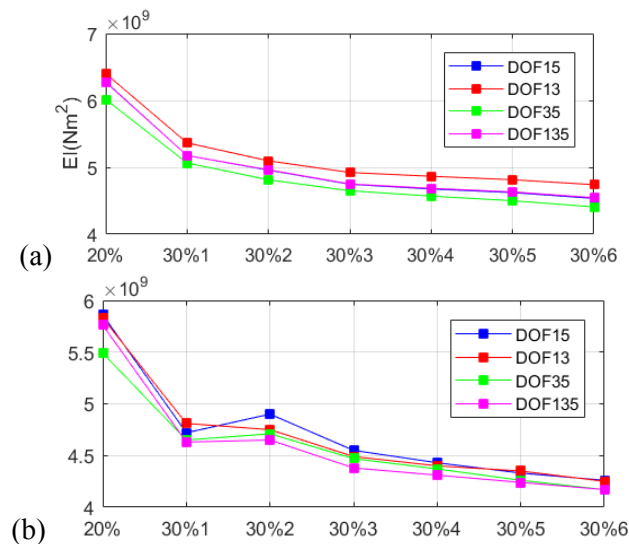


Figure 4.47 Takatori 20% case using measurement scheme of DOF 1&3;
(a) comparison of earthquake displacement; (b) comparison of earthquake acceleration

Table 4.5 earthquake acceleration estimation errors

ID	DOF 1&5	DOF 1&3	DOF 3&5	DOF 1,3&5
Takatori20%	12%	26%	16%	13%
Takatori30%1	11%	20%	14%	13%
Takatori30%2	18%	37%	21%	19%
Takatori30%3	15%	29%	18%	16%
Takatori30%4	15%	24%	16%	16%
Takatori30%5	15%	28%	16%	15%
Takatori30%6	14%	23%	16%	15%

The parameter identification results under a series of Takatori earthquake excitations are shown in Figure 4.48(a). For each excitation case, the identification results show similarity with those of Takatori20% case, i.e. identification results of the second and third measurement schemes in Figure 4.43 are maximum and minimum respectively. The overall stiffness variations for the four measurement schemes are almost parallel with each other; specifically, the stiffness values dramatically decrease between Takatori 20% and 30%1 case, i.e. about 15%, and gradually decrease in the following cases.



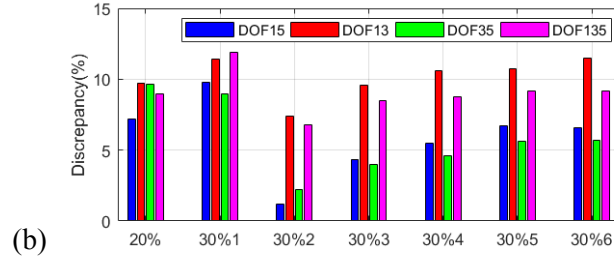


Figure 4.48 comparison of EI value identification results;

(a) results based on unknown inputs; (b) results based on known inputs; (c) discrepancies

The parameters are also identified with known inputs based on an EKF-RM method to make comparisons with the results considering unknown inputs. In this case, earthquake accelerations are treated as inputs in order to reduce inputs error coming from integrated displacement and velocity signals which has already discussed in section 4.4. The four measurement schemes are also employed here, of which the results are shown in Figure 4.48(b). The identification results do not present similar parallel consistencies as in the unknown input cases; the stiffness variations, on the other hand, show similar trends as the previous ones. Generally, the identified stiffness values in the known input cases are smaller than those of unknown input cases, e.g. the stiffness values are ranging between $4.28 \times 10^9 \sim 5.88 \times 10^9 \text{ Nm}^2$ for the first measurement scheme with known input, while they are $4.54 \times 10^9 \sim 6.28 \times 10^9 \text{ Nm}^2$ considering unknown input. These stiffness discrepancies are shown in Figure 4.48(c) as bar graph. Basically, the discrepancies of DOF 1&3 scheme and DOF1,3&5 scheme are larger, i.e. around 10% for all excitation cases, than the rest two, which are around 10% for the first two excitation cases and 5% for the rest of cases. In fact, for all measurement schemes, the discrepancies of the first two cases are slightly larger than others.

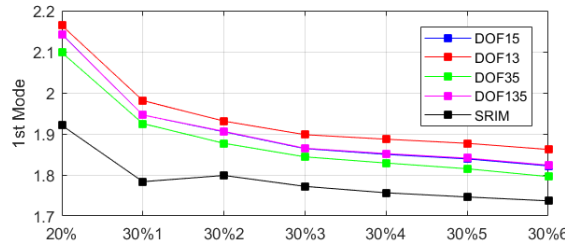


Figure 4.49 comparison of modal frequencies

In this study, the SRIM method has also been employed to estimate modal frequencies of the structure. All of four acceleration signals along the pier are used, but only the 1st mode is estimated with high confidence. The results are compared with those computed using the identified stiffness values based on the adaptive EKF-UI method, which are shown in Figure 4.49. Even though large frequency discrepancies are found, which is actually expectable considering the identified parameters with unknown inputs are larger than those based on known inputs as previously presented, the tendencies of frequency variations from both methods and different measurement schemes are similar.

Besides the small earthquake cases analyzed previously, the proposed method is also applied to two strong earthquake cases here, i.e. Takatori100%1 and Takatori100%2. In these cases, the bridge pier suffered severe damage in its bottom part and presented strong nonlinearity as the hysteresis loop shown in Figure 3.48. Similar to the small earthquake cases, the absolute displacements of the structure will be calculated as the sum of the integrated earthquake ground motions and the measured relative displacements. However, in the two cases, residual displacements exist in the relative displacements as introduced in section 3.4.1. Considering in practice displacement is expected to be

obtained by double integrating acceleration and high-pass filtering, the measured relative displacements are first filtered by a high-pass filter with 0.2Hz cutoff frequency and then summed with integrated earthquake ground motions. Figure 4.50 and Figure 4.51 show the identified EI values using the aforementioned four measurement schemes for Takatori100%1 and Takatori100%2 case respectively. In the same figures, the identification results using track mode of EKF-RM method with known input are also presented and compared with the unknown input cases. Generally, the identified EI values with known or unknown input share the same order after about 5 seconds; the identified EI values with unknown input can be regarded as the equivalent linear stiffness corresponding to the time-variant stiffness identified by track mode with known input.

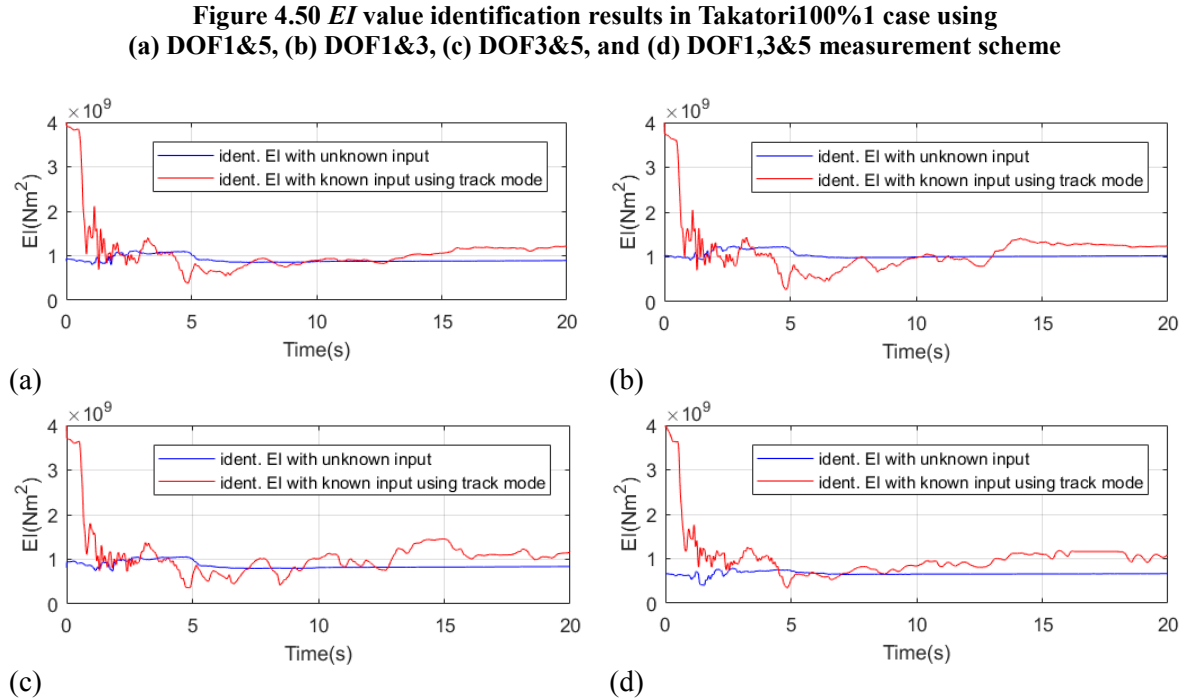
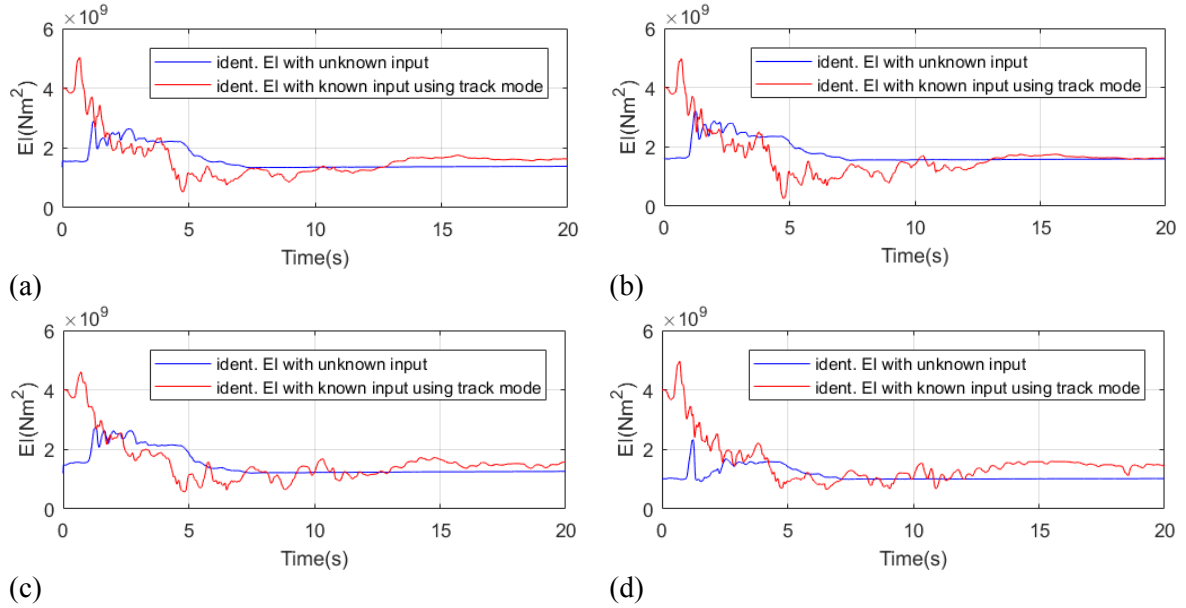


Figure 4.51 EI value identification results in Takatori100%2 case using (a) DOF1&5, (b) DOF1&3, (c) DOF3&5, (d) DOF1,3&5 measurement scheme

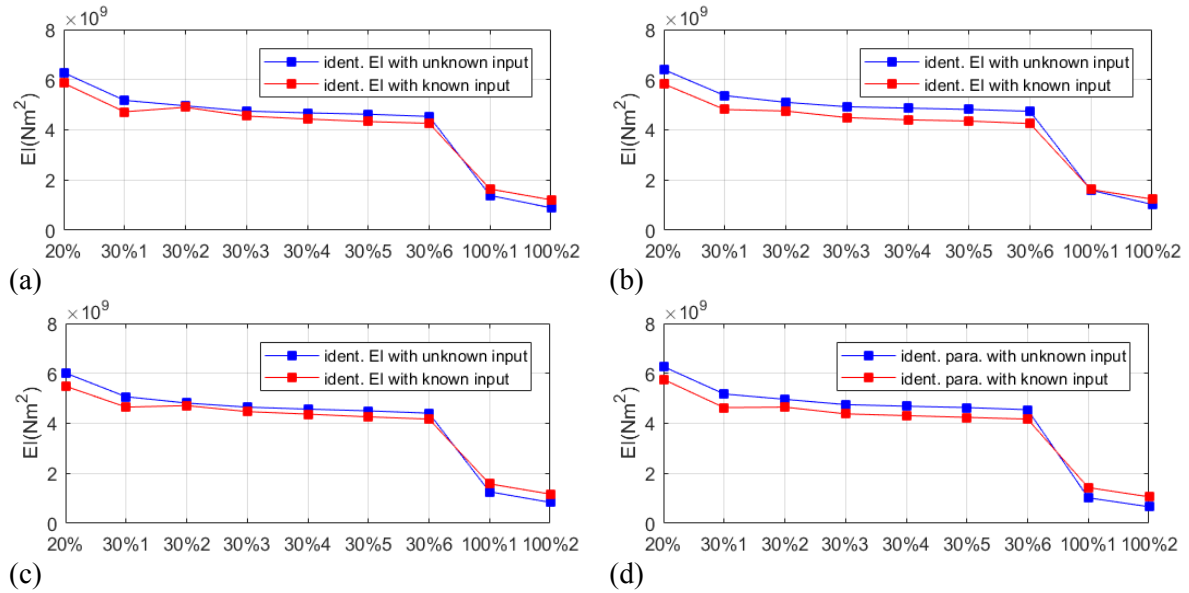


Figure 4.52 comparison of EI value identification results using (a) DOF1&5, (b) DOF1&3, (c) DOF3&5, and (d) DOF1,3&5 measurement scheme

Figure 4.52 summarizes the EI value variations under not only small earthquake but also strong earthquake excitations for the four measurement schemes. In terms of the identified values with known input, for the Takatori100% and Takatori100%2 case, the averaged ones over the last 5 seconds of identification histories (shown in Figure 4.50 and Figure 4.51) are employed. It is clear that significant stiffness reductions happened from the Takatori100%1 case and the overall EI variations identified with unknown input match well with those obtained considering known input.

Furthermore, in order to verify the identified parameters and inputs, the system responses are reproduced using the identified parameters and inputs based on forward simulation. The parameters and inputs used for the simulations are from the last iterations of identifications, specifically the parameters are the last values of identification histories. Figure 4.53 and Figure 4.54 show the simulated signals of NO.1 DOF using the results from the DOF1&5 measurement scheme in Takatori30%1 and Takatori100%1 case respectively. The simulated signals match well with the real observed ones. The errors of the simulated accelerations based on equation (2.21) in a series of excitation cases are summarized in Table 4.6.

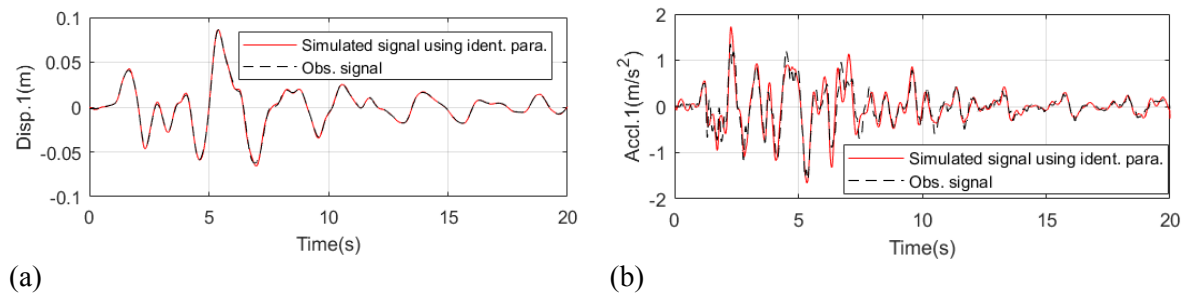


Figure 4.53 simulated signals of NO.1 DOF using identified results from DOF1&5 measurement scheme in Takatori30%1 case: (a) displacement; (b) acceleration

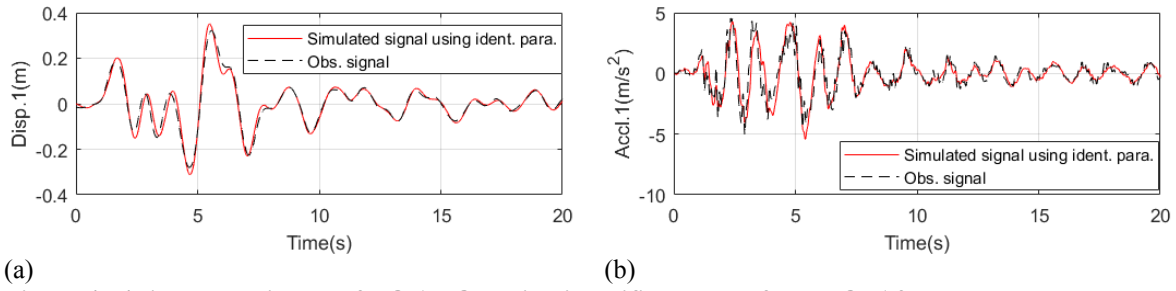


Figure 4.54 simulated signals of NO.1 DOF using identified results from DOF1&5 measurement scheme in Takatori100%1 case: (a) displacement; (b) acceleration

Table 4.6 simulated acceleration errors of NO.1 DOF using identified results from DOF1&5 measurement scheme

ID	Acceleration error
Takatori20%	49.5%
Takatori30%1	44.3%
Takatori30%2	50.0%
Takatori30%3	41.8%
Takatori30%4	38.2%
Takatori30%5	37.3%
Takatori30%6	35.8%
Takatori100%1	46.7%
Takatori100%2	42.5%

Finally, in this experiment validation, substructure method is also applied to identify cross section stiffness EI of upper part of the bridge pier model as shown in Figure 4.55, i.e. the EI of the upper two elements is assumed as equal. Because of sensor configurations in the experiment, the angular input at the bottom of the substructure, i.e. DOF6, is to be estimated. In order to obtain reasonable stiffness results, the angular responses on NO.1 node (DOF2) are also involved besides the three translational responses. The calculation of it is exactly same as in section 2.5.1 .

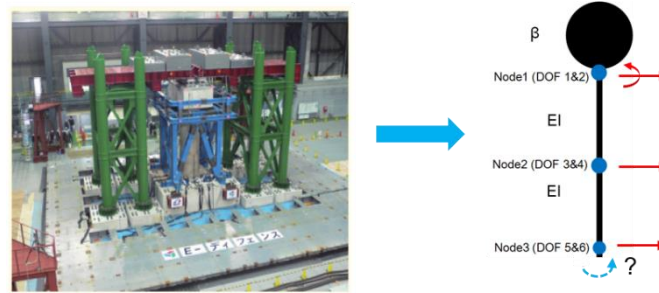


Figure 4.55 substructure model

In this case, \mathbf{Q} matrix is initially set as $\text{diag}([10^{-8}\mathbf{I}, 10^{-6}\mathbf{I}, 10^{-4}\mathbf{I}, \mathbf{0}, 2.5 \times 10^{-7}\mathbf{I}])$, i.e. process noise corresponding to angular input is 0.5×10^{-3} . The values corresponding to angular displacement and acceleration in \mathbf{R} matrix are 2×10^{-9} and 5×10^{-5} respectively, which are approximately 15% of signals' RMS. Thus here the \mathbf{R} matrix is set as $\text{diag}([5 \times 10^{-9}, 2 \times 10^{-9}, 5 \times 10^{-9}, 5 \times 10^{-9}, 10^{-4}, 5 \times 10^{-5}, 10^{-4}, 10^{-4}])$. Except the aforementioned information, other computational and system information are exactly same as previous case.

Figure 4.56 shows the stiffness estimation results at each iteration and the convergence history at the last iteration for Takatori 20% case. The parameter converges to stable value after about 10

iterations in this case. The cross section stiffness is also identified considering known earthquake acceleration input with the same measurement scheme. EI values for the upper two elements and bottom element are identified. The results have been shown in section 2.5.1, but only the upper part EI is presented in Figure 4.56(b). the value with known input, i.e. $9.66 \times 10^9 \text{ Nm}^2$, is larger than the one with unknown input which is $7.56 \times 10^9 \text{ Nm}^2$. Figure 4.57 compares the identification results under a series of Takatori excitation cases. Basically, the identified values fluctuate around $9.60 \times 10^9 \text{ Nm}^2$ and $7.50 \times 10^9 \text{ Nm}^2$ for known and unknown input cases respectively. Discrepancies between the two type of values are below 30% which are consistent among these excitation cases.

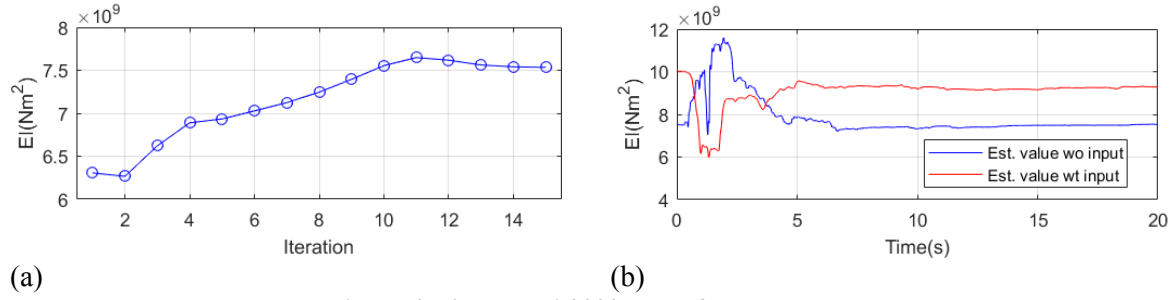


Figure 4.56 Takatori 20% case of substructure;
(a) EI at each iteration; (b) EI convergence at the last iteration

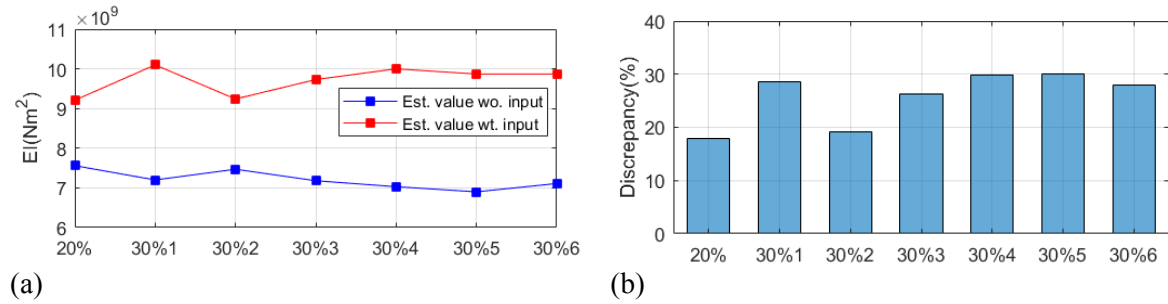


Figure 4.57 (a) comparison of parameter identification results; (b) parameter discrepancies

Comparing to discrepancies above, i.e. generally below 15% for all cases, the errors here are much larger, i.e. the largest one is about 30%. The reasons might be that 1) the structure system is stiffer and the errors are easily larger as previously discussed; 2) the identified unknown inputs are not accurate enough. Figure 4.58 compares the estimated unknown input, i.e. DOF6 response, with the responses estimated on the DOF6 based on known earthquake input for Takatori 20% case. Obviously, the discrepancy of DOF6 displacement is observable rather than those trivial ones shown in Figure 4.46 and Figure 4.47, and it is more evident for DOF6 acceleration. Table 4.7 summarizes the discrepancy values for all the excitation cases. The maximum value for displacement and acceleration are 28% and 54% respectively. As discussed in section 4.4.1, substructure with known accurate angular input is expected to possess higher estimation accuracy and needs to be experimentally validated in the future work.

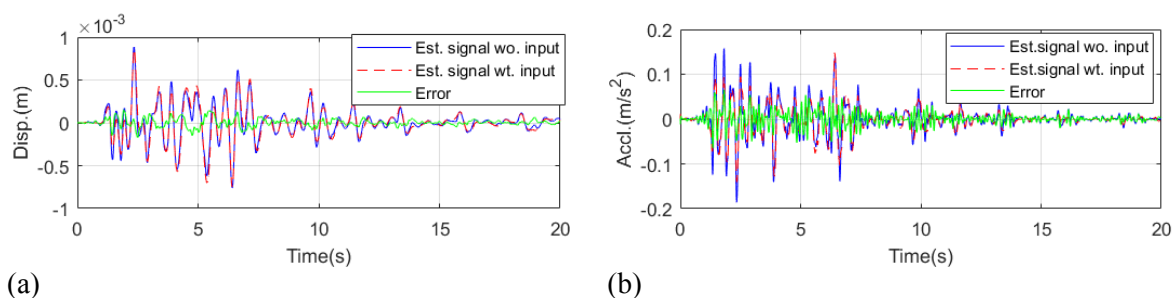


Figure 4.58 Takatori 20% case of DOF6 response comparison;
(a) displacement; (b) acceleration

Table 4.7 unknown input estimation errors

ID	Displacement	Acceleration
Takatori20%	28%	52%
Takatori30%1	21%	44%
Takatori30%2	22%	54%
Takatori30%3	18%	47%
Takatori30%4	17%	41%
Takatori30%5	17%	46%
Takatori30%6	15%	42%

4.5.2 Full scale four story frame building experiment

The target structure in this section is the experiment model introduced in section 2.5.2 . Basic information about the experiment model has already been introduced before; therefore, they will not be repeated here again. Acceleration measurements on shaking table and each floor of the building, with 200 Hz sampling frequency, are mainly used here. Displacement and velocity signals are integrated from the accelerations then applied with a high pass filter of 0.2 Hz cutoff frequency. The earthquake excitation cases are same as those in section 2.5.2 as well.

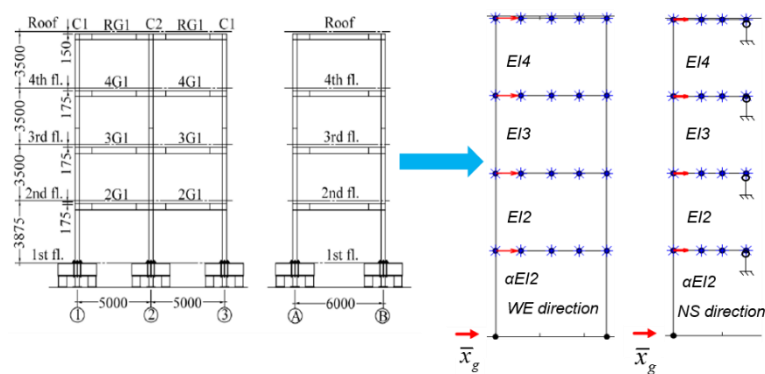


Figure 4.59 simplified FEM model

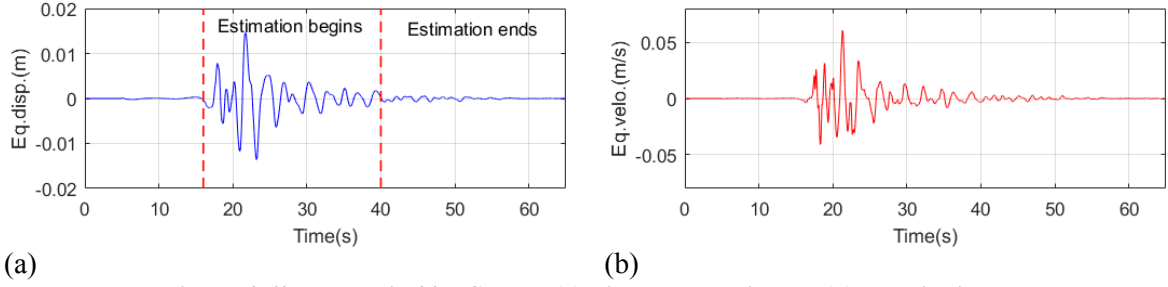
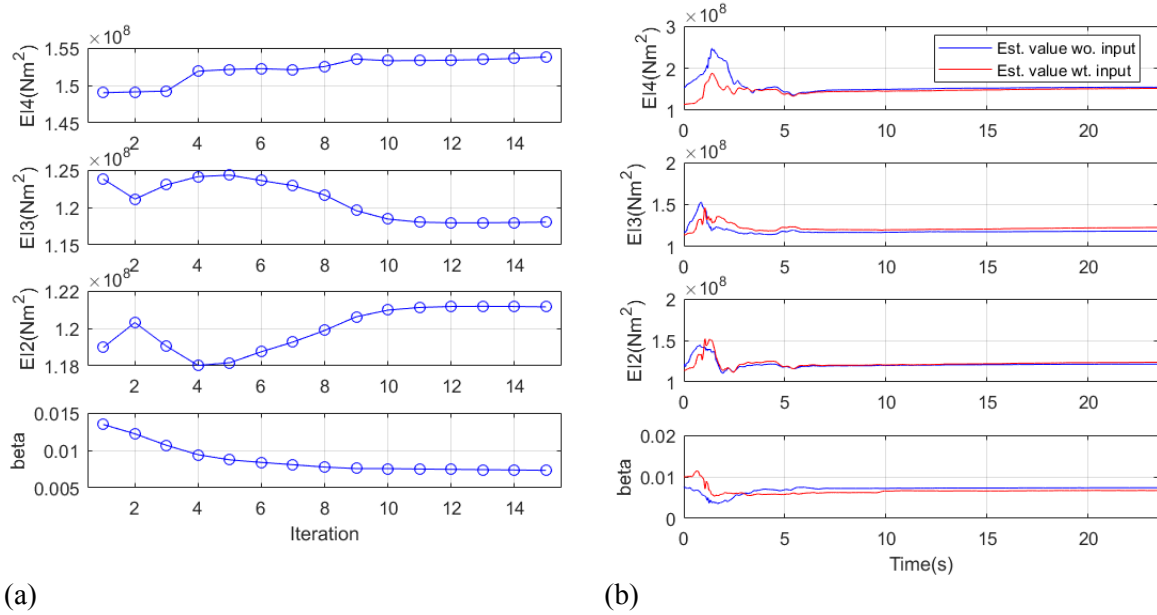


Figure 4.60 Takatori 5% NS case; (a) displacement input; (b) velocity input

Since in this experiment there is no measurement point on the columns of the first floor, the earthquake input and stiffness of the first floor cannot be estimated simultaneously. In order to take advantage of the experiment data here, the EI value of each floor is firstly identified considering known earthquake acceleration input for all excitation cases. The ratios of the first and second floor stiffness are calculated; they are then introduced as known values in the estimation with unknown input. For NS direction, $EI1=1.20 EI2$; for WE direction, $EI1=1.05 EI2$. Therefore, in the experiment validation, only the EI values from the second to top floor, stiffness damping coefficient β as well as unknown earthquake inputs are to be identified. The simplified 2D FEM models for the two directions are shown in Figure 4.59. Similar to previous case with known input, the half structures are employed here in order to reduce computation burden. For all excitation and direction cases, process noise covariance matrix \mathbf{Q} is initially set as $\text{diag}([10^{-8}\mathbf{I}, 10^{-6}\mathbf{I}, 10^{-4}\mathbf{I}, \mathbf{0}, 10^{-4}\mathbf{I}])$; measurement noise for displacements and accelerations are 10^{-4} and 10^{-2} respectively, i.e. \mathbf{R} matrix is $\text{diag}([10^{-8}\mathbf{I}, 10^{-4}\mathbf{I}])$.



**Figure 4.61 Takatori 5% NS case;
(a) EI identification at each iteration; (b) EI convergence at the last iteration**

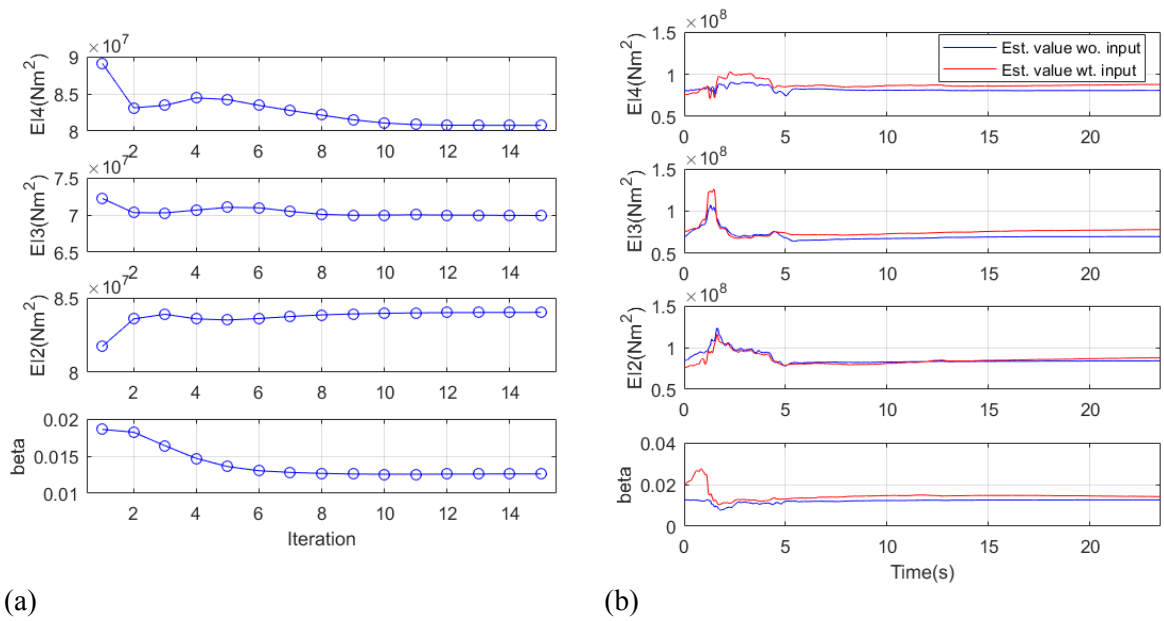
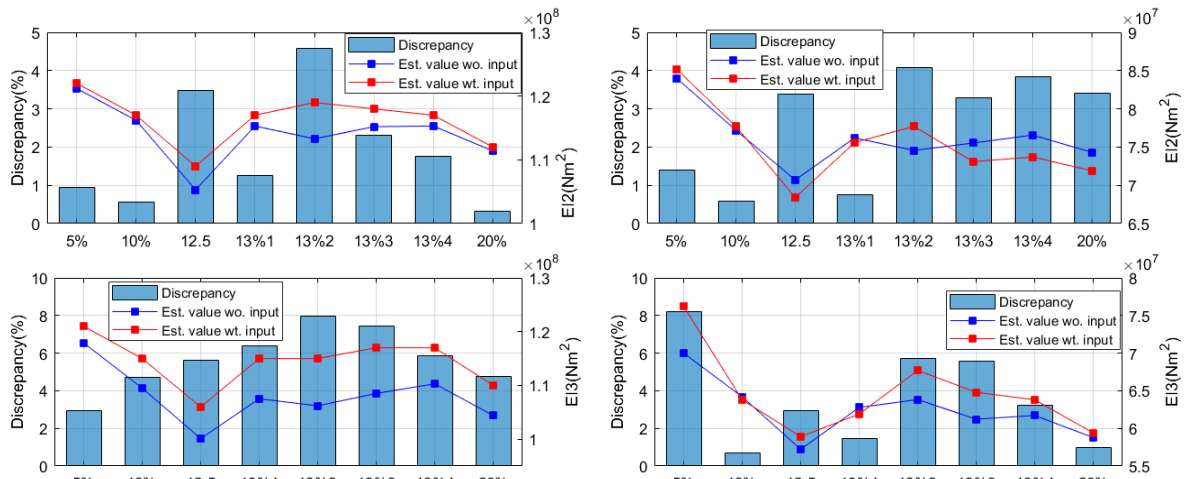


Figure 4.62 Takatori 5% WE case;
(a) EI identification at each iteration; (b) EI convergence at the last iteration

Figure 4.61 and Figure 4.62 shows the stiffness identification results at each iteration and the convergence histories of the last iteration for Takatori 5% NS and WE case respectively. Along with the convergence histories, identification results with known earthquake inputs are also plot. In these cases, the parameters converge to stable values after about 10 iterations and the discrepancies of identified values between unknown and known input case are relatively small. In fact, for most of iteration results here, parameters only change within some small ranges, but to make them settle down it takes a bit longer time. For all of other excitation cases, the phenomenon is similar. Under a series of Takatori excitation cases for NS and WE directions, identified values considering unknown and known inputs present similar tendencies; the identification discrepancies are all below 10%.



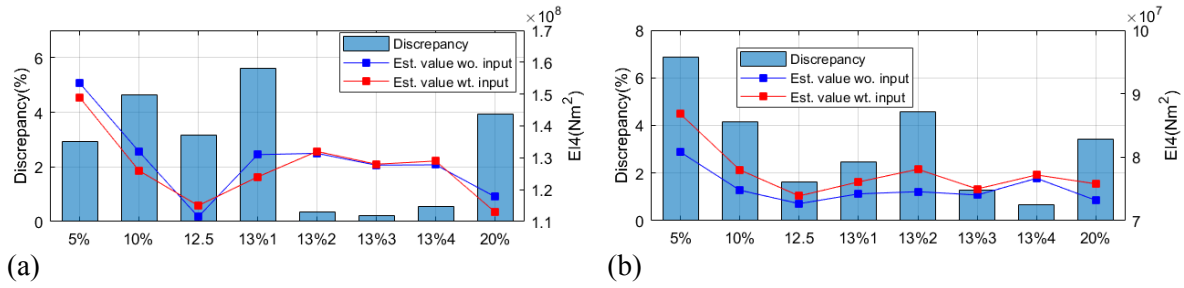


Figure 4.63 comparison of parameter identification results; (a) NS direction; (b) WE direction

Figure 4.64 and Figure 4.65 shows the input estimation results of Takatori 5% NS and WE case respectively. For earthquake displacement estimation, results of both directions coincide with real measured ones well; while for earthquake accelerations, result of WE direction is noisier than that of NS direction. It might be because that the stiffness of each bottom column in WE direction is smaller than that of NS direction; and intuitively stiffer bottom member give better input estimation. The phenomenon is consistent for all of other excitation cases as well as shown in Table 4.8.

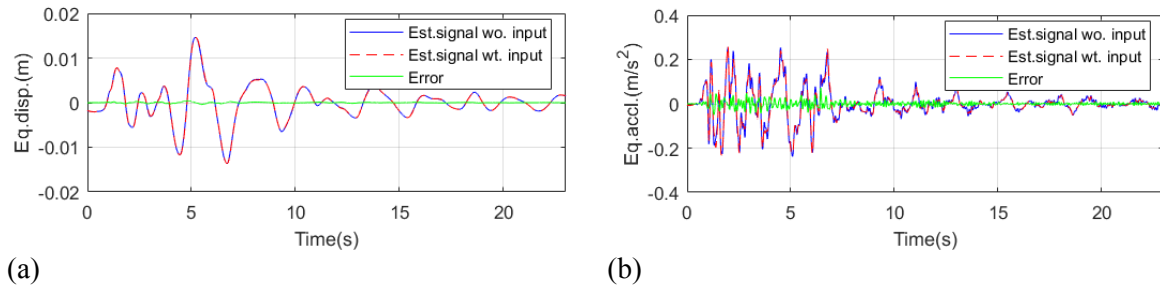


Figure 4.64 Takatori 5% NS case of unknown input estimation comparison; (a) displacement; (b) acceleration

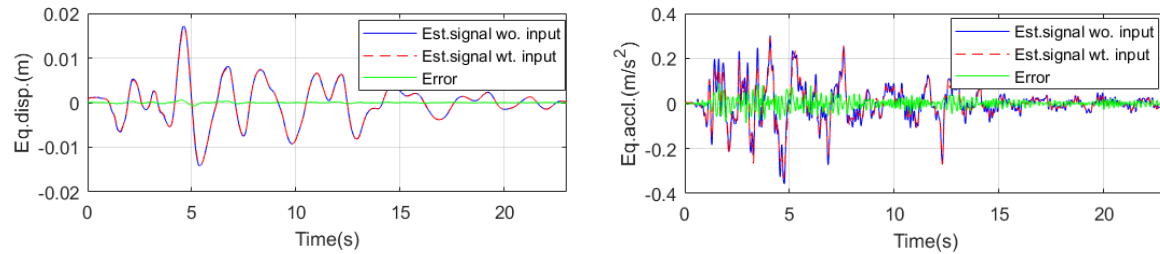


Figure 4.65 Takatori 5% WE case of unknown input estimation comparison; (a) displacement; (b) acceleration

Table 4.8 summary of earthquake input estimation errors

ID	NS-Disp. error	WE-Disp. error	NS-Accl. error	WE-Accl. error
Takatori5%	2.3%	3.3%	17%	28%
Takatori10%	2.0%	2.5%	18%	23%
Takatori12.5%	2.1%	2.7%	19%	22%
Takatori13%1	1.9%	2.3%	18%	24%
Takatori13%2	2.7%	4.3%	17%	23%
Takatori13%3	2.2%	3.1%	18%	21%
Takatori13%4	2.0%	2.8%	19%	24%
Takatori20%	1.6%	2.5%	21%	28%

Chapter 5 Conclusions

The thesis addresses three aspects of structural system evaluation using adaptive Kalman filter, i.e., parameter identification under known seismic excitations, displacement estimation for nonlinear SDOF system, and parameter identification under known seismic excitations.

In chapter 2, an EKF-RM method capable of structure system evaluation under seismic excitations is proposed. In this method, the process noise variance-covariance matrix \mathbf{Q} is adapted automatically based on RM algorithm. The EKF-RM method contains two computation modes, i.e. stable mode which focuses on time-invariant parameter estimation and track mode which can track parameter variation instantaneously. Robustness and effectiveness of the proposed method is demonstrated with numerical models and further validated using experiment data from E-defense database.

Three numerical models, including a SDOF model, a 4-DOF lumped mass model, and a 2D cable stayed bridge model, are firstly used for numerical verification. By applying the stable mode of the proposed method, accurate parameter identification results are achieved even with inappropriate initial \mathbf{Q} matrix while normal EKF cannot. The track mode is further verified through the 4-DOF lumped mass model with time-variant bottom stiffness. It is found that parameter variation can be tracked accurately and instantaneously based on the method. The selection of the computation mode is decided by the estimated velocity. If the estimated velocity shows large discrepancy from real observed one, identified parameter is considered time-variant and the track mode should be applied. Otherwise, stable mode is applied. Additionally, situations where simplified, rather than correct, system models are employed in EKF are also studied with two numerical examples. A 4-DOF lumped mass model and a 2D cable stayed bridge model are employed to estimate a 3D four story frame building and a 3D cable stayed bridge. Modal frequencies computed from the estimated parameters coincide with those of the complex structures in low order modes. However, in such situations, the identified parameter may become inconsistent depending on different earthquake excitations. Even with the process noise adaption method, the choice of an appropriate system model is crucial.

The EKF-RM method is further validate through three E-defense experiments, i.e. a full scale bridge pier experiment, a full scale four story frame building experiment, and a substructure experiment. The bridge pier structure is firstly estimated using the stable mode of the method considering different system models employed in EKF. The 1st modal frequencies computed from identified parameters in a series of excitation cases show consistent variation trend with the SRIM method results, even though the frequency values may differ from each other depending on system models. The four story frame building is also estimated based on the stable mode employing a 4-DOF lumped mass model and a 2D frame model. After tuning mass distribution of the structure carefully, the 1st and 2nd modal frequencies in a series of excitation cases can be reproduced fairly based on the 2D frame model, while only the 1st modal frequencies are accurately achieved with the 4-DOF lumped mass model. Accurate response estimation results are also presented based on the 2D frame model, demonstrating its reasonability. Finally, track mode of the EKF-RM method is validated through the substructure experiment which involves strong nonlinearities. Two SDOF models are decomposed from the experiment model for a bearing stiffness and a SR model stiffness identification in a series of excitation cases. Stiffness variations are tracked successfully. The reasonability and consistency of the results are confirmed by experiment report and comparison with the measured hysteresis loops. Finally, the issue of computation mode selection is re-emphasized in this section based on experiment data. Using track mode to the four story building experiment, results show unstable spikes in the parameter convergence history. Using stable mode to the substructure experiment, significant stiffness variation part is totally missed and estimated velocity shows large differences from the observed one indicating its time-variant parameter characteristics.

Thus, the selection of computation modes plays an important role.

In chapter 3, an EKF based dynamic displacement estimation method is proposed for nonlinear SDOF system under seismic excitation. In this method, the track mode of EKF-RM method is firstly employed to distinguish the time interval with strong nonlinearity of the system. By assuming known residual displacement, a displacement measurement signal is generated. In the beginning and ending parts, i.e. system in elastic phases, the combination of double integrated and residual displacement is employed, while in the middle part, i.e. system in nonlinear phase, a straight line (virtual displacement) with a large measurement noise is regarded as measurement. This displacement measurement and acceleration are observation for the EKF. In order to consider the nonlinearity during the virtual displacement part, two methods are employed, i.e. one using an augmented state vector with time-variant stiffness and the other assuming a bi-linear system model with optimized model parameters. In the first method, better results are usually obtained by updating the virtual displacement using results from the 1st computation results. Therefore, in fact, this two iteration scheme is employed for the first method. The EKF structures of both methods are based on incremental Newmark-beta method. Results from EKF are further smoothed by EKS which turn to be more accurate.

Two numerical models, a bi-linear model and a Bouc-Wen model, are numerically investigated in detail. By applying the proposed methods, accurate displacement results can be obtained. The effectiveness of the proposed methods is further verified with 24 simulated signals. They are generated using three hysteresis models, including bi-linear model, tri-linear model and Bouc-Wen model, excited by four different earthquakes of two PGA, i.e. 400gal and 800gal. The methods work well in most of the 24 cases, except in one case the estimation error is relatively large. In this case, the virtual displacement part is quite long (about 30s) due to strong nonlinearity of system.

The proposed methods are further validated using two E-defense experiments, i.e. a full scale bridge pier and a full scale four story building experiments. SDOF models are simplified from the prototype models and corresponding displacements are estimated in a series of earthquake excitation cases. For all of the 8 experiment cases, estimation results show good accuracies.

The limitation of the current methods includes: 1) residual displacement is assumed as known value beforehand, this may not be true for all cases in practical engineering; 2) the proposed methods can still be regarded as empirical since a two iteration scheme and a bi-linear model assumption are made in the methods; 3) the proposed methods can only be applied to SDOF system so far.

In chapter 4, an adaptive EKF method is proposed for structure system estimation under unknown seismic excitations. In this method, an offline noise estimation method is combined with the EKF method to adapt process noise covariance matrix \mathbf{Q} automatically. In order to enhance the stability of the filter, an acceleration-augmented state vector based on Generalized-alpha method is also introduced. Besides, some criteria about the joint input-state-parameter estimation problems are also discussed. Robustness and effectiveness of the proposed adaptive EKF-UI method is demonstrated with numerical simulations and further validated using experimental data from E-defense database.

Two numerical models, including a bridge pier model and a 2D four story frame structure model, are firstly numerically investigated. By applying the proposed method, accurate parameter identifications as well as input estimation can be achieved with inappropriate initial \mathbf{Q} matrix. Additionally, situations where inaccurate system model are applied in EKF is studied based on a bridge pier model of variant cross section stiffness with substructure. Consistent parameter identification results are obtained using multiple earthquake excitations even though the values are slightly different from those considering known earthquake inputs. The adaptive EKF-UI method combined with substructure method is also numerically investigated using the bridge pier model and a 3D cable stayed bridge model. Consistent parameter identification results can be obtained for parts of a whole complex structure based on the method. However, it is found that the method could be

sensitive to measurement noise and careful selection of substructure is important.

Furthermore, the adaptive EKF-UI method is validated through two E-defense experiments, i.e. a full scale bridge pier experiment and a full scale four story building experiment. For the bridge pier experiment, equivalent uniform EI values are identified based on several measurement schemes in a series of excitation cases. The identified values show consistent variation trends with those obtained considering known earthquake inputs, even though they differ from each other in different levels depending on measurement scheme. The 1st modal frequencies computed using the identified parameters are also compared with those obtained from SRIM method and similar phenomenon is found. Besides, the substructure based method is also employed to identify EI values of upper part of the bridge pier. In this case, however discrepancies of values from the two parts are larger than previous cases. In terms of the four story building experiment, since no measurement point is available on the first floor columns, prior constant ratios between the first and second floor stiffness are introduced for two vibration directions. Basically, the identified results show similar phenomenon as previous experiment case.

A limitation of the proposed method is that the absolute values of identified parameters may not be highly accurate, while experimental validations show that parameter variations under a series of excitation cases are consistent with those obtained considering known inputs. For practical applications, changes of identified values over multiple earthquakes are expected to be used as evaluation indices.

The study in the thesis addresses problems in the application of filtering methods in structural system evaluation using seismic response data. The filtering methods had been limited to ideal numerical simulations and oversimplified experiments. This study improves the methods and numerical stability and accuracy in the inverse problem. However, because of the complexity of some structures and their responses, the proposed methods are expected to be further improved for their wide-spread use in post-earthquake assessment of a variety of structures.

Appendix A. SHAKE algorithm

This section is a literal copy of the information provided in [125] and [143].

A.1 Theory

The theory considers the response associate with vertical propagation of shear waves through the linear viscoelastic system shown in Figure A.0.1. The system consists of N horizontal layers, which extend to infinity in the horizontal direction and has a half space as the bottom layer. Each layer is homogenous and isotropic and is characterized by the thickness h , mass density ρ , shear modulus G and damping factor β

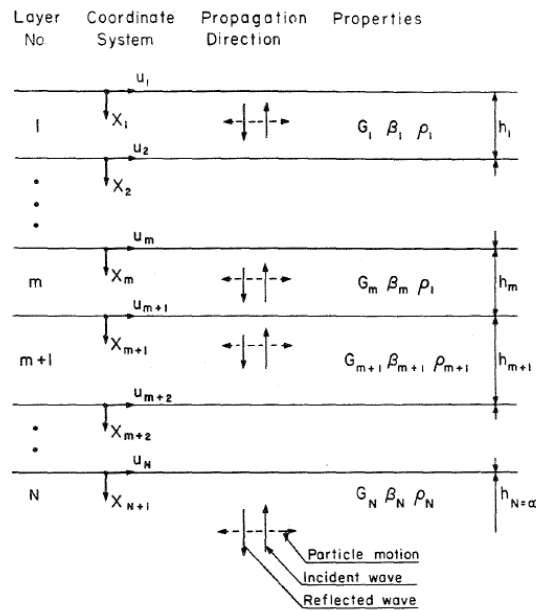


Figure A.0.1 One-dimension system (after Schnabel et al., 1972 [143])

A.2 Propagation of harmonic shear waves in a one-dimension system

Vertical propagation of shear waves through the system shown in Figure A.0.1 will cause horizontal displacements

$$u = u(x, t) \quad (A.1)$$

which must satisfy the wave equation

$$\rho \frac{\partial^2 u}{\partial t^2} = G \frac{\partial^2 u}{\partial x^2} + \eta \frac{\partial^3 u}{\partial x^2 \partial t} \quad (A.2)$$

Harmonic displacements with frequency ω can be written in the form

$$u(x, t) = U(x) \exp(i\omega t) \quad (A.3)$$

Substituting Eq. (A.3) into Eq. (A.2) results in an ordinary differential equation

$$(G + i\omega\eta) \frac{\partial^2 U}{\partial x^2} = \rho\omega^2 U \quad (\text{A.4})$$

which has the general solution

$$U(x) = E \exp(ikx) + F \exp(-ikx) \quad (\text{A.5})$$

in which

$$k^2 = \frac{\rho\omega^2}{G + i\omega\eta} = \frac{\rho\omega^2}{G^*} \quad (\text{A.6})$$

where k is the complex wave number and G^* is the complex shear modulus. The critical damping ratio β is related to the viscosity η by

$$\omega\eta = 2G\beta \quad (\text{A.7})$$

Experiments on many soil materials indicate that G and β are nearly constant over the frequency range which is of main interest in the analysis. It is therefore convenient to express the complex shear modulus in terms of the critical damping ratio instead of the viscosity:

$$G^* = G + i\omega\eta = G(1 + 2i\beta) \quad (\text{A.8})$$

Where G^* can be assumed to be independent of frequency

Eq. (A.3) and Eq. (A.5) give the solution to the wave equation for a harmonic motion of frequency ω

$$u(x, t) = E \exp(ikx + i\omega t) + F \exp(-ikx + i\omega t) \quad (\text{A.9})$$

Where the first term represents the incident wave traveling in the negative x -direction (upwards) and the second terms represents the reflected wave traveling in the positive x -direction (downwards).

Eq.(A.9) is valid for each of the layers in Figure A.0.1. Introducing a local coordinate system X for each layer, the displacements at the top and bottom of layer m are

$$u_m(X = 0) = (E_m + F_m) \exp(i\omega t) \quad (\text{A.10})$$

$$u_m(X = h_m) = [E_m \exp(ik_m h_m) + F_m \exp(-ik_m h_m)] \exp(i\omega t) \quad (\text{A.11})$$

The shear stress on a horizontal plane is

$$\tau(x, t) = G \frac{\partial u}{\partial x} + \eta \frac{\partial^2 u}{\partial x \partial t} = G^* \frac{\partial u}{\partial x} \quad (\text{A.12})$$

Or by Eq. (A.9)

$$\tau(x, t) = ikG^* [E \exp(ikx) - F \exp(-ikx)] \exp(i\omega t) \quad (\text{A.13})$$

And the shear stresses at the top and bottom of layer m are respectively

$$\tau_m(X=0) = ik_m G_m^* (E_m - F_m) \exp(i\omega t) \quad (\text{A.14})$$

$$\tau_m(X=h_m) = ik_m G_m^* [E_m \exp(ik_m h_m) - F_m \exp(-ik_m h_m)] \exp(i\omega t) \quad (\text{A.15})$$

Stresses and displacements must be continuous at all interfaces. Hence, by Eq. (A.10), (A.11), (A.14) and (A.15)

$$E_{m+1} + F_{m+1} = E_m \exp(ik_m h_m) + F_m \exp(-ik_m h_m) \quad (\text{A.16})$$

$$E_{m+1} - F_{m+1} = \frac{k_m G_m^*}{k_{m+1} G_{m+1}^*} [E_m \exp(ik_m h_m) - F_m \exp(-ik_m h_m)] \quad (\text{A.17})$$

Subtraction and addition of Eq. (A.16) and (A.17) yield the following recursion formulas for the amplitudes, E_{m+1} and F_{m+1} of the incident and reflected wave in layer $m+1$, expressed in terms of the amplitudes in layer m :

$$E_{m+1} = \frac{1}{2} E_m (1 + \alpha_m) \exp(ik_m h_m) + \frac{1}{2} F_m (1 - \alpha_m) \exp(-ik_m h_m) \quad (\text{A.18})$$

$$F_{m+1} = \frac{1}{2} E_m (1 - \alpha_m) \exp(ik_m h_m) + \frac{1}{2} F_m (1 + \alpha_m) \exp(-ik_m h_m) \quad (\text{A.19})$$

where α_m is the complex impedance ration

$$\alpha_m = \frac{k_m G_m^*}{k_{m+1} G_{m+1}^*} = \left(\frac{\rho_m G_m^*}{\rho_{m+1} G_{m+1}^*} \right)^{0.5} \quad (\text{A.20})$$

which again is independent of frequency.

At the free surface, the shear stresses must be zero. In addition, Eq. (A.13) with τ_l and X_l equal to zero gives $E_l = F_l$, i.e. the amplitudes of the incident and reflected waves are always equal at the free surface. Beginning with the surface layer, repeated use of the recursion formulas Eq. (A.18) and Eq. (A.19) leads to the following relationships between the amplitudes in the layer m and those in the surface layer

$$E_m = e_m(\omega) E_1 \quad (\text{A.21})$$

$$F_m = f_m(\omega) E_1 \quad (\text{A.22})$$

The transfer function e_m and f_m are simply the amplitudes for the case $E_l = F_l = 1$, and can be determined by substituting this condition into the above recursion formulas.

Other transfer functions are easily obtained from the e_m and f_m functions. The transfer function $A_{n,m}$ between the displacements at level n and m is defined by

$$A_{n,m}(\omega) = \frac{u_m}{u_n} \quad (\text{A.23})$$

And by substituting Eq. (A.10), (A.21) and (A.22)

$$A_{n,m}(\omega) = \frac{e_m(\omega) + f_m(\omega)}{e_n(\omega) + f_n(\omega)} \quad (\text{A.24})$$

Based on these equations the transfer function $A(\omega)$ can be found between any two layers in the system. Hence, if the motion is known in any one layer in the system, the motion can be computed in any other layer.

The amplitudes, E and F can thus be computed for all layers in the system, and the strain acceleration can be derived from the displacement function. Accelerations are expressed by the equation

$$\ddot{u}(x,t) = \frac{\partial^2 u}{\partial t^2} = -\omega^2 [E \exp(ikx + i\omega t) + F \exp(-ikx + i\omega t)] \quad (\text{A.25})$$

and strains by

$$\gamma = \frac{\partial u}{\partial x} = ik [E \exp(ikx + i\omega t) - F \exp(-ikx + i\omega t)] \quad (\text{A.26})$$

A.3 Transition motion

The expression developed above is valid for steady state harmonic motions. The theory can be extended to transient motions through the use of Fourier transformation.

A digitized seismograph with n equidistant acceleration values, $\ddot{u}_j(j\Delta t)$, $j=0, \dots, n-1$, can be represented by a finite sum of harmonic motions

$$\ddot{u}(t) = \sum_{s=0}^{n/2} [a_s \exp(i\omega_s t) + b_s \exp(-i\omega_s t)] \quad (\text{A.27})$$

where ω_s , $s=0, \dots, n/2$ are the equidistant frequencies

$$\omega_s = \frac{2\pi}{n\Delta t} s \quad (\text{A.28})$$

a_s and b_s designate the complex Fourier coefficients

$$a_s = \frac{1}{n} \sum_{j=0}^{n-1} \ddot{u}(t) \exp(-i\omega_s t) \quad b_s = \frac{1}{n} \sum_{j=0}^{n-1} \ddot{u}(t) \exp(i\omega_s t) \quad (\text{A.29})$$

And each term in Eq. (A.27) is a harmonic motion oscillating with frequency ω_s .

If the series in Eq. (A.27) represent the motion in a layer m , a new series representing the motion in any other layer n , is obtained by applying the appropriate factor from Eq. (A.24) to each term in the series

$$\ddot{u}_n(t) = \sum_{s=0}^{n/2} A_{m,n}(\omega_s) [a_{m,s} \exp(i\omega_s t) + b_{m,s} \exp(-i\omega_s t)] \quad (\text{A.30})$$

The representation of a discrete motion with its Fourier transform gives an exact representation of the motion at the discrete points $t=j\Delta t$, $j=0, \dots, n-1$. Cyclic repetition of the motion with the period $T=n\Delta t$ is implied in the solution. The solution applied, therefore, to an infinite train of

identical accelerograms rather than the given single accelerogram. For systems with damping this is not of any significant consequence since the individual accelerograms can be separated by a quiet zone of zeros causing the responses from one cycle to damp out before the beginning of the next cycle.

A.4 Description of Program SHAKE

Program SHAKE computes the response in a system of homogenous, visco-elastic layers of infinite horizontal extent subjected to vertically travelling shear waves. The system is shown in Figure A.0.1. the program is based on the continuous solution to the wave equation adapted for the use with transient motions through the Fast Fourier Transform algorithm. The nonlinearity of the shear modulus and damping is accounted for by the use of equivalent linear soil properties using an iterative procedure to obtain values for modulus and damping compatible with effective strains γ_{eff} in each layer. It is computed from the maximum strain γ_{max} as

$$\gamma_{eff} = \alpha \gamma_{max} \quad (A.31)$$

where α is a coefficient to be chosen in order to obtain a good prediction. The value of $\alpha=0.65$ has been frequently used in the engineering practice without much consideration.

Appendix B. SR model computation for grouped pile foundation in layered soil

This section is a literal copy of the information provided in [123, 124].

B.1 lateral vibration of single pile in Winkler medium

The lateral harmonic deflection $Y(z,t)=Y(z)\exp(i\omega t)$, of a vertical elastic pile embedded in a Winkler medium satisfies the following well-known equation

$$\frac{d^4 Y(z)}{dz^4} + 4\lambda(z, \omega)^4 Y(z) = \frac{q(z)}{EI} \quad (\text{B.1})$$

with $\lambda(z, \omega)$ given by

$$\lambda(z, \omega) = \left[\left(k^*(z, \omega) - m\omega^2 \right) / 4EI \right]^{1/4} \quad (\text{B.2})$$

where EI and m is flexural rigidity and mass per unit length of the pile, respectively; $q(z)$ is distributed forces along the pile; $k^*(z, \omega) = k(z, \omega) + i\omega c(z, \omega)$ is complex soil impedance encompassing the stiffness, inertial, radiation and hysteretic action of and in the soil; λ is a complex wavenumber associated with propagation of flexural waves along the pile.

In the special case of a pile of length L embedded in a homogenous soil of thickness $h=L$, the solution to Eq.(B.1) yields, after some straightforward algebra and enforcement of boundary conditions, the following closed form expression for the complex impedances $S_{ij}(\omega) = K_{ij}(\omega) + i\omega C_{ij}(\omega)$, at the head of the pile

$$S_{hh} = 4EI\lambda^3 \frac{\sin(2\lambda h) + \sinh(2\lambda h)}{\pm 2 + \cos(2\lambda h) + \cosh(2\lambda h)} \quad (\text{B.3})$$

$$S_{hr} = 2EI\lambda^2 \frac{-\cos(2\lambda h) + \cosh(2\lambda h)}{\pm 2 + \cos(2\lambda h) + \cosh(2\lambda h)} \quad (\text{B.4})$$

$$S_{rr} = 2EI\lambda \frac{-\sin(2\lambda h) + \sinh(2\lambda h)}{\pm 2 + \cos(2\lambda h) + \cosh(2\lambda h)} \quad (\text{B.5})$$

where S_{hh} , S_{rr} , and S_{hr} are the swaying, rocking, and cross-swaying-rocking impedances, respectively. The plus sign in the denominator of Eq. (B.3~5) corresponds to the special case of a pile completely free of stresses at the tip, whereas the minus sign corresponds to a perfectly fixed base pile. For an infinitely long pile, ratios on the right hand side of above equations tend to unity and thereby pile impedances converge to the well-known expressions

$$S_{hh} = 4EI\lambda^3 \quad S_{hr} = 2EI\lambda^2 \quad S_{rr} = 2EI\lambda \quad (\text{B.6})$$

B.2 Interaction between two piles

In addition to loading transmitted to piles from the superstructure through the cap, grouped piles experience additional dynamic loading imposed along their shafts by waves emitted from the neighboring piles. Such dynamic group effects can be treated approximately using complex

interaction factors, which account for the dynamic interplay between two piles. This type of analysis, referred to as the “superposition method,” provides good (although approximate) estimates of the dynamic response of a pile group.

The interaction factor α between two piles is defined based on the response of a pile carrying no load at its head (hereafter called pile2 or ‘receiver’ pile), subjected to the ground vibrations produced by a neighboring pile (hereafter called pile 1 or ‘source’ pile), which is loaded with either (1) a horizontal force or (2) a moment. The interaction factor then is defined as the response (translation or rotation) atop the receiver pile, normalized by the corresponding responses of the source pile caused by its own loading. In flexural vibrations the interaction factor is expressed by a 2×2 complex matrix

$$\alpha(s, \theta) = \begin{bmatrix} \alpha_{uP} & \alpha_{uM} \\ \alpha_{\phi P} & \alpha_{\phi M} \end{bmatrix} \quad (\text{B.7})$$

where α_{uP} is swaying interaction factor; $\alpha_{\phi M}$ is rocking interaction factor; α_{uM} and $\alpha_{\phi P}$ are cross-swaying-rocking factors; s is axis-to-axis distance between piles; and θ is aperture angle between the direction of loading and the line connecting the pile centers.

To compute the interaction factor α , an approximate method involving following three consecutive steps are presented:

1) Step1. The deflected shape of the source pile, hereafter referred to as $Y_{II}(z)$, to a unit force or moment applied at its head is determined using any pertinent analytical approach.

2) Step2. Cylindrical waves are emitted from the periphery of the source pile with amplitude equal to the deflected pile shape $Y_{II}(z)$. With the soil composed by distinct homogenous horizontal layers, it is assumed that the waves propagate in an essentially horizontal manner within each individual layer. This implies that the radial spreading of these waves, although different for each layer, still obeys (even if approximately) the plane-strain attenuation law expressed by attenuation function $\Psi(s, \theta)$.

$$\Psi(s, \theta) = \frac{U(s, \theta, z)}{U(d/2, \theta, z)} \approx \Psi(s, 0) \cos^2 \theta + \Psi(s, \pi/2) \sin^2 \theta \quad (\text{B.8})$$

$$\Psi(s, 0) \approx \left(\frac{2s}{d}\right)^{-0.5} \exp \left[-(\beta_s + i) \left(\frac{s}{d} - \frac{1}{2} \right) \frac{V_s}{V_{La}} a_0 \right] \quad (\text{B.9})$$

$$\Psi\left(s, \frac{\pi}{2}\right) \approx \left(\frac{2s}{d}\right)^{-0.5} \exp \left[-(\beta_s + i) \left(\frac{s}{d} - \frac{1}{2} \right) a_0 \right] \quad (\text{B.10})$$

where $U(s, \theta, z)$ is horizontal soil displacement; $\Psi(s, 0)$ and $\Psi(s, \pi/2)$ is attenuation functions corresponding to wave traveling along and perpendicular to the direction of loading, respectively; V_{La} is the so-called ‘Lysmer’s analogue’ wave velocity $V_{La} = 3.4V_s / [(1-\nu)\pi]$; β_s is hysteretic soil damping; $a_0 = \omega d / V_s$. Therefore, in the soil layer i , the free-field soil displacement at a distance s and angle θ

$$U(s, z, \theta) \approx \Psi(s, \theta)_i Y_{II}(z)_i \quad (\text{B.11})$$

where i is the number of the layer.

3) Step 3. The receiver pile does not follow exactly the free field motion of step 2. Its inertial and flexural resistance would give rise to an interaction between this (the receiver) pile and the surrounding soil, leading to a diffraction of the arriving wave field. Thereby, the pile displacement will be different than that given by (B.11). Moreover, a rotation is generated at the head of the

receiver pile, which cannot be calculated directly from (B.11). To account in a simple yet realistic way for this interaction, the receiver pile is modeled as a Winkler supported beam in which the excitation $U(s, z)$ is applied at the support of the distributed springs and dashpots attached to the pile. The mechanics of this loading is in a sense the reverse of step 1. In step 1 the source pile induces displacements on soil through its “reacting” springs-dashpots, whereas in step 3 the soil induces displacements on the receiver pile through its “transmitting” springs-dashpots.

For a receiver pile, the dynamic equilibrium of an infinitesimal pile segment produces the following equation governing the deflection $Y_{21}(z)$ of the pile

$$\frac{d^4 Y_{21}(z)}{dz^4} + 4\lambda^4 Y_{21}(z) = k(z, \omega) \Psi(s, \theta) Y_{11}(z) / EI \quad (B.12)$$

The forcing term on the right side of (B.12) is equal to the attenuated free-field soil displacement times the dynamic soil impedance, divided by the flexural rigidity of the pile; $Y_{11}(z)$ is the deflected shape of the source pile, obtained for each particular soil layer from the solution of the homogeneous part of (B.1).

$$Y_{11}(z) = \exp(\lambda z)(A_{11} \sin \lambda z + B_{11} \cos \lambda z) + \exp(-\lambda z)(C_{11} \sin \lambda z + D_{11} \cos \lambda z) \quad (B.13)$$

where A_{11} , B_{11} , C_{11} and D_{11} are integration constants determined from the boundary conditions of the source pile (step 1), The solution to (B.12) is

$$Y_{21}(z) = \frac{k(\omega)}{k(\omega) - m\omega^2} \Psi(s, \theta) \frac{\lambda z}{4} Y_{11}(z) + \exp(\lambda z)(A_{21} \sin \lambda z + B_{21} \cos \lambda z) + \exp(-\lambda z)(C_{21} \sin \lambda z + D_{21} \cos \lambda z) \quad (B.14)$$

where A_{11} , B_{11} , C_{11} and D_{11} are integration constants determined from the boundary conditions of the receiver pile (i.e. zero shear force and bending moment at the pile head and continuity of force, moment, displacement, and rotation at the various interfaces). Differentiating (B.14) with respect to z yields the flexural rotations, $\Theta_{21}(z)$ along the receiver pile. The interaction factors are calculated as: $\alpha_{uP} = Y_{21}(0)/Y_{11}(0)$, $\alpha_{\phi P} = \Theta_{21}(0)/\Theta_{11}(0)$, $\alpha_{uM} = Y_{21}(0)/Y_{11}(0)$, $\alpha_{\phi M} = \Theta_{21}(0)/\Theta_{11}(0)$.

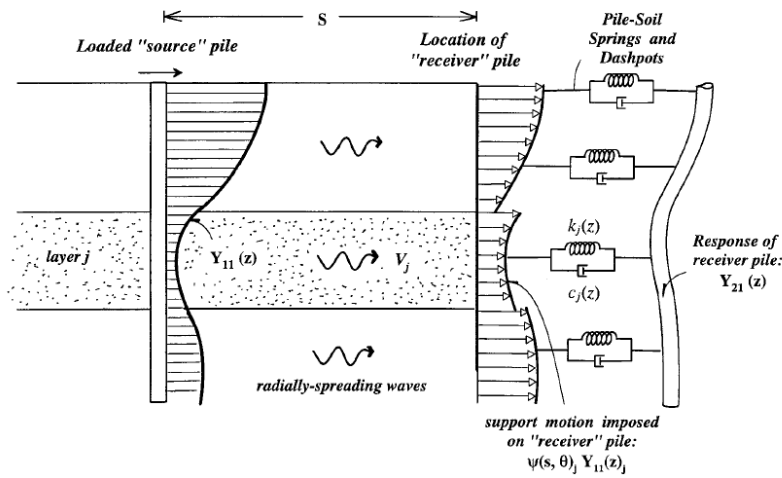


Figure B.1 Schematic illustration for computing influence of head-loaded source pile on adjacent receiver pile carrying no load at its head in layered soil[123]

B.3 Dynamic stiffness of SR model of a group of piles

Knowledge of the dynamic stiffness of the single pile and the dynamic interaction factors between any two piles allow the computation of the dynamic stiffness of a group of piles using the concept of superposition. For example, let y_i be the horizontal displacement of pile I belonging to a group of N piles. Superposition of displacement leads to

$$y_i = \sum_{j=1}^N \alpha(i, j) y_j \quad (\text{B.15})$$

where $\alpha(i, j)$ is calculated as in section B.2 . The value y_j is displacement of a single (solitary) pile which is obtained as

$$y_j = \frac{F_j}{S_{[1]}} \quad (\text{B.16})$$

where F_j is force that this pile carries and $S_{[1]}$ is dynamic stiffness of the single pile. Since all piles are connected with a rigid cap, the displacement group $y_{[G]}$ is equal to y_i for all i . Substitution of Eq.B(16) into Eq.(B.15) gives

$$y_{[G]} S_{[1]} = \sum_{j=1}^N \alpha(i, j) F_j \quad (\text{B.17})$$

Repeating Eq.(B.17) for all N piles of the pile group, one obtains the matrix equation

$$\begin{bmatrix} \alpha(1,1) & \alpha(1,2) & \cdots & \alpha(1,N) \\ \alpha(2,1) & \alpha(2,2) & \cdots & \alpha(2,N) \\ \vdots & \vdots & & \vdots \\ \alpha(N,1) & \alpha(N,2) & \cdots & \alpha(N,N) \end{bmatrix} \begin{bmatrix} F_1 \\ F_2 \\ \vdots \\ F_N \end{bmatrix} = y_{[G]} S_{[1]} \begin{bmatrix} 1 \\ 1 \\ \vdots \\ 1 \end{bmatrix} \quad (\text{B.18})$$

Eq.(B.18) can be solved for the force vector.

$$\begin{bmatrix} F_1 \\ F_2 \\ \vdots \\ F_N \end{bmatrix} = \begin{bmatrix} \alpha(1,1) & \alpha(1,2) & \cdots & \alpha(1,N) \\ \alpha(2,1) & \alpha(2,2) & \cdots & \alpha(2,N) \\ \vdots & \vdots & & \vdots \\ \alpha(N,1) & \alpha(N,2) & \cdots & \alpha(N,N) \end{bmatrix}^{-1} y_{[G]} S_{[1]} \begin{bmatrix} 1 \\ 1 \\ \vdots \\ 1 \end{bmatrix} \quad (\text{B.19})$$

Since $P_{[G]} = S_{[G]} y_{[G]} = \sum_i F_i$, the dynamic stiffness of the pile group is simply

$$S_{[G]} = [1 \quad 1 \quad \cdots \quad 1] \begin{bmatrix} \alpha(1,1) & \alpha(1,2) & \cdots & \alpha(1,N) \\ \alpha(2,1) & \alpha(2,2) & \cdots & \alpha(2,N) \\ \vdots & \vdots & & \vdots \\ \alpha(N,1) & \alpha(N,2) & \cdots & \alpha(N,N) \end{bmatrix}^{-1} S_{[1]} \begin{bmatrix} 1 \\ 1 \\ \vdots \\ 1 \end{bmatrix} \quad (\text{B.20})$$

SR model stiffness of other component could be calculated in the similar manner.

References

- [1] *Road maintenance in japan: Problems and solutions*. 2015.
- [2] Soyoz, S. and M.Q. Feng, *Instantaneous damage detection of bridge structures and experimental verification*. Structural Control and Health Monitoring, 2008. **15**(7): p. 958-973.
- [3] Juang, J.N. and R.S. Pappa, *An Eigensystem Realization Algorithm for Modal Parameter Identification and Model Reduction*. J Guidance Control & Dynamics, 1985. **8**(5): p. 620-627.
- [4] Peeters, B. and G. De Roeck, *Stochastic System Identification for Operational Modal Analysis: A Review*. Journal of Dynamic Systems, Measurement, and Control, 2001. **123**(4): p. 659-667.
- [5] Peeters, B. and G.D. Roeck, *REFERENCE-BASED STOCHASTIC SUBSPACE IDENTIFICATION FOR OUTPUT-ONLY MODAL ANALYSIS*. Mechanical Systems & Signal Processing, 1999. **13**(6): p. 855-878.
- [6] Chaudhary, M.T.A., et al., *System identification of two base-isolated bridges using seismic records*. Journal of Structural Engineering, 2000. **126**(10): p. 1187-1195.
- [7] Chaudhary, M.T.A., M. Abé, and Y. Fujino, *Performance evaluation of base-isolated Yama-agé bridge with high damping rubber bearings using recorded seismic data*. Engineering Structures, 2001. **23**(8): p. 902-910.
- [8] Chaudhary, M., M. Abe, and Y. Fujino, *Identification of soil–structure interaction effect in base-isolated bridges from earthquake records*. Soil Dynamics and Earthquake Engineering, 2001. **21**(8): p. 713-725.
- [9] Smyth, A.W., J.S. Pei, and S.F. Masri, *System identification of the Vincent Thomas suspension bridge using earthquake records*. Earthquake Engineering & Structural Dynamics, 2003. **32**(3): p. 339-367.
- [10] Siringoringo, D.M. and Y. Fujino, *System identification applied to long - span cable - supported bridges using seismic records*. Earthquake Engineering & Structural Dynamics, 2008. **37**(3): p. 361-386.
- [11] Siringoringo, D.M. and Y. Fujino, *Observed dynamic performance of the Yokohama - Bay Bridge from system identification using seismic records*. Structural Control and Health Monitoring: The Official Journal of the International Association for Structural Control and Monitoring and of the European Association for the Control of Structures, 2006. **13**(1): p. 226-244.
- [12] Wan, E.A. and R. Van Der Merwe. *The unscented Kalman filter for nonlinear estimation*. in *Adaptive Systems for Signal Processing, Communications, and Control Symposium 2000. AS-SPCC. The IEEE 2000*. 2000. Ieee.
- [13] Julier, S.J., J.K. Uhlmann, and H.F. Durrant-Whyte. *A new approach for filtering nonlinear systems*. in *Proceedings of 1995 American Control Conference-ACC'95*. 1995. IEEE.
- [14] Julier, S.J. and J.K. Uhlmann. *New extension of the Kalman filter to nonlinear systems*. in *Signal processing, sensor fusion, and target recognition VI*. 1997. International Society for Optics and Photonics.
- [15] Särkkä, S., *Bayesian filtering and smoothing*. Vol. 3. 2013: Cambridge University Press.
- [16] Julier, S.J. *The spherical simplex unscented transformation*. in *Proceedings of the 2003 American Control Conference, 2003*. 2003. IEEE.
- [17] Haseltine, E.L. and J.B. Rawlings, *Critical evaluation of extended Kalman filtering and moving-horizon estimation*. Industrial & engineering chemistry research, 2005. **44**(8): p. 2451-2460.
- [18] Kandepu, R., L. Imsland, and B.A. Foss. *Constrained state estimation using the unscented Kalman filter*. in *Control and Automation, 2008 16th Mediterranean Conference on*. 2008. Citeseer.
- [19] Kandepu, R., B. Foss, and L. Imsland, *Applying the unscented Kalman filter for nonlinear state estimation*. Journal of process control, 2008. **18**(7-8): p. 753-768.
- [20] Teixeira, B.O., et al. *Unscented filtering for interval-constrained nonlinear systems*. in *Decision and Control, 2008. CDC 2008. 47th IEEE Conference on*. 2008. IEEE.
- [21] Xu, Y., X. Chen, and Q. Li, *Adaptive iterated extended kalman filter and its application to autonomous integrated navigation for indoor robot*. The Scientific World Journal, 2014. **2014**.
- [22] Trigo, F.C. and R. Gonzalez-Lima, *Iterated extended Kalman filter with adaptive state noise estimation for electrical impedance tomography*. Technology Meets Surgery International in 2005 by ABCM, 2005.
- [23] Zhan, R. and J. Wan, *Iterated Unscented Kalman Filter for Passive Target Tracking*. IEEE Transactions on Aerospace and Electronic Systems, 2007. **43**(3): p. 1155-1163.
- [24] Xie, Z. and J. Feng, *Real-time nonlinear structural system identification via iterated unscented Kalman filter*. Mechanical Systems and Signal Processing, 2012. **28**: p. 309-322.
- [25] Wu, P., X. Li, and Y. Bo, *Iterated square root unscented Kalman filter for maneuvering target tracking*

- using TDOA measurements. *International Journal of Control, Automation and Systems*, 2013. **11**(4): p. 761-767.
- [26] Sibley, G., G. Sukhatme, and L. Matthies, *The Iterated Sigma Point Kalman Filter with Applications to Long Range Stereo*. Vol. 8. 2006.
- [27] Yun, C.-B. and M. Shinozuka, *Identification of Nonlinear Structural Dynamic Systems*. *Journal of Structural Mechanics*, 1980. **8**(2): p. 187-203.
- [28] Hoshiya, M. and E. Saito, *Structural identification by extended Kalman filter*. *Journal of engineering mechanics*, 1984. **110**(12): p. 1757-1770.
- [29] Koh, C.G., L.M. See, and T. Balendra, *Estimation of structural parameters in time domain: a substructure approach*. *Earthquake Engineering & Structural Dynamics*, 1991. **20**(8): p. 787-801.
- [30] Yang, J.N., et al., *An adaptive extended Kalman filter for structural damage identification*. *Structural Control and Health Monitoring: The Official Journal of the International Association for Structural Control and Monitoring and of the European Association for the Control of Structures*, 2006. **13**(4): p. 849-867.
- [31] Lei, Y., H. Zhou, and Z.-L. Lai, *A Computationally Efficient Algorithm for Real-Time Tracking the Abrupt Stiffness Degradations of Structural Elements*. *Computer-Aided Civil and Infrastructure Engineering*, 2016. **31**(6): p. 465-480.
- [32] Corigliano, A. and S. Mariani, *Parameter identification in explicit structural dynamics: performance of the extended Kalman filter*. *Computer Methods in Applied Mechanics and Engineering*, 2004. **193**(36-38): p. 3807-3835.
- [33] Ebrahimian, H., R. Astroza, and J.P. Conte, *Extended Kalman filter for material parameter estimation in nonlinear structural finite element models using direct differentiation method*. *Earthquake Engineering & Structural Dynamics*, 2015. **44**(10): p. 1495-1522.
- [34] Wu, M. and A.W. Smyth, *Application of the unscented Kalman filter for real - time nonlinear structural system identification*. *Structural Control and Health Monitoring: The Official Journal of the International Association for Structural Control and Monitoring and of the European Association for the Control of Structures*, 2007. **14**(7): p. 971-990.
- [35] Mariani, S. and A. Ghisi, *Unscented Kalman filtering for nonlinear structural dynamics*. *Nonlinear Dynamics*, 2007. **49**(1-2): p. 131-150.
- [36] Omrani, R., R. Hudson, and E. Taciroglu, *Parametric identification of nondegrading hysteresis in a laterally and torsionally coupled building using an unscented Kalman filter*. *Journal of Engineering Mechanics*, 2013. **139**(4): p. 452-468.
- [37] Chatzi, E.N. and A.W. Smyth, *The unscented Kalman filter and particle filter methods for nonlinear structural system identification with non - collocated heterogeneous sensing*. *Structural Control and Health Monitoring: The Official Journal of the International Association for Structural Control and Monitoring and of the European Association for the Control of Structures*, 2009. **16**(1): p. 99-123.
- [38] Bisht, S.S. and M.P. Singh, *An adaptive unscented Kalman filter for tracking sudden stiffness changes*. *Mechanical Systems & Signal Processing*, 2014. **49**(1-2): p. 181-195.
- [39] Zhou, L., S. Wu, and J.N. Yang, *Experimental study of an adaptive extended Kalman filter for structural damage identification*. *Journal of Infrastructure Systems*, 2008. **14**(1): p. 42-51.
- [40] Chatzis, M.N., E.N. Chatzi, and A.W. Smyth, *An experimental validation of time domain system identification methods with fusion of heterogeneous data*. *Earthquake Engineering & Structural Dynamics*, 2015. **44**(4): p. 523-547.
- [41] Chatzi, E.N., A.W. Smyth, and S.F. Masri, *Experimental application of on-line parametric identification for nonlinear hysteretic systems with model uncertainty*. *Structural Safety*, 2010. **32**(5): p. 326-337.
- [42] Shodja, A.H. and F.R. Rofooei, *Using a lumped mass, nonuniform stiffness beam model to obtain the interstory drift spectra*. *Journal of Structural Engineering*, 2014. **140**(5): p. 04013109.
- [43] Kuleli, M., *Stiffness condition assessment of bridge lateral resisting systems with unscented Kalman filter using seismic acceleration response measurements*, in *Department of Civil Engineering*. 2018, The University of Tokyo.
- [44] Nassif, H.H., M. Gindy, and J. Davis, *Comparison of laser Doppler vibrometer with contact sensors for monitoring bridge deflection and vibration*. *Ndt & E International*, 2005. **38**(3): p. 213-218.
- [45] Celebi, M., *GPS in dynamic monitoring of long-period structures*. *Soil Dynamics and Earthquake Engineering*, 2000. **20**(5-8): p. 477-483.
- [46] Olaszek, P., *Investigation of the dynamic characteristic of bridge structures using a computer vision method*. *Measurement*, 1999. **25**(3): p. 227-236.

- [47] Skolnik, D.A. and J.W. Wallace, *Critical assessment of interstory drift measurements*. Journal of structural engineering, 2010. **136**(12): p. 1574-1584.
- [48] Yang, J., J. Li, and G. Lin, *A simple approach to integration of acceleration data for dynamic soil-structure interaction analysis*. Soil dynamics and earthquake engineering, 2006. **26**(8): p. 725-734.
- [49] Çelebi, M. *Real-time monitoring of drift for occupancy resumption*. in *Proc. 14th World Conference on Earthquake Engineering (14WCEE)*. 2008.
- [50] Lee, H.S., Y.H. Hong, and H.W. Park, *Design of an FIR filter for the displacement reconstruction using measured acceleration in low - frequency dominant structures*. International Journal for Numerical Methods in Engineering, 2010. **82**(4): p. 403-434.
- [51] Gomez, F., J.W. Park, and B.F. Spencer Jr, *Reference -free structural dynamic displacement estimation method*. Structural Control and Health Monitoring, 2018. **25**(8): p. e2209.
- [52] Park, J.-W., S.-H. Sim, and H.-J. Jung, *Development of a wireless displacement measurement system using acceleration responses*. Sensors, 2013. **13**(7): p. 8377-8392.
- [53] Kana, I., *Displacement estimation based on measured acceleration responses and non-linear hysteresis parameter identification*, in *Department of Civil Engineering*. 2020, The University of Tokyo.
- [54] Smyth, A. and M. Wu, *Multi-rate Kalman filtering for the data fusion of displacement and acceleration response measurements in dynamic system monitoring*. Mechanical Systems and Signal Processing, 2007. **21**(2): p. 706-723.
- [55] Chang, C. and X. Xiao, *An integrated visual-inertial technique for structural displacement and velocity measurement*. Smart Structures and Systems, 2010. **6**(9): p. 1025-1039.
- [56] Kim, K., et al., *Dynamic displacement estimation by fusing biased high-sampling rate acceleration and low-sampling rate displacement measurements using two-stage Kalman estimator*. Smart Struct. Syst, 2016. **17**(4): p. 647-667.
- [57] Kim, J., K. Kim, and H. Sohn, *Autonomous dynamic displacement estimation from data fusion of acceleration and intermittent displacement measurements*. Mechanical Systems and Signal Processing, 2014. **42**(1-2): p. 194-205.
- [58] Zheng, Z., et al., *Data fusion based multi-rate Kalman filtering with unknown input for on-line estimation of dynamic displacements*. Measurement, 2019. **131**: p. 211-218.
- [59] Park, J.-W., S.-H. Sim, and H.-J. Jung, *Displacement estimation using multimetric data fusion*. IEEE/ASME Transactions On Mechatronics, 2013. **18**(6): p. 1675-1682.
- [60] Lourens, E., et al., *Joint input-response estimation for structural systems based on reduced-order models and vibration data from a limited number of sensors*. Mechanical Systems and Signal Processing, 2012. **29**: p. 310-327.
- [61] Lourens, E., et al., *An augmented Kalman filter for force identification in structural dynamics*. Mechanical Systems and Signal Processing, 2012. **27**: p. 446-460.
- [62] Maes, K., et al., *Design of sensor networks for instantaneous inversion of modally reduced order models in structural dynamics*. Mechanical Systems and Signal Processing, 2015. **52**: p. 628-644.
- [63] Wen, Y.-K., *Method for random vibration of hysteretic systems*. Journal of the engineering mechanics division, 1976. **102**(2): p. 249-263.
- [64] Ismail, M., F. Ikhouane, and J. Rodellar, *The hysteresis Bouc-Wen model, a survey*. Archives of Computational Methods in Engineering, 2009. **16**(2): p. 161-188.
- [65] Li, H., C. Mao, and J. Ou, *Identification of hysteretic dynamic systems by using hybrid extended Kalman filter and wavelet multiresolution analysis with limited observation*. Journal of Engineering Mechanics, 2012. **139**(5): p. 547-558.
- [66] Wang, N., L. Li, and Q. Wang, *Adaptive UKF-Based Parameter Estimation for Bouc-Wen Model of Magnetorheological Elastomer Materials*. Journal of Aerospace Engineering, 2018. **32**(1): p. 04018130.
- [67] Ortiz, G.A., D.A. Alvarez, and D. Bedoya-Ruiz, *Identification of Bouc-Wen type models using the transitional Markov chain Monte Carlo method*. Computers & Structures, 2015. **146**: p. 252-269.
- [68] Kontoroupi, T. and W. Smyth Andrew, *Online Noise Identification for Joint State and Parameter Estimation of Nonlinear Systems*. ASCE-ASME Journal of Risk and Uncertainty in Engineering Systems, Part A: Civil Engineering, 2016. **2**(3): p. B4015006.
- [69] Shan, J., W. Shi, and X. Lu, *Model -reference health monitoring of hysteretic building structure using acceleration measurement with test validation*. Computer - Aided Civil and Infrastructure Engineering, 2016. **31**(6): p. 449-464.
- [70] Shan, J., et al., *Interstory drift estimation of nonlinear structure using acceleration measurement with*

- test validation. *Journal of Engineering Mechanics*, 2015. **141**(10): p. 04015032.
- [71] Yang, J.N., S. Pan, and H. Huang, *An adaptive extended Kalman filter for structural damage identifications II: unknown inputs*. *Structural Control and Health Monitoring: The Official Journal of the International Association for Structural Control and Monitoring and of the European Association for the Control of Structures*, 2007. **14**(3): p. 497-521.
- [72] Lei, Y., Y. Jiang, and Z. Xu, *Structural damage detection with limited input and output measurement signals*. *Mechanical Systems and Signal Processing*, 2012. **28**: p. 229-243.
- [73] Lei, Y., et al., *A novel unscented Kalman filter for recursive state-input-system identification of nonlinear systems*. *Mechanical Systems and Signal Processing*, 2019. **127**: p. 120-135.
- [74] Pan, S., et al., *A general extended Kalman filter for simultaneous estimation of system and unknown inputs*. *Engineering Structures*, 2016. **109**: p. 85-98.
- [75] Al - Hussein, A. and A. Haldar, *Unscented Kalman filter with unknown input and weighted global iteration for health assessment of large structural systems*. *Structural Control and Health Monitoring*, 2016. **23**(1): p. 156-175.
- [76] Katkhuda, H., R. Martinez, and A. Haldar, *Health assessment at local level with unknown input excitation*. *Journal of Structural Engineering*, 2005. **131**(6): p. 956-965.
- [77] Chen, J. and J. Li, *Simultaneous identification of structural parameters and input time history from output-only measurements*. *Computational Mechanics*, 2004. **33**(5): p. 365-374.
- [78] Xu, B., et al., *Structural parameters and dynamic loading identification from incomplete measurements: approach and validation*. *Mechanical systems and signal processing*, 2012. **28**: p. 244-257.
- [79] Ding, Y., et al., *Simultaneous identification of structural parameter and external excitation with an improved unscented Kalman filter*. *Advances in Structural Engineering*, 2015. **18**(11): p. 1981-1998.
- [80] Naets, F., J. Croes, and W. Desmet, *An online coupled state/input/parameter estimation approach for structural dynamics*. *Computer Methods in Applied Mechanics and Engineering*, 2015. **283**: p. 1167-1188.
- [81] Dertimanis, V.K., et al., *Input-state-parameter estimation of structural systems from limited output information*. *Mechanical Systems and Signal Processing*, 2019. **126**: p. 711-746.
- [82] Song, W., *Generalized minimum variance unbiased joint input-state estimation and its unscented scheme for dynamic systems with direct feedthrough*. *Mechanical Systems and Signal Processing*, 2018. **99**: p. 886-920.
- [83] Gillijns, S. and B. De Moor, *Unbiased minimum-variance input and state estimation for linear discrete-time systems with direct feedthrough*. *Automatica*, 2007. **43**(5): p. 934-937.
- [84] Gillijns, S. and B. De Moor, *Unbiased minimum-variance input and state estimation for linear discrete-time systems*. *Automatica*, 2007. **43**(1): p. 111-116.
- [85] Maes, K., et al., *Dynamic strain estimation for fatigue assessment of an offshore monopile wind turbine using filtering and modal expansion algorithms*. *Mechanical Systems and Signal Processing*, 2016. **76**: p. 592-611.
- [86] Azam, S.E., E. Chatzi, and C. Papadimitriou, *A dual Kalman filter approach for state estimation via output-only acceleration measurements*. *Mechanical Systems and Signal Processing*, 2015. **60**: p. 866-886.
- [87] Astroza, R., et al., *Bayesian nonlinear structural FE model and seismic input identification for damage assessment of civil structures*. *Mechanical Systems and Signal Processing*, 2017. **93**: p. 661-687.
- [88] Erazo, K. and S. Nagarajaiah, *An offline approach for output-only Bayesian identification of stochastic nonlinear systems using unscented Kalman filtering*. *Journal of Sound and Vibration*, 2017. **397**: p. 222-240.
- [89] Huang, H., J.N. Yang, and L. Zhou, *Adaptive quadratic sum - squares error with unknown inputs for damage identification of structures*. *Structural Control and Health Monitoring*, 2010. **17**(4): p. 404-426.
- [90] Lei, Y., C. Liu, and L. Liu, *Identification of multistory shear buildings under unknown earthquake excitation using partial output measurements: numerical and experimental studies*. *Structural Control and Health Monitoring*, 2014. **21**(5): p. 774-783.
- [91] Mehra, R.K. *Approaches to adaptive filtering*. in *1970 IEEE Symposium on Adaptive Processes (9th) Decision and Control*. 1970.
- [92] Bavdekar, V.A., A.P. Deshpande, and S.C. Patwardhan, *Identification of process and measurement noise covariance for state and parameter estimation using extended Kalman filter*. *Journal of Process Control*, 2011. **21**(4): p. 585-601.
- [93] Kokkala, J., A. Solin, and S. Särkkä. *Expectation maximization based parameter estimation by sigma-point and particle smoothing*. in *17th International Conference on Information Fusion (FUSION)*.

2014. IEEE.

- [94] Soken, H.E. and S.-i. Sakai, *Adaptive tuning of the unscented Kalman filter for satellite attitude estimation*. Journal of Aerospace Engineering, 2014. **28**(3): p. 04014088.
- [95] Soken, H.E. and C. Hajiyeve, *Adaptive fading UKF with Q-adaptation: application to picosatellite attitude estimation*. Journal of Aerospace Engineering, 2011. **26**(3): p. 628-636.
- [96] Hajiyeve, C. and H.E. Soken, *Robust adaptive unscented Kalman filter for attitude estimation of pico satellites*. International Journal of Adaptive Control and Signal Processing, 2014. **28**(2): p. 107-120.
- [97] Van Der Merwe, R., *Sigma-point Kalman filters for probabilistic inference in dynamic state-space models*. 2004, OGI School of Science & Engineering at OHSU.
- [98] Calabrese, A., S. Strano, and M. Terzo, *Adaptive constrained unscented Kalman filtering for real - time nonlinear structural system identification*. Structural Control and Health Monitoring, 2018. **25**(2): p. e2084.
- [99] Lai, Z., et al., *Moving-window extended Kalman filter for structural damage detection with unknown process and measurement noises*. Measurement, 2016. **88**: p. 428-440.
- [100] Kuleli, M. and T. Nagayama, *A robust structural parameter estimation method using seismic response measurements*. Structural Control and Health Monitoring, 2020. **27**(3): p. e2475.
- [101] Robbins, H. and S. Monro, *A Stochastic Approximation Method*. Ann. Math. Statist., 1951. **22**(3): p. 400-407.
- [102] *Technical Report for Full-scale Shaking Table Collapse Experiment on 4-story Steel Moment Frame, E-Defense Steel Building Projects*. National Research Institute for Earth Science and Disaster Resilience, [ASEBI] <https://www.edgrid.jp>.
- [103] *Technical Report for Large-scale Shaking Table Experiment on a Component Model (C1-1model) Using E-Defense, Experiment on a RC Column Build in 1970s which Fails in Flexure*. National Research Institute for Earth Science and Disaster Resilience, [ASEBI] <https://www.edgrid.jp>.
- [104] *Technical Report for Condition Assessment of Structures-Soils and Underground Structures, Maintenance and Recovery of Functionality in Urban Infrastructures*. National Research Institute for Earth Science and Disaster Resilience, [ASEBI] <https://www.edgrid.jp>.
- [105] Zhou, Y., et al., *A New Adaptive Square-Root Unscented Kalman Filter for Nonlinear Systems with Additive Noise*. Vol. 2015. 2015.
- [106] Zheng, B., et al., *A Robust Adaptive Unscented Kalman Filter for Nonlinear Estimation with Uncertain Noise Covariance*. Sensors, 2018. **18**(3): p. 808.
- [107] Zhao, L. and X. Wang. *An adaptive UKF with noise statistic estimator*. in *Industrial Electronics and Applications, 2009. ICIEA 2009. 4th IEEE Conference on*. 2009. IEEE.
- [108] Zhang, Y.-A., D. Zhou, and G.-r. Duan. *An adaptive iterated Kalman filter*. in *Computational Engineering in Systems Applications, IMACS Multiconference on*. 2006. IEEE.
- [109] Yang, Y., H. He, and G. Xu, *Adaptively robust filtering for kinematic geodetic positioning*. Journal of geodesy, 2001. **75**(2-3): p. 109-116.
- [110] Yang, Y. and W. Gao, *An optimal adaptive Kalman filter*. Journal of Geodesy, 2006. **80**(4): p. 177-183.
- [111] Song, Q. and J.-D. Han, *An adaptive UKF algorithm for the state and parameter estimations of a mobile robot*. Acta Automatica Sinica, 2008. **34**(1): p. 72.
- [112] Shi, Y., C. Han, and Y. Liang. *Adaptive UKF for target tracking with unknown process noise statistics*. in *Information Fusion, 2009. FUSION'09. 12th International Conference on*. 2009. IEEE.
- [113] Mohamed, A.H. and K.P. Schwarz, *Adaptive Kalman Filtering for INS/GPS*. Journal of Geodesy, 1999. **73**(4): p. 193-203.
- [114] Majeed, M. and I.N. Kar, *Aerodynamic parameter estimation using adaptive unscented Kalman filter*. Aircraft Engineering & Aerospace Technology, 2013. **85**(4): p. 267-279.
- [115] Deng, F., J. Chen, and C. Chen, *Adaptive unscented Kalman filter for parameter and state estimation of nonlinear high-speed objects*. Journal of Systems Engineering and Electronics, 2013. **24**(4): p. 655-665.
- [116] Haykin, S., *Kalman filtering and neural networks*. Vol. 47. 2004: John Wiley & Sons.
- [117] Sum, J.P., C. Leung, and L. Chan, *Extended Kalman filter in recurrent neural network training and pruning*. Shatin, Hong Kong: Chinese University of Hong Kong, 1996.
- [118] Havlicek, M., et al., *Dynamic modeling of neuronal responses in fMRI using cubature Kalman filtering*. Neuroimage, 2011. **56**(4): p. 2109-2128.
- [119] Ramadurai, S., et al. *Application of unscented kalman filter to a cable driven surgical robot: A simulation study*. in *2012 IEEE International Conference on Robotics and Automation*. 2012. IEEE.

- [120] Akhlaghi, S., N. Zhou, and Z. Huang. *Adaptive adjustment of noise covariance in Kalman filter for dynamic state estimation*. in *Power & Energy Society General Meeting, 2017 IEEE*. 2017. IEEE.
- [121] Xie, W. and L. Sun, *Experimental and numerical verification on effects of inelastic tower links on transverse seismic response of tower of bridge full model*. *Engineering Structures*, 2019. **182**: p. 344-362.
- [122] *Strong-motion Seismograph Networks*. 2020.
- [123] Mylonakis, G. and G. Gazetas, *Lateral vibration and internal forces of grouped piles in layered soil*. *Journal of Geotechnical and Geoenvironmental Engineering*, 1999. **125**(1): p. 16-25.
- [124] Mylonakis, G. and G. Gazetas, *Vertical vibration and additional distress of grouped piles in layered soil*. *Soils and foundations*, 1998. **38**(1): p. 1-14.
- [125] Ordonez, G.A., *SHAKE2000: A computer program for the 1D analysis of geotechnical earthquake engineering problems*. Geomotions, LLC, USA, 2000.
- [126] Lee, K.J. and C.B. Yun, *Parameter identification for nonlinear behavior of RC bridge piers using sequential modified extended Kalman filter*. *Smart Struct. Syst*, 2008. **4**(3): p. 319-342.
- [127] Aucejo, M., O. De Smet, and J.-F. Deü, *Practical issues on the applicability of Kalman filtering for reconstructing mechanical sources in structural dynamics*. *Journal of Sound and Vibration*, 2019. **442**: p. 45-70.
- [128] Southall, B., B.F. Buxton, and J.A. Marchant. *Controllability and Observability: Tools for Kalman Filter Design*. in *BMVC*. 1998.
- [129] MacRae, G.A. and K. Kawashima, *Post - earthquake residual displacements of bilinear oscillators*. *Earthquake engineering & structural dynamics*, 1997. **26**(7): p. 701-716.
- [130] Kawashima, K., et al., *Residual displacement response spectrum*. *Journal of Structural Engineering*, 1998. **124**(5): p. 523-530.
- [131] Chatzi, E.N. and C. Fuggini, *Online correction of drift in structural identification using artificial white noise observations and an unscented Kalman filter*. *Smart Struct. Syst*, 2015. **16**(2): p. 295-328.
- [132] Naets, F., J. Cuadrado, and W. Desmet, *Stable force identification in structural dynamics using Kalman filtering and dummy-measurements*. *Mechanical Systems and Signal Processing*, 2015. **50**: p. 235-248.
- [133] Rauch, H.E., F. Tung, and C.T. Striebel, *Maximum likelihood estimates of linear dynamic systems*. *AIAA journal*, 1965. **3**(8): p. 1445-1450.
- [134] Kitada, Y., *Identification of nonlinear structural dynamic systems using wavelets*. *Journal of Engineering Mechanics*, 1998. **124**(10): p. 1059-1066.
- [135] Ma, F., et al., *Parameter analysis of the differential model of hysteresis*. *J. Appl. Mech.*, 2004. **71**(3): p. 342-349.
- [136] Charalampakis, A.E. *Parameters of Bouc-Wen hysteretic model revisited*. in *9th HSTAM International Congress on Mechanics*. 2010.
- [137] Chung, J. and G. Hulbert, *A time integration algorithm for structural dynamics with improved numerical dissipation: the generalized- α method*. *Journal of applied mechanics*, 1993. **60**(2): p. 371-375.
- [138] Kalman, R.E., *Mathematical description of linear dynamical systems*. *Journal of the Society for Industrial and Applied Mathematics, Series A: Control*, 1963. **1**(2): p. 152-192.
- [139] Chatzis, M.N., E.N. Chatzi, and A.W. Smyth, *On the observability and identifiability of nonlinear structural and mechanical systems*. *Structural Control and Health Monitoring*, 2015. **22**(3): p. 574-593.
- [140] Anguelova, M., *Nonlinear observability and identifiability: General theory and a case study of a kinetic model for S. cerevisiae*. 2004.
- [141] Sedoglavic, A., *A probabilistic algorithm to test local algebraic observability in polynomial time*. *Journal of Symbolic Computation*, 2002. **33**(5): p. 735-755.
- [142] Zhao, X., et al., *Hybrid identification method for multi-story buildings with unknown ground motion: theory*. *Journal of sound and vibration*, 2006. **291**(1-2): p. 215-239.
- [143] Schnabel, P.B., *SHAKE a computer program for earthquake response analysis of horizontally layered sites*. EERC Report, Univ. of California, Berkeley, 1972.

Acknowledgement

First and foremost, I would like to express my deepest gratitude to my supervisor, Assoc. Prof. Tomonori Nagayama for his constant and meticulous guidance on my research. His patient attitude always encouraged me in my academic life especially during this final time. Without his support and guidance, I cannot get this far.

I sincerely appreciate the efforts of my committee members, Prof. Takeshi Ishihara, Prof. Koichi Kusunoki, Prof. Tsuyoshi Ichimura and Assoc. Prof. Di Su for their valuable comments on my study, thesis and the presentation. These comments inspired me to make the study improved.

I would like to thank all of the Bridge & Wind Engineering Laboratory research group members. Dr. Kai Xue, Dr. Lilin Wang, Dr. Doingqin Zhang and Mr. Qi Hu for encouraging me when I experienced the toughest period of time in the three years and providing their valuable suggestions during my presentation. I also want to extend my gratitude to one of the former members of our group, Ryuta Kuniyoshi-san, for helping me regarding my daily issues in Japan. Without his support, my daily life in Japan would have been much harder.

This study could not have been conducted without the generous scholarship granted by Japanese Ministry of Education, Culture, Sports, Science and Technology (MEXT).

I'm sincerely appreciative of the support of my friends in China throughout the three years. I'm thankful to them for listening my complaints, sharing ideas. I would like to extend my gratitude to Dr. Zhixiang Shang and Mr. Jipeng Yang for giving me encouragement. I wish they could be able to achieve their goals in academic and non-academic life soon.

Finally, and most importantly, I would like to thank my parents, for their love, support, and understanding, not only during my Ph.D. study, but throughout my entire life. I'm very thankful for their support on my education throughout my life. This dissertation is dedicated to my family.